SYNTHESIS AND APPLICATIONS OF EARLY TRANSITION METAL OXIDES

By

CORY K. PERKINS

Bachelor of Science in Chemistry
Western Oregon University
Monmouth, Oregon
2009

Submitted to the Faculty of the
Graduate College of the
Oklahoma State University
in partial fulfillment of
the requirements for
the Degree of
DOCTOR OF PHILOSOPHY
May, 2014

SYNTHESIS AND APPLICATIONS OF

EARLY TRANSITION

METAL OXIDES

Dissertation Approved:

Dr. Allen Apblett

Dissertation Adviser

Dr. Frank Blum

Dr. Nicholas Materer

Dr. Charles Weinert

Dr. Gary Foutch

"Imagination is more important than knowledge. For knowledge is limited, whereas imagination embraces the entire world, stimulating progress, giving birth to evolution."

-Albert Einstein

ACKNOWLEDGEMENTS

Thanking all of the people who have helped me through the process of completing this degree is a very humbling process. I would not have been as successful in my endeavors without the help of many people, some of whom I would like to take the time to acknowledge in this document.

I would first like to extend my deepest appreciation to my advisor, Dr. Allen Apblett. The amount of knowledge I have gained from his guidance is an invaluable asset that, I am sure, will have a lasting impact on my life and career as a scientist. Both his problem solving abilities and approach to chemistry are attributes that I hope to emulate throughout my career. Again, I would like to thank Dr. Apblett for all of his priceless advice, constructive criticism, encouragement, optimism, and patience over these five years. I am very lucky that I was able to be a part of your research group.

I would like to thank my committee members: Drs. Materer, Blum, Weinert, and Foutch for serving on my committee and for their valuable advice. I would also like to acknowledge Dr. A. J. Johannes for filling in for Dr. Foutch during my dissertation defense. I would like to also thank Dr. Iob, with whom I worked with as a teaching assistant, for his always friendly advice. I would like to thank both Terry Colberg and Lisa Whitworth for all of their help teaching me to use the AFM, SEM and TEM.

I would like to thank Dr. Kevin Barber for "showing me the ropes" as an undergraduate REU student and his leadership when I was a first year graduate student. I would like to thank Dr. Cody Cannon for all of his help keeping our instruments running and his help with the solid state NMR experiments. I would also like to thank his loving family for their generosity and great friendship. My gratitude goes to Evangline Rukundo for her integral help (and patience) teaching me to use the liquid NMR, along with Asma Alothman and Ahmed Moneeb, for their willingness to help with all of the XRD experiments. I would also like to thank my dear friend, Dr. Abdulaziz Bagabas for all of his advice and friendship; I look forward to collaborating with more in the future. I also must extend a very large thank you to Travis Reed, David Corter, and Zach Brown for always proof reading my manuscripts and giving me valuable feedback. On this note, Travis Reed was extremely helpful while I was writing this dissertation by proof reading every chapter; Travis, I thank you very much! I would also like to thank Ahmedul Kabir for selflessly cooking for the entire lab group on multiple occasions. I would also like to thank the rest of the Apblett Research Group, past and present, for their assistance and friendships; you guys have made this a very joyful journey.

I would be remiss if I failed to thank the professor that first got me excited about pursuing chemistry as a career, Dr. Arlene Courtney. Thank you for believing in me and pushing me to become a better student and chemist. I hope to someday match your love for teaching, inspiring students to also pursue careers in chemistry. If it was not for you, I would not be in the position I am today. I would also like to thank Dr. Pete Poston for advising me as an undergraduate researcher and being a great teacher. Also, I would like to thank my undergraduate degree advisor, Dr. M. Rahim Kazerouni, for being a great instructor and all of the countless hours he sacrificed to teach me general and physical chemistry. Western Oregon University is a very special place due to the great instructors like you three.

I would like to thank my family for all of their love, patience, and faith in me. To the Benson Family (Dee, Juana, Jameson, and Jay), who has become my "adoptive" Oklahoma family: I would like to thank you for treating me like a member of your family since the first Thanksgiving I was able to share with you back in 2009. You guys have made my transition to Oklahoma very painless, giving me a place that literally feels like home. Again, thank you and I love you guys. I would also like to thank James Dunning and his family for their love and great friendship. I would like to thank Larry and Michelle Weber for all of their love and support. I would like to thank my aunt, Virginia Reinhard, who as always believed in me, loved and supported me my entire life. I would like to thank the Strange Family for always welcoming me home and for their love and support. I would like to thank my brothers, Justin and Brandon, and my sister in-law, Tina, for all of their love and support. I would like to also thank my parents, Connie and Jeff Perkins. Words cannot express how lucky I am to have such great parents. You have supported me throughout my life, in everything I have done, including moving to Oklahoma to pursue this doctorate. I would like to thank you guys for all of your invaluable advice throughout my entire life and always being willing to help me with whatever I need. To my family, I love you all very much and again, thank you!

To Stephanie Young, who has been a rock during the ups and downs of the graduate school, I love you and I am so grateful for all of your love and support through this journey. Your gusto for life is something that I strive to match every day. You are a wonderful woman and I am so lucky to have you in my life. Thank you for everything!

And finally, to anyone I forgot to mention, I am sorry. There has been so many people who have helped shape my life and to all of them I owe my extreme gratitude. I hope to make you all proud!

Name: Cory Perkins

Date of Degree: May 2014

Title of Study: SYNTHESIS AND APPLICATIONS OF EARLY TRANSITION METAL OXIDES

Major Field: Chemistry

An optimized synthesis of sodium molybdenum bronze was presented using 1/3 of the expensive $Na_2MoO_4 \cdot 2H_2O$ buffer as the conventional method. The need for a N_2 atmosphere was also eliminated. Further, the reaction time was increased from 3 hours to 24 hours, yielding a product with composition of $Na_{0.29}H_{0.04}MoO_3 \cdot 0.45H_2O$. Using low-cost $Na_2HPO_4 \cdot 7H_2O$ as a buffer produced a pure sodium bronze, with a composition of $Na_{0.30}MoO_3 \cdot 0.52\ H_2O$ and improving the yield from 66% to 73%.

Metal tungstates and molybdates were produced by a variety of methods, all producing nanocrystalline materials with very high yields. A nanometric suspension of MoO_3 proved to be highly reactive towards Cs^+, Ag^+, and Pb^{2+} allowing direct conversion to molybdates and polymolybdate materials. Scheelite-type alkaline earth metal tungstates were produced via a reaction of the metal acetates with tungsten oxide and tungstic acid, with acetic acid as the only byproduct. However, using $Mg(CH_3COO)_2$ produced a novel magnesium polytungstate. A single-source precursor method based on alpha-hydroxycarboxylate complexes was also reported for the synthesis in a wide variety of useful metal molybdates and tungstates, all in very high yields.

Numerous environmentally friendly materials were developed as sorbents for heavy metals, precious materials, and radionuclides. $Al_2W_3O_{12}$ proved to be an ideal candidate for the recovery of gallium from water and industrial waste streams. MoO_3 proved to be highly reactive towards aqueous lead, however toxicity of the sorbent becomes an issue due to the solubility of the sorbent. Using non-toxic and insoluble WO_3 as a sorbent was more appropriate for potable water remediation applications. The surface areas of the WO_3 sorbents correlated to both their reactivity and capacity for the uptake of heavy metals. Mesoporous-WO_3 proved to be the most reactive material towards lead. $CaWO_4$ showed a very high reactivity for the divalent heavy metals: Pb^{2+}, Cu^{2+}, and Cd^{2+}, with the highest reactivity towards lead and lowest towards cadmium. $CaWO_4$ was shown to be an excelled sorbent for the radionuclide surrogates Sr^{2+} and UO_2^{2+}. H_2WO_4 on high-surface area pellets proved to be an excellent sorbent for UO_2^{2+}. Finally, all of the materials were able to be recycled with only NaCl or NH_4Cl as byproducts, allowing for both the sorbents and the analytes to be recovered in very high yields.

TABLE OF CONTENTS

LIST OF TABLES

CHAPTER VIII

CHAPTER IX

CHAPTER X

CHAPTER XI

APPENDIX A

APPENDIX B

APPENDIX C

LIST OF FIGURES

CHAPTER I

CHAPTER II

CHAPTER III

CHAPTER IV

CHAPTER V

CHAPTER VI

CHAPTER VII

CHAPTER VIII

CHAPTER IX

CHAPTER X

CHAPTER XI

CHAPTER I

INTRODUCTION

Group (VI) transition metals have been found to have very rich chemistries due to their partially filled d-orbitals yielding a wide range of possible oxidation states. Among the group (VI) elements, molybdenum and tungsten oxides have received much attention for their interesting and useful properties. Due to these properties, both molybdenum and tungsten based materials have been widely used in industrial applications. This introduction will provide a brief explanation of some of the structures and applications of the materials used in this dissertation.

Molybdenum (VI) Oxide

Molybdenum trioxide, MoO_3, is one of the many transition metal oxides that have been used in a number of technically important applications, including electrochromism,[1] photochromism,[2] and catalysis,[3-5] among others. The MoO_3 crystal structure is comprised of a very interesting orthorhombic layered structure, representing a transitional stage between tetrahedral and octahedral coordination.[6] As illustrated in Figure 1, the structure may be considered to be built up of infinite chains of MoO_4 octahedra connected by the sharing of two oxygen corners with two neighboring tetrahedra on the *c* axis. In taking advantage of the layers, insertion of ions has led to a number of interesting materials. The intercalation of sodium, producing the nonstoichiometric sodium molybdenum bronze Na_xMoO_3, has found use in several applications. Among these include ion-exchange technologies,[7-8] peroxide-based explosive detection and neutralization,[9] and electrochromic devices.[10]

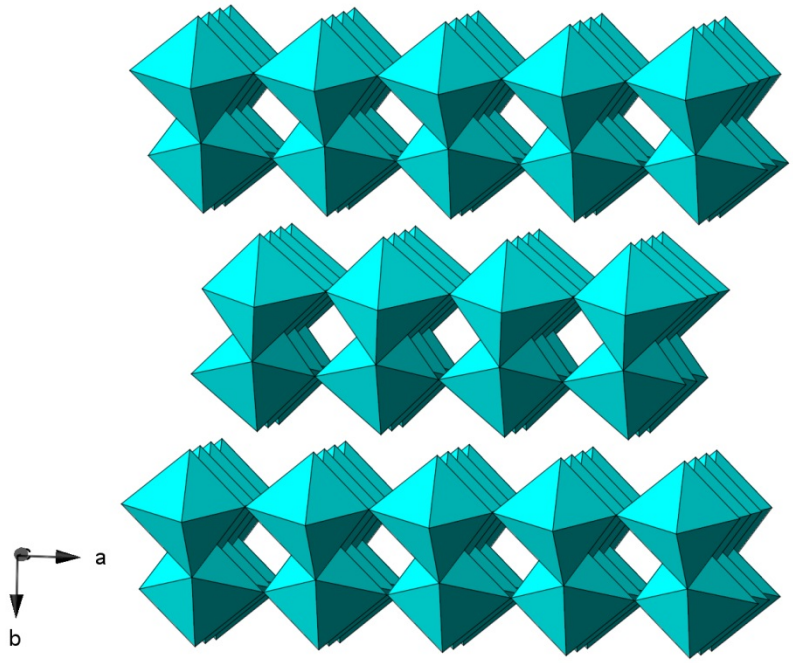

Figure 1: Layered Structure of MoO_3

Metal molybdates have been found to be useful for many applications due to their interesting properties. For example, lead molybdate, which adopts the scheelite-type structure, has been widely studied for its interesting and useful optical properties allowing it to be incorporated in several applications including scintillation detectors and in photocatalysis.[11-23] Further, aluminum and zirconium molybdates and tungstates have been studied for their interesting negative thermal expansion properties.[24-27]

Tungsten (VI) Oxide

Despite its rather simple stoichiometry, the chemistry of WO_3 is very rich and it has found use in applications such as photo-,[28] electro-,[10, 29] and thermochromic[30] devices, along with use in gas sensing applications.[31-33] The structure of WO_3 consists of a three-dimensional array of corner linked WO_6 octahedra, shown in Figure 2. Its rich chemical properties likely stem from the materials ability to undergo numerous facile crystallographic transitions at or near room temperature, as WO_3 has at least seven know polymeric forms.[34]

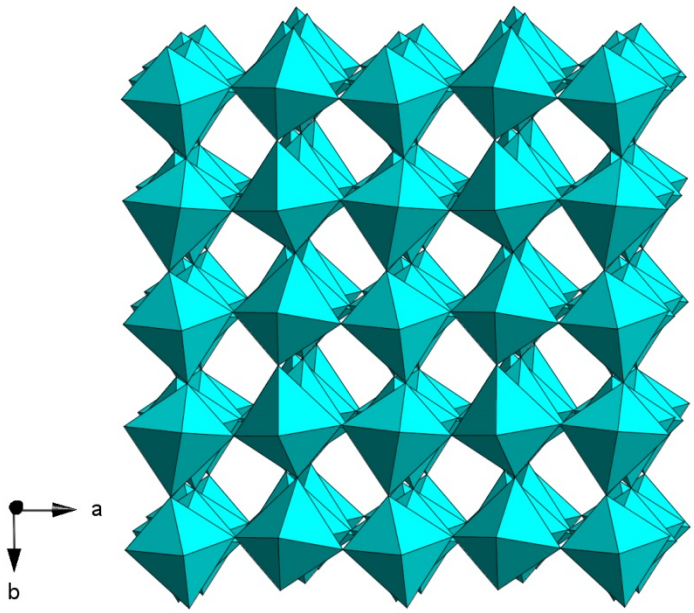

Figure 2: Three Dimensional Structure of WO3

Metal Tungstates

Owing to their interesting, highly useful, properties metal tungstates have also received much interest. For example, alkaline earth metal tungstates have been employed in a variety of roles in material science as phosphors,[35] laser media,[36-38] scintillation detectors,[39] and electro-optic materials.[40-41] Moreover, owing to their low permittivities and high Q_f values, scheelite ceramics are regarded as promising materials for microwave substrate applications.[42] Most divalent metal tungstate ($M^{2+}WO_4$) compounds are known to crystallize with either the scheelite or wolframite structures. Typically larger cations tend to adopt the scheelite structure, while smaller, more electronegative cations tend to adopt the wolframite-type structure.[43] For example, calcium tungstate ($CaWO_4$), which adopts the scheelite structure, shown in Figure 3, contains 8-coordinate calcium ions where the oxygen are arranged in an irregular deltahedral shape called a blunt disphenoid. Further, each cation in the scheelite structure is surrounded by four near-neighbor cations of the same kind and eight near-neighbor cations of the other kind.[44]

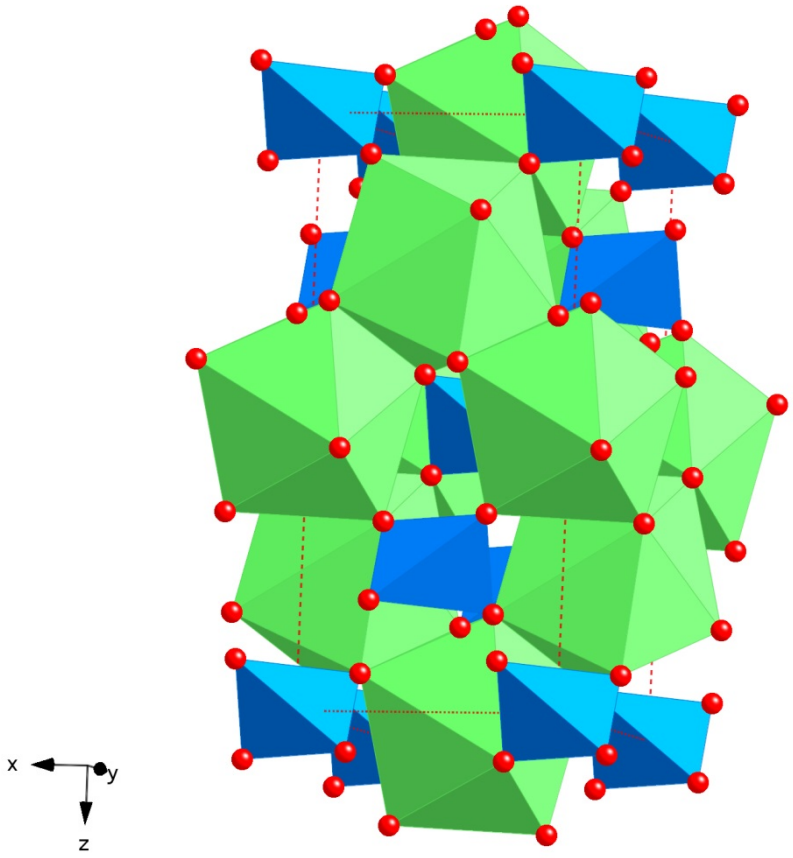

Figure 3: Structure of Calcium Tungstate

Purpose and Scope of the Research

The main objective of the research reported herein was to investigate the effectiveness of molybdenum and tungsten based reagents for their abilities to be applied to water remediation technologies, furthering research previously established by the Apblett research group. The investigation was also aimed at the synthesis of highly reactive nanometric materials using interesting reagents and a single source precursor approach. The resulting products have applications in a variety of fields, but were only applied to water remediation technologies. Moreover, the research presented in this dissertation highlights a single source precursor method to synthesize a wide range of nanometric metal molybdates and tungstates with very high yields.

The effectiveness of the produced materials to remove toxic heavy metals and radionuclides is reported herein. This study will also show the effect of particle size, porosity, and supporting the metal oxides on their ability to uptake aqueous heavy metals and radionuclides. Further, by building on the discovery of the catalytic behavior of Ca^{2+} in the sorption of toxic materials by tungstic acid,[45] calcium tungstate was directly synthesized and studied for its ability to sorb heavy metals and radionuclides. The attractiveness of using tungstate-based sorbents is the ability to recover the sorbents with high yields and the ability to repurpose the analytes for industrial applications.

Also presented in this study, is the optimization of a widely used synthetic method for synthesizing the nonstoichiometric sodium molybdenum bronze, which uses an extreme excess of reagents.[46] Further, a method for synthesizing the material utilizing a much more cost efficient buffer was discovered and will also be discussed.

References:

1. S.-Y. Lin, C.-M. Wang, K.-S. Kao, Y.-C. Chen, and C.-C. Liu, Electrochromic properties of MoO3 thin films derived by a sol–gel process. *Journal of Sol-Gel Science and Technology* **2010,** *53* (1), 51-58.

2. J. N. Yao, B. H. Loo, and A. Fujishima, A Study of the Photochromic and Electrochromic Properties of MoO3 Thin Films. *Berichte der Bunsengesellschaft für physikalische Chemie* **1990,** *94* (1), 13-17.

3. A. S. C. Brown, J. S. J. Hargreaves, and S. H. Taylor, A study of "superacidic" MoO3/ZrO2 catalysts for methane oxidation. *Catalysis Letters* **1999,** *57* (3), 109-113.

4. M. Jiang, B. Wang, Y. Yao, Z. Li, X. Ma, S. Qin, and Q. Sun, Effect of sulfidation temperature on CoO-MoO3/[gamma]-Al2O3 catalyst for sulfur-resistant methanation. *Catalysis Science & Technology* **2013,** *3* (10), 2793-2800.

5. J. C. Yori, C. L. Pieck, and J. M. Parera, Alkane isomerization on MoO3/ZrO2 catalysts. *Catalysis Letters* **2000,** *64* (2-4), 141-146.

6. M. Itoh, K. Hayakawa, and S. Oishi, Optical properties and electronic structures of layered MoO 3 single crystals. *Journal of Physics: Condensed Matter* **2001,** *13* (31), 6853.

7. B. P. Kiran, A. W. Apblett, and M. M. Chehbouni, Selective Absorption of Heavy Metals and Radionuclides from Water in a Direct-to-Ceramic Process. *Ceramic Transactions* **2003,** *143*, 385-394.

8. S. Son, F. Kanamaru, and M. Koizumi, Synthesis and characterization of the nickel(II)-rubeanic acid complex on interlamellar surfaces of molybdenum trioxide. *Inorganic Chemistry* **1979,** *18* (2), 400-402.

9. A. W. Apblett, B. P. Kiran, S. Malka, N. F. Materer, and A. Piquette, Nanotechnology for Neutralization of Terrorist Explosives. In *Ceramic Nanomaterials and Nanotechnologies IV*, John Wiley & Sons, Inc.: 2006; pp 29-35.

10. C. M. Lampert, Electrochromic materials and devices for energy efficient windows. *Solar Energy Materials* **1984,** *11* (1–2), 1-27.

11. M. Shen, Q. Zhang, H. Chen, and T. Peng, Hydrothermal fabrication of PbMoO4 microcrystals with exposed (001) facets and its enhanced photocatalytic properties. *CrystEngComm* **2011,** *13*, 2785.

12. J. C. Sczancoski, M. D. R. Bomio, L. S. Cavalcante, M. R. Joya, P. S. Pizani, J. A. Varela, E. Longo, M. S. Li, and J. A. Andrés, Morphology and Blue Photoluminescence Emission of PbMoO4 Processed in Conventional Hydrothermal. *The Journal of Physical Chemistry C* **2009,** *113* (14), 5812-5822.

13. M. Tyagi, Sangeeta, D. G. Desai, and S. C. Sabharwal, New observations on the luminescence of lead molybdate crystals. *Journal of Luminescence* **2008,** *128*, 22-26.

14. D. Piwowarska, S. M. Kaczmarek, and M. Berkowski, Dielectric, optical and EPR studies of PbMoO4 single crystals, pure and doped with cobalt ions. *Journal of Non-Crystalline Solids* **2008,** *354* (35–39), 4437-4442.

15. J. Chen, Q. Zhang, T. Liu, and Z. Shao, First-principles study of color centers in PbMoO4 crystals. *Physica B: Condensed Matter* **2008,** *403* (4), 555-558.

16. J. Chen, T. Liu, D. Cao, and G. Zhao, First-principles study of the electronic structures and absorption spectra for the PbMoO4 crystal with lead vacancy. *Physica Status Solidi (B)* **2008,** *245* (6), 1152-1155.

17. D. Spassky, S. Ivanov, I. Kitaeva, V. Kolobanov, V. Mikhailin, L. Ivleva, and I. Voronina, Optical and luminescent properties of a series of molybdate single crystals of scheelite crystal structure. *Physica Status Solidi (C)* **2005,** *2* (1), 65-68.

18. M. Hashim, C. Hu, X. Wang, X. Li, and D. Guo, Synthesis and photocatalytic property of lead molybdate dendrites with exposed (0 0 1) facet. *Applied Surface Science* **2012,** *258*, 5858-5862.

19. A. Kudo, M. Steinburg, A. J. Bard, A. Campion, M. A. Fox, T. E. Mallouk, S. E. Webber, and J. M. White, Photoactivity of ternary lead-group IVB oxides for hydrogen and oxygen evolution. *Catalysis Letters* **1990,** (5), 61-66.

20. Y. Shimodaira, H. Kato, H. Kobayashi, and A. Kudo, Investigations of Electronic Structures and Photocatalytic Activities Under Visible Light Irradiation of Lead Molybdate Replaced with Chromium(VI). *Bulletin of the Chemistry Society of Japan.* **2007,** *80* (5), 885-893.

21. M. Shen, X. Zhang, K. Dai, H. Chen, and T. Peng, Hierarchical PbMoO4 microspheres: hydrothermal synthesis, formation mechanism and photocatalytic properties. *CrystEngComm* **2013,** *15* (6), 1146-1152.

22. M. Minowa, K. Itakura, S. Moriyama, and W. Ootani, Measurement of the property of cooled lead molybdate as a scintillator. *Nuclear Instruments and Methods in Physics Research Section A: Accelerators, Spectrometers, Detectors and Associated Equipment* **1992,** *320* (3), 500-503.

23. G. P. Pazzi, P. Fabeni, C. Susini, M. Nikl, P. Bohacek, E. Mihokova, A. Vedda, M. Martini, M. Kobayashi, and Y. Usuki, Recombination luminescence in lead tungstate scintillating crystals. *Radiation Measurements* **2004,** *38* (4–6), 381-384.

24. A. W. Sleight, Negative thermal expansion materials. *Current Opinion in Solid State and Materials Science* **1998,** *3* (2), 128-131.

25. A. W. Sleight, ISOTROPIC NEGATIVE THERMAL EXPANSION. *Annual Review of Materials Science* **1998,** *28* (1), 29-43.

26. T. Varga, J. L. Moats, S. V. Ushakov, and A. Navrotsky, Thermochemistry of A2M3O12 negative thermal expansion materials. *Journal of Materials Research* **2007,** *22* (09), 2512-2521.

27. M. Ari, K. Miller, B. Marinkovic, P. Jardim, R. Avillez, F. Rizzo, and M. White, Rapid synthesis of the low thermal expansion phase of Al2Mo3O12 via a sol–gel method using polyvinyl alcohol. *Journal of Sol-Gel Science and Technology* **2011,** *58* (1), 121-125.

28. Y. Shen, H. Zhu, R. Huang, L. Zhao, and S. Yan, Synthesis and photochromic properties of WO3 powder induced by oxalic acid. *Science in China Series B: Chemistry* **2009,** *52* (5), 609-614.

29. D. S. Dalavi, R. S. Devan, R. A. Patil, R. S. Patil, Y.-R. Ma, S. B. Sadale, I. Kim, J.-H. Kim, and P. S. Patil, Efficient electrochromic performance of nanoparticulate WO3 thin films. *Journal of Materials Chemistry C* **2013,** *1* (23), 3722-3728.

30. J.-H. Cho, Y.-J. Byun, J.-H. Kim, Y.-J. Lee, Y.-H. Jeong, M.-P. Chun, J.-H. Paik, and T. H. Sung, Thermochromic characteristics of WO3-doped vanadium dioxide thin films prepared by sol–gel method. *Ceramics International* **2012,** *38, Supplement 1* (0), S589-S593.

31. R. F. Garcia-Sanchez, T. Ahmido, D. Casimir, S. Baliga, and P. Misra, Thermal Effects Associated with the Raman Spectroscopy of WO3 Gas-Sensor Materials. *The Journal of Physical Chemistry A* **2013,** *117* (50), 13825-13831.

32. T. Siciliano, A. Tepore, G. Micocci, A. Serra, D. Manno, and E. Filippo, WO3 gas sensors prepared by thermal oxidization of tungsten. *Sensors and Actuators B: Chemical* **2008,** *133* (1), 321-326.

33. W. Yu-De, C. Zhan-Xian, L. Yan-Feng, Z. Zhen-Lai, and W. Xing-Hui, Electrical and gas-sensing properties of WO3 semiconductor material. *Solid-State Electronics* **2001,** *45* (5), 639-644.

34. N. N. Greenwood and A. Earnshaw, Oxides of Chromium, Molybdenum, and Tungsten. In *Chemistry of the elements*, Pergamon Press: 1984; pp 1171-1175.

35. G. Born, A. Hofstaetter, A. Scharmann, and G. Schwarz, Luminescence mechanism of tungstate phosphors. *Journal of Luminescence* **1970,** *1–2* (0), 641-650.

36. T. T. Basiev, M. E. Doroshenko, V. V. Osiko, S. E. Sverchkov, and B. I. Galagan, New mid IR (1.5–2.2 μm) Raman lasers based on barium tungstate and barium nitrate crystals. *Laser Physics Letters* **2005,** *2* (5), 237.

37. L. I. Ivleva, T. T. Basiev, I. S. Voronina, P. G. Zverev, V. V. Osiko, and N. M. Polozkov, SrWO4:Nd3+ – new material for multifunctional lasers. *Optical Materials* **2003,** *23* (1–2), 439-442.

38. D. Christofilos, S. Ves, and G. A. Kourouklis, Pressure Induced Phase Transitions in Alkaline Earth Tungstates. *Physica Status Solidi (B)* **1996,** *198* (1), 539-544.

39. F. Zhang, M. Y. Sfeir, J. A. Misewich, and S. S. Wong, Room-Temperature Preparation, Characterization, and Photoluminescence Measurements of Solid Solutions of Various Compositionally-Defined Single-Crystalline Alkaline-Earth-Metal Tungstate Nanorods. *Chemistry of Materials* **2008,** *20* (17), 5500-5512.

40. G. Blasse and W. J. Schipper, Low-temperature photoluminescence of strontium and barium tungstate. *Physica Status Solidi (A)* **1974,** *25* (2), K163-K165.

41. G. Blasse and G. J. Dirksen, Photoluminescence of Ba3W2O9: Confirmation of a structural principle. *Journal of Solid State Chemistry* **1981,** *36* (1), 124-126.

42. M. Maček Kržmanc, M. Logar, B. Budič, and D. Suvorov, Dielectric and Microstructural Study of the SrWO4, BaWO4, and CaWO4 Scheelite Ceramics. *Journal of the American Ceramic Society* **2011,** *94* (8), 2464-2472.

43. A. W. Sleight and M. S. Licis, Crystal data for mercuric molybdate and tungstate. *Materials Research Bulletin* **1971,** *6* (5), 365-369.

44. A. W. Sleight, Accurate cell dimensions for ABO4 molybdates and tungstates. *Acta Crystallographica Section B* **1972,** *28* (10), 2899-2902.

45. H. Albusaidi and A. W. Apblett, Adsorption and Separation of Uranium Using Tungsten Oxides. In *Environmental Issues and Waste Management Technologies in the Materials and Nuclear Industries XII*, John Wiley & Sons, Inc.: 2009; pp 39-46.

46. D. M. Thomas and E. M. McCarron III, The composition and proposed structure of the alkali metal layered molybdenum bronzes. *Materials Research Bulletin* **1986,** *21* (8), 945-960.

CHAPTER II

IMPROVED SYNTHESIS OF SODIUM MOLYBDENUM BRONZE

Introduction:

The chemistry of nonstoichiometric alkali metal layered molybdates has been widely studied due to their intriguing properties. Sodium molybdenum bronze, for example, has been applied to applications in ion-exchange technologies,1-2 peroxide-based explosive detection,3 and electrochromic devices.4 Early synthetic methods for sodium molybdenum bronzes mostly utilized the ceramic method.5-7 However, Thomas and McCarron developed a method for direct ion insertion from chemical reduction using sodium dithionite ($Na_2S_2O_4$) as the reducing agent.8 This popularized method (over 75 citations) uses copious amounts of expensive $Na_2MoO_4 \cdot 2H_2O$ (60 grams in 250 mL) as a buffer for the reaction. Even though the buffer is in extreme excess (21.6 mol $Na_2MoO_4 \cdot 2H_2O$ to 1.0 mol $Na_2S_2O_4$), researchers have continued to utilize this method in the study of sodium molybdenum bronzes. Furthermore, their conclusion that this process produces a material that is intercalated with only Na^+, without protons, is incorrect, as noted here and elsewhere.7, 9, 10 The aim of this study was to optimize reaction conditions for the synthesis of the bronze, using the Thomas and McCarron method. The materials were characterized by thermal gravimetric analysis, X-ray diffraction, iodometry to determine the number of reducing equivalents, and flame photometry to determine the amount of sodium in the samples.

Experimental:

All reagents were commercial products, of ACS grade or better and were used without further purification. The sodium molybdate dihydrate was received from Sigma-Aldrich and the molybdenum trioxide (99% metal bases) was received from Alfa-Aesar, along with the 0.01 N iodine solution used to determine the reducing equivalents of the prepared samples. The $Na_2HPO_4 \cdot 7H_2O$ was received from Fisher Scientific and the sodium dithionite (83%) was received from J.T. Baker and the purity was determined by ion chromatography.[11] The water used in all of the experiments was purified by reverse osmosis followed by deionization. The original experiment as described by Thomas and McCarron was carried out to determine the identity of the produced material and compare it to the materials from the altered syntheses. However, in order to not waste large amounts of material, the reactants used for the syntheses were halved. The materials were characterized by thermal gravimetric analysis using a Mettler-Toledo TGA/DSC 1 with a rate of 5 °C/min and X-ray powder diffraction using a Bruker D8-A25-Advance with a LynxEye detector.

Determination if N_2 is Necessary

To determine if the bubbled nitrogen was needed, two samples of the Thomas and McCarron bronzes were synthesized in side-by-side reaction. Both syntheses were carried out as follows: two separate round bottom flasks with 2.5 g of MoO_3, previously sintered at 600 °C for 24 hours, were stirred in 125 mL of deionized water, one with N_2 bubbling through the system and one reacted under ambient air in a rubber-stoppered round-bottom flask. After 30 minutes of stirring, solid mixtures of 30 g of $Na_2MoO_4 \cdot 2H_2O$ and 1.2 g of $Na_2S_2O_4$ (83%) were added to each solution. After letting the solutions react for 3 hours, which produced a dark blue solid with a metallic sheen, the solutions were separated by vacuum filtration using fine-frit glass filters. The filtrate was dark green indicating some loss of an unidentified molybdenum compound occurs. The solids were then dried *in vacuo*, until they reached constant weight.

Optimization of Buffer

As stated previously, this method uses a large excess of base in this reaction. To determine the optimal amount of buffer to use, it is helpful to determine the species present in the solution. The oxidation of sodium dithionite ($Na_2S_2O_4$) can produce a maximum of 6 molar equivalents of protons, as shown in Equation 1. The protons produced by this reaction must be buffered to allow sodium atoms, rather than the protons, to intercalate.

$$S_2O_4^{2-}{}_{(aq)} + 4H_2O_{(l)} \rightarrow 2HSO_4^{-}{}_{(aq)} + 6H^{+}{}_{(aq)} + 6e^{-}$$

Equation 1: The Oxidation Reaction of Dithionite in Water

An experiment was performed using reactants in the molar ratio of 3 MoO_3: 3 $Na_2MoO_4{\cdot}2H_2O$: 1 $Na_2S_2O_4$, allowing for the exhaustion of the buffer. Thus, the reaction consisted of 2.5 g of MoO_3 that was stirred in 125 mL of deionized water for 30 minutes, to which was added 1.2 g of $Na_2S_2O_4$ (83%) and 5.0 g of $Na_2MoO_4{\cdot}2H_2O$. After the mixture reacted for 3 hours, producing a dark blue solution, the solution was separated by vacuum filtration using fine-frit glass filters. The dark metallic blue solids were then dried *in vacuo* until they achieved constant weight. This reaction was repeated using the molar ratio of 3 MoO_3: 6 $Na_2MoO_4{\cdot}2H_2O$: 1 $Na_2S_2O_4$, giving the reaction a one fold excess of the buffer.

Determination of Optimal Sintering Temperature

In order to improve the yields, an excess amount of MoO_3 was sintered at 760 °C, increasing the particle size. Side-by-side reactions using the 3:3:1 molar ratio, were conducted using both the 760 °C and 600 °C sintered MoO_3. These were reacted under the same conditions as the previous section.

Determination of Optimal Reaction Time

The results from the reaction using the MoO_3 sintered at 760 °C gave evidence that the reaction time could also be a factor in the sodium bronze synthesis. Therefore, a reaction with optimized conditions was performed for 24 hours, rather than just three hours. Upon completion, the blue suspensions were separated by vacuum filtration using fine-frit glass filters. The solids were then dried *in vacuo*, until they reached constant weight.

Synthesis of Sodium Molybdenum Bronze using a Sodium Phosphate Buffer

After optimizing the Thomas and McCarron synthetic method, a similar synthesis was performed using a much more cost-effective buffer. Multiple reactions were run to determine the optimum conditions with respect to percent yield and overall composition. A typical reaction would entail a solution with 2.5 g of the 600°C sintered MoO_3 being stirred in 125 mL of deionized water. After thirty minutes, a solid mixture of the $Na_2HPO_4 \cdot 7H_2O$ buffer and 1.2 g of $Na_2S_2O_4$ was added to the solution. The solutions were allowed to react while being magnetically stirred for 24 hours in a rubber-stoppered round-bottom flask. Upon completion, the solutions were separated by vacuum filtration using fine-frit glass filters. The solids were then dried *in vacuo* to constant mass.

Determination of Reducing Equivalents by Iodometry

Determination of the reducing equivalents of the materials was carried out by iodometry. A typical reaction consisted of reacting 50 mg of the bronze with approximately 20 mL of a 0.01 N iodine solution. The residual iodine concentration was determined by UV-Visible absorbance spectroscopy using a Cary 100 Bio UV-Visible spectrophotometer, allowing for the determination of the number of reducing equivalents per mole of the bronze. The λ_{max} for the iodine solutions was measured at 445 nm using a 0.1 cm quartz cuvette. To ensure the absorbance was linear in this range, a calibration curve was made using the stock iodine solution (Figure 1).

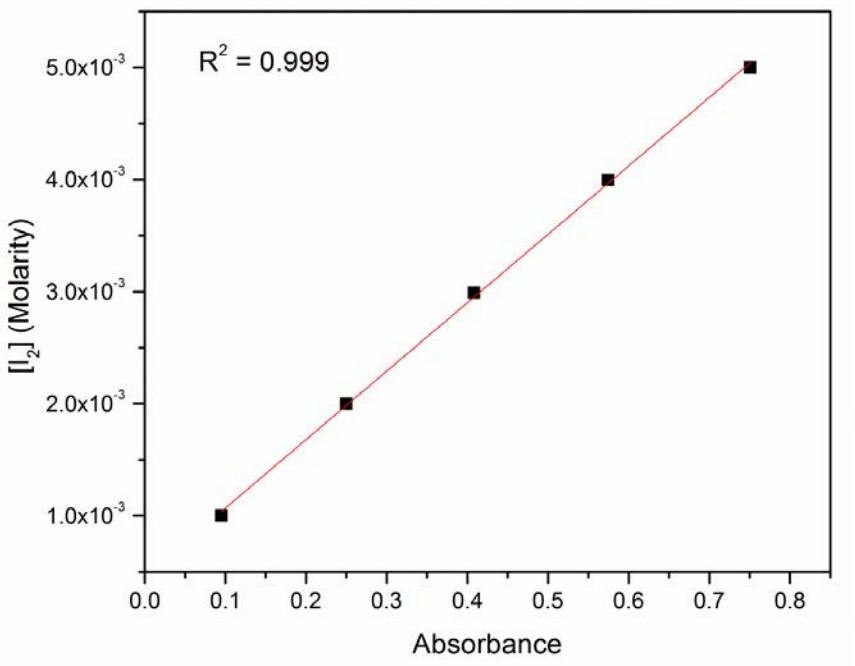

Figure 1: Calibration Curve for [I_2] by UV-Visible Spectroscopy

Determination of Sodium Composition

Flame photometry was employed to determine the sodium concentration of all of the sodium bronzes. A typical reaction required a mass of 5 mg of the sodium bronze that was dissolved in 20 mL of 0.725 M NH_4OH. Using a 100 ppm sodium standard (Fisher), a calibration curve (Figure 2) was created over the range from 0-25 ppm using a Jenway PFP7 Flame Photometer.

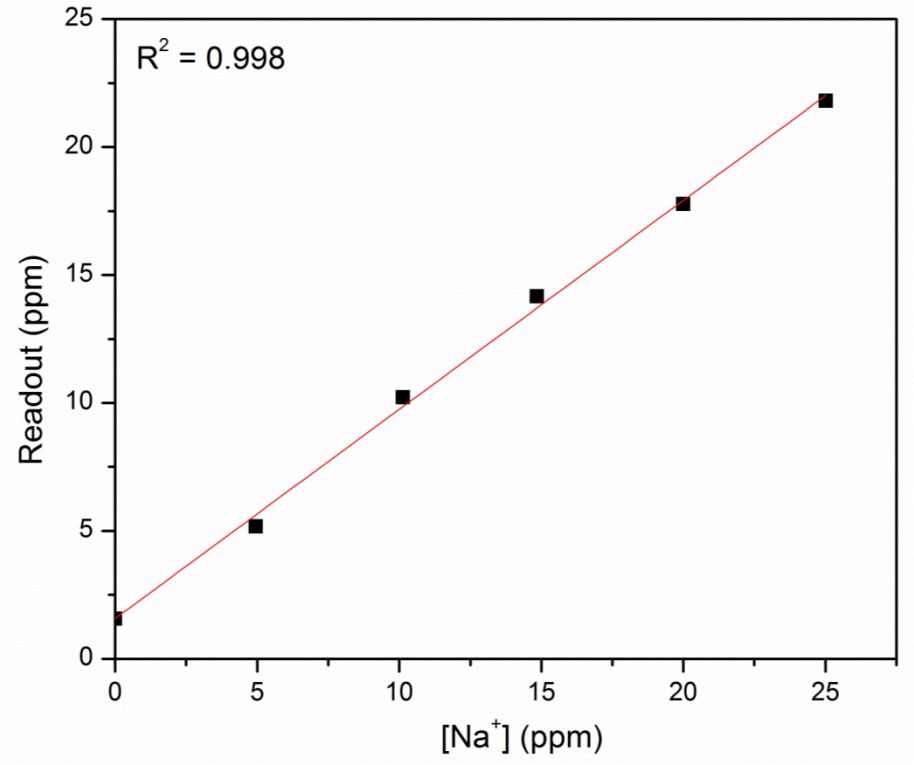

Figure 2: Calibration Curve for Sodium Concentration by Flame Photometry

Results and Discussion:

The synthesis of the sodium molybdenum bronze under nitrogen was compared to the sodium molybdenum bronze made in a limited air supply with a closed vessel that had approximately 125 mL of headspace. Both samples gave similar yields, sodium contents and reducing equivalents, as summarized in Table 1. These results suggest that the supposition that the synthesis requires nitrogen is incorrect.

Table 1: Results for the Synthesis with and without Nitrogen

Sample	Yield (%)	pH	Reducing Equivalents	mol Na/mol Mo
Thomas and McCarron with N_2	71.9%	6.9	0.286	0.24
Thomas and McCarron	73.5%	6.9	0.283	0.24

The next step was to determine the optimum buffer conditions to synthesize the sodium bronze. The synthesis of the bronze in the ratio of 3:3:1 gave a blue suspension characteristic of molybdenum bronzes. The yield of the solid was better than that of the reproduced Thomas and McCarron method, but had slightly lower reducing equivalents. However, the molar sodium content of the material was roughly half of the measured reducing equivalents, suggesting the produced solid was $Na_{0.14}H_{0.11}MoO_3$. The pH of this solution was 5.9, which is very close the pK_a reported for the $HMoO_4^-$-MoO_4^{2-} system of 6.0.[12] These results suggest that a stoichiometric amount of sodium molybdate is insufficient to prevent proton intercalation into the product. That is the molybdate does not act simply as a stoichiometric reagent. As a buffer, the buffer point would occur with equal amounts of MoO_4^{2-} and $HMoO^{4-}$. Therefore the reaction was performed with six equivalents of Na_2MoO_4 per mole of $Na_2S_2O_4$.

To improve the yields of the bronzes, molybdenum trioxide was sintered at 760 °C for 24 hours to increase the particle size. This material was then used to synthesize the sodium bronze using the 3:3:1 ratio method. The reaction of the larger particle size MoO_3, when compared to a similar reaction using the 600 °C sintered MoO_3, gave an improved yield of roughly 7%. However, the molar reducing equivalents were lower than that of the bronze made from the MoO_3 sintered at 600 °C, 0.244 vs. 0.185. These results suggest the reaction time of 3 hours was not sufficient for the reaction to be completed. The two different MoO_3 starting materials were reacted side-by-side and allowed to react for 24 hours. Both the yields and the molar reducing equivalents were within 1% of each other, suggesting that the extent of the reaction had been reached. Further, the molar reducing equivalents were improved from 0.244 to 0.389 per mole with a sodium content of 0.143. When the original reaction reported by Thomas and McCarron was run for 24 hours, the molar reducing equivalents were also improved to 0.312, similar to the reducing equivalents measured for the synthesis using the 3:6:1 ratio.

When doubling the amount of sodium molybdate buffer, a reaction with a ratio of 3:6:1, all of the protons should be buffered by the $HMoO_4^-$-MoO_4^{2-} system. The reaction was carried out in a similar fashion as the original Thomas and McCarron method, although with the increased reaction time. The synthesis produced a product with a similar yield and a higher sodium to reducing equivalent ratio, using only one third of the sodium molybdate buffer that was originally reported. The results, summarized in Table 2, show that the optimized synthetic method gives the best results for the synthesis of sodium molybdenum bronzes.

Table 2: Summary of the Results for the Thomas and McCarron Method

Sample	Yield (%)	pH	Reducing Equivalents*	mol Na/mol Mo	Na/Red. Equiv. (%)
Thomas and McCarron 3hr	73.5%	6.9	0.283	0.24	85%
Thomas and McCarron 24hr	66.7%	6.8	0.312	0.25	80%
3:3:1 600°C 3hr	82.3%	5.9	0.244	0.14	57%
3:3:1 760°C 3hr	89.2%	5.9	0.185	0.12	65%
3:3:1 600°C 24 hr	84.3%	6.0	0.389	0.14	36%
3:3:1 760°C 24 hr	83.6%	5.9	0.386	0.14	36%
3:6:1 600°C 24 hr	65.7%	6.3	0.326	0.29	89%

*Per mole of Mo

Further, the materials were characterized by XRD, matching the previously material from the ICDD database (PDF 00-039-0634) depicted in Figure 3. The materials were characterized by TGA to determine their H_2O content, Figure 4 shows the TGA of the synthesized optimized bronze. The data shows a weight loss of 5.2%, correlating to 0.45 mols of water per formula unit, consistent with the results reported by Thomas and McCarron. From the gathered data, it can be noted that the optimized synthesis makes the same material as the original report.

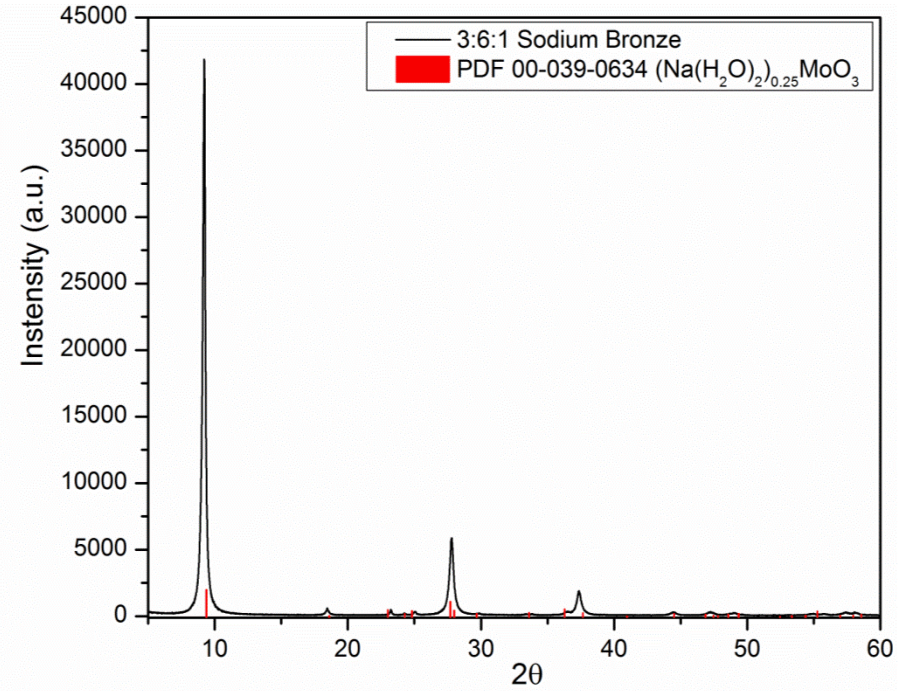

Figure 3: XRD Pattern for the Bronze Synthesized with the 3:6:1 Ratio

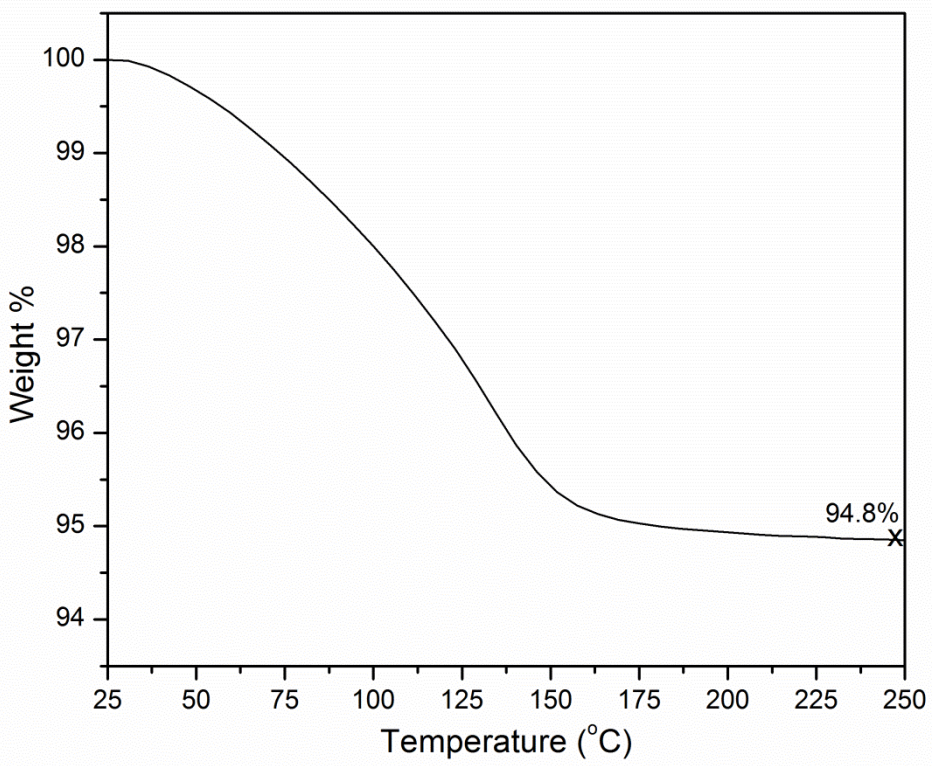

Figure 4: The TGA for the Bronze Synthesized with the 3:6:1 Ratio

Due to the high cost of sodium molybdate, a more economical buffer was investigated for the synthesis of the sodium molybdenum bronze. Due to the low cost and versatility, disodium phosphate, $Na_2HPO_4 \cdot 7H_2O$, was chosen for this study and the reactions were run under the same conditions detailed previously for the optimized Thomas and McCarron method. Varying amounts of the disodium phosphate buffer were used to optimize this reaction, from 0.075 M to 0.20 M solutions. The yields, molar reducing equivalents, and sodium contents are listed in Table 3. The results show that this method does not produce a bronze with intercalated protons, as the Thomas and McCarron method did. Further, the percent yield of the material was improved to 73%, compared to the average 63% yield from the Thomas and McCarron method. X-ray fluorescence spectroscopy confirmed the material did not contain any phosphorous, as the formation of molybdophosphates was a possibility using the phosphate buffer. The XRD of the material was consistent with the sodium molybdenum bronzes synthesized by the Thomas and McCarron method, shown in Figure 5. Further, the TGA data gave similar results for the material synthesized by the Thomas and McCarron method, with a weight loss 5.8%, consistent with 0.52 mols of water per formula unit.

Table 3: Summary for the Synthesis of Sodium Bronze Using the Disodium Phosphate Buffer

Sample	Yield (%)	pH	Reducing Equivalents	mol Na/mol Mo
0.200 M Na_2HPO_4	59.5%	6.4	0.295	0.33
0.125 M Na_2HPO_4	73.6%	6.0	0.290	0.31
0.100 M Na_2HPO_4	72.3%	5.8	0.300	0.30
0.0750 M Na_2HPO_4	35.7%	4.3	0.300	0.30

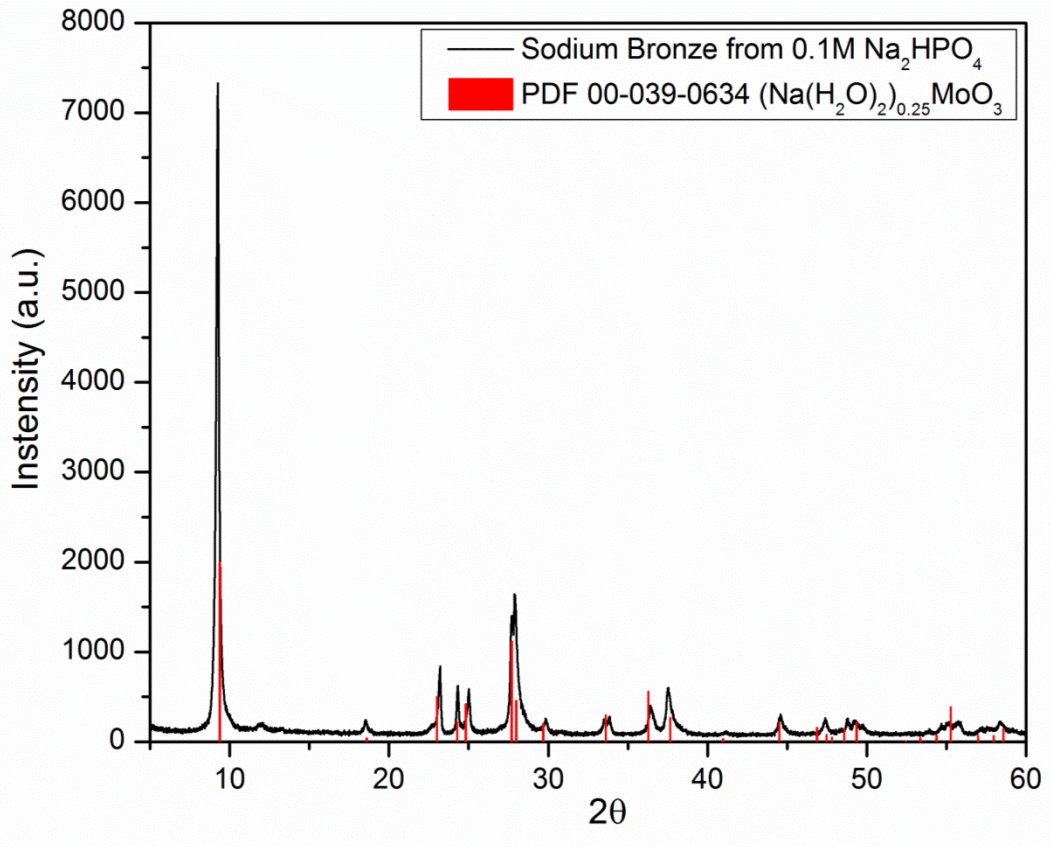

Figure 5: XRD Pattern for the Sodium Bronze Synthesized with the Phosphate Buffer

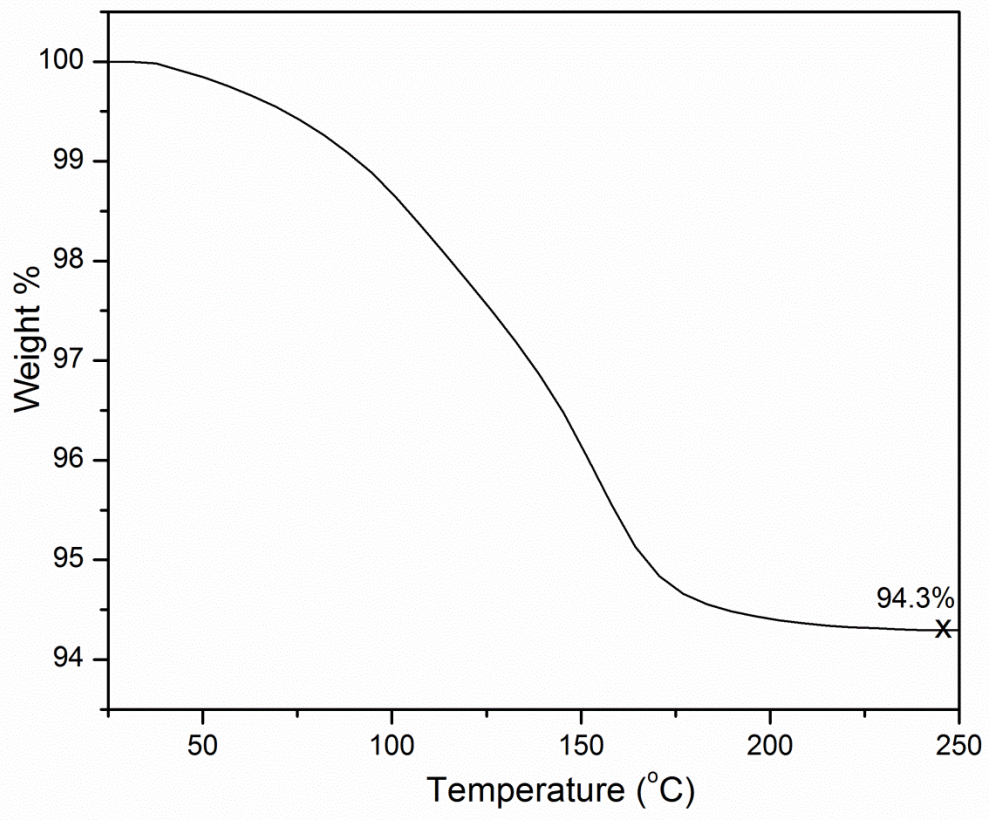

Figure 6: TGA of the Sodium Molybdenum Bronze Synthesized Using a Phosphate Buffer

Conclusion:

The synthesis of sodium molybdenum bronze was optimized by reducing the amount of sodium molybdate buffer needed in the synthesis by one third and eliminating the unneeded N_2 gas. The synthesis gave a product with a nearly identical composition as the product synthesized from the original method. Further, the reducing capacity of the material was improved by allowing the reaction to continue for 24 hours, ensuring the reaction was complete. Sodium molybdenum bronze was also able to be synthesized by employing a more economical buffer. The product from the disodium phosphate buffered solution gave a product with a similar composition as the Thomas and McCarron method, while giving a slightly improved yield. Further studies could be carried out to find other buffer systems to successfully synthesize sodium molybdenum bronzes.

References:

1. B. P. Kiran, A. W. Apblett, and M. M. Chehbouni, Selective Absorption of Heavy Metals and Radionuclides from Water in a Direct-to-Ceramic Process. *Ceramic Transactions* **2003,** *143*, 385-394.

2. S. Son, F. Kanamaru, and M. Koizumi, Synthesis and characterization of the nickel(II)-rubeanic acid complex on interlamellar surfaces of molybdenum trioxide. *Inorganic Chemistry* **1979,** *18* (2), 400-402.

3. A. W. Apblett, B. P. Kiran, S. Malka, N. F. Materer, and A. Piquette, Nanotechnology for Neutralization of Terrorist Explosives. In *Ceramic Nanomaterials and Nanotechnologies IV*, John Wiley & Sons, Inc.: 2006; pp 29-35.

4. C. M. Lampert, Electrochromic materials and devices for energy efficient windows. *Solar Energy Materials* **1984,** *11* (1–2), 1-27.

5. A. Yoshikawa, K. Yagisawa, M. Shimoda, F. Terasaki, N. Takano, and N. Naito, Single-crystal growth of a new sodium molybdenum bronze Na0.86Mo5O14. *Journal of Materials Science Letters* **1997,** *16* (8), 619-620.

6. A. Wold, W. Kunnmann, R. J. Arnott, and A. Ferretti, Preparation and Properties of Sodium and Potassium Molybdenum Bronze Crystals. *Inorganic Chemistry* **1964,** *3* (4), 545-547.

7. N. Sotani, K. Eda, and M. Kunitomo, Characterization of hydrated sodium molybdenum bronzes. *Journal of Solid State Chemistry* **1990,** *89* (1), 123-129.

8. D. M. Thomas and E. M. McCarron III, The composition and proposed structure of the alkali metal layered molybdenum bronzes. *Materials Research Bulletin* **1986,** *21* (8), 945-960.

9. K. Eda, M. Suzuki, F. Hatayama, and N. Sotani, Potassium-sodium ion exchange on hydrated molybdenum bronze. *Journal of Materials Chemistry* **1997,** *7* (5), 821-826.

10. K. Eda, T. Miyazaki, F. Hatayama, M. Nakagawa, and N. Sotani, Cesium–Sodium Ion Exchange on Hydrated Molybdenum Bronze and Formation of New Cesium Molybdenum Bronze by a Low-Temperature Synthesis Route. *Journal of Solid State Chemistry* **1998,** *137* (1), 12-18.

11. T. James, A. Apblett, and N. F. Materer, Rapid Quantification of Sodium Dithionite by Ion Chromatography. *Industrial & Engineering Chemistry Research* **2012,** *51* (22), 7742-7746.

12. M. Li, Z. Twardowski, F. Mok, and N. Tam, Sodium molybdate—a possible alternate additive for sodium dichromate in the electrolytic production of sodium chlorate. *J Appl Electrochem* **2007,** *37* (4), 499-504.

CHAPTER III

CONVERSION OF A NANOMETRIC SUSPENSION OF MOLYBDENUM TRIOXIDE TO NANOMETRIC METAL MOLYBDATES

Introduction:

Metal molybdates have been found to be useful for many applications due to their interesting properties. More specifically, the interesting and useful optical properties of lead molybdate, $PbMoO_4$,[1-7] has allowed it to be incorporated in several applications including scintillation detectors,[8-9] birefringent filters,[10] fiber optics,[11-12] photoconductive,[13] luminescent,[14-15] and thermoluminescent devices,[16] and in photocatalysis.[17-20] A variety of techniques have been used for the production of nanoparticulate lead molybdate including chemical precipitation,[21-23] hydrothermal reactions, [2, 20] sonochemical synthesis,[24] solid state reactions,[25] and crystal growing methods.[3, 26] Unfortunately, there are drawbacks to these techniques including high temperatures, long reaction times, and side reactions that take place if conditions are not precisely controlled. Further, it has been reported that under uncontrolled conditions, the formation of roughly 87 unwanted phases, such as Pb_2MoO_5 and other lead polymolybdates, have occurred.[27]

This investigation utilized an unusual reagent, dissolved molybdenum trioxide that is itself a nanometric material. The Apblett group has previously shown that bulk molybdenum trioxide reacts with heavy metals, actinides, and lanthanides to form metal molybdates.[28-32] The

work reported herein was prompted by the reported solubility of molybdenum trioxide in water that suggested a solution-based procedure for production of metal molybdates was possible, leading to a publication in CrystEngComm.[33] Further this work was extended to determine if this method could be used for the synthesis of other metal molybdates.

Experimental:

All reagents were commercial products, of ACS grade or better and used without further purification. To prepare a solution of dissolved molybdenum, an excess amount of solid MoO_3 (5 g/L) was refluxed in water for 24 hours. X-ray fluorescence (XRF) spectroscopy was used in order to determine the concentration of the dissolved MoO_3 solution using a QuanX EC XRF spectrometer. To produce the $PbMoO_4$ precipitate, a 500 mL portion of this solution was reacted with a one molar equivalent of lead nitrate solution by dissolving 1.35 g in 500 mL of water. The materials were characterized by infrared spectroscopy (IR) obtained as a KBr pellet using a Nicolet Magna 750 IR spectrometer, Raman spectroscopy using a Nicolet NXR 9610 Raman spectrometer, and UV-Visible spectroscopy on a Cary-50 Bio spectrometer. Particle size analysis was measured using dynamic light scattering (DLS) on a Malvern HPPS instrument. Thermo-gravimetric analysis was performed on a Mettler-Toledo TGA/DSC 1 at a rate of 5°C/min on the synthesized materials to determine the amount of bound water. X-ray powder diffraction (XRD) was used to determine the identity and the crystalline phases of the materials, obtained using a Bruker D8-A25-Advance with a LynxEye detector. Scanning electron microscopy (SEM) and transmission electron microscopy (TEM) with Evex energy-dispersive X-ray spectroscopy were used in to determine the grain boundaries, particle sizes, and morphologies of the materials using a FEI Quanta 600 field emission gun environmental scanning electron microscope and a JEOL JEM-2100 transmission electron microscope (TEM) instrument, respectively.

Results and Discussion:

To determine the concentration of the MoO_3 solutions, the residual solid was removed from the solution via vacuum filtration and the filtrate was analyzed by XRF, indicating a concentration of approximately 750 ppm Mo or 1130 ppm of MoO_3. A 500 mL sample of this solution was reacted with a one molar equivalent of lead nitrate solution (1.35 g) dissolved in 500 ml of water. Upon mixing of the solutions an immediate reaction occurred to produce a white precipitate. The material, separated by vacuum filtration, was dried in a vacuum oven, to yield 1.44 g of lead molybdate, a 96.7% yield after correction for water content.

The XRD pattern (Figure 1) of the precipitate matched that of $PbMoO_4$ (PDF 01-074-1075) present in the ICDD database. The peaks were broadened so the full width at half maximum (FWHM) of the (112) peak was determined using the Pearson VII profiling function. This, along with the results from a highly crystalline corundum standard, were used to determine the lower limit of grain size to be 49 nm via the Scherer equation.

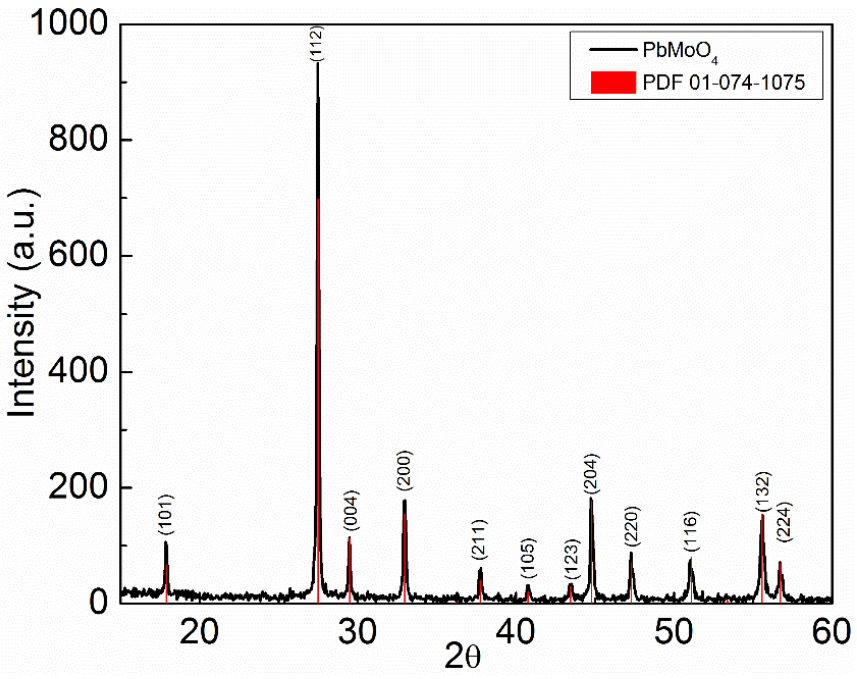

Figure 1: The XRD of Nanometric $PbMoO_4$

If each of the reactants are diluted by a factor of 10, a small amount of precipitate along with a stable suspension of nanoparticles was produced. The suspension showed a strong Tyndall effect so that in scattered light it appears slightly opalescent white but is yellow in transmitted light as shown in Figure 2. Correspondingly, the UV-visible spectrum (Figure 3) of the suspended solution showed a broad peak from 200-800 nm that is likely due to scattering by the particles. There is a peak superimposed upon this broad envelope that has λ_{max} of 365 nm that is characteristic of $PbMoO_4$ with particle sizes between 30 nm and 52 nm as reported by Anandakumar and Khadar.[34] They reported that increasing grain size correlates to the broadening of the absorption peak along with a bathochromic shift. The result from UV-Visible spectroscopy was consistent when compared to DLS analysis (Figure 4) that showed an average particle diameter of 47 nm. This is markedly smaller than the nanoparticles of the MoO_3 nanosuspension that was used (190 nm), further suggesting that the formation of $PbMoO_4$ proceeds by a dissolution/reprecipitation mechanism. Interestingly, the particle size is very close to the grain size (49 nm) of the $PbMoO_4$ precipitated with higher concentrations of reactants, implying a preference for formation of a finite crystal size in these reactions.

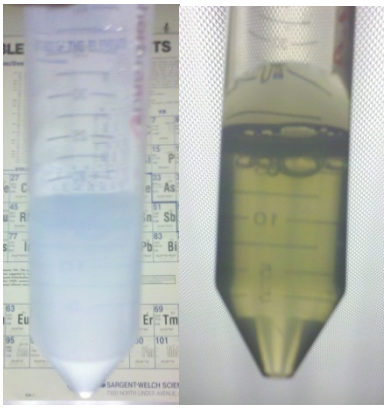

Figure 2: The Tyndall Effect Observed as the Lead Molybdate Solution Shown as a White Suspension (left), as it is Held up to a Light the Solution Turns from White to Yellow (right)

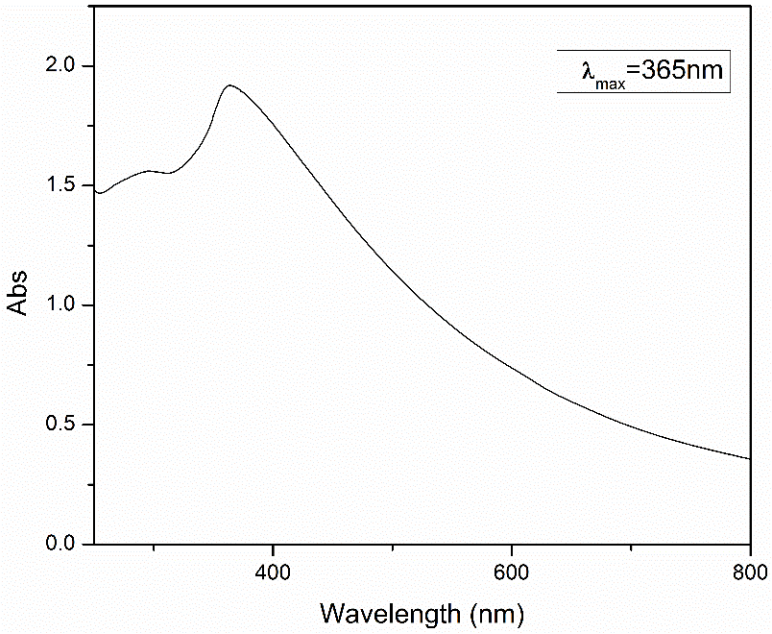

Figure 3: UV-Visible Spectrum of the 1:10 Dilution of the Suspension

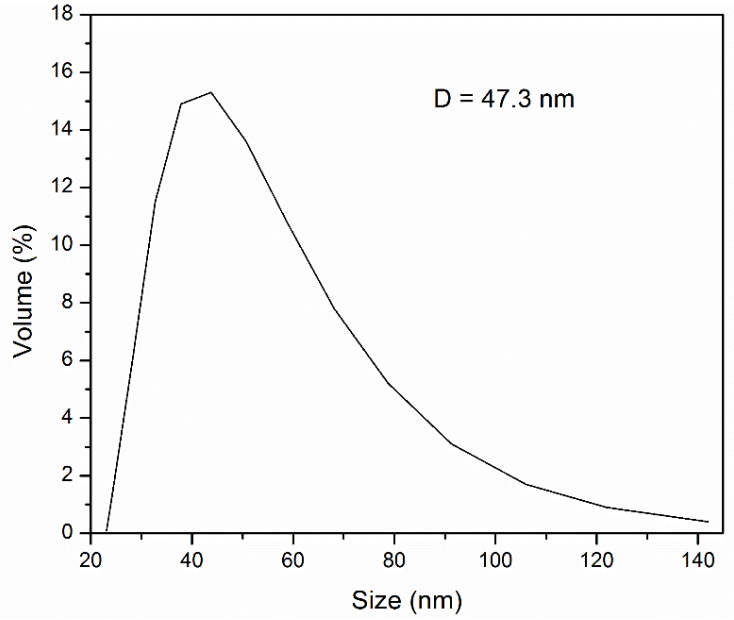

Figure 4: DLS of the Precipitated $PbMoO_4$

Scanning electron microscopy using a showed that the primary particles were aggregated into larger agglomerates such as the 10 micron sized chicken shown in Figure 5. Embedding and

sectioning of these agglomerates with a microtome allowed their nanocrystalline nature to be imaged by transmission electron microscopy. The resulting micrographs, shown in Figure 6, clearly shows rounded tabular particles with an average size of 47 ± 16 nm, measured using ImageJ image processing software. Lattice fringes could be observed for a few of the particles and Figure 6 shows two particles in which the lattice fringes correspond to the 210 and 200 planes of lead molybdate. It is evident that the aggregated nanoparticles are not crystallographically aligned.

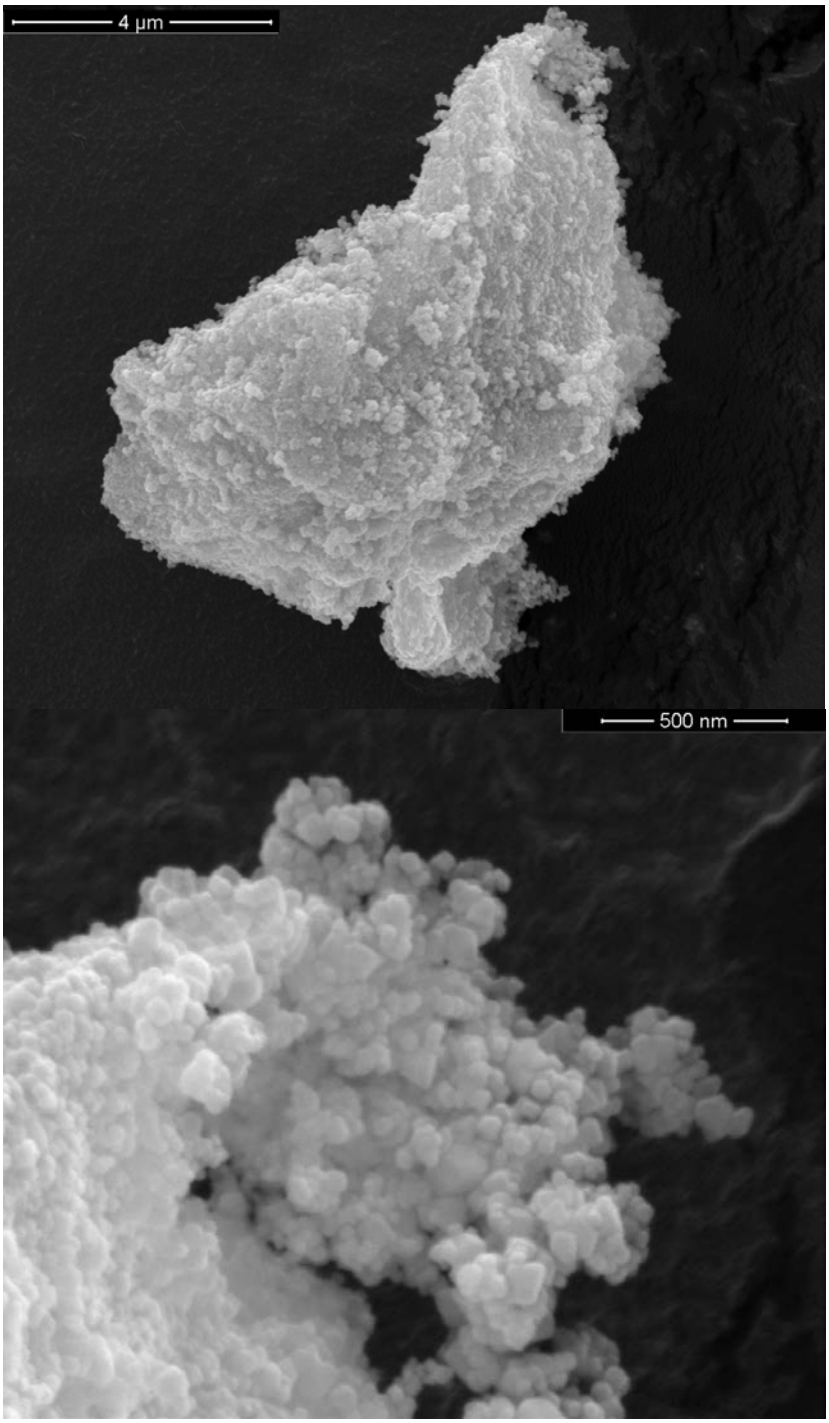

Figure 5: SEM Micrographs of $PbMoO_4$

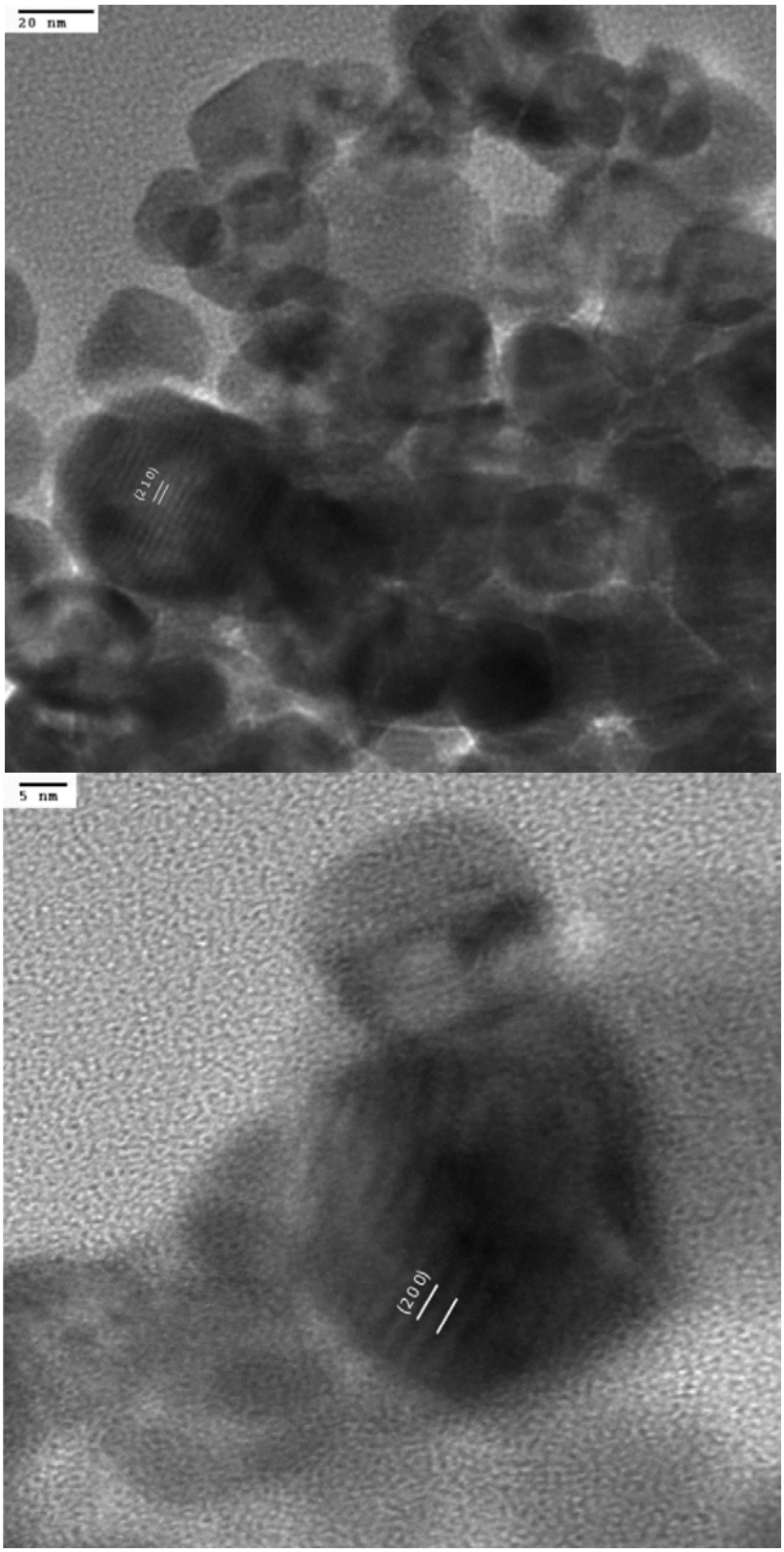

Figure 6: HRTEM of Sectioned Nanoparticulate $PbMoO_4$

The nanocrystalline nature of the product suggested that the surface of the particles might be terminated by species such as bound water or nitrate ions. Analysis by X-ray emission in the SEM did not show the presence of nitrogen in the particles so bound water was suspected. The infrared (IR) spectrum (Figure 7) contained a single peak at 752 cm^{-1} that was attributable to the anti-symmetric Mo–O stretching mode of the tetrahedral MoO_4^{2-} ion.[24, 35-37] Bound water is also indicated in the spectrum by peaks at 3438 and 1617 cm^{-1}. The bound water was also apparent in the TGA data, which showed a 1.99% weight loss upon heating to 900°C, corresponding to a molecular formula of $PbMoO_4 \cdot 0.4H_2O$.

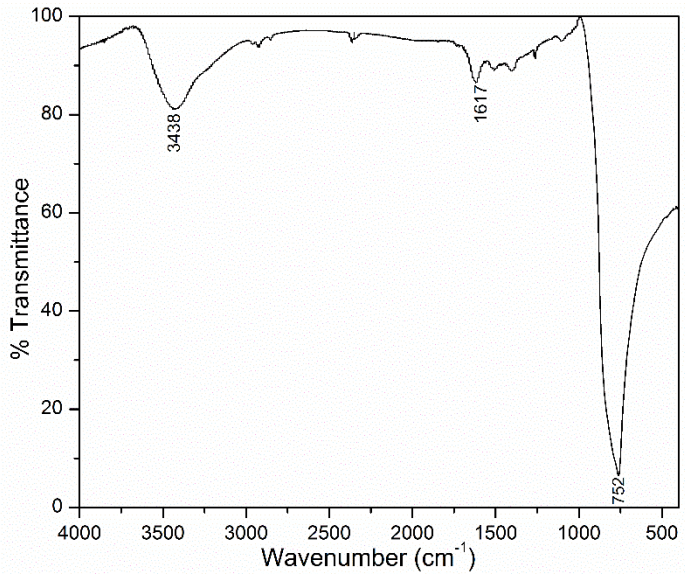

Figure 7: The Infrared Spectrum of $PbMoO_4$ Showing the Charge Transfer Band of Mo-O and the Bound Water

The Raman spectrum (Figure 8) showed the characteristic $\nu_1(A_g)$ symmetric stretching band for the tetrahedral molybdate ion at 870 cm^{-1}.[35] The peaks at 767 and 744 cm^{-1} correspond to the splitting of the ν_3 mode, with the band the higher energy band being the $\nu_3(B_g)$ vibration while the second one is due to the $\nu_3(E_g)$ vibration of molybdate. The ν_2 mode is also split into two bands, with the strong $\nu_2(A_g)$ vibration of the molybdate occurring at 318 cm^{-1} and the weaker $\nu_2(B_g)$ vibration present at 350 cm^{-1}.[38] The small band at 189 cm^{-1} can be attributed to the ν(Pb-

O), while the peak 166 cm^{-1} can be ascribed to the translational mode of MoO_4^{2-} around the z-axis.[39-41]

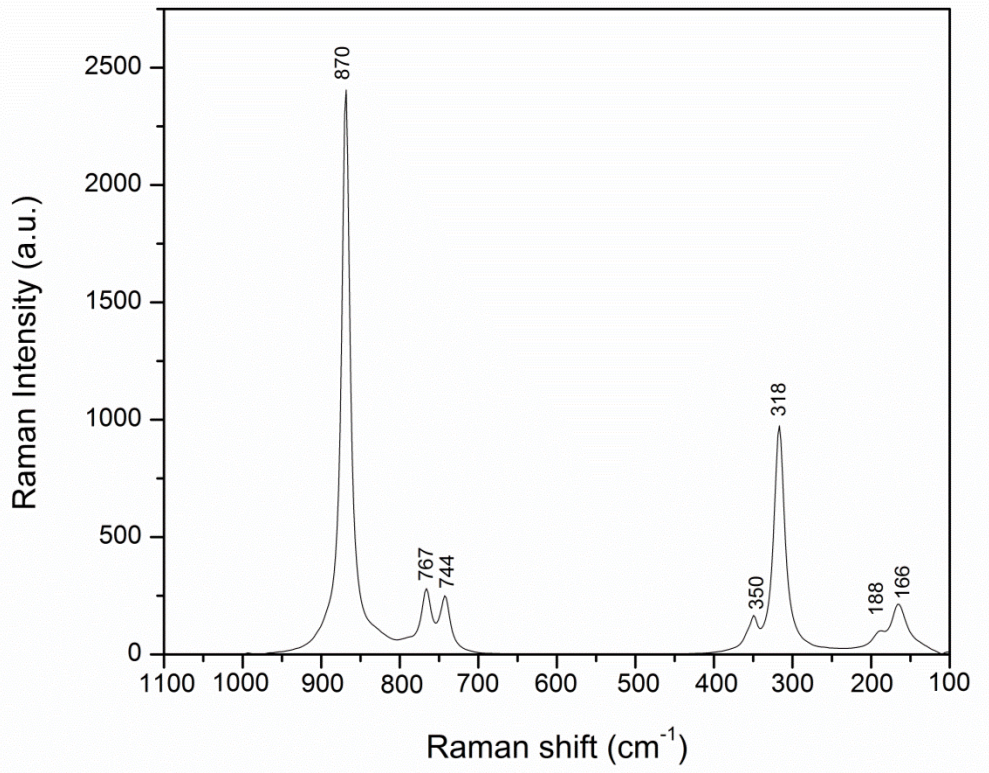

Figure 8: The Raman Spectrum of Nanometric $PbMoO_4$ Showing Mo-O and Pb-O Interactions

Further, very high dilution of the reactants (1:150) gave a reaction where a visible precipitate was no longer present. This mixture was characterized by transmission electron spectroscopy after evaporating a drop of solution on a TEM grid. The resulting micrographs (Figure 9) showed a significant uniformity in both particle size and shape. The primary nanoparticles have a square tabular morphology and a size of 250±38 nm. These are slightly larger than the particles in the MoO_3 nanosuspension utilized for their preparation. It appears that under high dilution individual MoO_3 nanoparticles react with lead ions to form lead molybdate nanoparticles. The square tiles are arranged in overlapping offset stacks that have shapes that resemble German iron crosses. Notably, these structures are different in shape from the rounded

tabular primary particles (Figure 9) found in the precipitates produced by reaction of higher-concentration reactants and are also surprisingly larger than the latter particles and the suspended nanoparticles produced in less dilute sample.

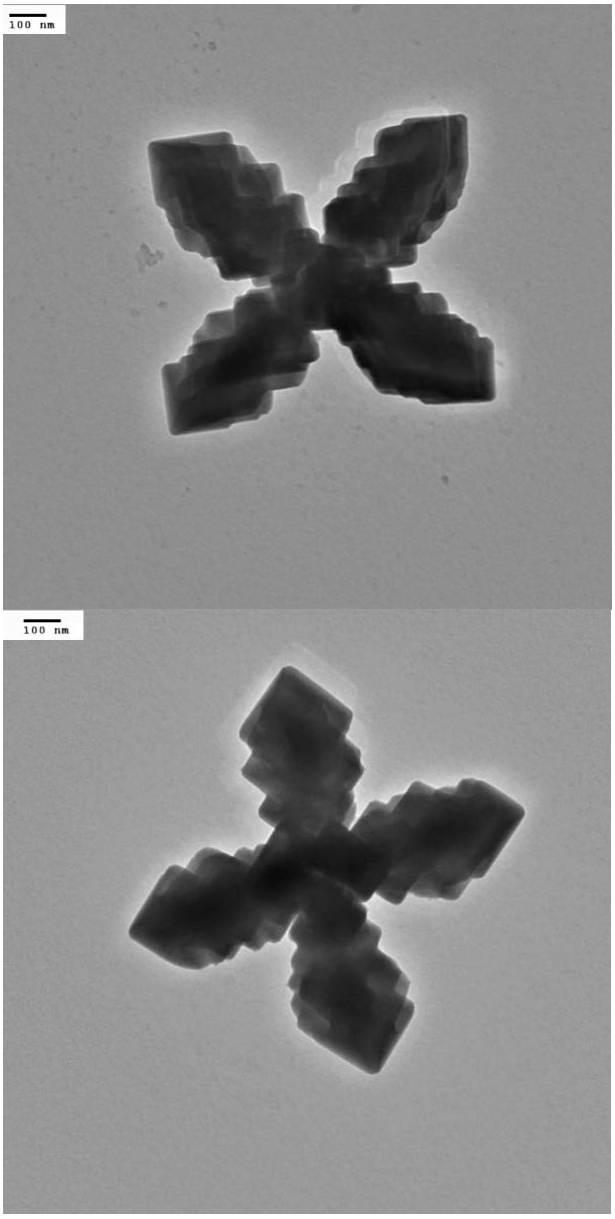

Figure 9: TEM Micrographs of $PbMoO_4$ from Highly Dilute Starting Materials. Notice the Perpendicular Axis of Growth.

The nanometric suspension of MoO_3 starting material had a much different morphology than the particles reacted with Pb^{2+}. It was imaged by diluting 150 fold and then placing a drop of the resulting suspension on a TEM grid. The nanometric suspension produced tabular particles, similar to the bulk $PbMoO_4$ material, but with a size much more similar to that of the 1:150 diluted $PbMoO_4$ with a diameter of 133 ± 22 nm, shown in Figure 10. Further, the material showed lattice fringes with spacing much greater than reported for MoO_3.

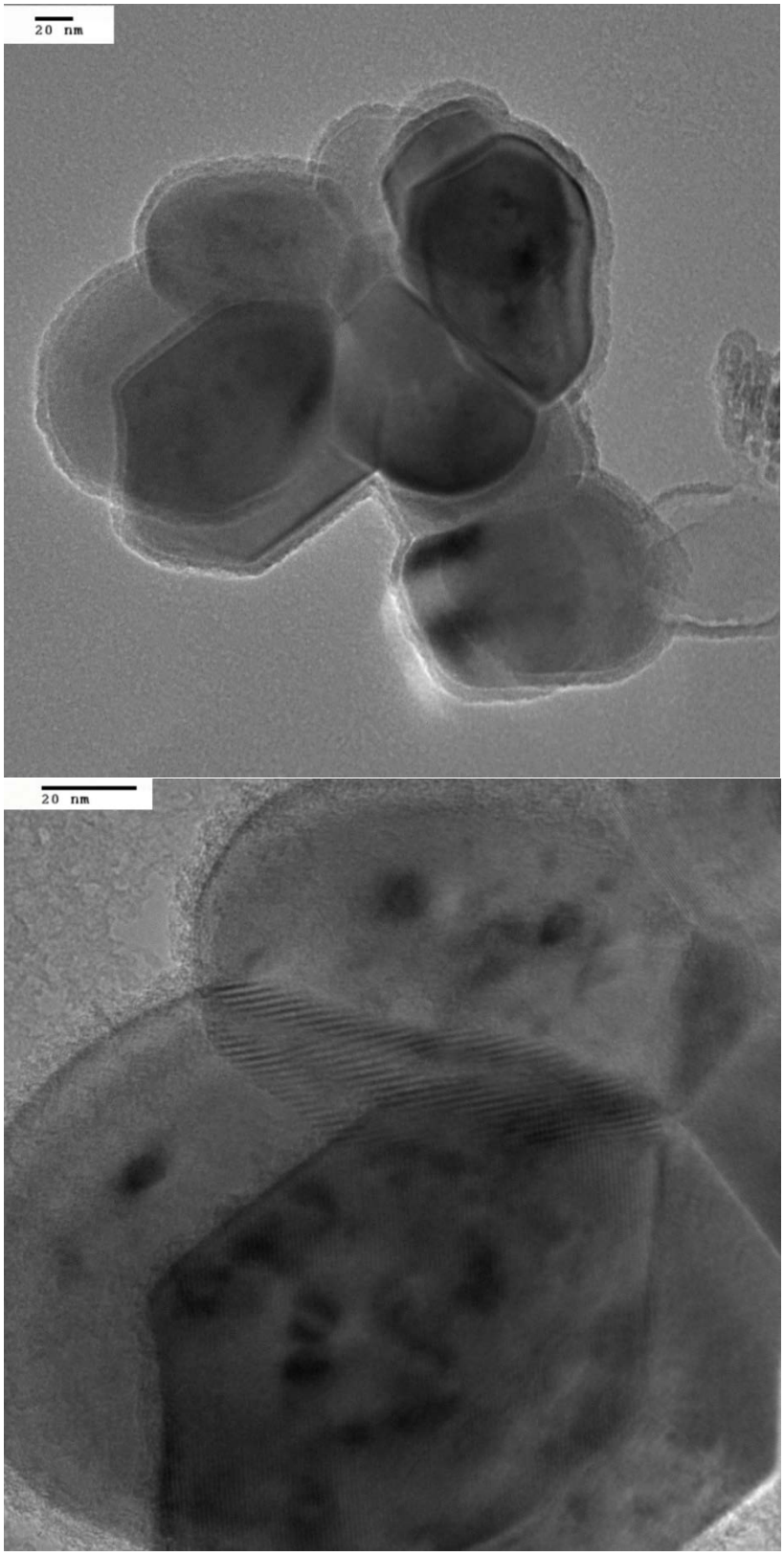

Figure 10: HRTEM of the Suspension of MoO_3

To determine if this reaction was unique to lead salts, the suspension was reacted with the nitrate salts of copper, cobalt, nickel, and uranyl. The only one of these salts that produced a visible precipitate when reacted with nanometric suspension was uranyl, producing a yellow-colored amorphous product. When the suspension was reacted individually with the nitrate salts of Ag^+ and Cs^+, precipitation occurred. However, the silver-molybdate solid was amorphous and also could not be characterized by Raman spectroscopy due to burning of the sample. The material should be further studied as silver molybdate has received much attention due to its interesting properties and has been used as a photocatalyst,[42] as a component in conductive glasses,[43] and in battery applications.[44] On the other hand the MoO_3 reaction with cesium formed a crystalline product shown in Figure 11, although not one that has been previously been reported. This material should also be further studied to determine the materials identity, which could possibly lead to determining a proper material for aqueous Cs^+ mitigation. This would be particularly useful for radioactive cesium removal from aqueous systems. Both of the newly formed materials were analyzed by SEM and EDEX, showing both materials contained the monovalent ion and molybdenum with a similar morphology to the precipitated $PbMoO_4$.

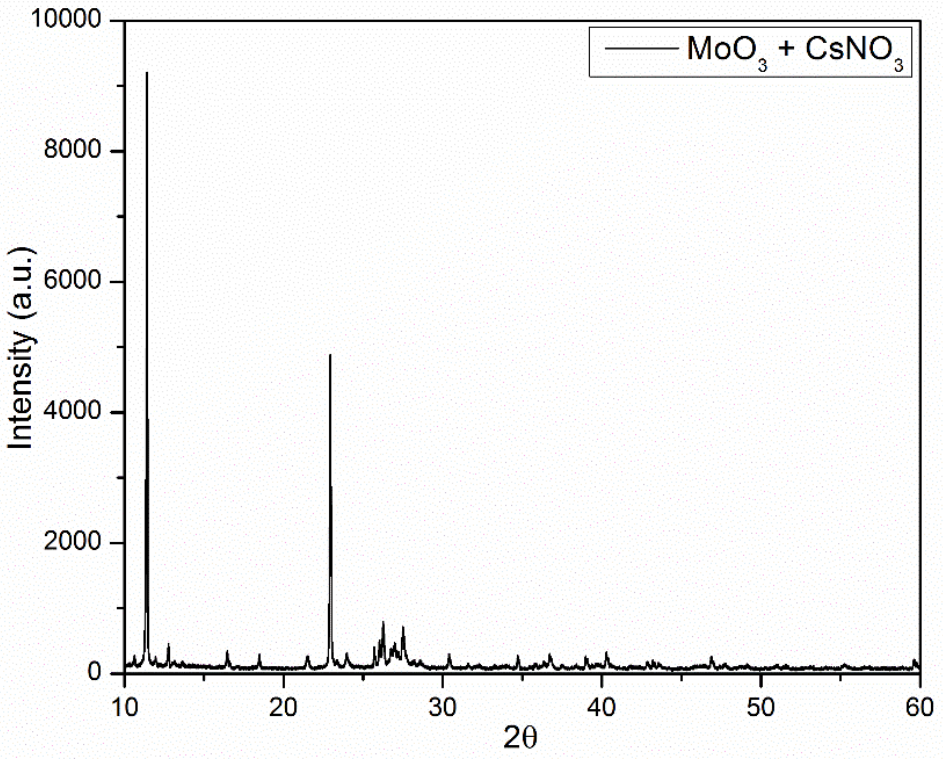

Figure 11: XRD of the Material from Reacting MoO_3 with $CsNO_3$

Conclusion:

This study showed that it is possible to synthesize nanometric $PbMoO_4$ by a unique method that utilizes a nanoparticle suspension produced by exfoliating molybdenum trioxide in refluxing water. These react rapidly with aqueous lead ions to form lead molybdate as either a nanocrystalline precipitate or a stable suspension of ca. 47 nm nanoparticles depending on the concentration of the reagents. Unexpectedly, the reaction under high dilution produced nanoparticles that were larger than those formed at higher concentration. This unusual result bears further study but it does seem that at high dilution the parent MoO_3 nanoparticles are transformed directly on a 1:1 basis to $PbMoO_4$ particles while at higher concentrations higher nucleation rates and/or calving of smaller nanoparticles occurs. The ready conversion of MoO_3 nanoparticles to nanoparticulate molybdates provides a novel and versatile method for the preparation of a wide range useful materials including many useful catalysts and electronic, optical, and structural

materials. This study also shows that the careful selection of the divalent metal is required to yield a nanometric precipitate. The reaction of the suspension of MoO_3 with the two monovalent metals should be furthered as to elucidate the nature of the products. Moreover, the study of the suspension should be expanded to determine if other functional nanometric metal molybdates could be synthesized in using the nanometric suspension of MoO_3.

References:

1. M. Shen, Q. Zhang, H. Chen, and T. Peng, Hydrothermal fabrication of PbMoO4 microcrystals with exposed (001) facets and its enhanced photocatalytic properties. *CrystEngComm* **2011,** *13*, 2785.

2. J. C. Sczancoski, M. D. R. Bomio, L. S. Cavalcante, M. R. Joya, P. S. Pizani, J. A. Varela, E. Longo, M. S. Li, and J. A. Andrés, Morphology and Blue Photoluminescence Emission of PbMoO4 Processed in Conventional Hydrothermal. *The Journal of Physical Chemistry C* **2009,** *113* (14), 5812-5822.

3. M. Tyagi, Sangeeta, D. G. Desai, and S. C. Sabharwal, New observations on the luminescence of lead molybdate crystals. *Journal of Luminescence* **2008,** *128*, 22-26.

4. D. Piwowarska, S. M. Kaczmarek, and M. Berkowski, Dielectric, optical and EPR studies of PbMoO4 single crystals, pure and doped with cobalt ions. *Journal of Non-Crystalline Solids* **2008,** *354* (35–39), 4437-4442.

5. J. Chen, Q. Zhang, T. Liu, and Z. Shao, First-principles study of color centers in PbMoO4 crystals. *Physica B: Condensed Matter* **2008,** *403* (4), 555-558.

6. J. Chen, T. Liu, D. Cao, and G. Zhao, First-principles study of the electronic structures and absorption spectra for the PbMoO4 crystal with lead vacancy. *Physica Status Solidi (B)* **2008,** *245* (6), 1152-1155.

7. D. Spassky, S. Ivanov, I. Kitaeva, V. Kolobanov, V. Mikhailin, L. Ivleva, and I. Voronina, Optical and luminescent properties of a series of molybdate single crystals of scheelite crystal structure. *Physica Status Solidi (C)* **2005,** *2* (1), 65-68.

8. M. Minowa, K. Itakura, S. Moriyama, and W. Ootani, Measurement of the property of cooled lead molybdate as a scintillator. *Nuclear Instruments and Methods in Physics Research Section A: Accelerators, Spectrometers, Detectors and Associated Equipment* **1992,** *320* (3), 500-503.

9. G. P. Pazzi, P. Fabeni, C. Susini, M. Nikl, P. Bohacek, E. Mihokova, A. Vedda, M. Martini, M. Kobayashi, and Y. Usuki, Recombination luminescence in lead tungstate scintillating crystals. *Radiation Measurements* **2004,** *38* (4–6), 381-384.

10. P. Tournois, Acousto-optic programmable dispersive filter for adaptive compensation of group delay time dispersion in laser systems. *Optics Communications* **1997,** *140* (4–6), 245-249.

11. S. Saltiel, K. Koynov, K. Kirov, and K. Petrova, Cross-phase modulation caused by cascading of third-order processes. *Journal of the Optical Society of America B* **1999,** *16* (2), 262-266.

12. S. K. Yao and E. H. Young, Acousto-Optical Multiplexer for Fiber Optical Systems. *IEEE Transactions on Sonics and Ultrasonics* **1977,** *24*, 214.

13. H. F. Folkerts, J. Zuidema, and G. Blasse, THE LUMINESCENCE OF Pb2+ IN LEAD COMPOUNDS WITH ONE-DIMENSIONAL CHAINS. *Solid State Communications* **1996,** *99* (9), 655-658.

14. J. A. Groenink and G. J. Blasse, Some New Observations on the Luminescence of PbMoO4 and PbW04. *Journal of Solid State Chemistry* **1980,** *32*, 9-20.

15. Y. A. Hizhnyi and S. G. Nedilko, Investigation of the luminescent properties of pure and defect lead tungstate crystals by electronic structure calculations. *Journal of Luminescence* **2003,** *102-103*, 688-693.

16. D. A. Spassky, S. N. Ivanov, V. N. Kolobanov, V. V. Mikhailina, V. N. Zemskov, B. I. Zadneprovski, and L. I. Potkin, Optical and luminescent properties of the lead and barium molybdates. *Radiation Measurements* **2004,** *38*, 607-610.

17. M. Hashim, C. Hu, X. Wang, X. Li, and D. Guo, Synthesis and photocatalytic property of lead molybdate dendrites with exposed (0 0 1) facet. *Applied Surface Science* **2012,** *258*, 5858-5862.

18. A. Kudo, M. Steinburg, A. J. Bard, A. Campion, M. A. Fox, T. E. Mallouk, S. E. Webber, and J. M. White, Photoactivity of ternary lead-group IVB oxides for hydrogen and oxygen evolution. *Catalysis Letters* **1990,** (5), 61-66.

19. Y. Shimodaira, H. Kato, H. Kobayashi, and A. Kudo, Investigations of Electronic Structures and Photocatalytic Activities Under Visible Light Irradiation of Lead Molybdate Replaced with Chromium(VI). *Bulletin of the Chemical Society of Japan.* **2007,** *80* (5), 885-893.

20. M. Shen, X. Zhang, K. Dai, H. Chen, and T. Peng, Hierarchical PbMoO4 microspheres: hydrothermal synthesis, formation mechanism and photocatalytic properties. *CrystEngComm* **2013,** *15* (6), 1146-1152.

21. V. M. Anandakumar and M. A. Khadar, Synthesis, characterization and optical properties of nanocrystalline lead molybdate. *Physica Status Solidi (A)* **2008,** *205* (11), 2666-2672.

22. D. B. Hernández-Uresti, A. Martínez-de la Cruz, and L. Torres-Martínez, Photocatalytic properties of PbMoO4 synthesized by co-precipitation method: organic dyes degradation under UV irradiation. *Research on Chemical Intermediates* **2012,** *38* (3-5), 817-828.

23. H. Chu, X. Li, G. Chen, Z. Jin, Y. Zhang, and Y. Li, Inorganic hierarchical nanostructures induced by concentration difference and gradient. *Nano Research* **2008,** *1* (3), 213-220.

24. A. Phuruangrat, T. Thongtem, and S. Thongtem, Analysis of lead molybdate and lead tungstate synthesized by a sonochemical method. *Current Applied Physics* **2010,** *10*, 342-345.

25. A. Y. Neiman, A. F. Guseva, and A. R. Sharafutdinov, Origin of potential difference self generated by reaction and transport processes. *Solid State Ionics* **1997,** *101-103*, 367-372.

26. S. Takano, S. Esashi, K. Mori, and T. Namikata, Growth of high-quality single crystals of lead molybdate. *Journal of Crystal Growth* **1974,** *24–25* (0), 437-440.

27. H. C. Zeng, Synthesis of stoichiometric lead molybdate PbMoO4: An x-ray diffraction, Fourier transform infrared spectroscopy, and differential thermal analysis study. *Journal of Materials Research* **1996,** *11* (03), 703-715.

28. A. W. Apblett, M. Chehbouni, and B. P. Kiran, Selective Absorption of Heavy Metals and Radionuclides from Water in a Direct-to-Ceramic Process. *Ceramic Transactions* **2003,** *143* (385-394).

29. A. W. Apblett, B. P. Kiran, and M. Chehbouni, Molybdenum-Oxide Based Sorbants for Toxic Metals. *Ceramic Transactions* **2006,** *176*, 15-23.

30. K. N. Barber and A. W. Apblett, Green Process for Recovery of Copper. *Ceramic Transactions* **2009,** *207*, 171-175.

31. M. Chehbouni, H. Al-Busaidi, and A. W. Apblett, Green Process for Uranium Separations Utilizing Molybdenum Trioxide. In *Nuclear Energy and the Environment*, American Chemical Society: 2010; Vol. 1046, pp 155-167.

32. B. P. Kiran and A. W. Apblett, Process for Selective Removal and Concentration of Actinides and Heavy Metals from Water. *Ceramic Transactions* **2004,** *155*, 371-380.

33. C. K. Perkins, K. N. Barber, and A. W. Apblett, Direct conversion of a nanometric suspension of molybdenum trioxide into nanometric lead molybdate. *CrystEngComm* **2014,** *16* (14), 2869-2873.

34. V. M. Anandakumar and M. A. Khadar, Microhardness studies of nanocrystalline lead molybdate. *Materials Science and Engineering A* **2009,** *519*, 141-146.

35. F. D. Hardcastle and I. E. Wachs, Determination of Molybdenum-Oxygen Bond Distances and Bond Orders by Raman Spectroscopy. *Journal of Raman Spectroscopy* **1990,** *21*, 683-691.

36. J. T. Kloprogge, M. L. Weier, W. N. Martens, and R. L. Frost, Microwave assisted synthesis and characterisation of divalent metal tungstate nanocrystalline minerals: ferberite, hübnerite, sanmartinite, scheelite and stolzite. *Material Chemistry and Physics* **2004,** *88*, 438-443.

37. A. Phuruangrat, T. Thongtem, and S. Thongtem, Synthesis of lead molybdate and lead tungstate via microwave irradiation method. *Journal of Crystal Growth* **2009,** *311*, 4076-4081.

38. A. P. de Azevedo Marques, D. M. A. de Melo, C. A. Paskocimas, P. S. Pizani, M. R. Joya, E. R. Leite, and E. J. Longo, Photoluminescent BaMoO4 nanopowders prepared by complex polymerization method (CPM). *Journal of Solid State Chemistry* **2006,** *179*, 671-678.

39. T. Thongtem, A. Phuruangrat, and S. Thongtem, Sonochemical synthesis of MMoO4 (M = Ca, Sr and Ba) nanocrystals. *Journal of Ceramic Processing Research* **2008,** *9* (2), 189-191.

40. H. S. Lee, S. D. Lee, and J. H. Lee, Raman Spectra of Lead Molybdate Single Crystals. *Ferroelectics* **1990,** *107*, 151-154.

41. J. Xu, S. Wang, M. H. Manghnani, L. C. Ming, and J. Bologh, High Pressure Raman Study pf PbMoO4. *High Pressure Research* **1990,** *3*, 254-256.

42. K. Saito, S. Kazama, K. Matsubara, T. Yui, and M. Yagi, Monoclinic Ag2Mo2O7 Nanowire: A New Ag–Mo–O Nanophotocatalyst Material. *Inorganic Chemistry* **2013,** *52* (15), 8297-8299.

43. K. Hariharan and C. Sangamithra, Mixed mobile ion effect in copper and silver molybdate glasses. *Materials Chemistry and Physics* **1992,** *32* (3), 240-243.

44. A. K. Arof, K. C. Seman, A. N. Hashim, R. Yahya, M. J. Maah, and S. Radhakrishna, A new silver ion conductor for battery applications. *Materials Science and Engineering: B* **1995,** *31* (3), 249-254.

CHAPTER IV

SYNTHESIS OF ALKALINE EARTH METAL TUNGSTATES

Introduction:

Metal tungstates have received much interest due to their interesting and useful properties. More specifically, alkaline earth metal tungstates MWO_4 (M: Mg, Ca, Sr, and Ba) have been employed in a variety of roles in material science as phosphors,[1] laser media,[2-4] scintillation detectors,[5] and electro-optic materials.[6-7] Moreover, owing to their low permittivities and high Q_f values, scheelite ceramics are regarded as promising materials for microwave substrate applications.[8] The metal tungstates have also proven very valuable as pure phosphors, exhibiting luminescence without the presence of activators due to transitions between the $5d^0$ and $2p^6$ orbitals of the W^{6+} and O^{2-} respectively.[9]

The metal tungstate structure depends crucially on the ionic radius of the A^{2+} cation in the formula unit AWO_4. Metal tungstates with the ionic radius of the metal cation exceeding 0.99 Å tend to adopt the scheelite structure, while cations with ionic radii less than 0.77 Å assume the wolframite structure. Thus, the Ca^{2+}, Sr^{2+}, and Ba^{2+} tungstates crystallize in the tetragonal scheelite structure, while $MgWO_4$ adopts the monoclinic wolframite structure.[10-13]

A variety of techniques have been employed to synthesize alkaline earth metal tungstates, including the ceramic method,[14-15] sol-gel processes,[16] precipitation reactions,[17-18] precursor

methods,[19] et cetera. Many of these techniques allow for the synthesis of high precision materials, due to mixing on the molecular level, which is very important for preparing multi-component systems.[20-21] Specifically, the intercalation of magnesium into tungsten oxides is of particular interest as a possible electrode for a magnesium battery, due to the similar ionic radii of the widely used lithium ion.[22]

Solution based synthetic methods for alkaline earth metal tungstates, such as hydrothermal synthesis, can overcome three of the major limitations of the solid state method: long diffusion paths, inclusion of impurities, and agglomeration of particles.[18] However, these methods also have their drawbacks since precursor methods can be energy intensive and the byproducts of precipitation reactions are difficult to recover and/or recycle. Additionally, the use of sodium tungstate as the tungstate source often leads to hydrated tungstic acid and polytungstate byproducts. Therefore, the formation of many metal tungstates are pH dependent, requiring that pH should be strictly controlled for aqueous preparation.[23-24]

The discovery that both tungsten trioxide and tungstic acid can react with aqueous uranyl salts to produce uranium tungstate suggests that a similar reaction could be utilized for the synthesis of other metal tungstates.[25] Thus, judicious choice of the metal salt can result in a process where only harmless byproducts are produced. The research reported in this chapter explored the effectiveness of the reaction of alkaline earth metal acetates with both tungsten trioxide and tungstic acid, yielding a green synthetic process with only acetic acid as a byproduct.

Experimental:

All reagents were commercially available products of ACS reagent grade or higher and were used without further purification. The water used in this is study was purified by reverse osmosis and deionized to a resistivity of 18 MΩ. Bulk pyrolysis was performed in ambient air in a digitally controlled muffle furnace with a ramp rate of 10 ^{o}C/min and a hold time of 6 hours.

The X-ray diffraction patterns for the oxides were obtained using a Bruker D8-A25-Advance with a LynxEye detector. Crystalline phases were identified and matched to powder diffraction files (PDF) from the International Centre for Diffraction Data. The Raman spectra were recorded as neat powders on a Nicolet NXR 9610 Raman spectrometer. The pH of the filtrate was measured using a model IQ125 pH meter equipped with an ISFET electrode.

Reaction of Alkaline Earth Metal Acetates with Tungsten Oxides:

In a typical reaction, one molar equivalent of tungsten oxide (WO_3 or H_2WO_4) would be reacted with an excess (four equivalents) of the alkaline earth metal acetates dissolved in approximately 100 mL of deionized water. The reactions were run with excess metal acetates to prevent exhaustion of the buffering provided by the acetate ions. Once mixed, the reactants were allowed to react under reflux conditions until a visible color change was observed; typically the reactions were complete after roughly 72 hours. However, the time was adjusted to 2 weeks for the $Ba(OAc)_2$ reactions, as intercalation and reaction of the larger ion took more time as evident by the rate of color change from green (WO_3) or yellow (H_2WO_4) to the final white product. Once complete, the cooled slurry would be filtered through a fine-frit glass filter and washed with 500 mL of deionized water. The resultant solids were dried *in vacuo* until the masses were stabilized. The experimental details are provided in Table 1.

Results and Discussion:

The reaction of tungsten trioxide with aqueous solutions containing excess alkaline metal acetates gave very high yields of the metal tungstates in all cases except for $MgWO_4$ (Table 1). The moles of water were calculated from the TGA data and are based on the formation of only MWO_4. In all cases, the reaction caused a large pH change of the solution due to the production of protons which accompany the formation of the metal tungstate (Equation 1). Furthermore, the buffering ability of the acetates successfully kept the pHs from dropping below a desirable value.

Table 1: Percent Yields of the Alkaline Earth Metal Acetates with WO_3 (*Percent Yields Based on Pure MWO_4)

Product	mmoles WO_3	mmoles $M(OAc)_2$	Yield (g)	Mol H_2O	Theoretical Yield (g)	Percent Yield (%)	$pH_{initial}$	pH_{final}
$MgWO_4$	6.023	12.115	1.379	2.708	1.639	84.1	8.1	4.9
$CaWO_4$	6.000	12.029	1.612	0.129	1.728	93.3	7.8	5.8
$SrWO_4$	6.006	11.995	1.932	0.224	2.015	95.9	7.6	5.0
$BaWO_4$	6.793	12.004	2.216	0.421	2.321	95.4	7.3	5.0

$$A^{2+} + WO_3 + H_2O \rightarrow AWO_4 + 2H^+$$

Equation 1: Schematic Reaction of M(II) with WO_3

The reactions with tungstic acid proceeded much more rapidly, likely due to its layered structure allowing for a more facile intercalation reaction. For example, the reaction to produce $CaWO_4$ was found to be complete within 30 minutes of the reflux. Similar to the reaction with tungsten trioxide, tungstic acid produced the metal tungstates in high yields, this time with both $MgWO_4$ and $BaWO_4$ as the outliers. It is possible the lower yields are due to the formation of polytungstates, possibly consequence of using the excess metal acetates.

Table 2: Percent Yields of the Alkaline Earth Metal Acetates with H_2WO_4 (*Percent Yields Based of Pure MWO_4)

Product	mmoles H_2WO_4	mmoles $M(OAc)_2$	Yield (g)	Mol H_2O	Theoretical Yield (g)	Percent Yield (%)	$pH_{initial}$	pH_{final}
$MgWO_4$	5.996	12.030	1.379	2.877	1.632	84.5	8.1	5.2
$CaWO_4$	6.000	12.020	1.351	0.323	1.728	100	7.8	4.4
$SrWO_4$	5.996	11.995	1.329	0.309	2.012	99.6	7.6	4.6
$BaWO_4$	5.993	12.031	1.304	0.414	2.308	84.8	7.3	5.2

$$M^{2+} + H_2WO_4 \rightarrow MWO_4 + 2H^+$$

Equation 2: Schematic Reaction of M(II) with Tungstic Acid

The X-ray diffraction patterns of the products from both WO_3 and H_2WO_4 that crystallize in the scheelite structure (Ca, Sr, and Ba) were found to be phase pure and highly crystalline. The

materials produced from the reaction with tungstic acid show slightly broadened diffraction patterns, with the most broadened product being $CaWO_4$ (Figure 1). This result suggests that tungstic acid produced more fine grained products with crystallite sizes in the nanocrystalline regime. It is possible that the yields of the tungstates that are not produced quantitatively are diminished by the formation of nanoparticles during the reaction. Since tungstic acid produces more nanocrystalline products, it appears to be affected more by this phenomenon. Note that the XRD of the $BaWO_4$ (Figure 3) from the lower yielding tungstic acid gives an almost identical diffraction pattern to that of the reaction using tungsten trioxide. Furthermore, the absence of any starting material suggests the reaction is favorable to the formation of products and the lower solubility is not consequence of an incomplete reaction.

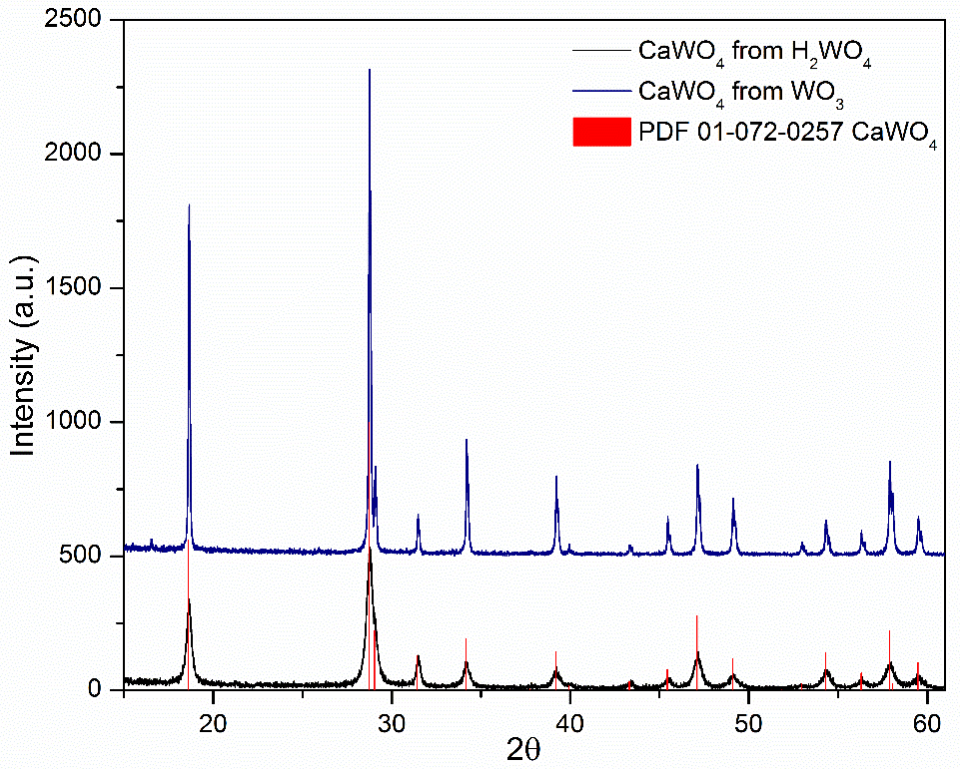

Figure 1: XRD Patterns for the $CaWO_4$ from both WO_3 and H_2WO_4

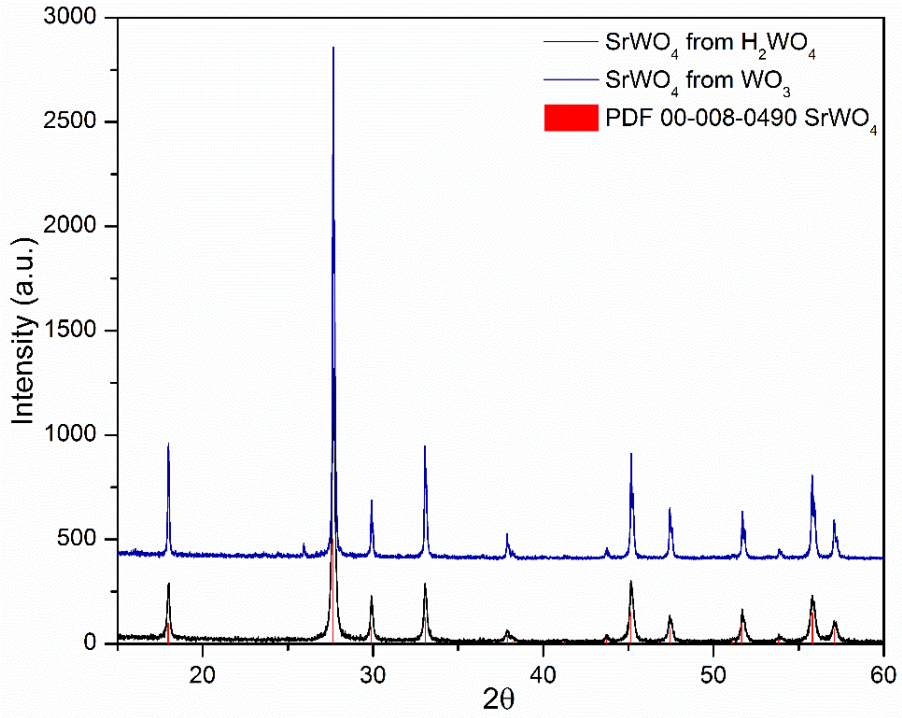

Figure 2: XRD Patterns for the $SrWO_4$ from both WO_3 and H_2WO_4

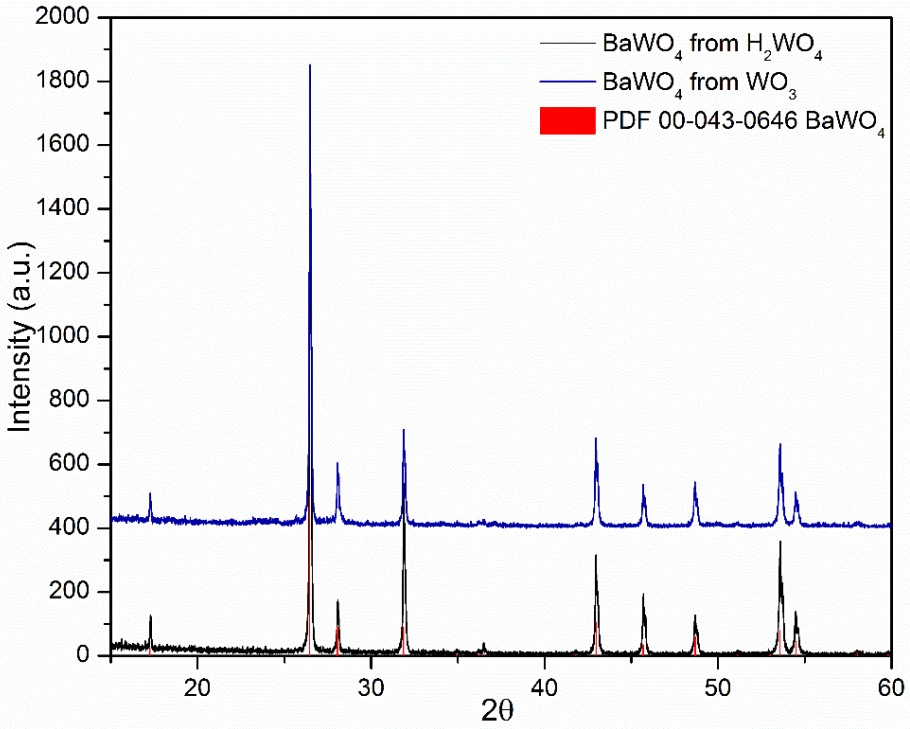

Figure 3: XRD Patterns for the $BaWO_4$ from both WO_3 and H_2WO_4

In the case of the product from the reactions with magnesium acetate, the reaction produced a material that does not have a match in the ICDD database (Figure 4). Furthermore, the products for WO_3 and H_2WO_4 appeared to be identical in terms of phase and crystallinity.

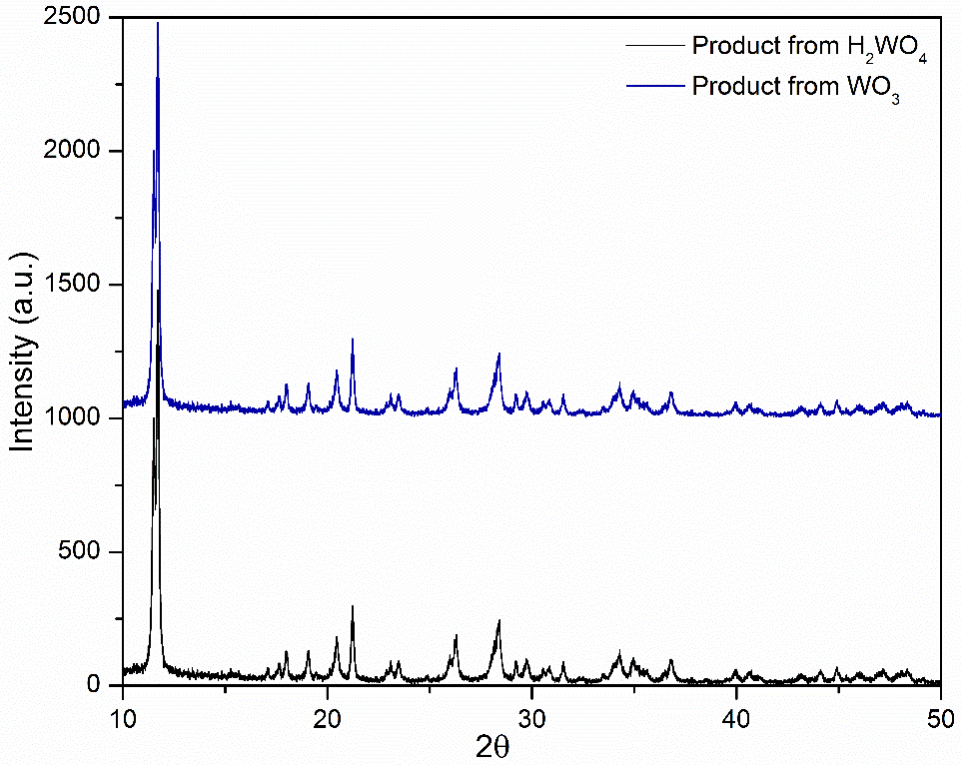

Figure 4: XRD of the Magnesium Product from both WO_3 and H_2WO_4

The material produced could be an undocumented hydrated form of $MgWO_4$, thus the material was heated to 600 °C to ensure the removal of any organic species and lattice water. However, the XRD of the calcined product showed that phase separation of the material to a combination of WO_3 and $MgWO_4$ (Figure 5) occurred. This result suggests that the material produced from the reaction with magnesium acetate produces a magnesium polytungstate. Also, since the water content was high, the material is a hydrate with 2.7 to 2.9 water molecules per tungsten ion (see later discussion concerning this product).

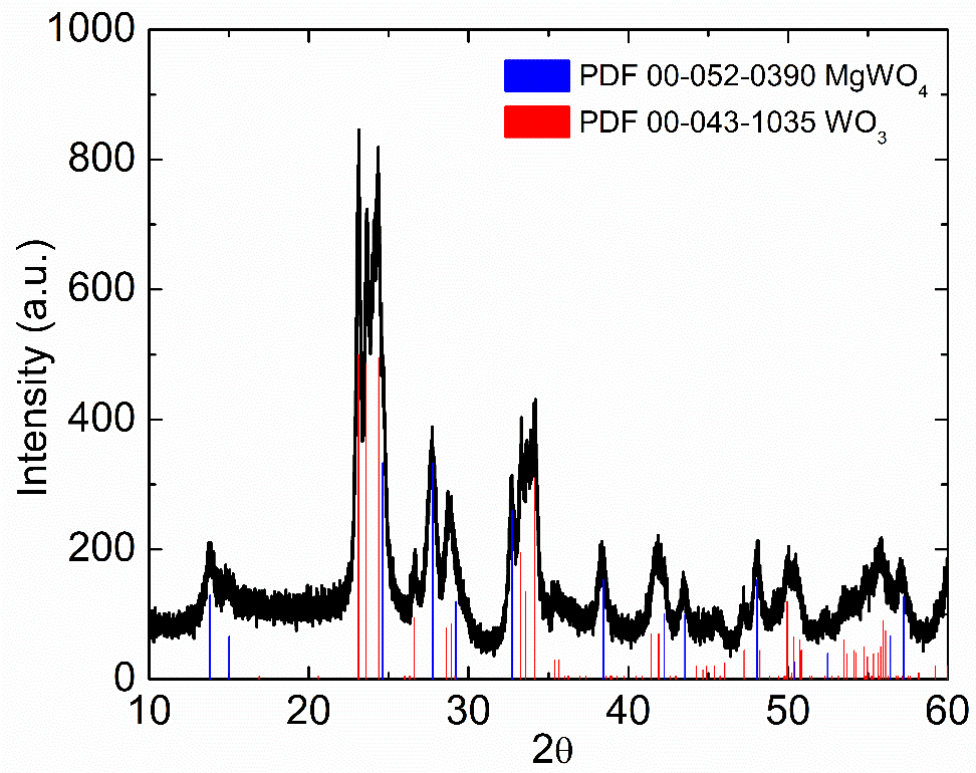

Figure 5: XRD of the calcined magnesium tungstate product

The Raman spectra of the scheelite materials also gave characteristic stretches for each of the tungstates. Similar to the results from the XRD, both tungsten-containing starting materials yielded products that had nearly identical Raman spectra. The Raman spectrum (Figure 6) of $CaWO_4$ from H_2WO_4 shows the characteristic $V_1(A_{1g})$ stretch at 909 cm^{-1} that corresponds to the internal symmetrical vibration of the WO_4^{2-} tetrahedron.[26] The peaks at 836 and 795 cm^{-1} correspond to a splitting of the ν_3 mode, with the band the higher energy band being the $\nu_3(B_g)$ vibration while the lower energy one is due to the $\nu_3(E_g)$ vibration of the tungstate unit. The ν_4 mode shows the weak $\nu_4(B_g)$ vibration occurring at 399 cm^{-1}. The ν_2 stretch, observed at 332 cm^{-1}, can be assigned to the $\nu_2(A_g)$ vibrational mode. Finally, the stretch observed at 209 cm^{-1} is due to the translational mode, ν(Ca-O). The spectrum also contains the external Raman-active vibration at 116 cm^{-1}. [27-33]

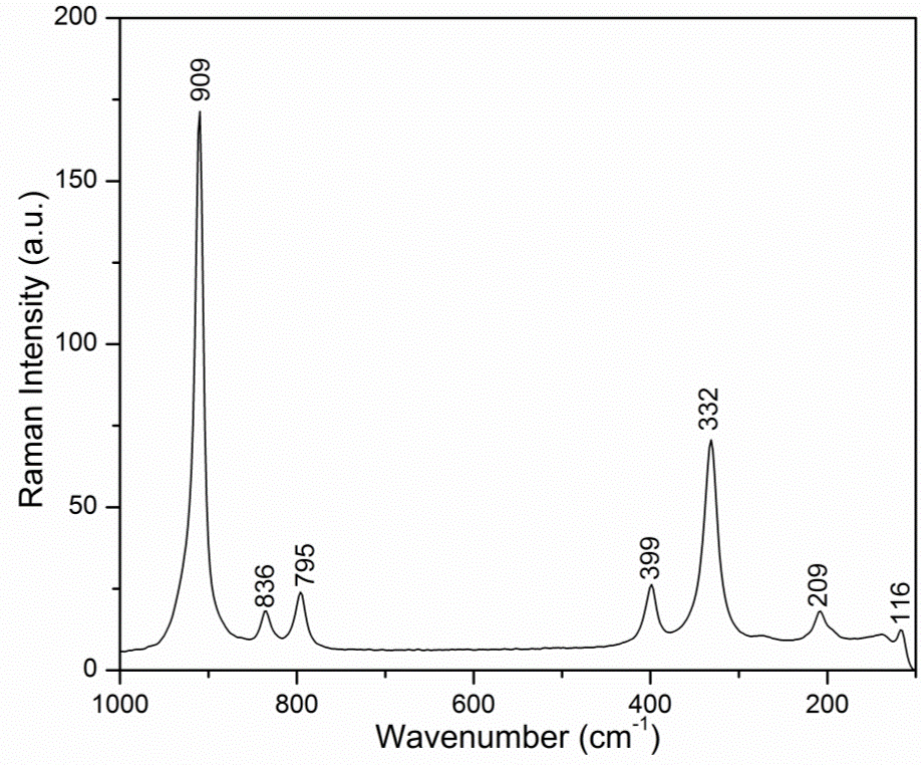

Figure 6: Raman Spectra of $CaWO_4$ from H_2WO_4

The Raman spectrum (Figure 7) of $SrWO_4$ from H_2WO_4 gives the characteristic symmetric stretch of the tungstate ion, $\nu_1(A_{1g})$, at 918 cm^{-1}. The peak at 835 cm^{-1} corresponds to the high energy band $\nu_3(B_g)$ of the split ν_3 mode of the tungstate unit, while the lower energy $\nu_3(E_g)$ stretch is observed at 796 cm^{-1}. The weak $\nu_4(B_g)$ vibration occurs at 370 cm^{-1}, while the more intense ν_2 vibrational mode was observed at 334 cm^{-1}, as the $\nu_2(A_g)$ vibrational mode. The translational mode of the heavier ν(Sr-O) was shifted as compared to Ca-O, from 209 to 184 cm^{-1} and the external Raman-active vibration, A_g, was observed at 131 cm^{-1}.[26-27, 33]

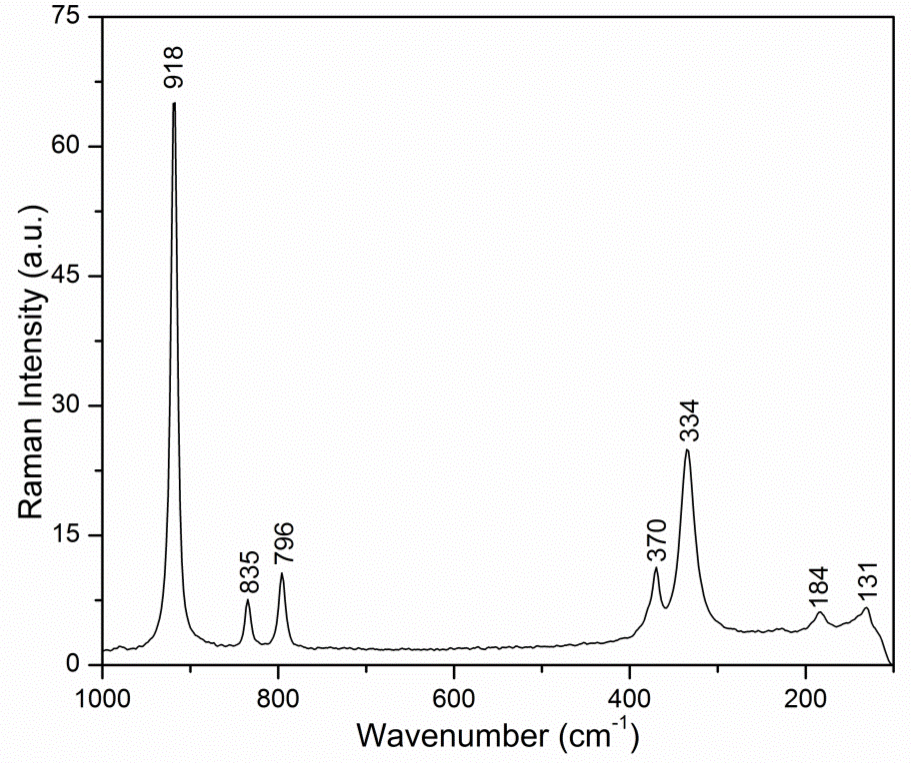

Figure 7: Raman Spectrum of $SrWO_4$ from H_2WO_4

The Raman spectrum (Figure 8) of $BaWO_4$ from H_2WO_4 was the only material that showed an appreciable amount of fluorescence at the lower wavelengths. The spectrum gives the characteristic ν_1 stretch at 924 cm^{-1} for the tungstate tetrahedral group. The peaks at 830 and 793 cm^{-1} correspond to a splitting of the ν_3 mode of the tungstate unit to $\nu_3(B_g)$ and $\nu_3(E_g)$, respectively. The ν_4 mode appears split as the weak $\nu_4(B_g)$ vibration was observed at 344 cm^{-1} and the $\nu_4(E_g)$ band appearing as a shoulder at 353 cm^{-1}. The ν_2 vibrational mode was observed at 331 cm^{-1} and translational mode, ν(Ba-O), was observed at 185 cm^{-1}. Like the other two spectra, this spectrum also contains the external Raman-active vibration at 145 cm^{-1}.[2, 17, 26, 28, 33]

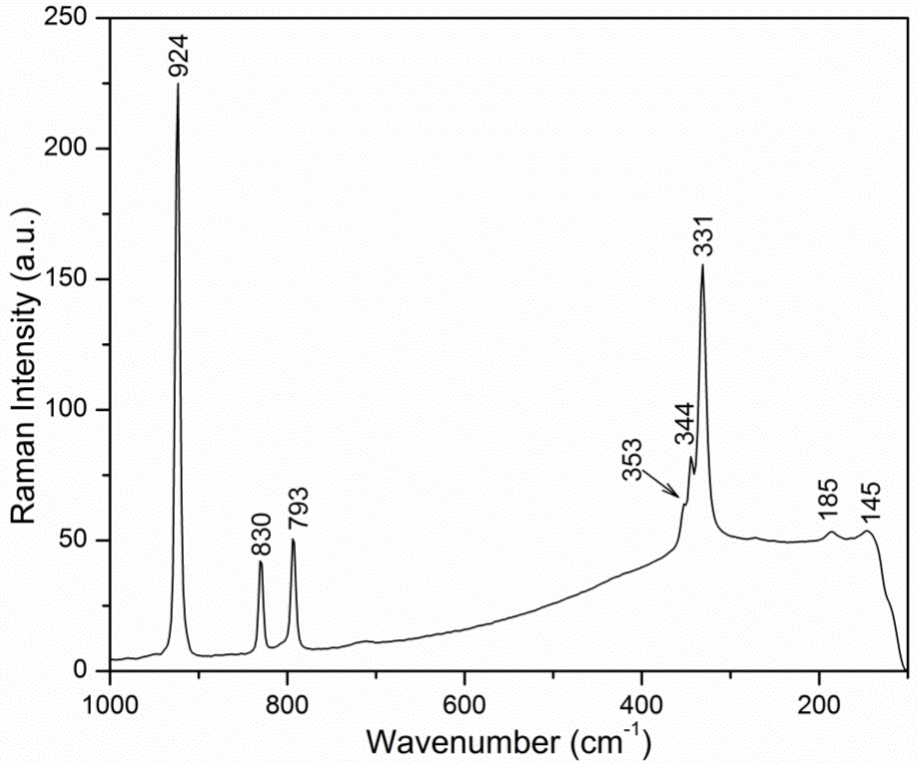

Figure 8: Raman Spectrum of $BaWO_4$ from H_2WO_4

Figure 9 shows the Raman spectrum of the material produced from reacting magnesium acetate with tungstic acid. The Raman vibrations were not consistent with the wolframite structure, nor were they consistent with the tungstic acid starting material or tungsten trioxide. Moreover, the vibrations are not consistent with previously reported MgW_2O_7, suggesting the formation of an unreported hydrated magnesium polytungstate.[34]

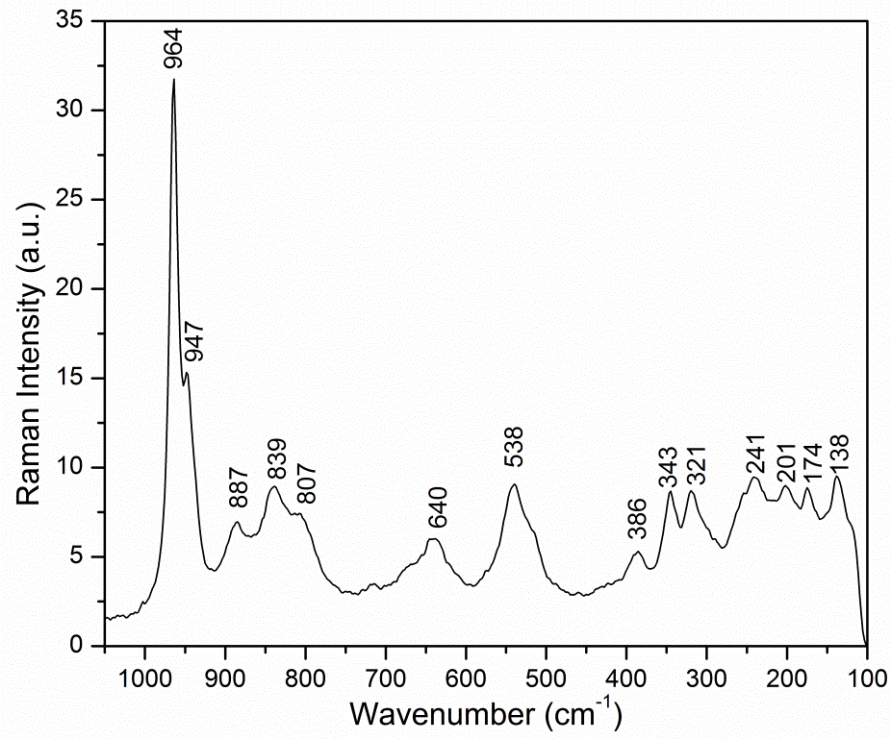

Figure 9: Raman Spectrum of the Product from the Reaction of $Mg(OAc)_2$ and H_2WO_4

The Raman spectrum (Figure 10) of the material post-calcination also did not produced stretches consistent with the wolframite structure, but gave peaks consistent for only tungsten trioxide. The peaks 974, 804, 710, 327, 266, 187 and 133 cm^{-1} are all consistent with monoclinic WO_3.[34-35]

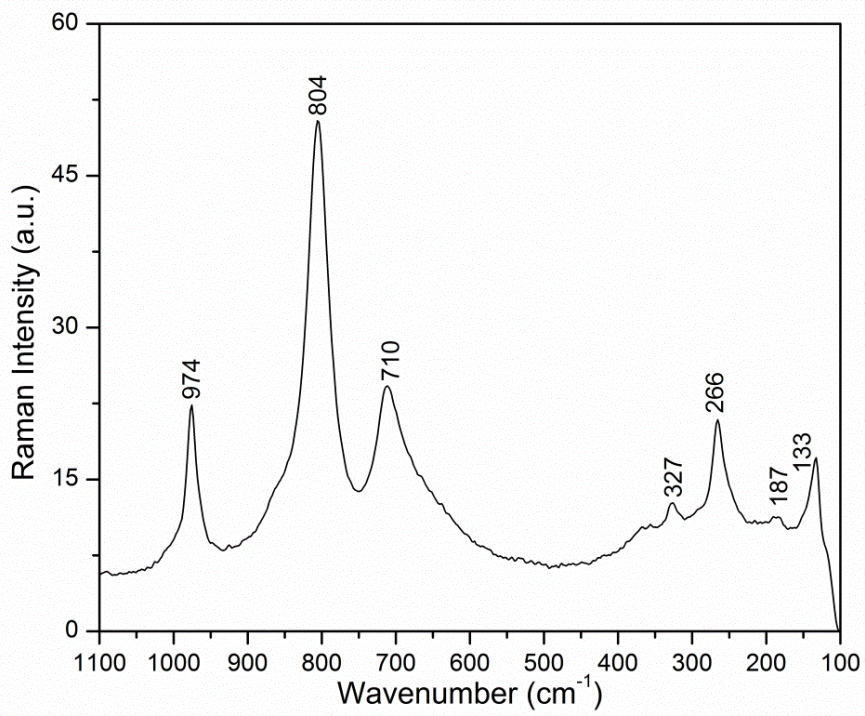

Figure 10: The Raman Spectrum of the $Mg(OAc)_2$-H_2WO_4 Product After Calcination

To determine the identity of the magnesium tungstate product, a sample was reacted with 30% ammonium hydroxide. The reaction of the sample with the strong base gave the soluble ammonium tungstate complex that could be separated by centrifugation from the insoluble $Mg(OH)_2$ precipitate formed in this reaction. The soluble ammonium tungstate solution was then dried and calcined at 700 °C, to produce WO_3. The precipitated $Mg(OH)_2$ was also recovered and dried to determine the amount of magnesium in the solid. The molar ratio of the two components was 2:3 for Mg and W, respectively. Further, Figure 11 shows that thermal gravimetric analysis revealed the original sample had 16% weight loss at 150 °C, likely associated with the both loss of hydroxyl groups and water. A similar material has been reported with the same 2:3 ratio of Mg:W which also phase separates upon calcination.[36] However, the TGA data shows that the produced material has a much larger weight loss than possible for the material reported by Günter. Further, the two XRD patterns do not match, further suggesting the synthesized and previously reported materials are not the same. However, excess waters of crystallization, as

compared to the previously reported material, could explain the difference in the water content and structure. Further research must be done to determine molecular formula of the synthesized polytungstate.

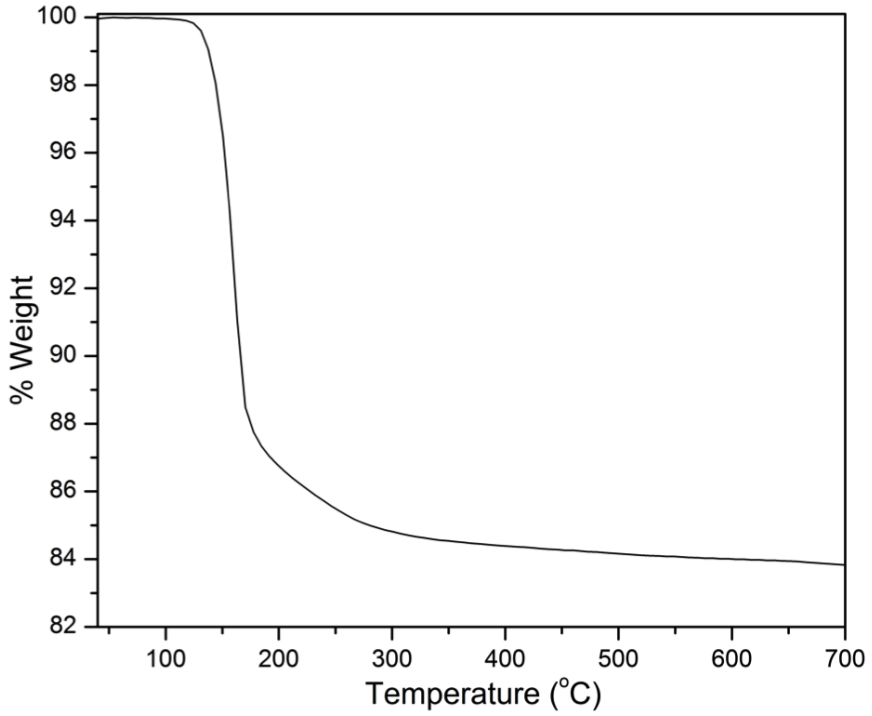

Figure 11: TGA of the Product from the Reflux of H_2WO_4 and $Mg(OAc)_2$

Conclusion:

This study provides a promising environmentally friendly synthetic method for highly crystalline alkaline earth metal tungstates that adopt the scheelite structure from both tungsten trioxide and tungstic acid with high yields. Further, this method produces a novel magnesium polytungstate under the same reaction conditions. This synthetic method is also a cost-effective approach to synthesizing metal tungstates as compared to solid-state synthetic measures used to produce alkaline earth metal tungstates for industrial applications. Future research into developing transition metal tungstates through this process should be pursued, with emphasis on characterizing the effect of cation size on the produced material.

References:

1. G. Born, A. Hofstaetter, A. Scharmann, and G. Schwarz, Luminescence mechanism of tungstate phosphors. *Journal of Luminescence* **1970,** *1–2* (0), 641-650.

2. T. T. Basiev, M. E. Doroshenko, V. V. Osiko, S. E. Sverchkov, and B. I. Galagan, New mid IR (1.5–2.2 μm) Raman lasers based on barium tungstate and barium nitrate crystals. *Laser Physics Letters* **2005,** *2* (5), 237.

3. L. I. Ivleva, T. T. Basiev, I. S. Voronina, P. G. Zverev, V. V. Osiko, and N. M. Polozkov, SrWO4:Nd3+ – new material for multifunctional lasers. *Optical Materials* **2003,** *23* (1–2), 439-442.

4. D. Christofilos, S. Ves, and G. A. Kourouklis, Pressure Induced Phase Transitions in Alkaline Earth Tungstates. *Physica Status Solidi (B)* **1996,** *198* (1), 539-544.

5. F. Zhang, M. Y. Sfeir, J. A. Misewich, and S. S. Wong, Room-Temperature Preparation, Characterization, and Photoluminescence Measurements of Solid Solutions of Various Compositionally-Defined Single-Crystalline Alkaline-Earth-Metal Tungstate Nanorods. *Chemistry of Materials* **2008,** *20* (17), 5500-5512.

6. G. Blasse and W. J. Schipper, Low-temperature photoluminescence of strontium and barium tungstate. *Physica Status Solidi (A)* **1974,** *25* (2), K163-K165.

7. G. Blasse and G. J. Dirksen, Photoluminescence of Ba3W2O9: Confirmation of a structural principle. *Journal of Solid State Chemistry* **1981,** *36* (1), 124-126.

8. M. Maček Kržmanc, M. Logar, B. Budič, and D. Suvorov, Dielectric and Microstructural Study of the SrWO4, BaWO4, and CaWO4 Scheelite Ceramics. *Journal of the American Ceramic Society* **2011,** *94* (8), 2464-2472.

9. F. A. Cotton, G. Wilkinson, C. A. Murillo, and M. Bochmann, *Advanced Inorganic Chemistry*. 6th ed.; Wiley India Pvt. Limited: 2007.

10. A. Sleight, Accurate cell dimensions for ABO4 molybdates and tungstates. *Acta Crystallographica Section B* **1972,** *28* (10), 2899-2902.

11. V. Thangadurai, C. Knittlmayer, and W. Weppner, Metathetic room temperature preparation and characterization of scheelite-type ABO4 (A = Ca, Sr, Ba, Pb; B = Mo, W) powders. *Materials Science and Engineering: B* **2004,** *106* (3), 228-233.

12. A. Kuzmin and J. Purans, Local atomic and electronic structure of tungsten ions in AWO4 crystals of scheelite and wolframite types. *Radiation Measurements* **2001,** *33* (5), 583-586.

13. J. Macavei and H. Schulz, The crystal structure of wolframite type tungstates at high pressure. *Zeitschrift für Kristallographie* **1993,** *207*, 193.

14. Z. Shan, Y. Wang, H. Ding, and F. Huang, Structure-dependent photocatalytic activities of MWO4 (M =Ca, Sr, Ba). *Journal of Molecular Catalysis A: Chemical* **2009,** *302* (1–2), 54-58.

15. G. K. Shurdumov, Z. V. Shurdumova, Z. A. Cherkesov, and A. M. Karmokov, Synthesis of alkaline-earth metal tungstates in melts of [NaNO3-M(NO3)2]eut-Na2WO4 (M = Ca, Sr, Ba) systems. *Russian Journal of Inorganic Chemistry* **2006,** *51* (4), 531-532.

16. T. J. Boyle, P. Yang, K. Hattar, B. A. Hernandez-Sanchez, M. L. Neville, and S. Hoppe, Synthesis and Characterization of Solvothermal Processed Calcium Tungstate Nanomaterials from Alkoxide Precursors. *Chemistry of Materials* **2013,** *26* (2), 965-975.

17. S. M. M Zawawi, R. Yahya, A. Hassan, H. N. M. E. Mahmud, and M. N. Daud, Structural and optical characterization of metal tungstates (MWO4; M=Ni, Ba, Bi) synthesized by a sucrose-templated method. *Chemistry Central Journal* **2013,** *7* (1), 80.

18. A. Sen and P. Pramanik, A chemical synthetic route for the preparation of fine-grained metal tungstate powders (M=Ca, Co, Ni, Cu, Zn). *Journal of the European Ceramic Society* **2001,** *21* (6), 745-750.

19. R. G. Gordon, S. T. Barry, X. Liu, and D. J. Teff, Liquid Compounds for CVD of Alkaline Earth Metals. *MRS Online Proceedings Library* **1999,** *574*, null-null.

20. D. Chen, G. Shen, K. Tang, H. Zheng, and Y. Qian, Low-temperature synthesis of metal tungstates nanocrystallites in ethylene glycol. *Materials Research Bulletin* **2003,** *38* (14), 1783-1789.

21. L. G. Hubert-Pfalzgraf, To what extent can design of molecular precursors control the preparation of high tech oxides? *Journal of Materials Chemistry* **2004,** *14* (21), 3113-3123.

22. P. G. Bruce, F. Krok, J. Nowinski, V. C. Gibson, and K. Tavakkoli, Chemical intercalation of magnesium into solid hosts. *Journal of Materials Chemistry* **1991,** *1* (4), 705-706.

23. S. H. Yu, B. Liu, M. S. Mo, J. H. Huang, X. M. Liu, and Y. T. Qian, General Synthesis of Single-Crystal Tungstate Nanorods/Nanowires: A Facile, Low-Temperature Solution Approach. *Advanced Functional Materials* **2003,** *13* (8), 639-647.

24. X. Cui, S. H. Yu, L. Li, L. Biao, H. Li, M. Mo, and X. M. Liu, Selective Synthesis and Characterization of Single-Crystal Silver Molybdate/Tungstate Nanowires by a Hydrothermal Process. *Chemistry – A European Journal* **2004,** *10* (1), 218-223.

25. H. Al-Busaidi and A. W. Apblett, Adsorption and Separation of Uranium Using Tungsten Oxides. In *Environmental Issues and Waste Management Technologies in the Materials and Nuclear Industries XII*, John Wiley & Sons, Inc.: 2009; pp 39-46.

26. T. T. Basiev, A. A. Sobol, P. G. Zverev, L. I. Ivleva, V. V. Osiko, and R. C. Powell, Raman spectroscopy of crystals for stimulated Raman scattering. *Optical Materials* **1999,** *11* (4), 307-314.

27. R. L. Frost, L. Duong, and M. Weier, Raman microscopy of selected tungstate minerals. *Spectrochimica Acta Part A: Molecular and Biomolecular Spectroscopy* **2004,** *60* (8–9), 1853-1859.

28. M. Liegeois-Duyckaerts and P. Tarte, Vibrational studies of molybdates, tungstates and related compounds—II: New Raman data and assignments for the scheelite-type compounds. *Spectrochimica Acta Part A: Molecular Spectroscopy* **1972,** *28* (11), 2037-2051.

29. S. P. S. Porto and J. F. Scott, Raman Spectra of CaWO4, SrWO4, CaMoO4, and SrMoO4. *Physical Review* **1967,** *157* (3), 716-719.

30. J. P. Russell and R. Loudon, The first-order Raman spectrum of calcium tungstate. *Proceedings of the Physical Society* **1965,** *85* (5), 1029.

31. W. P. Griffith, Raman studies on rock-forming minerals. Part II. Minerals containing MO3, MO4, and MO6 groups. *Journal of the Chemical Society A: Inorganic, Physical, Theoretical* **1970,** (0), 286-291.

32. R. K. Khanna, W. S. Brower, B. R. Guscott, and E. R. Lippincott, Laser induced Raman spectra of some tungstates and molybdates. *Journal of Research of the Notional Bureau af Standards - A. Physics and Chemistry* **1967,** *72A* (1), 81-84.

33. G. Z. Petr, T. B. Tasoltan, A. A. Sobol, V. V. Skornyakov, I. I. Lyudmila, N. M. Polozkov, and V. O. Vyacheslav, Stimulated Raman scattering in alkaline-earth tungstate crystals. *Quantum Electronics* **2000,** *30* (1), 55.

34. E. I. Ross-Medgaarden and I. E. Wachs, Structural Determination of Bulk and Surface Tungsten Oxides with UV−vis Diffuse Reflectance Spectroscopy and Raman Spectroscopy. *The Journal of Physical Chemistry C* **2007,** *111* (41), 15089-15099.

35. M. Regragui, M. Addou, A. Outzourhit, J. C. Bernéde, E. El Idrissi, E. Benseddik, and A. Kachouane, Preparation and characterization of pyrolytic spray deposited electrochromic tungsten trioxide films. *Thin Solid Films* **2000,** *358* (1–2), 40-45.

36. J. R. Günter, H. W. Schmalle, and E. Dubler, Crystal structure and properties of a new magnesium heteropoly-tungstate, Mg7(MgW12O42)(OH)4(H2O)8, and the isostructural compounds of manganese, iron, cobalt and nickel. *Solid State Ionics* **1990,** *43* (0), 85-92.

CHAPTER V

UPTAKE OF URANIUM BY TUNGSTIC ACID ON HIGH SURFACE AREA CATALYST SUPPORTS

Introduction:

Uranium is a widespread contaminant of ground water and can arise from both natural and anthropogenic sources. Uranium contamination has been attributed to the development of nuclear power and weapons, mine tailings, and agricultural drainage.[1-3] Furthermore, uranium occurs naturally in the earth's crust and in surface and ground waters. When bedrock consisting mainly of uranium-rich granitoids and granites comes in contact with soft, slightly alkaline bicarbonate waters under oxidizing conditions uranium will solubilize over a wide pH range. These conditions occur widely throughout the world. For example, in Finland exceptionally high uranium concentrations (up to 12,000 ppb) are found in wells drilled in the bedrock.[4] Concentrations of uranium up to 700 ppb have been found in private wells in Canada while a survey in the United States of drinking water from 978 sites found a mean concentration of 2.55 ppb.[5-6] However, some sites in the United States have serious contamination with uranium. For example, in the Simpsonville-Greenville area of South Carolina, high concentrations of uranium (30 to 9,900 ppb) were found in 31 drinking water wells, which is believed to be the result of veins of uranium containing pegmatite that occur naturally in the area.[7]

Besides entering drinking water from naturally occurring deposits, uranium can also contaminate the water supply as the result of human activity, such as uranium mining, mill tailings, and even agriculture.[8-9] Phosphate fertilizers often contain uranium at an average concentration of 150 ppm and therefore are a sizeable contributor of uranium to groundwater.[10] The Fry Canyon mine site in Utah is a good example of the dangers of uranium mine tailings. The uranium concentrations measured in groundwater at this site are as high as 16,300 ppb with a median concentration of 840 ppb before remedial actions were taken.[11] Depleted uranium ammunition has also been demonstrated to be a source of drinking water contamination.[12]

Nuclear sites such as the Hanford Nuclear Reservation, located in Hanford, Washington, have also contributed to uranium pollution in the environment. This site featured nine nuclear reactors and four reprocessing plants that produced nearly two-thirds of the plutonium used in the United States for government purposes.[13] The site operations at Hanford created enormous volumes of radioactive and chemical waste. Some of the contaminants were released directly into the environment, exposing people who lived downwind and downstream. Currently, measures are being taken to prevent leakage and prevent mobilization of the radionuclide contamination in the more than 1,600 waste sites that have been identified on the Hanford Site.[14-15] Uranium and plutonium enrichment processes at the Hanford Site have resulted in the release of 202,703 kg of uranium into the ground surface in a variety of aqueous solutions.[16]

Exposure studies suggest the major health effects from ingestion of uranium are similar to those of other heavy-metals, resulting in chemical toxicity to the kidney rather than a radiation hazard.[17] Both functional and histological damage to the proximal tubules of the kidney have been demonstrated.[18] Little is known about the long-term effects of environmental uranium exposure in humans but there is an association of uranium exposure with increased urinary glucose, alkaline phosphatase, and β-microglobulin excretion as well as increased urinary albumin levels. [19-20] As a result of such studies, the World Health Organization has proposed a

guideline value of 15 ppb for uranium in drinking water while the US EPA has specified a limit of 30 ppb. [21-22]

Current municipal treatment practices are not effective in removing uranium. However, experimentation indicates that uranium removal can be accomplished by a variety of processes such as modification of pH and/or chemical treatment (e.g. alum).[23] Several sorbents have been shown to be useful for removal of uranium from water. Activated carbon, iron powder, magnetite, anion exchange resin and cation exchange resin were shown to be capable of adsorbing more than 90% of the uranium from drinking water. However, two common household treatment devices were found not to be totally effective for uranium removal.[7]

Besides treatment of well water, there is also a strong need for the prevention of the spread of uranium contamination from concentrated sources such as uranium mine tailings. Commonly used aboveground water treatment processes are not cost-effective and do not provide an adequate solution to this problem. However, permeable reactive barriers (Figure 1) have been demonstrated to be economically viable and elegant alternatives to the active pump-and-treat remediation systems. Such barriers composed of metallic iron, ferric oxyhydroxide, and bone char phosphate have been designed and proven effective for uranium. Iron metal performed the best and consistently lowered the input uranium concentration by more than 99.9% after the contaminated groundwater had traveled 1.5 feet into the permeable reactive barrier. [11]

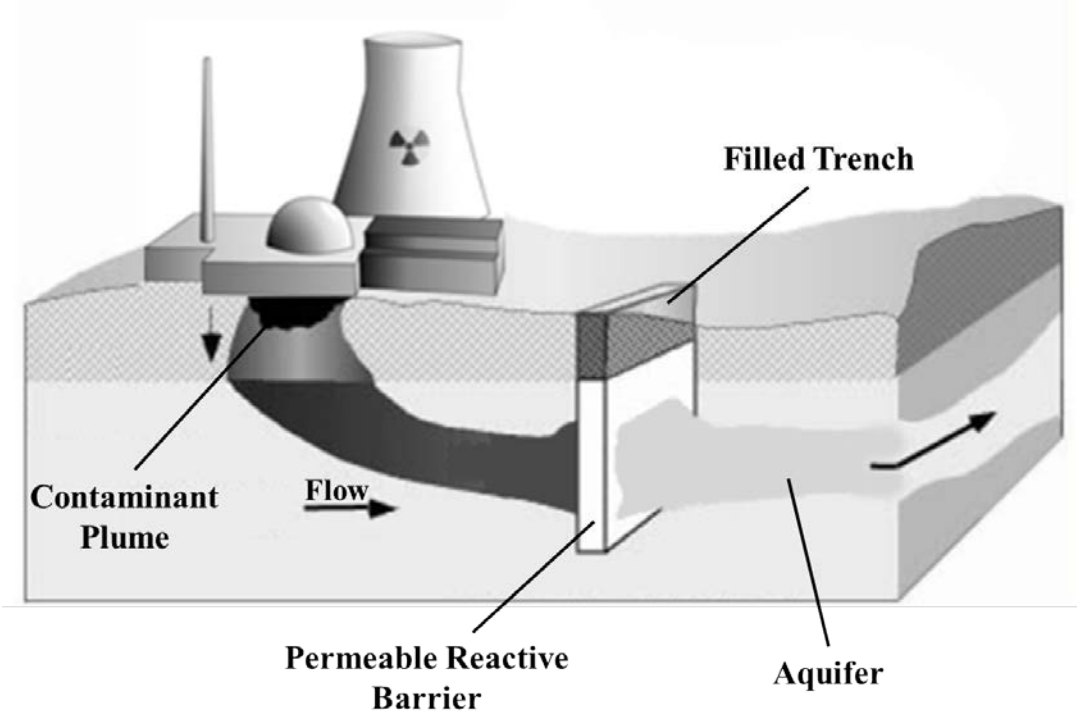

Figure 1: Operation of a Permeable Reactive Barrier

Molybdenum hydrogen bronze (also called molybdenum blue), HMo_2O_6, has been demonstrated to be useful for removal of uranium from aqueous solutions and the possible use in a cyclic process for uranium recovery.[24] In the latter respect, it was thought that the protons would provide ion exchange sites on the material in its reduced form while oxidation would remove these sites and release the uranium in concentrated form. However, it was found that oxidation of the blue reagent occurred during the adsorption process so that the reagent turned from blue to yellow. The study also showed that molybdenum blue had a very large capacity (122% by weight) for uranium.[25] Unfortunately, due to molybdenum trioxide's slight solubility in water, it is possible that toxicity issues may make the use of MoO_3 unsuitable for the purification of drinking water. Therefore, an investigation was conducted to determine whether non-toxic tungsten trioxide and/or tungstic acid could be used for removal of uranium from water.[26] The study showed that these compound do, in fact, show an affinity towards uranium. The study provided insight into the reaction of both tungsten trioxide and tungstic acid's reaction with

dissolved uranium (in the form of uranium acetate) to produce amorphous hydrated mixed oxides, along with their reaction kinetics. The study showed that tungstic acid, which possesses a similar layered structure as molybdenum trioxide (Figure 2), intercalates uranyl (UO_2^{2+}) ions faster than both tungsten and molybdenum trioxides.[26] The present study was undertaken to determine the effect of increasing the surface area on the sorption kinetics of uranyl by tungstic acid.

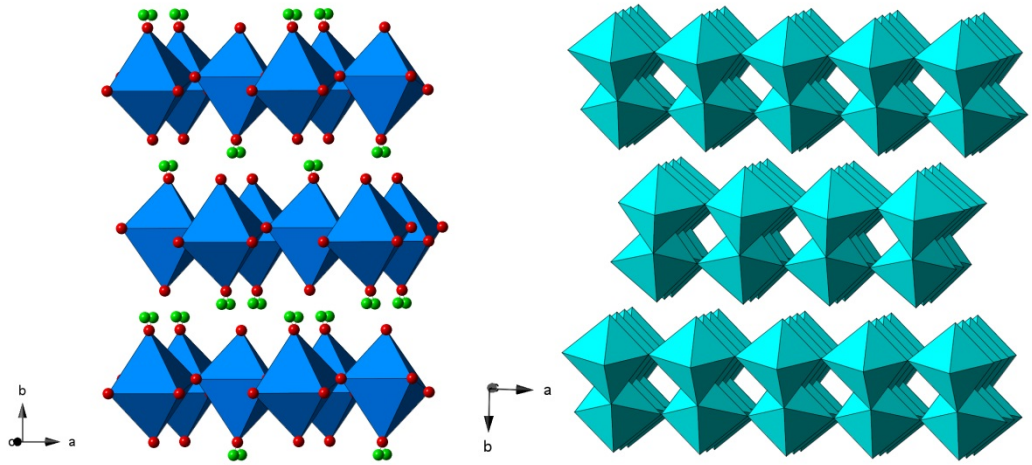

Figure 2: Structure of Layered Tungstic Acid (left) and the Similar Layered Structure of MoO_3 (right)

Experimental:

The chemicals used in this investigation were $Na_2WO_4 \cdot 2H_2O$, concentrated HNO_3, and $_2$ high surface area silica support pellets, obtained from Aldrich, Fischer, and Alfa-Aesar respectively. The stock uranium solution was made with $UO_2(CH_3COO)_2 \cdot 2H_2O$ purchased from Aldrich. All reagents were commercial products (ACS Reagent grade or higher) and were used without further purification. The water used in this study was purified to 18 MΩ via deionization of water previously purified by reverse osmosis. X-ray fluorescence spectroscopy (XRF) was performed on a Thermo electron QuanX XRF spectrometer to determine the concentrations of uranium. A uranium concentration curve was created on the XRF using a 960 ppm NIST standard purchased from Aldrich chemical company. The X-ray powder diffraction of the starting material

was obtained on a Bruker D8-A25-Advance with a LynxEye detector The surface area of the supported tungstic acid was determined via nitrogen physisorption using the Brunauer, Emmett, and Teller (BET) technique of surface area analysis.[27] The starting material was characterized by X-ray powder diffraction.

Supported H_2WO_4 was prepared by vacuum impregnation of high surface area silica catalyst support pellets. A mass of roughly 40 g of high surface area supports were impregnated using 200 mL of an approximately 33% by mass (approximately 1 M) solution of $Na_2WO_4 \cdot 2H_2O$. The solution was introduced through a rubber septum by a syringe needle to the pellets *in vacuo*. After approximately 6 hours under vacuum, the excess solution was poured off and the pellets were rinsed with roughly 100 mL of deionized water to remove any excess sodium tungstate. The pellets were then placed under vacuum in order to uniformly dry the pellets. Once dry, 200 mL of 6 M HNO_3 was added to the supports and the mixture was allowed to sit for approximately 6 hours. This procedure produced a brilliant yellow color shown in Figure 3, and had an indicative of tungstic acid. The pellets were then washed with 500 mL of deionized water to remove any excess $NaNO_3$ and unreacted HNO_3 and then dried under vacuum, yielding a mass increase of 7.3%. BET surface area analysis showed the impregnated pellets had a surface area of 111 m^2/g, which is roughly five times larger than commercial grade tungstic acid. Further, Figure 4 shows the X-ray diffraction pattern of the starting material, matching a pattern for H_2WO_4 in the ICDD data base (PDF 01-084-0886).

Figure 3: Tungstic Acid on Silica

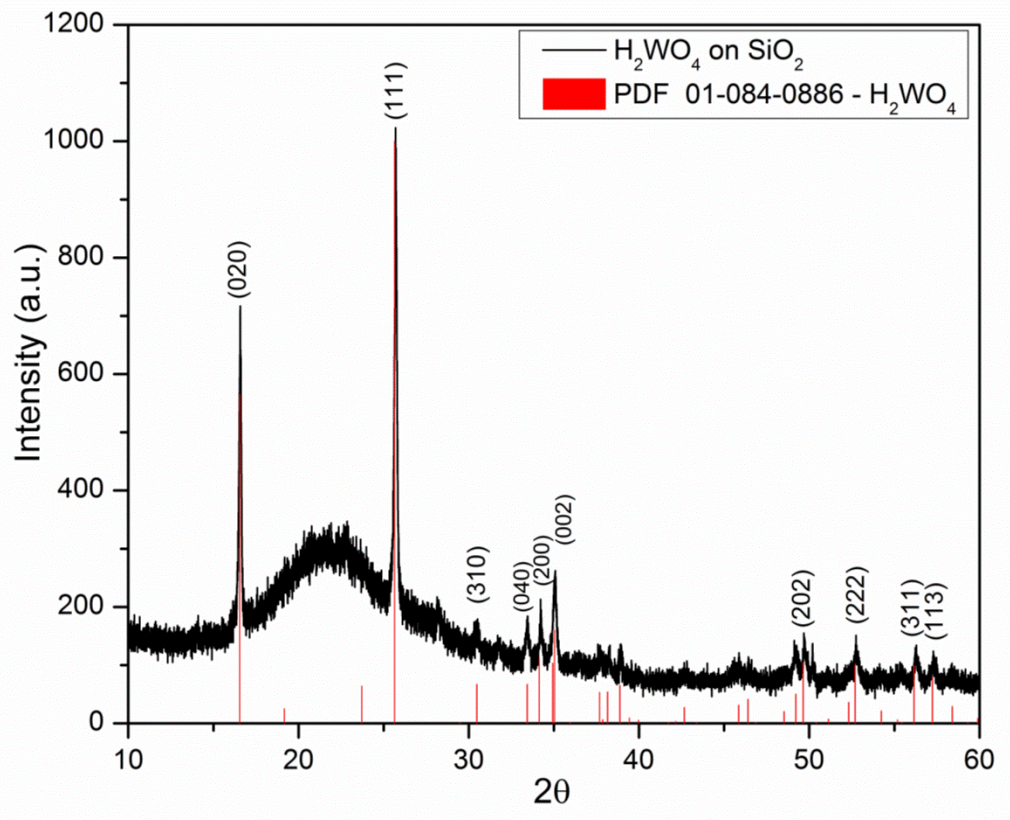

Figure 4: XRD of H2WO4 on High Surface Area Silica

Kinetic experiments were conducted by using varying weights of supported tungstic acid to treat roughly 20 mL solutions of a 125 ppm uranyl solution made from $UO_2(CH_3COO)_2 \cdot 2H_2O$. Three different masses of the 7.3% H_2WO_4 pellets were reacted with the 125 ppm UO_2^{2+} solutions to determine the effect of sorbent dosages. Since pH has been shown to play a large role

in sorption kinetics, the acetate salt was chosen to buffer the pH of the treated solution, as each H_2WO_4 releases $2H^+$ for every UO_2^{2+} exchanged.[28] During the reaction, samples were agitated to eliminate the possibility of forming concentration gradients. Concentrations of the treated solutions were monitored by XRF spectroscopy to determine the time required for the sorption to reach an equilibrium state. The rate constants were calculated by using the conventional rate expression. The sorption capacity (q_t) at given time (t) was calculated from Equation 1, where C_t is the concentration of uranyl ions in the solution at time t, C_0 is the starting concentration, V is the volume of the analyte, and m is the mass of the sorbent.[29]

$$q_t = \frac{(C_0 - C_t)V}{m}$$

Equation 1: The Sorption Capacity Equation

Results and Discussion:

Knowledge of the kinetics of target contaminant uptake is integral for determining the optimum operating conditions for full-scale batch processes. The kinetic rate of uranyl ion sorption is one of the important characteristics defining the efficiency of a sorbent. The uptake isotherm (Figure 5) shows that the rate of sorption of uranyl ions onto the supported tungstic acid is very fast and starts leveling off as the vast majority of sorbate is removed. For the highest molar ratio (380:1), equilibrium is reached within the first 60 minutes, which represents 83% of uranyl ions removed. For the lowest molar ratio (91:1), the equilibrium state is reached more slowly, with the 85% being removed in roughly 48 hours; thereafter, the sorption proceeds at a slower rate until the uranium is removed below the detection limit of the instrument. The kinetics of the sorption processes were analyzed using pseudo first-order and pseudo second-order models commonly used to model sorption processes.

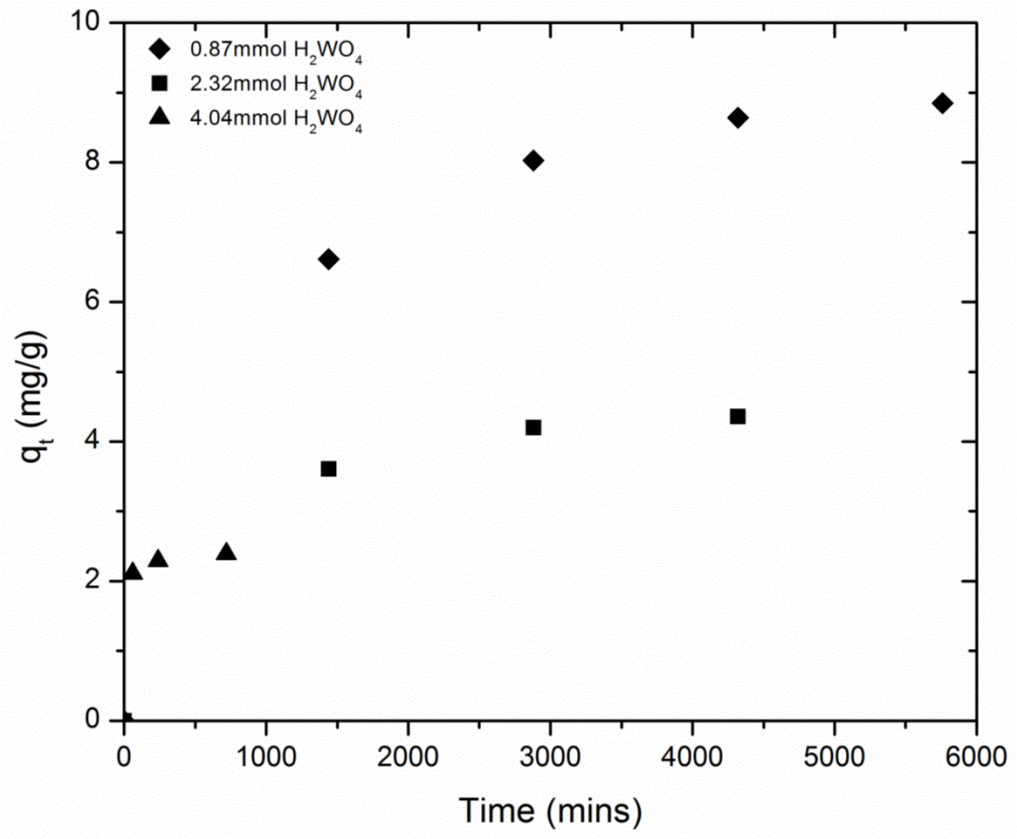

Figure 5: Uptake Curve for the Sorption of UO_2^{2+} by H_2WO_4 on Silica

The pseudo first-order rate expression described by Lagergren, is shown in Equation 2. In this expression, q_t is the amount of the uranyl ions sorbed at time t, k_1 is the rate constant of the pseudo first-order sorption process, and q_e is the amount of analyte sorbed at equilibrium.[30] The values of k_1 and q_e can be determined from the slope and intercept, respectively, of the linear plot of $\log(q_e-q_t)$ vs. time. Figure 6 shows that the pseudo first-order kinetic model does not apply throughout the various sorbent loadings, with the sample treated with 4.04 millimoles of the tungstic acid reagent, exhibiting a large deviation from linearity, as evident from the correlation coefficient (R^2) values listed in Table 1. Furthermore, the estimated values of q_e calculated from the equation differ substantially from those measured experimentally, owing to the fact this sorption process cannot be explained satisfactorily by the linear pseudo first-order model. The discrepancy is most likely due to the similar concentrations of uranyl ions and reactions sites on the sorbent.[31]

$$\log(q_e - q_t) = \log(q_e) - \frac{k_1}{2.303} t$$

Equation 2: The Linearized Formula for Pseudo First-Order Kinetics

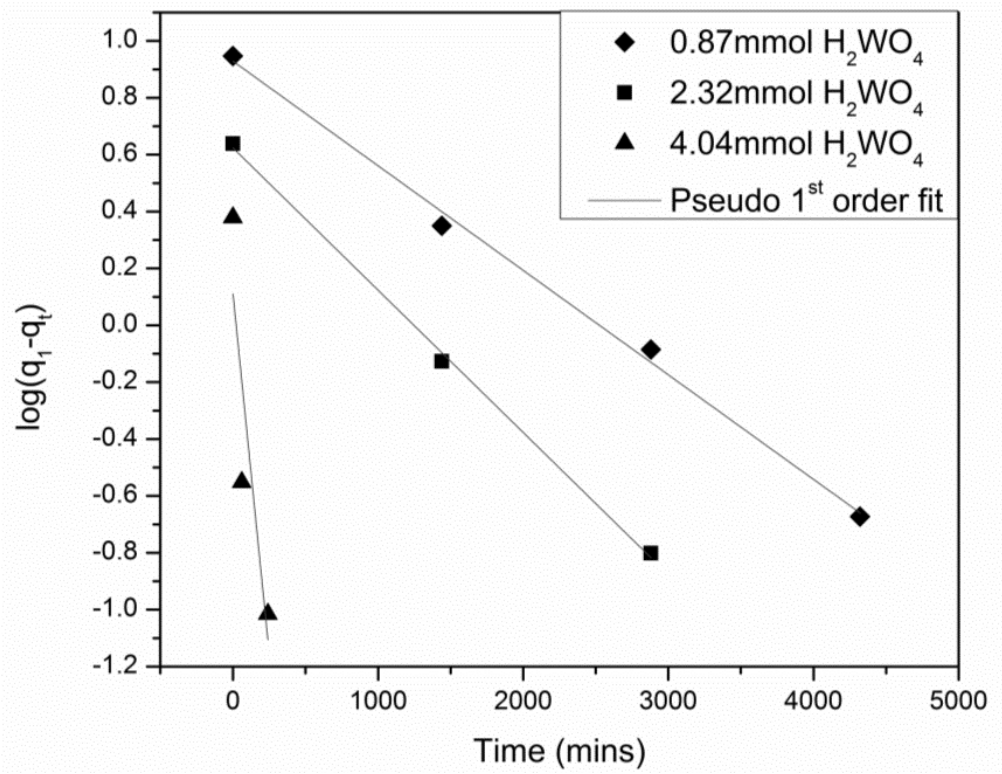

Figure 6: Linear Pseudo First-Order Model for Uranium Uptake by Supported H_2WO_4

Table 1: Kinetic Data and Results from the Linear Plots of the Pseudo First-Order Model

H_2WO_4 (mmol)	k_1 (min^{-1})	q_e (mg/g)	q_e (mg/g) Experimental	R^2
0.87	8.45E-04	8.49	8.85	0.996
2.32	1.15E-03	4.21	4.36	0.999
4.04	1.17E-02	1.29	2.39	0.793

Ho and McKay proposed a pseudo-second order kinetic model, which is represented by the Equation 3,where k_2 is the rate constant of the pseudo second-order sorption process, with the units g mg^{-1} min^{-1}. [32]

$$\frac{t}{q_t} = \frac{1}{k_2 q_e^2} + \frac{1}{q_e} t$$

Equation 3: The Linearized Pseudo Second-Order Rate Equation

The above equation can be further simplified to Equation 4, by substituting h in place of $k_2q_e^2$. In this equation h is considered to be the initial sorption rate, as t/q_t approaches 0. The slope and the intercept of the plot of t/q_t versus t give the values of the constants q_e and h, respectively.[31] Using the values of q_e (the slope) and h (the intercept), the rate constant, k_2, can be obtained.

$$\frac{t}{q_t} = \frac{1}{h} + \frac{1}{q_e} t$$

Equation 4: The Linearized Initial Rate Pseudo Second-Order Rate Equation

Figure 7 shows the linear pseudo second-order plot for the sorption of uranyl ions onto tungstic acid. All of the experiments fit the linear pseudo second-order model much better than that of the pseudo first-order, with the linear regression correlation coefficient R^2 values being very high (R^2>0.99) and the calculated values of q_e are in closer agreement with the experimental data (as summarized in Table 2). However, the pseudo second-order rate constants (k_2) do not display an obvious correlation with respect to the differing amounts of solid used.

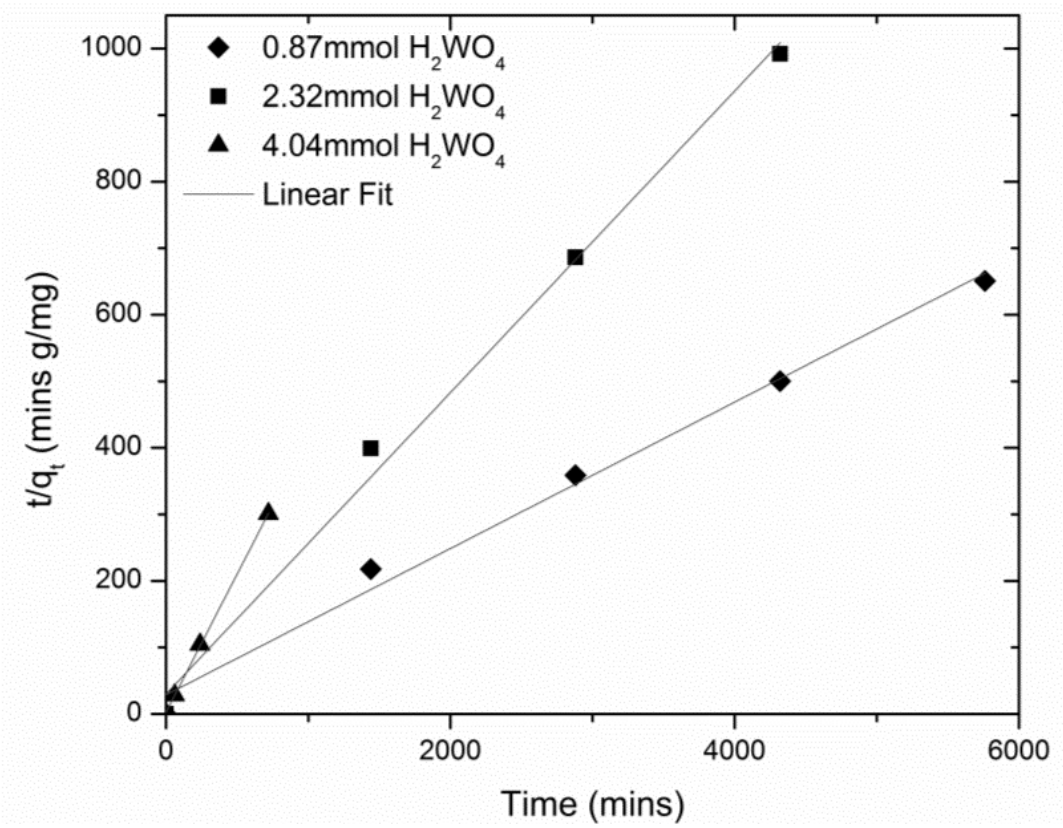

Figure 7: Linear Pseudo Second-Order Model

Table 2: Kinetic Data from the Linear Pseudo Second-Order Equations

H_2WO_4 (mmol)	k_2 (g/mg min)	h (mg/g min)	q_e (mg/g)	q_e (mg/g) Experimental	R^2
0.87	4.92E-03	4.07E-01	9.09	8.85	0.992
2.32	1.72E-03	3.35E-02	4.41	4.36	0.994
4.04	6.03E-03	3.49E-02	2.39	2.39	0.999

Kumar has shown that modeling sorption processes using nonlinear equations was more appropriate for modeling the sorption of methylene blue on activated carbon.[33] This was done using the nonlinear pseudo first-order equation (equation 5). The nonlinear pseudo second-order equation was also used to model the sorption process (equation 6). Figure 8 shows the plotted nonlinear pseudo first and pseudo second-order fits with the sorption data.

$$q_t = q_e(1 - e^{-k_1 t})$$

Equation 5: The Nonlinear Pseudo First-Order Equation

$$q_t = \frac{k_2 q_e^2 t}{1 + k_2 q_e t}$$

Equation 6: The Nonlinear Pseudo Second-Order Equation

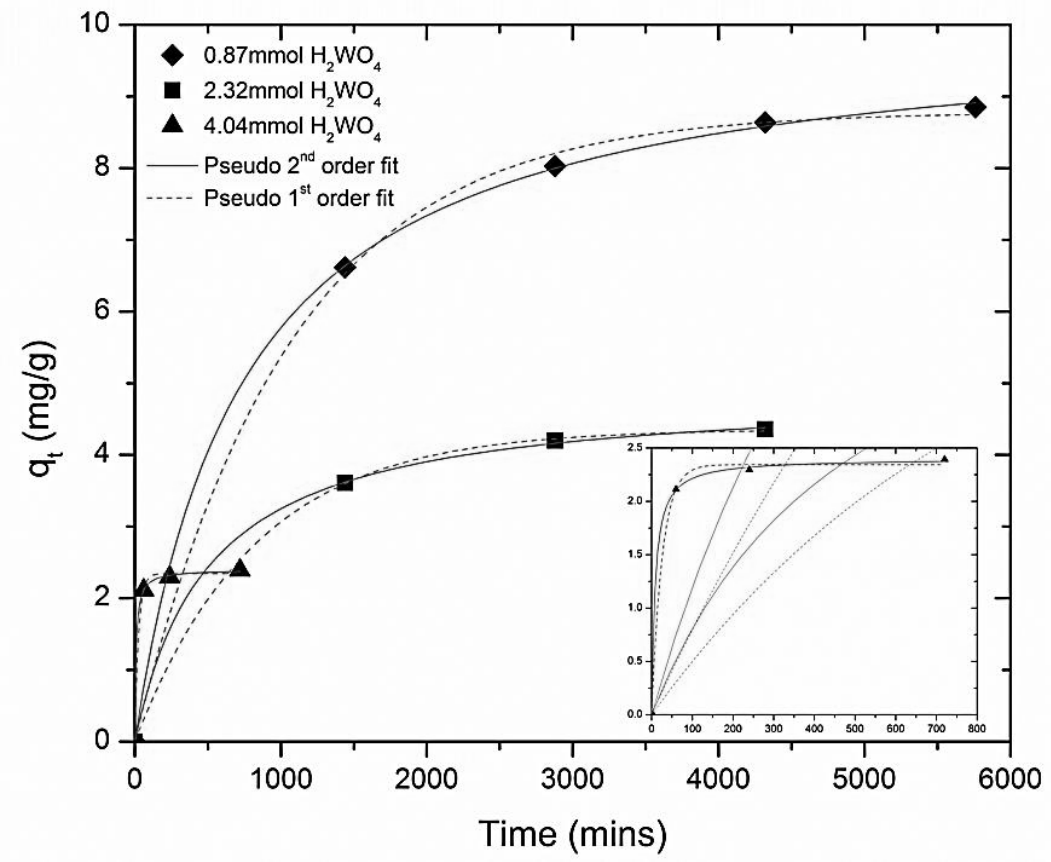

Figure 8: Nonlinear Pseudo First and Second-Order Models

The correlation coefficients associated with both models, from tables 3 and 4, are all very good (R^2>0.99) suggesting that the nonlinear modeling methods may be a more effective way of representing the data. Similar to the linear methods, the pseudo second-order model aligns better with the larger mass of sorbent, while the nonlinear pseudo first-order equation agrees well with the lower concentrations of solid. The nonlinear pseudo first-order model gives calculated q_e

values that are much closer to that of the experimental values, compared to all models. In all cases, the nonlinear pseudo second-order model overestimates q_e values. However, the linear pseudo second-order model gives q_e values which are much more consistent with the observed data. Further, the rate constants (k_2) for the nonlinear model show, as expected, an increase with the increasing mass of the sorbent material.

Table 3: The Summarized Kinetic Data from the Nonlinear Pseudo First-Order Model

H_2WO_4 (mmol)	k_1 (min^{-1})	q_e (mg/g)	q_e (mg/g) Experimental	R^2
0.87	9.44E-04	8.79	8.85	0.998
2.32	1.22E-03	4.36	4.36	0.999
4.04	3.85E-02	2.23	2.39	0.998

Table 4: The Summarized Kinetic Data from the Nonlinear Pseudo Second-Order Model

H_2WO_4 (mmol)	k_2 (g/mg min)	h (mg/g min)	q_e (mg/g)	q_e (mg/g) Experimental	R^2
0.87	1.34E-04	1.36E-02	10.04	8.85	0.999
2.32	4.05E-04	9.67E-03	4.88	4.36	0.999
4.04	4.96E-02	2.86E-01	2.40	2.39	0.999

As previously demonstrated, the spent materials can be easily recovered allowing a cyclic green process for uranium isolation.[26] Figure 9 shows the process to recover both the uranium and tungstic acid. This is achieved by treating the post sorption materials with ammonium hydroxide. The uranium is easily separated from the tungsten by filtration as insoluble uranium containing yellow cake and the soluble ammonium tungstate. The yellow cake can then be calcined and repurposed as uranium oxide (U_3O_8) with a very high yield. The soluble ammonium tungstate can then be protonated with the addition of acid to return the original tungstic acid starting material, also with a very high yield. The only byproduct in this process is nontoxic ammonium chloride. However, unlike the powder sorbent, the yellow cake produced in the cyclic process stays on the pellet which eliminates the need for vacuum filtration to recover the uranium containing product. Further, the uranium then can be recovered by employing an acid to strip the pellets, dried, and calcined to produce the desired U_3O_8.

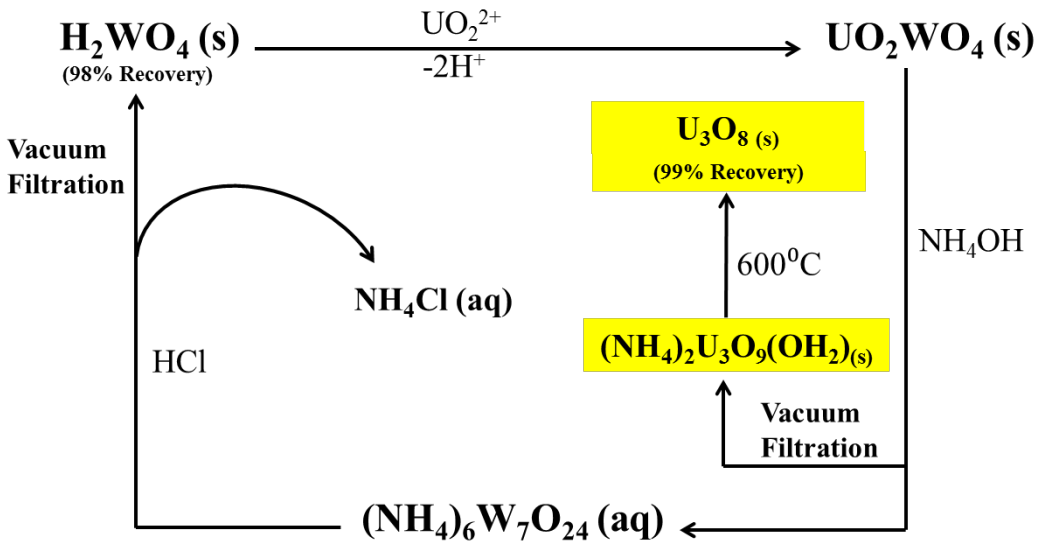

Figure 9: The Cyclic-Green Process for the Recovery of Uranium

Conclusions:

Tungstic acid on high surface area catalyst supports provides a very attractive avenue for the remediation and recovery of aqueous uranium. Due to the high surface area of the supported materials, much improved kinetic results were achieved. This reaction provides the means to remove uranium from drinking water and a method to treat contaminated ground water with a permeable reactive barrier. Moreover, the high surface area catalyst supports provide facile means for the separation of the spent sorbent from the system. The modeling of the sorption of uranyl on tungstic acid gave good results using the linear pseudo-second order and both the nonlinear pseudo first and second-order models, but the nonlinear first-order method describes the system most accurately.

References:

1. R. G. Riley, J. M. Zachara, and F. J. Wobber, Chemical Contaminants on DOE Lands and Selection of Contaminant Mixtures for Subsurface Science Research. *US Department of Energy, Office of Energy Research* **1992,** (Subsurface Science Program).

2. P. Robinson, Uranium Mill Tailings Remediation Performed by the US DOE: An Overview. Southwest Research and Information Center: Albuquerque, New Mexico, 2004.

3. G. R. Bradford, D. Bakhtar, and D. Westcot, Uranium, vanadium, and molybdenum in saline waters of California. *Journal of Environmental Quality* **1990,** *19*, 105-108.

4. L. Salonen, 238U Series Radionuclides as a Source of Increased Radioactivity in Groundwater Originating from Finnish Bedrock. In *Future Groundwater Resources at Risk* Soveri, J.; Suokko, T., Eds. International Association of Hydrological Sciences: Wallingford, UK, 1994; pp 71-84.

5. M. A. Moss, R. F. McCurdy, K. C. Dooley, M. L. Givner, L. C. Dymond, J. M. Slayter, and M. M. Courneya, Uranium in drinking water - report on clinical studies in Nova Scotia. In *Chemical Toxicology and Clinical Chemistry of Metals*, Brown, S. S.; Savory, J., Eds. Academic Press: London, UK, 1983; pp 149-152.

6. Occurrence and Exposure Assessment for Uranium in Public Drinking Water Supplies. United States Environmental Protection Agency 1990.

7. J. D. Navratil, Advances in Treatment Methods for Uranium Contaminated Soil and Water. *Archive of Oncology* **2001,** *9* (2), 57-60.

8. C. R. Cothern and W. L. Lappenbusch, Occurrence of Uranium in Drinking Water in the U.S. *Health Physics* **1983,** *45* (89).

9. D. R. Dreesen, J. M. Williams, M. L. Marple, E.S.Gladney, and D. R. Perrin, Mobility and Bioavailability of Uranium Mill Tailings Constituents. *Environmental Science & Technology* **1982,** *16* (702).

10. R. F. Spalding and W. M. Sackett, Uranium in Runoff from the Gulf of Mexico Distributive Province: Anomalous Concentrations. *Science* **1972,** *175* (629).

11. Field Demonstration Of Permeable Reactive Barriers To Remove Dissolved Uranium From Groundwater, Fry Canyon, Utah. United States Environmental Protection Agency Washington, DC, 2000.

12. Depleted Uranium in Bosnia and Herzegovina Post-Conflict Environmental Assessment Revised Edition. United Nations Environment Programme: Switzerland, 2003.

13. R. E. Gephart, A Short History of Hanford Waste Generation, Storage, and Release. Pacific Northwest National Laboratory, U.S. Department of Energy: Richland, Washington, 2003.

14. J. Szecsody, M. Truex, L. Zhong, M. Williams, C. Resch, and J. McKinley, Remediation of Uranium in the Hanford Vadose Zone Using Gas-Transported Reactants: Laboratory-Scale

Experiments. Pacific Northwest National Laboratory, U.S. Department of Energy: Richland, Washington, 2010.

15. DOE resumes plutonium stabilization at Hanford plutonium finishing plan. U.S. Department of Energy-Richland Operations Office: Richland, Washington. , 1999.

16. B. C. Simpson, R. A. Corbin, M. J. Anderson, and C. T. Kincaid, Hanford Soil Inventory Model (SIM) Rev. 2 User's Guide. U.S. Department of Energy: Richland, Washington, 2007.

17. D. M. Taylor and S. K. Taylor, Environmental Uranium and Human Health. *Reviews on Environmental Health* **1997,** *12*, 147-157.

18. D. P. Haley, Morphologic Changes in Uranyl Nitrate-Induced Acute Renal Failure in Saline- and Water-Drinking Rats. *Laboratory Investigation* **1982,** *46*, 196-208.

19. M. L. Zamora, B. L. Tracy, J. M. Zielinski, D. P. Meyerhof, and M. A. Moss, Chronic Ingestion of Uranium in Drinking Water: a Study of Kidney Bioeffects in Humans. *Toxicological Science* **1998,** *43*, 68-77.

20. Y. Mao, M. Desmeules, D. Schaubel, D. Bérubé, R. Dyck, D. Brûlé, and B.Thomas, Inorganic Components of Drinking Water and Microalbuminuria. *Environmental Research* **1995,** *71*, 135-140.

21. S. Bastians, G. Crump, W. P. Griffith, and R. Withnall, Raspite and studtite: Raman spectra of two unique minerals. *Journal of Raman Spectroscopy* **2004,** *35* (8-9), 726-731.

22. National Primary Drinking Water Regulations. Environmental Protection Agency: 2009; pp 1-6.

23. S. K. White and E. A. Bondietti, Removing Uranium by Current Municipal Water Treatment Processes. *Journal of the American Water Works Association* **1983,** *75* (374).

24. B. P. Kiran, A. W. Apblett, and M. M. Chehbouni, Selective Absorption of Heavy Metals and Radionuclides from Water in a Direct-to-Ceramic Process. *Ceramic Transactions* **2003,** *143*, 385-394.

25. M. Chehbouni, H. Al-Busaidi, and A. W. Apblett, Green Process for Uranium Separations Utilizing Molybdenum Trioxide. In *Nuclear Energy and the Environment*, American Chemical Society: 2010; Vol. 1046, pp 155-167.

26. H. Albusaidi and A. W. Apblett, Adsorption and Separation of Uranium Using Tungsten Oxides. In *Environmental Issues and Waste Management Technologies in the Materials and Nuclear Industries XII*, John Wiley & Sons, Inc.: 2009; pp 39-46.

27. S. Brauner, P. H. Emmett, and E. Teller, Adsorption of Gases in Multimolecular Layers. *Journal of the American Chemical Society* **1938,** *60* (2), 309-319.

28. K. S. Smith, Metal sorption on mineral surfaces: An overview with examples relating to mineral deposits. . *Reviews in Economic Geology* **1999,** *6A-B*, 161-182.

29. C. Dwivedi, S. K. Pathak, Manmohan Kumar, S. C. Tripathi, and a. P. N. Bajaj, Potassium cobalthexacyanoferrate–gel beads for cesium removal: kinetics and sorption studies. *RSC Advances* **2013,** *3*, 22102-22110.

30. S. Lagergren, Zur theorie der sogenannten adsorption gelöster stoffe. Kungliga Svenska Vetenskapsakademiens. *Handlingar* **1898,** *24* (4), 1-39.

31. S. Azizian, Kinetic models of sorption: a theoretical analysis. *Journal of Colloid and Interface Science* **2004,** *276*, 47–52.

32. Y. S. Ho and G. McKay, Pseudo-second order model for sorption processes. *Process Biochemistry* **1999,** *34*, 451-465.

33. K. V. Kumar, Linear and non-linear regression analysis for the sorption kinetics of methylene blue onto activated carbon. *Journal of Hazardous Materials B* **2006,** *137*, 1538-1544.

CHAPTER VI

SINGLE SOURCE PRECURSOR APPROACH FOR THE SYNTHESIS OF NANOCRYSTALLINE MOLYBDATES AND TUNGSTATES

Introduction:

Metal tungstates and molybdates have received much interest due to their interesting and useful properties. For example, aluminum and zirconium molybdates and tungstates have been studied for their interesting negative thermal expansion properties.[1-4] Further, metal molybdates and tungstates have found applications as scintillators,[5-6] in optics,[7-9] and catalysis,[10] among others. However, for the scope of this investigation they will find use as ion-exchange materials for water remediation technologies. The development of single-source precursor methods for synthesizing materials has been well established.[11-13] Moreover, low-temperature methods, in many cases yield nanocrystalline materials upon decomposition of the precursor materials.[14-16] The single-source precursor approach is also favorable due to the ability to control the stoichiometry of the products, allowing for the development of tunable materials.[17] Water soluble α-hydroxycarboxylic acids have been shown to chelate many transition metal oxides, thus were a good candidate for the dissolution of tungstic acid and molybdenum trioxide in this study.[18] Furthermore, research has been conducted as to elucidate the structure of α-hydroxycarboxylate complexes with group-(VI) metal oxides.[19-20] Development of a water soluble single-source

precursor approach allows for the precursor material to be deposited on substrates while using a green solvent, such as water.

Experimental:

Materials

All chemicals (reagent grade or higher) were used as received without further purification. Water was purified to a resistance of 18MΩ using reverse osmosis. The tungstic acid, $Mg(OH)_2$, calcium D-gluconate, α-hydroxyisobutyric acid (98%), and zinc gluconate were obtained from Alfa-Aesar. The L-lactic acid (85+ %), $Al(C_2H_3O_2)_2OH$, and $Zr(OH)_x(C_2H_3O_3)_y$ (x + y = 4) were all received from Aldrich. The $Ca(OH)_2$, $Zn(C_2H_3O_2)_2{\cdot}2H_2O$, $Ba(OH)_2$, $Sr(OH)_2$, and sodium gluconate used were obtained from Fisher Scientific. The glycolic acid (67%) and the gluconic acid (50%) were received from Arcos Organics. Deuterated water from Aldrich was used for the liquid state NMR experiment.

Preparation of the Single Source Precursor

The typical synthesis of the metal carboxylate precursors was done using either an acid-base reaction in a 2:1 molar ratio of the acid to the metal hydroxides or a ligand exchange in the case of the metal acetates with the same ratios. The solutions of the resulting hydroxy carboxylic salts were evaporated at 80 °C in an oven until the sample was reduced to a solid. The salts were then reacted with the group (VI) oxide (MoO_3 or H_2WO_4), always in a 1:1 molar ratio under reflux conditions. For example, to synthesize a single source precursor for $CaWO_4$ using α-hydroxyisobutyric (methyl lactic) acid, the reaction consisted of adding 0.74 g of $Ca(OH)_2$ (10 mmol) to a 100 mL solution with 2.09 g of α-hydroxyisobutyric acid (20 mmol) dissolved in deionized water. The solid product was obtained in a 99.4% yield (2.01 g with 22.2% crystalline H_2O) by drying at 80 °C in an oven. The salt was then dissolved and reacted with an equimolar amount, 2.50 g (10 mmol), of tungstic acid under reflux conditions for approximately 24 hours.

Any residual solid was removed from the resultant solution by vacuum filtration to yield a transparent-brown solution in every case. The resultant filtrates from every precursor were allowed to evaporate at room temperature to allow for possible crystallization to take place. However, the only single-source precursors that produced crystals suitable for X-ray diffraction were the methyl lactate precursors. To produce the metal oxides, the precursors were pyrolyzed at their decomposition temperatures obtained from thermal gravimetric analysis.

Characterization

Each of the single-source precursors were characterized by thermal gravimetric analysis, performed on a Mettler-Toledo TGA/DSC 1 with a heating rate of 5°C/min, in order to determine the amount of bound water and the thermal decomposition temperatures. Raman spectra were recorded of both the single-source precursors and final products on a Nicolet NXR 9610 Raman spectrometer. The X-ray diffraction patterns for both the precursors and oxide products were obtained using a Bruker D8-A25-Advance diffractometer equipped with a LynxEye detector. Fourier transformed infrared (FT-IR) spectroscopy was performed as KBr pellets using a Nicolet Magna 750 IR spectrometer. The crystal structures were obtained by single crystal X-ray diffraction performed at the University of Oklahoma using a Bruker-AXS APEX CCD area detector on a D8 platform goniometer with a sealed-tube X-ray generator and a mono-capillary collimator. The solid state nuclear magnetic resonance spectroscopy (SS-NMR) data was acquired using a Varian/Chemagnetics CMX-II 300 MHz SS-NMR spectrometer and liquid NMR spectra were obtained using a Varian UNITY INOVA 400 MHz NB NMR system.

Results and Discussion:

All of the single-source precursors were allowed to slowly evaporate to allow the formation of crystals suitable for X-ray diffraction, but only the α-hydroxyisobutyric acid analogues produced suitable crystals. The resulting structures (Figures 1 and 2) are very similar to

the structures predicted for tungstenyl α-hydroxycarboxylate complexes, including a D-gluconic acid analogue.[20, 34] The structure consists of a tungstenyl group (cis-WO_2^{2+} group) chelated by two doubly deprotonated α-hydroxyisobutyrate groups (deprotonated at both the carboxylic acid and α-hydroxyl groups). Hexaaqua calcium and magnesium ions are present as counter ions of the resulting tungsten-containing anions. In both cases, the cations and anions are extensively hydrogen bonded to each other. The five-membered chelate rings formed by the carboxylate are close to planar and the two methyl groups project out of this plane into two different environments. One methyl group (C4) projects into the same plane as one of the tungstenyl oxo groups while the second (C3) points away from this oxo group.

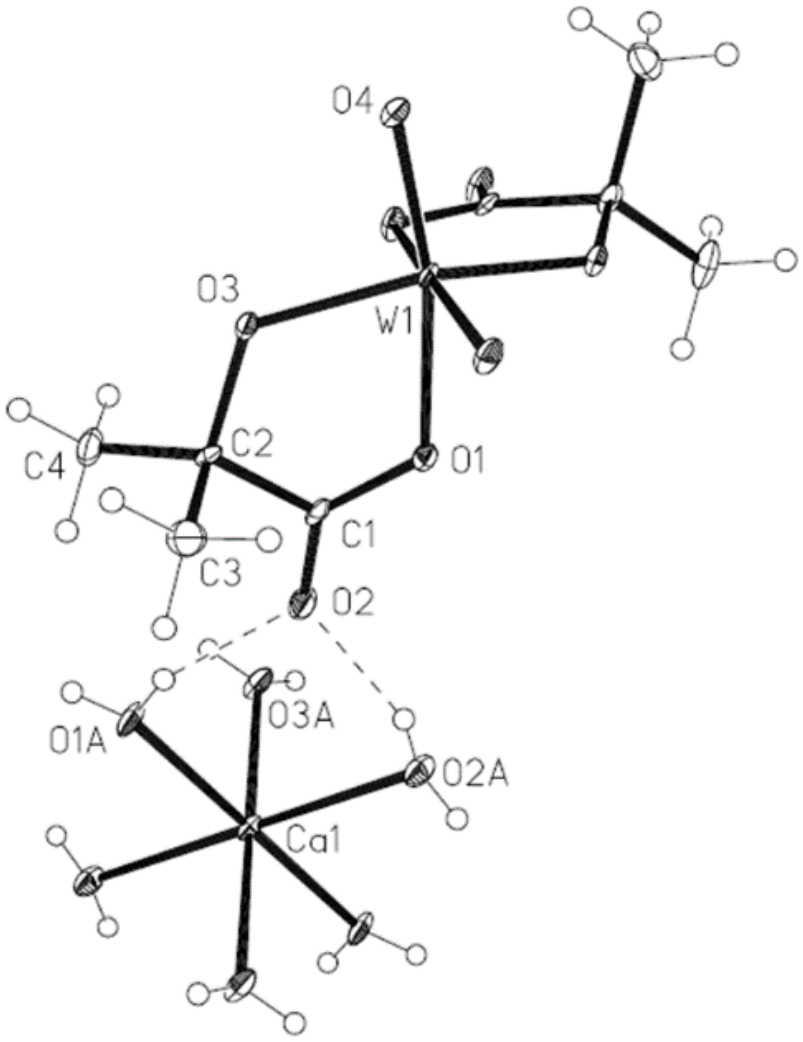

Figure 1: Crystal Structure of the Methyl Lactate Single-Source Precursors with Ca^{2+}, with Displacement Ellipsoids Drawn at the 50% Probability Level

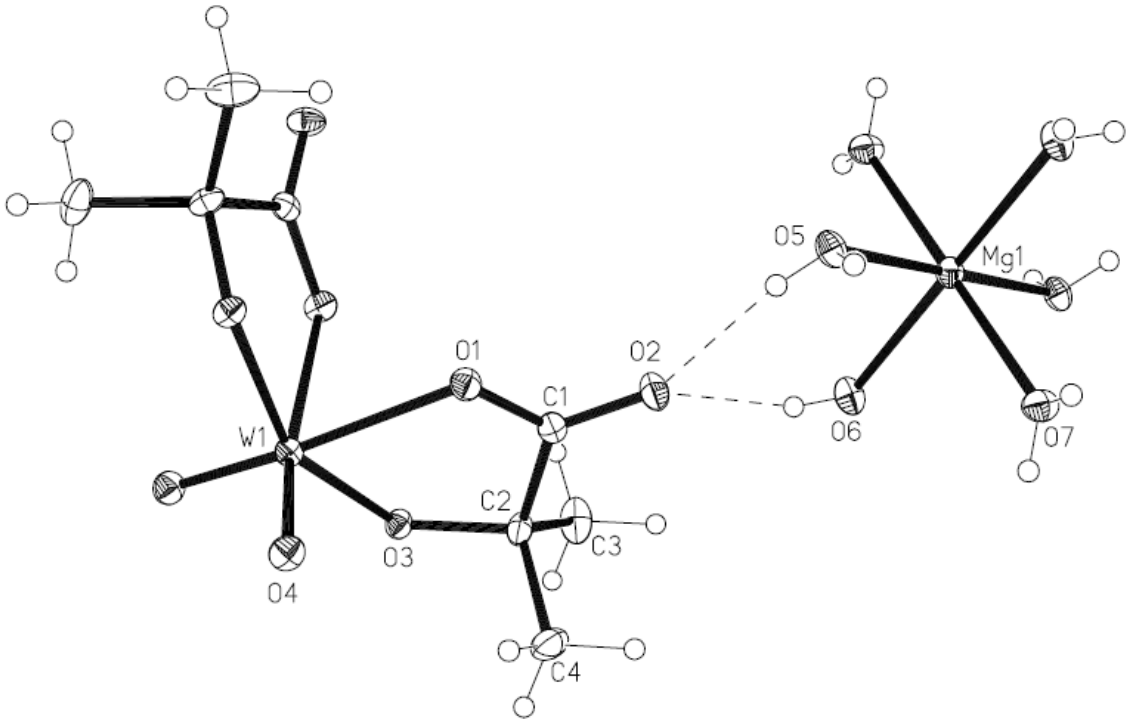

Figure 2: Crystal Structure of the Methyl Lactate Single-Source Precursors with Mg^{2+}, with Displacement Ellipsoids Drawn at the 50% Probability Level

The crystalline calcium precursor and its calcium salt were both analyzed by solid state NMR spectroscopy and liquid ^{13}C NMR spectroscopy, and the results are summarized in Table 1. When the hydroxyl group from the carboxylate is chelated to tungsten, a roughly 12 ppm shift is observed for the quaternary carbon (C2) from 74 ppm to 86 ppm. Interestingly, this shift appears in both the solid state and liquid NMR spectra, suggesting the carboxylate remains chelated upon dissolution in water, yielding Ca^{2+} and the $[WO_2(OCO(CH_3)_2O)_2]^{2-}$ ions. Furthermore, two

separate peaks were resolved for the two non-equivalent methyl groups (C3 and C4) of the single-source precursor, as expected from the crystal structure, in both the solid state and liquid NMR spectra. Similarly, the ^{1}H NMR showed the two non-equivalent methyl groups with proton peaks at 1.37 and 1.40 ppm as listed in Table 2. A similar motif was observed for the magnesium salt as well.

Table 1: ^{13}C NMR Data for Calcium Methyl Lactate Salt and its Single Source Precursor

^{13}C		Functional Groups			
$Ca(OCO(CH_3)_2OH)_2$		CH_3-	CH_3-	-CO-	C=O
Solid State	δ (ppm)	27.1	N/A	74.0	181.8
Liquid	δ (ppm)	27.5	N/A	74.9	184.6
$CaWO_2(OCO(CH_3)_2OH)_2$					
Solid State	δ (ppm)	26.6	25.2	85.6	186.7
Liquid	δ (ppm)	26.8	26.0	86.0	189.2

Table 2: ^{1}H NMR Data for Calcium Methyl Lactate Salt and its Single Source Precursor

^{1}H		Functional Groups	
$Ca(OCO(CH_3)_2OH)_2$		CH_3-	CH_3-
Liquid	δ (ppm)	1.32	N/A
$CaWO_2(OCO(CH_3)_2OH)_2$			
Liquid	δ (ppm)	1.37	1.40

The methyl lactate precursor was also characterized by X-ray powder diffraction and Raman and FTIR spectroscopies. The XRD patterns (Figures 3 and 4) match very closely to that of the simulated patterns calculated from the single crystal structures, demonstrating that the crystal structures are representative of the bulk materials.

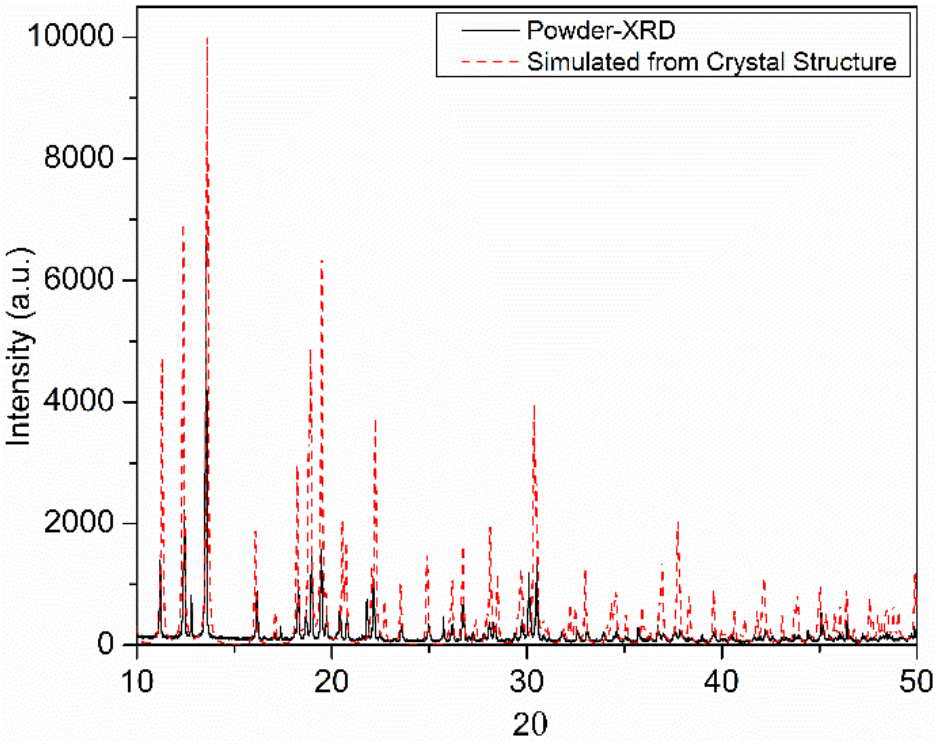

Figure 3: X-ray Powder and Single Crystal Diffraction Patterns of $[Ca(OH_2)_6][WO_2(2\text{-oxyisobutyrate})_2]$

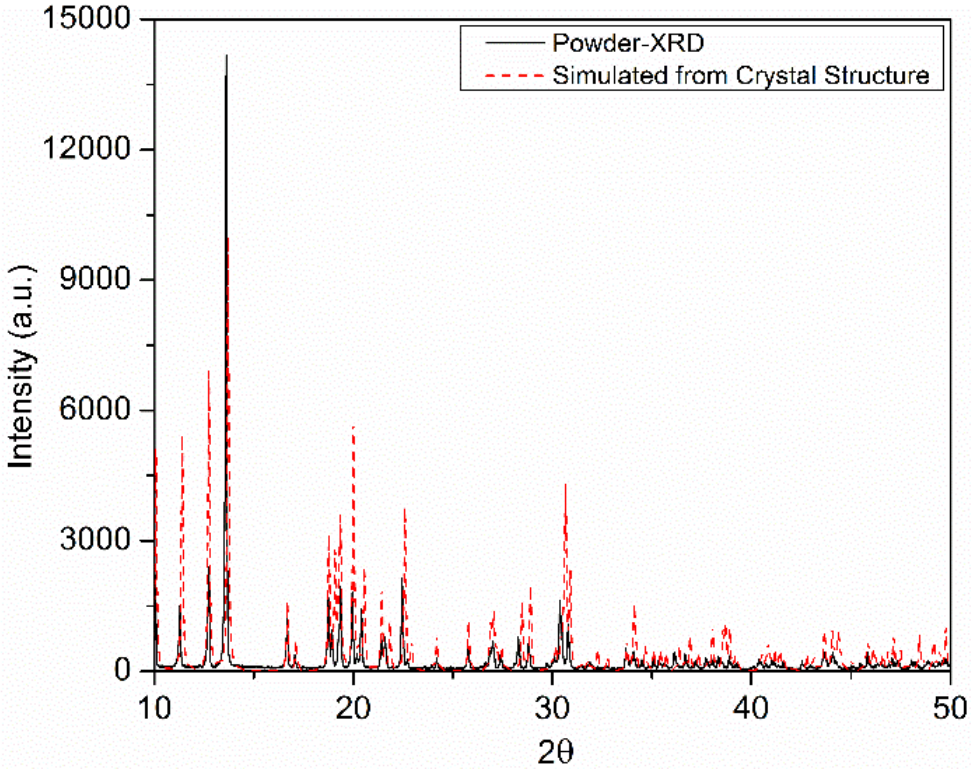

Figure 4: X-ray Powder and Single Crystal Diffraction Patterns of $[Mg(OH_2)_6][WO_2(2\text{-oxyisobutyrate})_2]$

The Raman spectrum (Figure 5) of the precursor shares many of the peaks previously reported for α-hydroxyisobutyric acid.[21] Furthermore, the intense peaks 934, 913, 862, and 852 cm^{-1} in the Raman spectrum can be attributed to the tungstate ion. Similarly, the IR spectrum shows a broad band at 937 cm^{-1}, along with bands at 883 cm^{-1} and 848 cm^{-1}, shown in Figure 6.

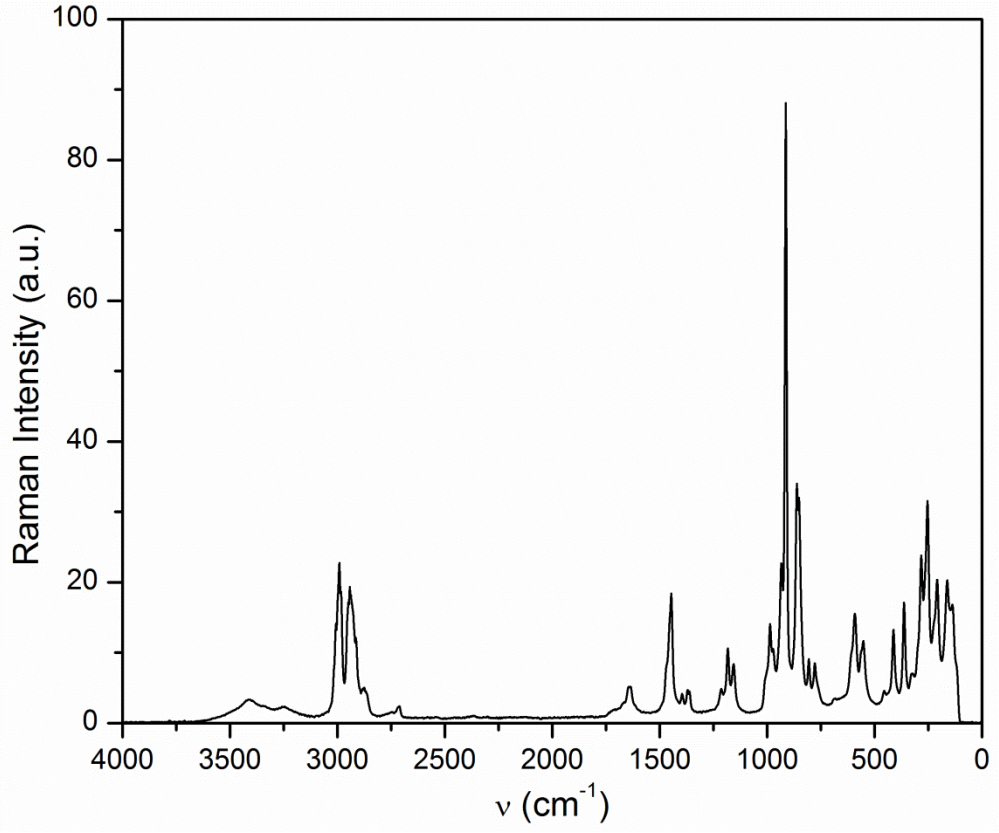

Figure 5: The Raman Spectrum of $[Ca(OH_2)_6][WO_2(2\text{-oxyisobutyrate})_2]$

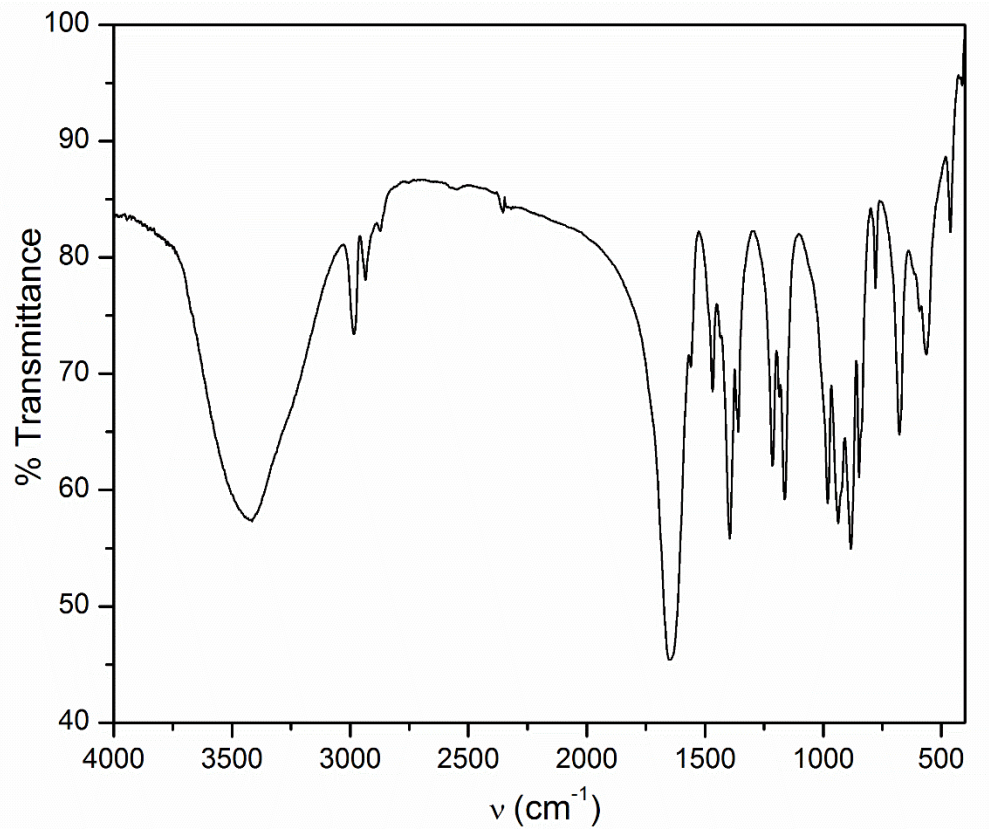

Figure 6: The Infrared Spectrum of $[Ca(OH_2)_6][WO_2(2\text{-oxyisobutyrate})_2]$

Each of the single-source precursors decomposition temperatures was determined via thermal gravimetric analysis. Figure 7 shows the TGA traces for the calcium precursors, showing the effect of chain length and structure on the decomposition temperature. Each of the precursors had relatively low decomposition temperatures, with the highest corresponding the longest chain, D-gluconate, precursor at around 485°C. The surface areas of the resulting $CaWO_4$ depended on the hydroxycarboxylate used in their preparation with the branched α-hydroxy acid having the highest surface area of 24 m^2/g.

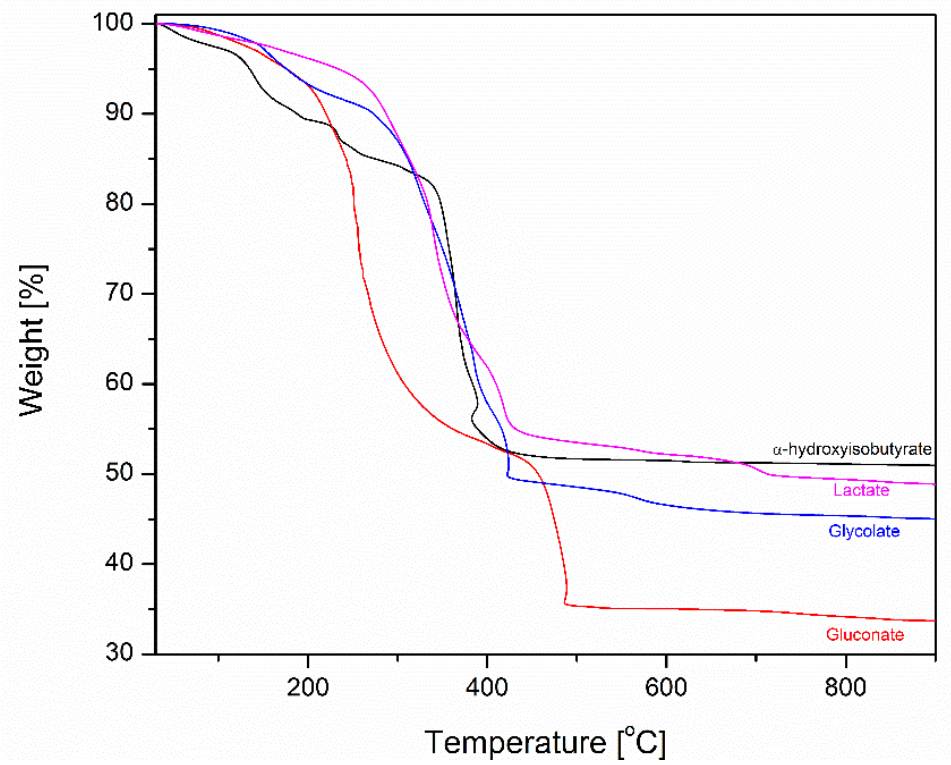

Figure 7: TGA Traces for each of the $CaWO_4$ Single-Source Precursors

Table 3: Yield, Decomposition Temperatures, and Surface Areas for each of the Ca^{2+} Precursors

Hydroxy Acid Used	Yield (%)	Decomposition Temperature (°C)	BET Surface Area (m^2/g)
Glycolic	98.1	400	18
Lactic	98.4	425	15
Methyl Lactic	99.2	425	24
Gluconic	99.4	485	8

The XRD pattern of $CaWO_4$ derived from the methyl lactate precursor (Figure 8) matched the pattern for $CaWO_4$ (PDF Card 01-072-0257), showing broadened diffraction peaks characteristic of nanocrystalline materials. The full width at half maximum (FWHM) of the (200) peak was determined using the Pearson VII profiling function. This, along with the results from a highly crystalline $CaWO_4$, was used to determine a lower limit of grain size of 14 nm via the Scherer equation. The crystallite sizes of the gluconate and glycolate were similar to the methyl

lactate (17 and 16 nm respectively) and the lactate precursor that had a larger crystallite size of 32 nm. The calcium tungstate produced from the methyl lactate precursor was used extensively for the experiments reported in this dissertation. XRDs were recorded for all of the synthesized metal tungstates and molybdates and matched with data from the ICDD database.

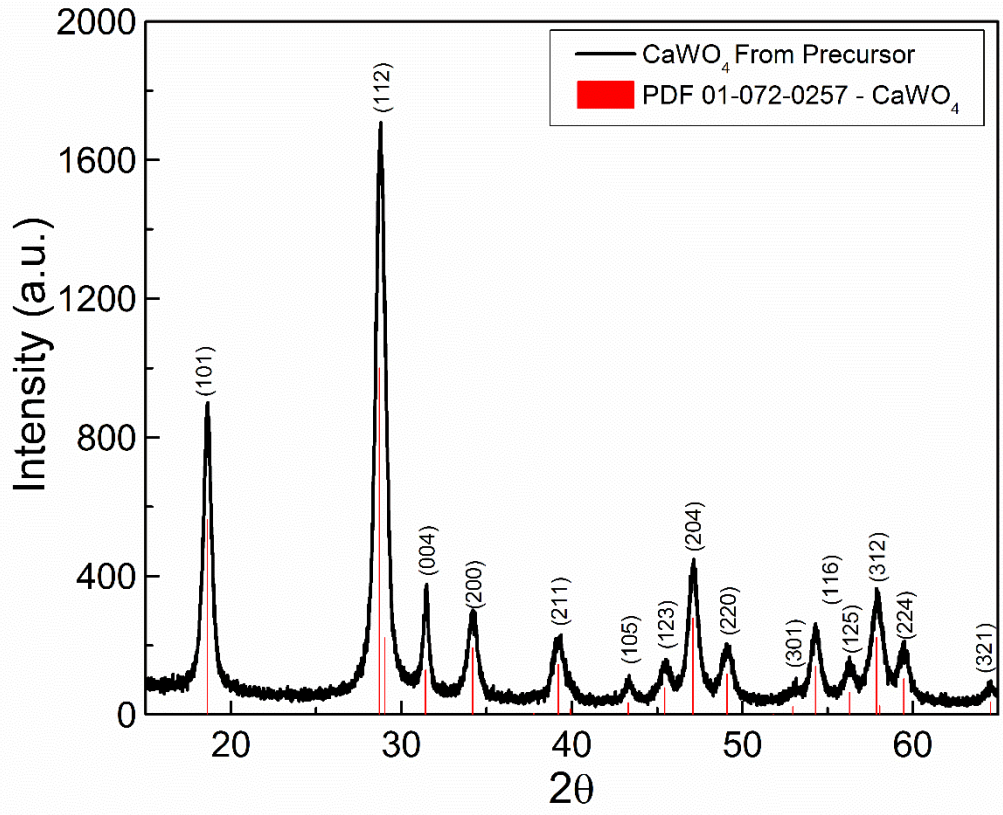

Figure 8: XRD of $CaWO_4$ from the Methyl Lactate Precursor

The Raman spectrum (Figure 9) of the $CaWO_4$ from the methyl lactate precursor shows the characteristic A_{1g} stretch at 911 cm^{-1} which corresponds to symmetric stretching vibration of tetrahedral WO_4^{2-}.[22] The peaks at 838 and 796 cm^{-1} correspond to a splitting of the ν_3 mode of the tungstate, with the band the higher energy band being the $\nu_3(B_g)$ vibration while the lower energy one is due to the $\nu_3(E_g)$ vibration of the tungstate unit. The ν_4 mode gives a weak absorption at 399 cm^{-1}. The peak at 331 cm^{-1} can be assigned to the $\nu_2(A_g)$ vibrational mode. Finally, the stretch observed at 208 cm^{-1} is due to the translational mode, ν(Ca-O).[23-28] Similarly, the FTIR

spectrum (Figure 10) shows the characteristic, though broad, $\nu_3(A_u) + \nu_3(E_u)$ charge transfer band at 801 cm^{-1} and the $\nu_3(B_g)$ band at 440 cm^{-1} for tetrahedral tungstate.[24] The spectrum also shows the presence of bound water at 3437 and 1635 cm^{-1}.

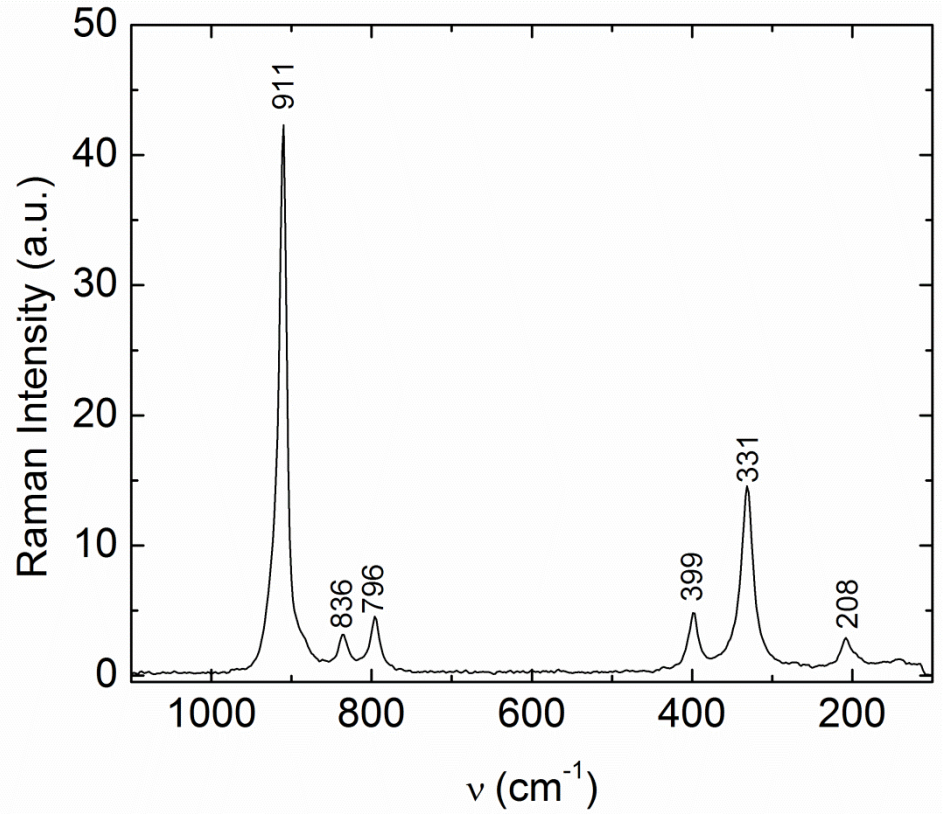

Figure 9: Raman Spectrum of $CaWO_4$ from the Methyl Lactate Precursor

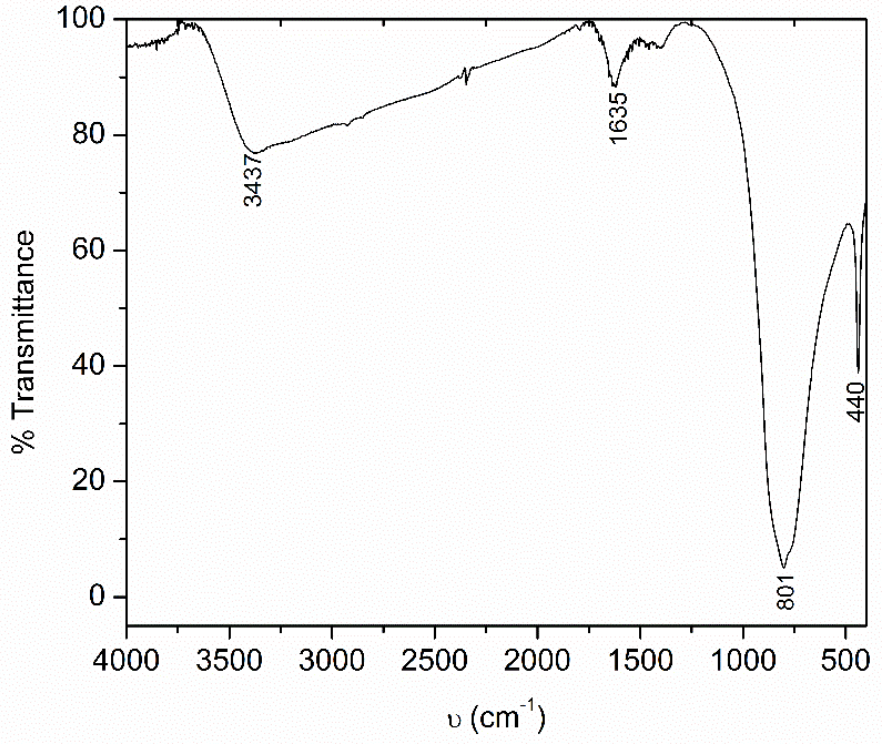

Figure 10: IR Spectrum of $CaWO_4$ from the Methyl Lactate Precursor

Synthesis of Other M^{2+} Tungstates

This synthetic route was applied to several other metals as a way to produce metal tungstates and molybdates. All of the oxides produced from pyrolysis from each of the precursors were analyzed X-ray powder diffraction. The $MgWO_4$ produced from this experiment was used for sorption of Ca^{2+} ions in solution and is an area that future research should focus on. Figure 11 shows the XRD pattern for $MgWO_4$ synthesized from the methyl lactate precursor. The reactions producing the strontium and barium methyl lactate precursors did not produce crystals suitable for X-ray diffraction, but upon calcination they produced nanocrystalline metal tungstates evident by the peak broadening in their respective XRD patterns, shown in Figures 12 and 13.

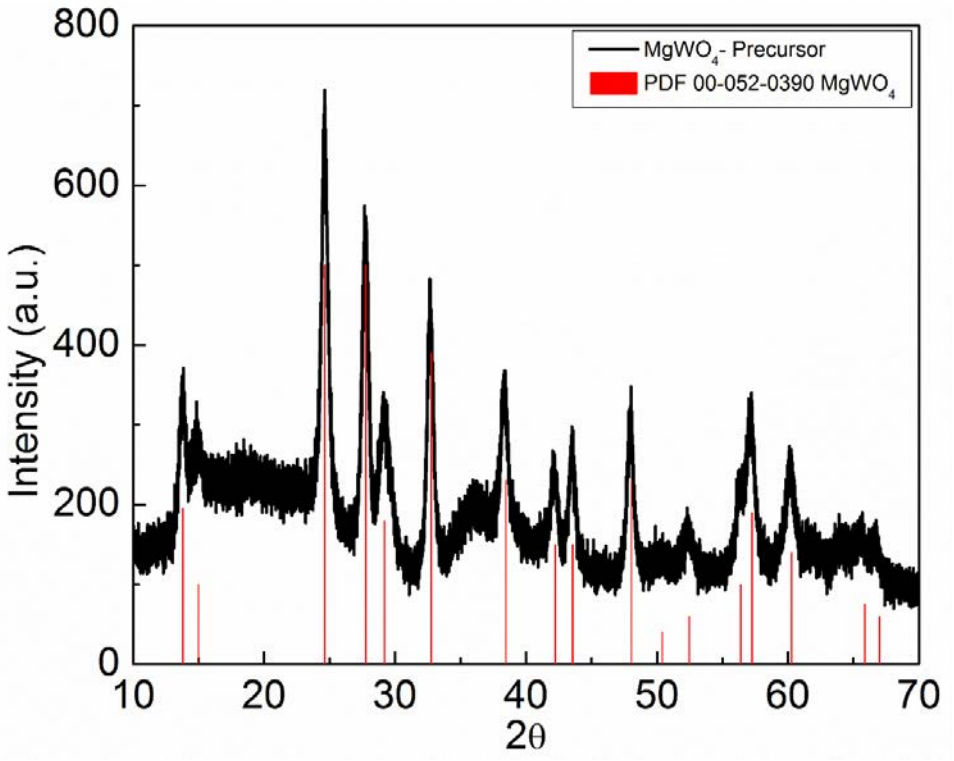

Figure 11: The XRD of $MgWO_4$ Synthesized from the Methyl Lactate Precursor

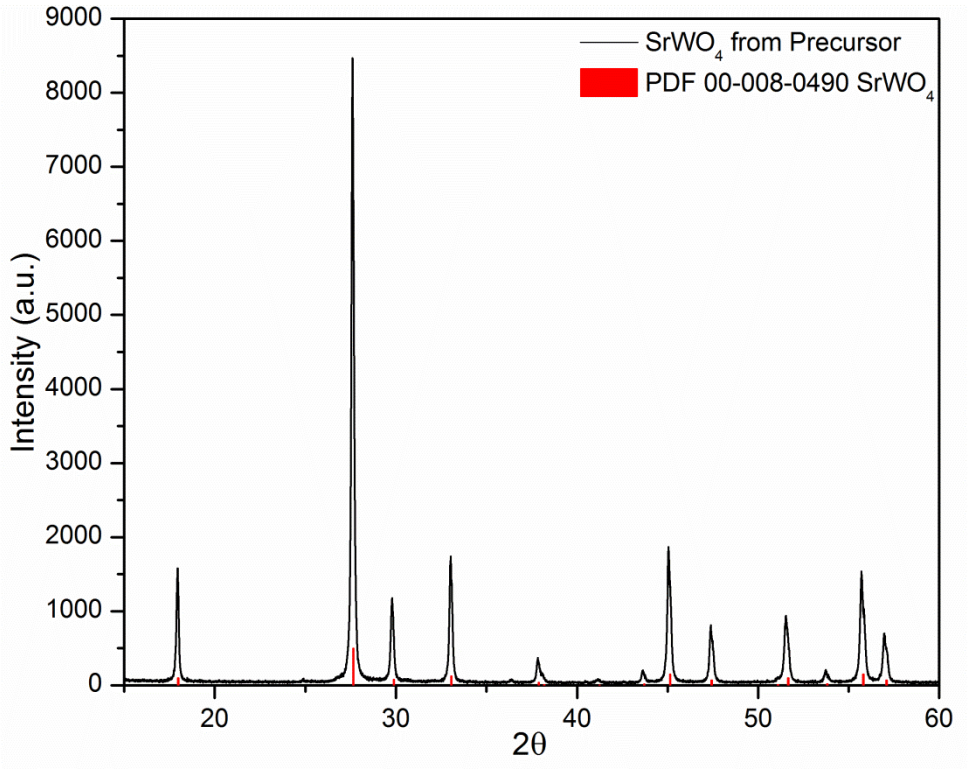

Figure 12: The XRD of $SrWO_4$ Synthesized from the Methyl Lactate Precursor

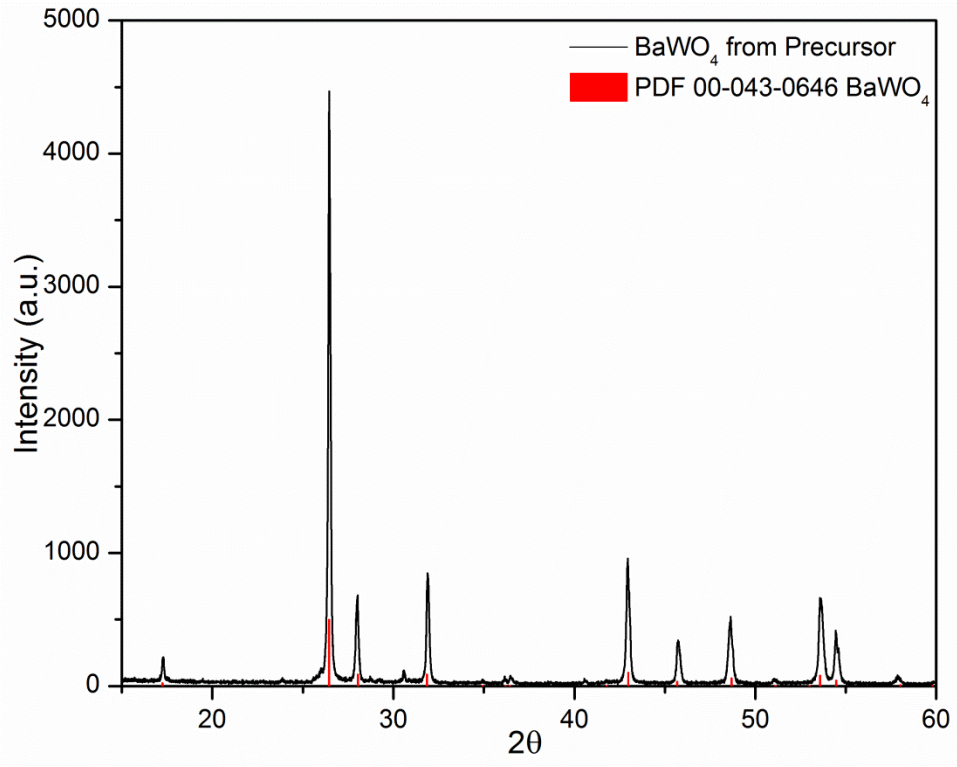

Figure 13: The XRD of $BaWO_4$ Synthesized from the Methyl Lactate Precursor

Zinc tungstate was produced using a zinc gluconate precursor, producing a crystalline product matching $ZnWO_4$ from the ICDD database (Figure 14). The product also showed peak broadening, characteristic of nanocrystalline materials. This material showed an affinity for lead when used to purify Zn^{2+} solutions during proof of concept experiments. The use of $ZnWO_4$ in such processes is an area of this research that should be further developed.

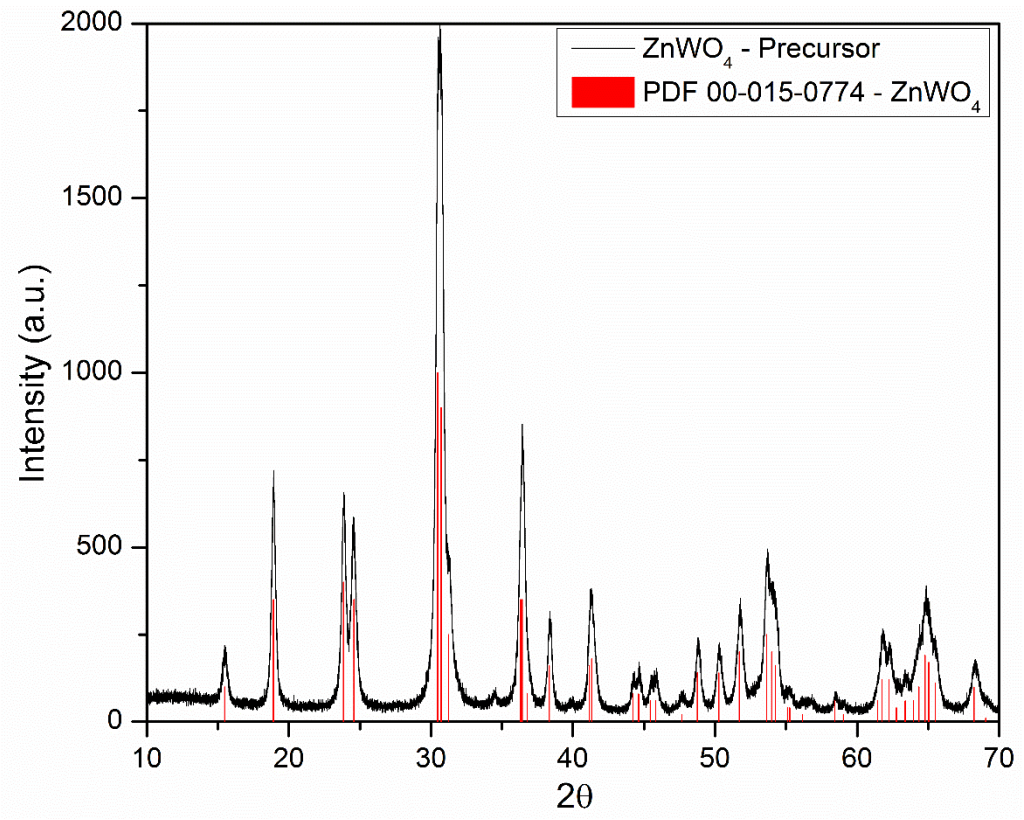

Figure 14: XRD of $ZnWO_4$ from the Gluconate Precursor

Synthesis of M^{3+} and M^{4+} Molybdates and Tungstates

All of the divalent metal tungstates were produced without any side products. However, due to the nature of how the carboxylates chelate to the group (VI) metals, the reactions were run with a 2 to 1 molar ratio of the carboxylates and the group (IV) metal source. Thus, for precursors which the target metal oxides do not have the 1:1 ratio, excess material must be present, even if they did not show characteristic properties when characterized by the Raman or XRD. For example, the aluminum tungstate produced exhausts the tungsten source before the aluminum, leading to a high surface area material (65 m^2/g) of $Al_2W_3O_{12}$ on Al_2O_3, although only target crystalline species were observed for both of these materials, shown in Figures 15 and 16.

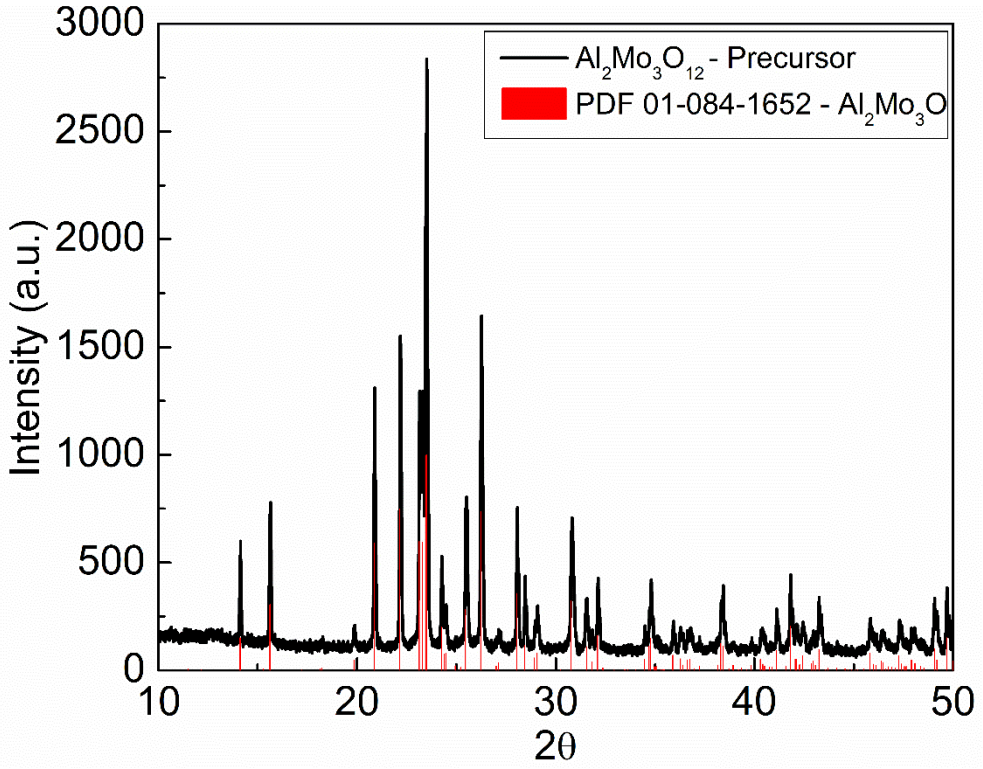

Figure 15: XRD of $Al_2Mo_3O_{12}$ Produced From the Gluconate Precursor

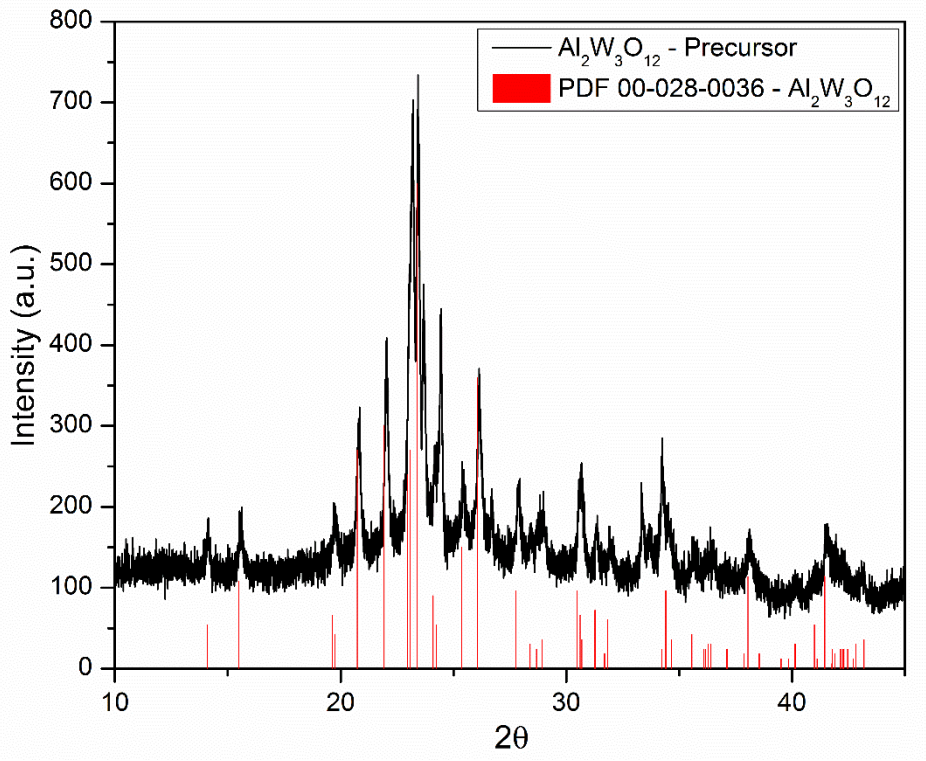

Figure 16: XRD of $Al_2Mo_3O_{12}$ Produced From the Gluconate Precursor

The reaction to produce a ZrW_2O_8 precursor was unsuccessful when reacting zirconyl gluconate with tungstic acid, only partially dissolving the tungstic acid starting material in the process. The precursor, however, upon calcination produced a material with characteristic peaks for both WO_3 and ZrO_2. In order to dissolve the entirety of the H_2WO_4, sodium gluconate was added with the intention of producing ZrW_2O_8 and Na_2WO_4. Interestingly, this precursor produced a crystalline material matching $Na_2ZrW_3O_{12}$ from the ICDD database, as shown in Figure 17. This is another material that should be further investigated as an ion exchange material due to its interesting structure.[29]

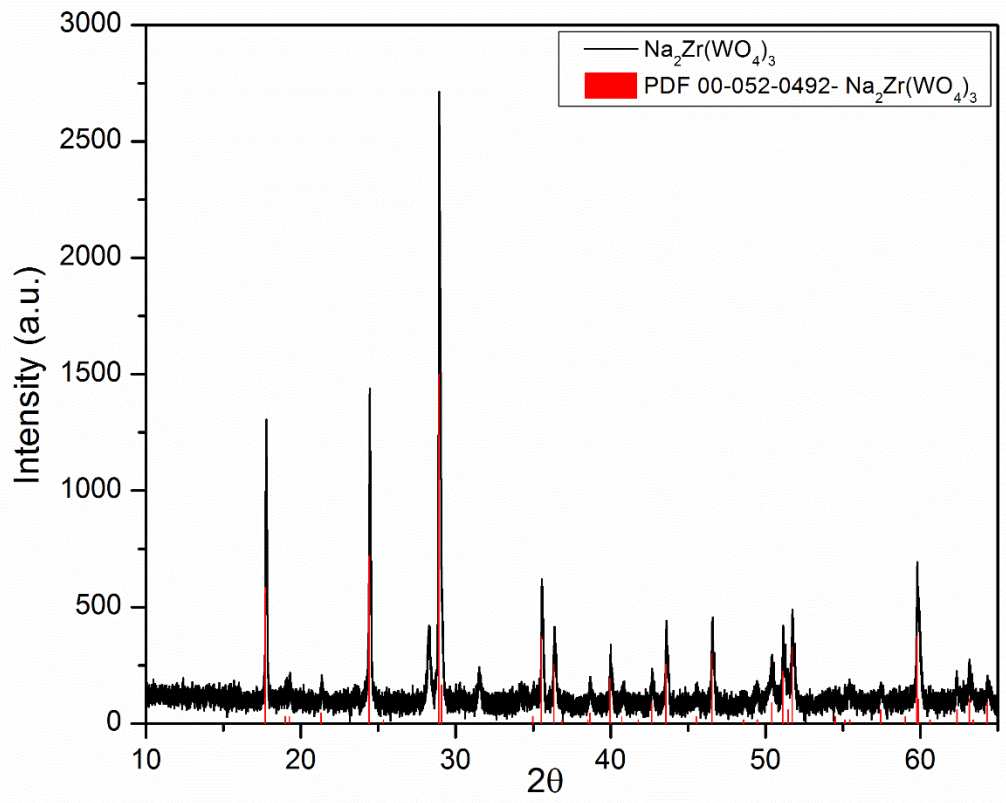

Figure 17: XRD Patter for $Na_2ZrW_3O_{12}$

Even though ZrW_2O_8 was unable to be synthesized, when zirconyl tungstate was reacted with MoO_3 the precursor, in fact, produced crystalline $ZrMo_2O_8$. This product, however, contained a crystalline impurity as shown in Figure 18.

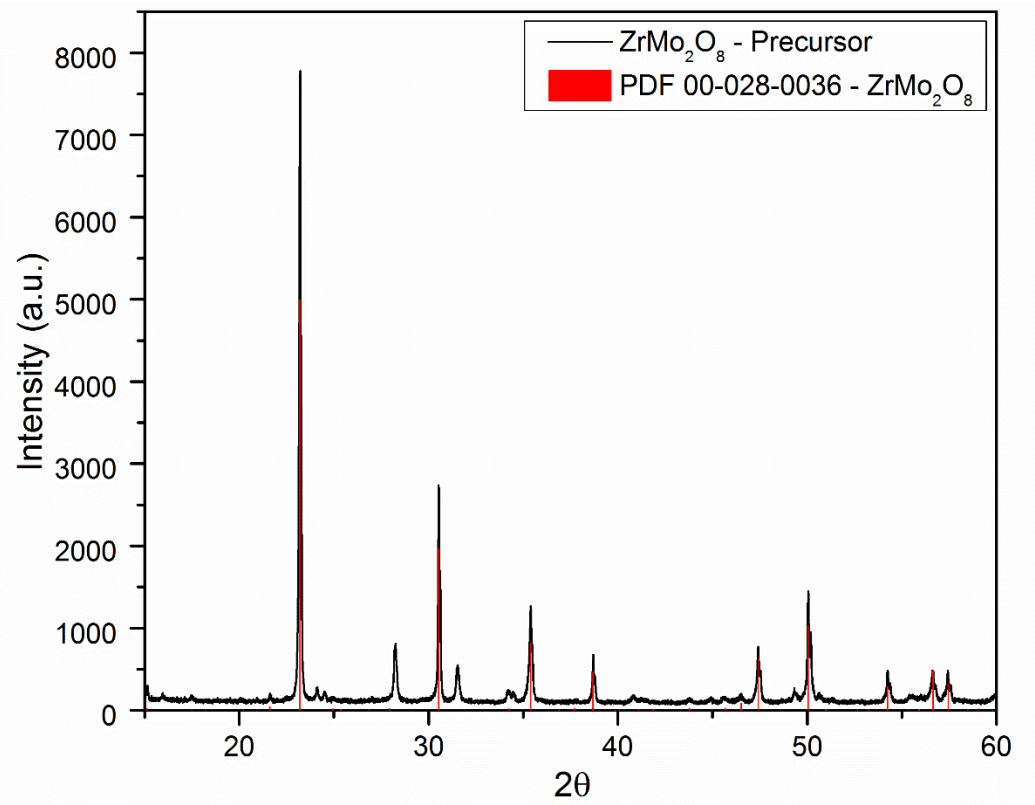

Figure 18: XRD of $ZrMo_2O_8$ Produced from the Zirconyl Gluconate Precursor

The presented precursor approach has been shown to produce nanocrystalline materials of interest in high yields, as summarized in Table 4. All of the materials presented in this study were of interest primarily for use as water treatment agents. However, this synthetic method should be applied to making materials for a variety of other applications.

Table 4: Percent Yields of the Oxides from the Precursors (based on H_2WO_4 or MoO_3)

Precursor	Percent Yield
$AlMoO_2(Gluconate)_2OH$	100
$AlWO_2(Glycolate)_2OH$	100
$AlWO_2(Lactate)_2OH$	96.7
$AlWO_2(Gluconate)_2OH$	100
$BaWO_2(Methyllactate)_2$	98.1
$CaWO_2(Glycolate)_2$	98.1
$CaWO_2(Lactate)_2$	98.4
$CaWO_2(Methyllactate)_2$	99.2
$CaWO_2(Gluconate)_2$	99.4
$MgWO_2(Methyllactate)_2$	97.6
$SrWO_2(Methyllactate)_2$	96.4
$ZrOMoO_2(Gluconate)_2$	97.1
$ZnWO_2(Gluconate)_2$	94.3

Conclusion:

This study has shown the versatility using α-hydroxy acids for the synthesis of metal molybdates and tungstates, producing materials with very high yields. Due to the wide use of metal molybdates and tungstates, this method could be applied to the synthesis of a wide variety of materials. Further, many of the materials presented in this study are used in a variety of different applications. This gives an avenue for further study of materials synthesized by this method to determine if they exhibit the properties suitable for use in the proposed applications. Moreover, utilizing water soluble precursors allows for an easy method to deposit the materials on substrates, a process that was taken advantage of for many of the applications was presented in this dissertation. Lastly, further research should be undertaken to develop the use of ion-exchange by $MgWO_4$, $ZnWO_4$, and $Na_2ZrW_3O_{12}$.

References:

1. A. W. Sleight, Negative thermal expansion materials. *Current Opinion in Solid State and Materials Science* **1998,** *3* (2), 128-131.

2. A. W. Sleight, Isotropic Negative Thermal Expansion. *Annual Review of Materials Science* **1998,** *28* (1), 29-43.

3. T. Varga, J. L. Moats, S. V. Ushakov, and A. Navrotsky, Thermochemistry of A2M3O12 negative thermal expansion materials. *Journal of Materials Research* **2007,** *22* (09), 2512-2521.

4. M. Ari, K. Miller, B. Marinkovic, P. Jardim, R. Avillez, F. Rizzo, and M. White, Rapid synthesis of the low thermal expansion phase of Al2Mo3O12 via a sol–gel method using polyvinyl alcohol. *Journal of Sol-Gel Science and Technology* **2011,** *58* (1), 121-125.

5. A. R. Phani, M. Passacantando, L. Lozzi, and S. Santucci, Structural characterization of bulk ZnWO4 prepared by solid state method. *Journal of Materials Science* **2000,** *35* (19), 4879-4883.

6. F. Zhang, M. Y. Sfeir, J. A. Misewich, and S. S. Wong, Room-Temperature Preparation, Characterization, and Photoluminescence Measurements of Solid Solutions of Various Compositionally-Defined Single-Crystalline Alkaline-Earth-Metal Tungstate Nanorods. *Chemistry of Materials* **2008,** *20* (17), 5500-5512.

7. Q. Zhang, X. Chen, Y. Zhou, G. Zhang, and S.-H. Yu, Synthesis of ZnWO4@MWO4 (M = Mn, Fe) Core−Shell Nanorods with Optical and Antiferromagnetic Property by Oriented Attachment Mechanism. *The Journal of Physical Chemistry C* **2007,** *111* (10), 3927-3933.

8. G. Blasse and W. J. Schipper, Low-temperature photoluminescence of strontium and barium tungstate. *Physica Status Solidi (A)* **1974,** *25* (2), K163-K165.

9. G. Blasse and G. J. Dirksen, Photoluminescence of Ba3W2O9: Confirmation of a structural principle. *Journal of Solid State Chemistry* **1981,** *36* (1), 124-126.

10. Z. Shan, Y. Wang, H. Ding, and F. Huang, Structure-dependent photocatalytic activities of MWO4 (M = Ca, Sr, Ba). *Journal of Molecular Catalysis A: Chemical* **2009,** *302* (1–2), 54-58.

11. A. W. Apblett, J. Lei, and G. D. Georgeva, Molecular Design of Carboxylic Precursors for Zirconia. *MRS Online Proceedings Library* **1992,** *271*.

12. A. W. Apblett, L. A. Cubano, G. D. Georgieva, and J. T. Mague, Synthesis, Thermal Behavior, and Structure of Hexaaquanickel(II) Chloro(hydrogenethylenediaminetetraacetato)ferrate(III): A Molecular Precursor for Stoichiometric Nickel Ferrite. *Chemistry of Materials* **1996,** *8* (3), 650-655.

13. A. W. Apblett, G. D. Georgieva, L. E. Reinhardt, and E. H. Walker, Precursors for Aqueous and Liquid-Based Processing of Ferroelectric Thin Films. In *Synthesis and Characterization of Advanced Materials*, American Chemical Society: 1997; Vol. 681, pp 95-105.

14. M. Veith, Molecular precursors for (nano) materials - a one step strategy. *Journal of the Chemical Society, Dalton Transactions* **2002,** (12), 2405-2412.

15. G. Mohammadnezhad, M. M. Amini, and H. R. Khavasi, A single source precursor for low temperature processing of nanocrystalline MgAl2O4 spinel: synthesis and characterization of [MgAl2([μ]3-O)([μ]2-OiPr)4(OiPr)2]4 *Dalton Transactions* **2010,** *39* (45), 10830-10832.

16. S. Shen, Y. Zhang, L. Peng, B. Xu, Y. Du, M. Deng, H. Xu, and Q. Wang, Generalized synthesis of metal sulfide nanocrystals from single-source precursors: size, shape and chemical composition control and their properties. *CrystEngComm* **2011,** *13* (14), 4572-4579.

17. L. G. Hubert-Pfalzgraf, To what extent can design of molecular precursors control the preparation of high tech oxides? *Journal of Materials Chemistry* **2004,** *14* (21), 3113-3123.

18. E. Bermejo, R. Carballo, A. Castiñeiras, and A. B. Lago, Coordination of α-hydroxycarboxylic acids with first-row transition ions. *Coordination Chemistry Reviews* **2013,** *257* (19–20), 2639-2651.

19. M. Hlaibi, S. Chapelle, M. Benaissa, and J.-F. Verchere, Structures and Stabilities of Tungstate Complexes of a-Hydroxy Acids. 183W NMR Study of the Influence of Ligand Substitution. *Inorganic Chemistry* **1995,** *34* (17), 4434-4440.

20. M. L. Ramos, M. M. Caldeira, and V. M. S. Gil, NMR spectroscopy study of the complexation of d-gluconic acid with tungsten(VI) and molybdenum(VI). *Carbohydrate Research* **1997,** *304* (2), 97-109.

21. S. Jarmelo and R. Fausto, Structure and vibrational spectra of [small alpha]-hydroxy isobutyric acid in the crystalline and glassy phases and isolated in inert gas matrixes. *Physical Chemistry Chemical Physics* **2002,** *4* (9), 1555-1563.

22. T. T. Basiev, A. A. Sobol, P. G. Zverev, L. I. Ivleva, V. V. Osiko, and R. C. Powell, Raman spectroscopy of crystals for stimulated Raman scattering. *Optical Materials* **1999,** *11* (4), 307-314.

23. R. L. Frost, L. Duong, and M. Weier, Raman microscopy of selected tungstate minerals. *Spectrochimica Acta Part A: Molecular and Biomolecular Spectroscopy* **2004,** *60* (8–9), 1853-1859.

24. M. Liegeois-Duyckaerts and P. Tarte, Vibrational studies of molybdates, tungstates and related compounds—II: New Raman data and assignments for the scheelite-type compounds. *Spectrochimica Acta Part A: Molecular Spectroscopy* **1972,** *28* (11), 2037-2051.

25. S. P. S. Porto and J. F. Scott, Raman Spectra of CaWO4, SrWO4, CaMoO4, and SrMoO4. *Physical Review* **1967,** *157* (3), 716-719.

26. J. P. Russell and R. Loudon, The first-order Raman spectrum of calcium tungstate. *Proceedings of the Physical Society* **1965,** *85* (5), 1029.

27. W. P. Griffith, Raman studies on rock-forming minerals. Part II. Minerals containing MO3, MO4, and MO6 groups. *Journal of the Chemical Society A: Inorganic, Physical, Theoretical* **1970,** (0), 286-291.

28. R. K. Khanna, W. S. Brower, B. R. Guscott, and E. R. Lippincott, Laser induced Raman spectra of some tungstates and molybdates. *Journal of Research of the Notional Bureau af Standards - A. Physics and Chemistry* **1967,** *72A* (1), 81-84.

29. R. F. Klevtsova, V. V. Bakakin, S. F. Solodovnikov, and L. A. Glinskaya, Combination of the wolframite and scheelite patterns in the crystal structure of sodium zirconium tungstate Na2ZrW3O12=Na2ZrW2O8(WO4). *Journal of Structural Chemistry* **1981,** *22* (6), 807-812.

CHAPTER VII

RECOVERY OF GALLIUM BY ALUMINUM TUNGSTATE

Introduction:

Gallium is a relatively rare element that is used extensively in and materials for semiconductor and electronics applications. There has been a large increase in demand for gallium that have led to skyrocketing prices.[1] Therefore, the ability to reclaim gallium from industrial effluents or natural waters has received much interest.[2] Such processes typically include fractional precipitation, electrochemical deposition, solvent extraction, and ion exchange.[3-8] Previously, the Apblett research group has shown the effectiveness of using group VI transition metal oxides for the sorption of contaminants.[9-14] The supposition that the sorption of gallium may undergo ion exchange for other M^{3+} metals led to the hypothesis that aluminum molybdate and aluminum tungstate may be attractive materials for the sorption of Ga^{3+}.

Experimental:

All chemicals (reagent grade or higher) were used as received without further purification. The water used was purified by reverse osmosis followed by ion exchange. Gallium nitrate, $Ga(NO_3)_3$ (Spectrum Chemicals), was used to prepare the gallium stock solution with a concentration of approximately 130 mg/L. The concentrations of the stock and treated solutions were determined using a Varian GTA120/AA240Z graphite furnace atomic absorption spectrometer (GFAAS) equipped with an auto sampler. A 100 mg/L Ga^{3+} standard (BDH

ARISTAR) was used to prepare the standard solutions used for analysis. Aliquots of the treated samples were taken at regular time intervals and diluted to the appropriate concentrations with a 1% HNO_3 solution, made using trace metal grade HNO_3 from Mallinckrodt. The materials used for the synthesis and the sorption process were discussed in Chapter VI.

Results and Discussion:

Aluminum molybdate was prepared to be used as a sorbent for Ga^{3+}, as previously described in Chapter VI. However, aluminum molybdate is apparently unstable in water, undergoing dissolution reaction to produce an insoluble amorphous material. To determine the nature of the reaction, 0.20 g of the aluminum molybdate was added to 50 mL of deionized water and placed on a sample rotator for a week. After the allotted time, the solid was separated by centrifugation and the filtrate was allowed to slowly evaporate, producing crystals suitable for X-ray diffraction. Figure 1 shows the crystal structure for the recovered material with the formula $[Al(OH_2)_6][Al(OH)_6Mo_6O_{18}]\cdot 4H_2O$. Thus, a reaction occurred to produce a material with a 1:3 Al:Mo ratio. The starting material had a ratio of 2Al:3Mo and the Al:Mo ratio in the amorphous material is approximately 1:1 (Figure 2) implying that the hydrolysis of $Al_2Mo_3O_{12}$ occurs according to Equation 1. The hydrolysis of $Al_2Mo_3O_{12}$ makes it unacceptable for remediation applications. However, this was not the case for $Al_2W_3O_{12}$ that did not dissolve or change its crystalline structure when subjected to the same conditions.

$$4Al_2Mo_3O_{12} + H_2O \rightarrow [Al(OH_2)_6][Al(OH)_6Mo_6O_{18}] \cdot 10H_2O + 6Al(OH)(MoO_4) \cdot H_2O$$

Equation 1: Hydrolysis Reaction of $Al_2Mo_3O_{12}$

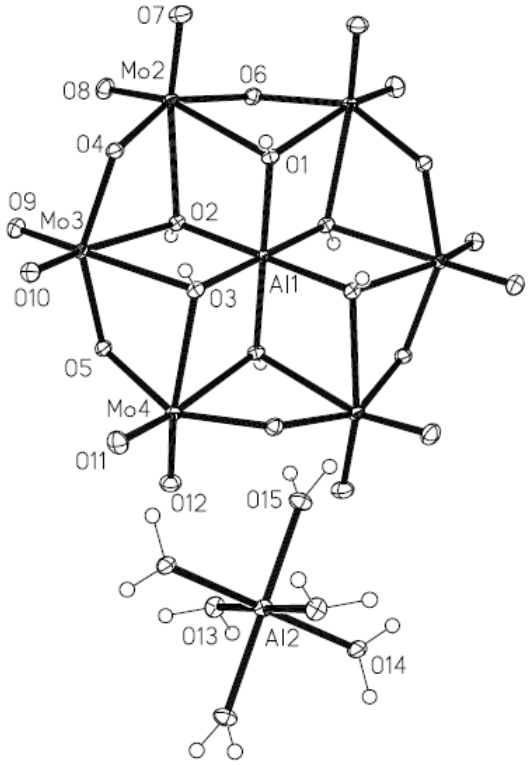

Figure 1: Crystal Structure for the Material Produced from the Dissolution of $Al_2Mo_3O_{12}$ in Water

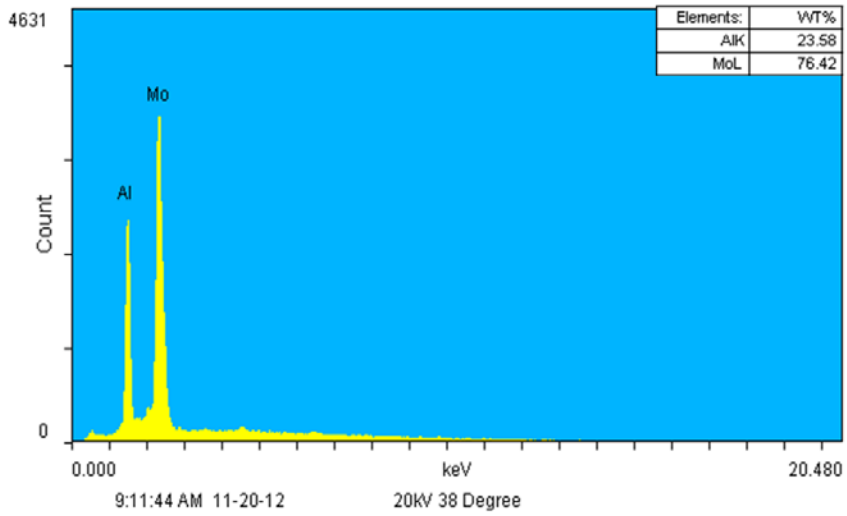

Figure 2: EDX Spectrum of the Amorphous Product Recovered from Putting $Al_2Mo_3O_{12}$ in Water

Sorption Kinetics Using $Al_2W_3O_{12}$

Since $Al_2Mo_3O_{12}$ proved to be unsuitable for reactions in aqueous media, $Al_2W_3O_{12}$ was the only material used as a sorbent for the recovery of Ga^{3+}. The sorption uptake curve (Figure 3) depicts the sorption of gallium by different amounts of aluminum tungstate. The uptake curves depict a process in which sorption is initially very fast and then starts to slow as the reaction approaches an equilibrium state. The lower sorbent loading experiments reach their respective equilibrium states later than the higher loadings. The kinetic uptake of Ga^{3+} was modeled by both the linear and nonlinear models of the commonly used pseudo first and second-order models.

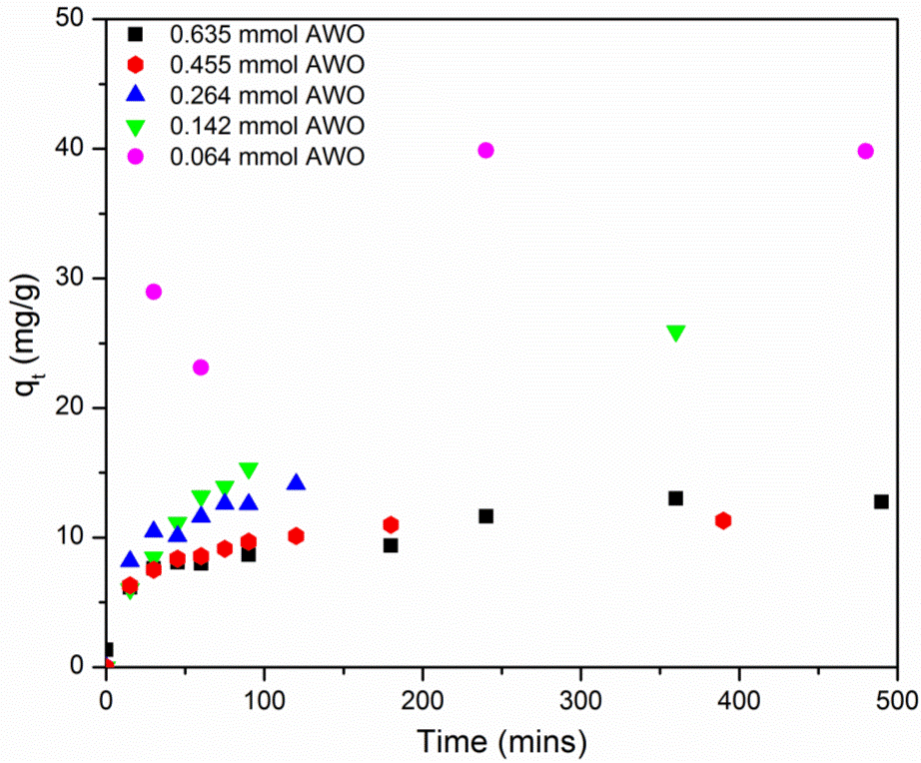

Figure 3: Sorption Uptake Curves for the Sorption of Ga^{3+}

The pseudo first-order rate expression described by Lagergren (Equation 1) is an exponential function where q_t is the amount of the analyte sorbed at time t, k_1 is the rate constant of the pseudo first-order sorption process, and q_e is the amount of analyte sorbed at equilibrium.[15]

Further, the natural log of Equation 2, yields a linear function (Equation 3) that gives the values of k_1 and q_e from the slope and intercept, respectively, of a plot of $\ln(q_e-q_t)$ vs. time.

$$q_t = q_e(1 - e^{-k_1 t})$$

Equation 2: The Nonlinear Pseudo First-Order Equation

$$ln(q_e - q_t) = ln(q_e) - k_1 t$$

Equation 3: The Linearized Formula for Pseudo First-Order Kinetics

Figure 4 shows that the linear pseudo first-order kinetic model does not apply throughout the various sorbent loadings. Although, the linear pseudo first-order does a fairly good job modeling the sorption process for the second lowest and the highest sorbent loadings, the model worsens for the other three, as is evident from the correlation coefficient (R^2) values listed in Table 1. The estimated q_e values, calculated from the equation, are in agreement with the experimental values for only the lowest sorbent loading, underestimating the equilibrium concentration for the other sorbents loadings. The deviation from linearity at higher loadings of sorbent is likely due to the similar concentrations of the analyte and reactions sites on the sorbent.[16]

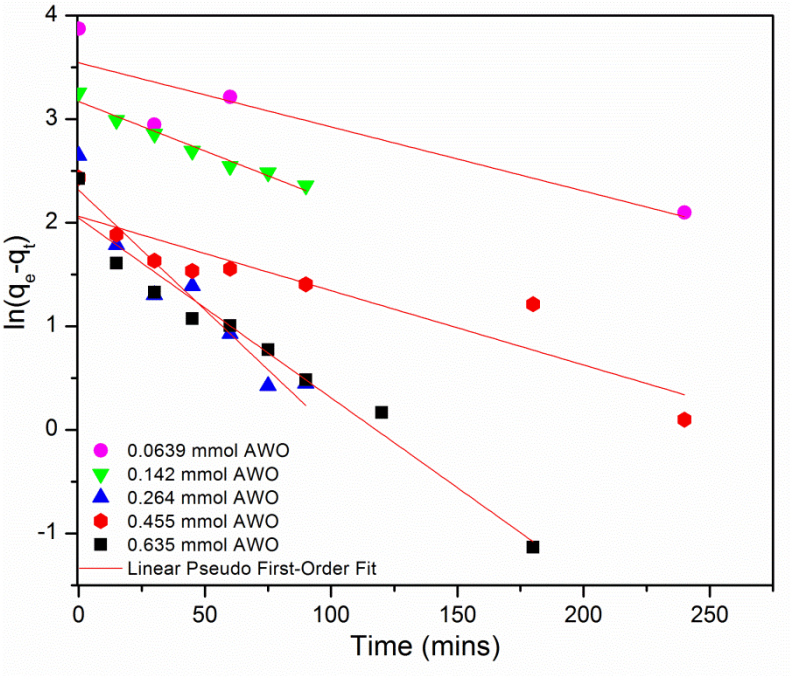

Figure 4: Linear Pseudo First-Order Plot for the Uptake of Ga^{3+} by $Al_2W_3O_{12}$

Table 1: Data and Results for Linear Pseudo First-Order Fitting of the Uptake of Ga^{3+} by $Al_2W_3O_{12}$

$Al_2W_3O_{12}$ (mmol)	k_1 (min^{-1})	q_e (mg/g)	q_e (mg/g) (experimental)	R^2
0.0639	6.19E-03	34.6	48.0	0.7411
0.142	9.55E-03	23.8	25.9	0.965
0.264	2.31E-02	10.1	14.1	0.893
0.455	7.18E-03	7.86	12.7	0.814
0.635	1.74E-02	7.74	11.3	0.957

It has been suggested that modeling sorption processes using the nonlinear pseudo first-order model can provide vastly improved results.[17] The nonlinear pseudo first-order equation (Equation 2) was used to fit the experimental data, and the results are presented in Figure 5. The data shows a good fit by the nonlinear equation, as indicated by the correlation coefficients in Table 2. Further, the model's prediction of q_e is in good agreement with the experimental values for all of sorbent loading besides the lowest loading. These results are in good agreement with

the hypothesis that the nonlinear method is far superior in modeling this sorption process than the linear method. However, the rate constants are random with respect to sorbent loading so the results from this model are still not adequate to describe this reaction.

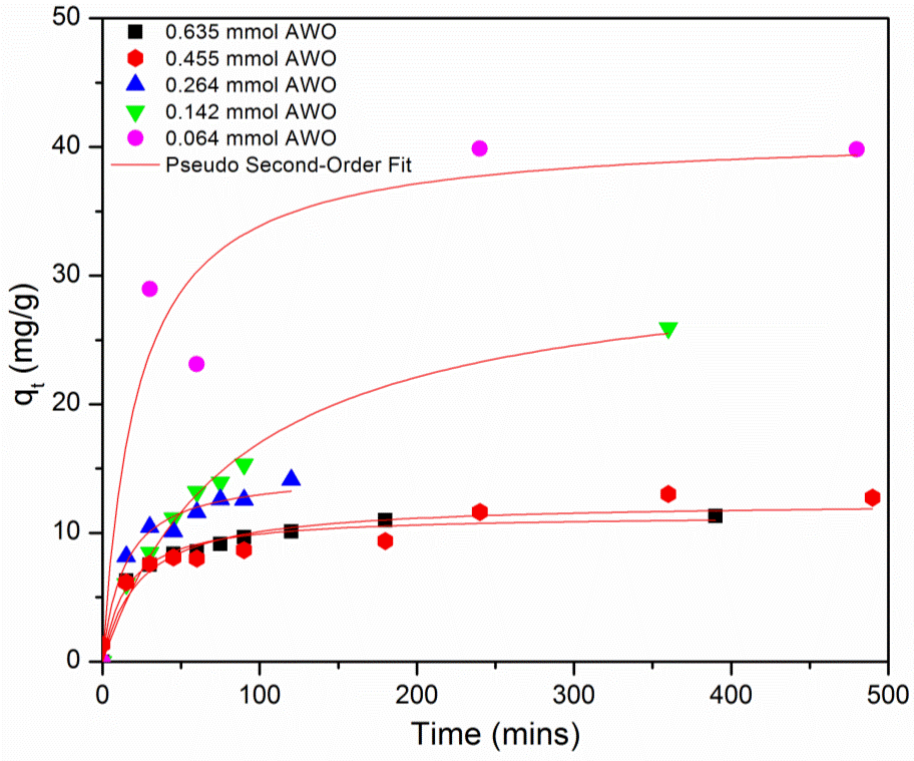

Figure 5: Nonlinear Pseudo First-Order Plot for the Uptake of Ga^{3+} by $Al_2W_3O_{12}$

Table 2: Data and Results for Nonlinear Pseudo First-Order Fitting of the Uptake of Ga^{3+} by $Al_2W_3O_{12}$

$Al_2W_3O_{12}$ (mmol)	k_1 (min^{-1})	q_e (mg/g)	q_e (mg/g) (experimental)	R^2
0.0639	2.80E-02	38.5	48.0	0.850
0.142	1.15E-02	25.9	25.9	0.976
0.264	5.58E-02	12.7	14.1	0.950
0.455	4.53E-02	10.2	12.7	0.938
0.635	3.09E-02	11.2	11.3	0.777

Ho and McKay proposed a pseudo second-order kinetic model represented by the Equation 3, where k_2 is the rate constant of the pseudo second-order sorption process, with the

units g mg^{-1} min^{-1}.[18] The equation can be further simplified to Equation 4, by substituting h in place of $k_2q_e^2$, where h can be considered to be the initial sorption rate, as t/q_t approaches 0. The slope and the intercept of the plot of t/q_t versus t gives the values of the constants q_e and h, respectively.[16] Using the value of q_e and h, the rate constant (k_2) can be obtained.

$$\frac{t}{q_t} = \frac{1}{k_2 q_e^2} + \frac{1}{q_e} t$$

Equation 4: The Linearized Pseudo Second-Order Rate Equation

$$\frac{t}{q_t} = \frac{1}{h} + \frac{1}{q_e} t$$

Equation 5: The Linearized Initial Rate Pseudo Second-Order Equation

The linear pseudo second-order plot for the sorption of gallium by aluminum tungstate, Figure 6, shows a very good linear fit to the data. The results of the fitting are provided in Table 3. All of the experiments fit the linear pseudo second-order model much better than the linear pseudo first-order model, with very high linear regression correlation coefficient (R^2) values. Most of the calculated q_e values are in fairly close agreement with the experimental data, although the model overestimates the values in every case but the highest sorbent loading where q_e is underestimated by a very small amount. However, it is not clear why the result for the 0.264 mmol loading is so far off, as compared to the experimental data. The pseudo second-order rate constants (k_2) display a correlation with respect to the varying amount of sorbent, as the amount increases the rate increases. However, the units of the pseudo second-order rate constant make the physical significance of rate constant very vague.

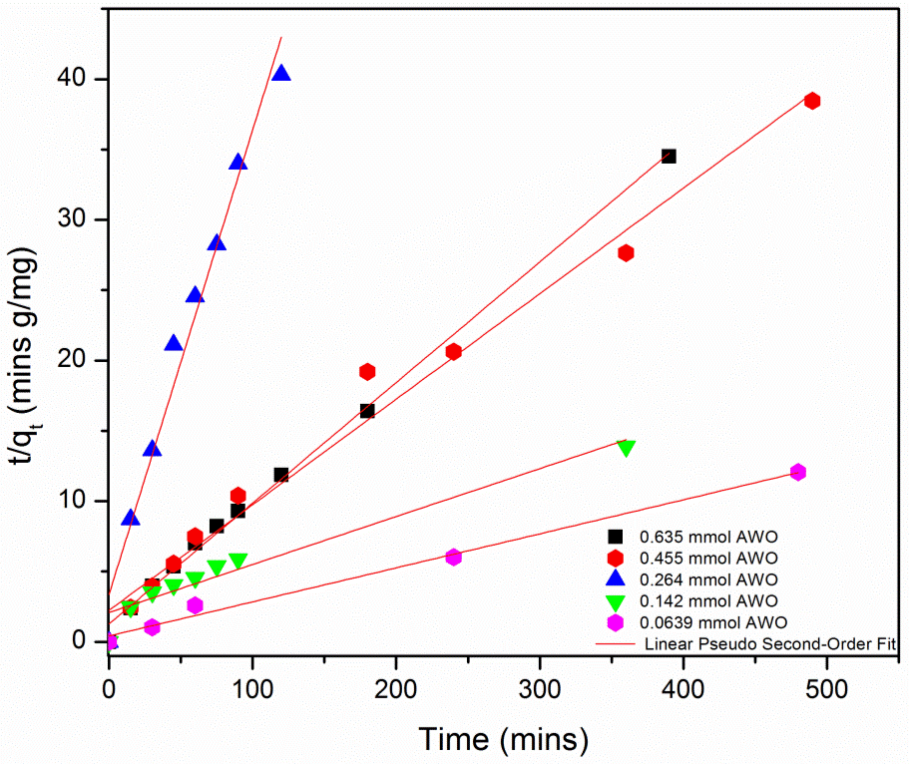

Figure 6: Linear Pseudo Second-Order Plot for the Uptake of Ga^{3+} by $Al_2W_3O_{12}$

Table 3: Data and Results for Nonlinear Pseudo Second-Order Fitting of the Uptake of Ga^{3+} by $Al_2W_3O_{12}$

$Al_2W_3O_{12}$ (mmol)	k_2 (g/mg min)	h (mg/g min)	q_e (mg/g)	q_e (mg/g) (experimental)	R^2
0.0639	1.39E-03	2.38	41.3	48.0	0.989
0.142	5.56E-04	0.478	29.3	25.9	0.937
0.264	3.23E-02	0.296	3.03	14.1	0.972
0.455	2.51E-03	0.445	13.3	12.7	0.981
0.635	5.73E-03	0.779	11.7	11.3	0.997

Previously, the nonlinear pseudo second-order equation (Equation 6) was used to effectively model the sorption process of methylene blue on activated carbon.[17] Figure 7 shows the plotted data fitted with the nonlinear pseudo second-order model with relatively good accuracy. Table 4 shows that the correlation coefficients for the nonlinear method are fairly good, similar to the linear model, suggesting that this method is also appropriate for modeling this

process. Similar to the linear method, the kinetic parameters of the nonlinear pseudo second-order appear to have little physical meaning. However, the equilibrium concentration values from the model are higher than the experimental values in three of the five cases, and underestimated for two of the sorbent loadings with no obvious correlation.

$$q_t = \frac{k_2 q_e^2 t}{1 + k_2 q_e t}$$

Equation 6: The Nonlinear Pseudo Second-Order Equation

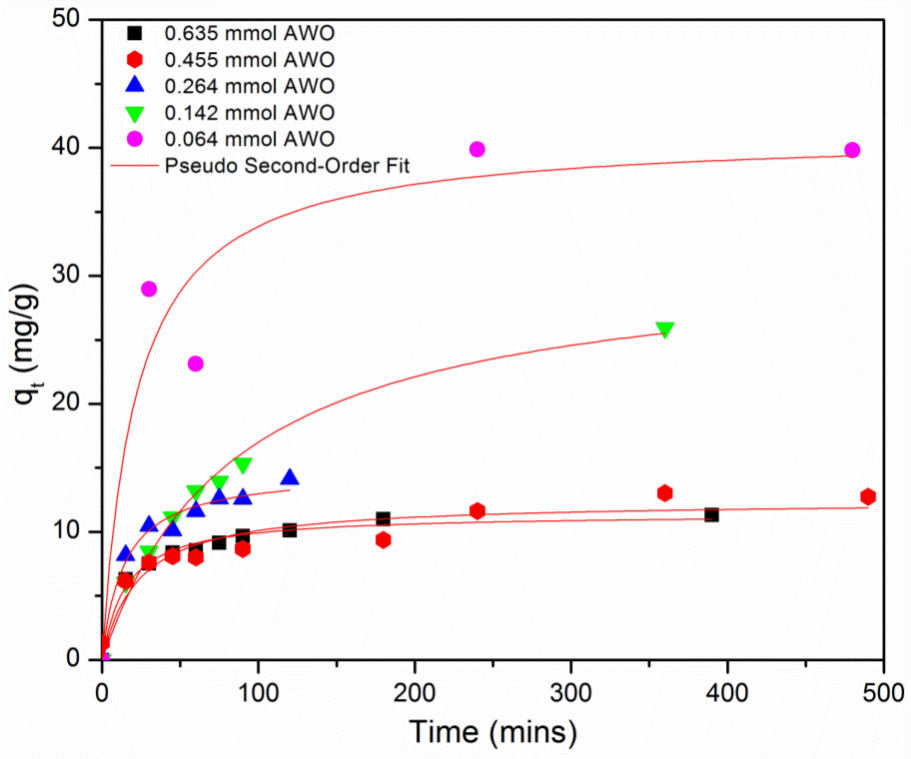

Figure 7: Nonlinear Pseudo Second-Order Plot for the by Uptake of Ga^{3+} $Al_2W_3O_{12}$

Table 4: Data and Results for Nonlinear Pseudo Second-Order Fitting of the Uptake of Ga^{3+} by $Al_2W_3O_{12}$

$Al_2W_3O_{12}$ (mmol)	k_2 (g/mg min)	h (mg/g min)	q_e (mg/g)	q_e (mg/g) (experimental)	R^2
0.0639	1.13E-03	1.92	41.1	48.0	0.900
0.142	3.68E-04	0.368	31.6	25.9	0.990
0.264	4.90E-03	1.07	14.8	14.1	0.976
0.455	3.49E-03	0.539	12.4	12.7	0.878
0.635	5.75E-03	0.751	11.4	11.3	0.986

The data presented suggests that the nonlinear pseudo first-order model is the best-suited method to model the sorption of Ga^{3+} by $Al_2W_3O_{12.}$ This is due not only to the predicted q_e and R^2 values, but also for the clear physical meaning of the pseudo first-order rate constant.

Sorption Kinetics for the Al_2O_3 Supported- $Al_2W_3O_{12}$

By supporting the $Al_2W_3O_{12}$ on a high surface area Al_2O_3 substrate, the surface area was improved from that of the $Al_2W_3O_{12}$ powder. The latter had a surface area of 65 m^2 g^{-1}, while that of the supported material was 177 m^2 g^{-1}. The impregnation method produced a product with 5.07% $Al_2W_3O_{12}$ on the Al_2O_3 support. The sorption uptake curves (Figure 8) show the sorption process where equilibrium was reached at roughly 120 minutes for all of the mass loadings. Furthermore, the equilibrium sorption capacities were improved in every case using the supported the material. However, the real advantage to using the supported material is the ease of implementation into a column type application that could be used for the recovery of gallium, as opposed to the powder materials which could prove difficult in these types of applications due to poor flow and high back pressure.

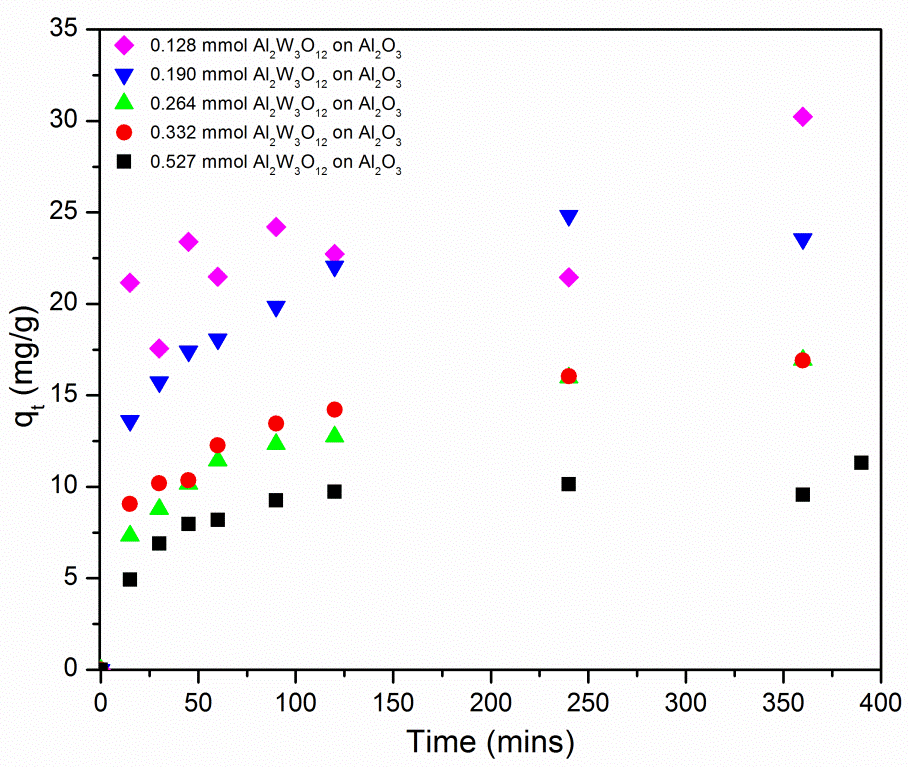

Figure 8: Sorption Uptake Curves for the Sorption of Ga^{3+} by $Al_2W_3O_{12}$ on Al_2O_3

Similar to the powdered $Al_2W_3O_{12}$, the linear pseudo first-order model gave very poor data for the supported materials (Figure 9). Further, the model gave drastically lower predictions for q_e than was observed experimentally (Table 5). This data, coupled with the data from the powder sorbents suggests this model is not adequate for modeling this sorption process.

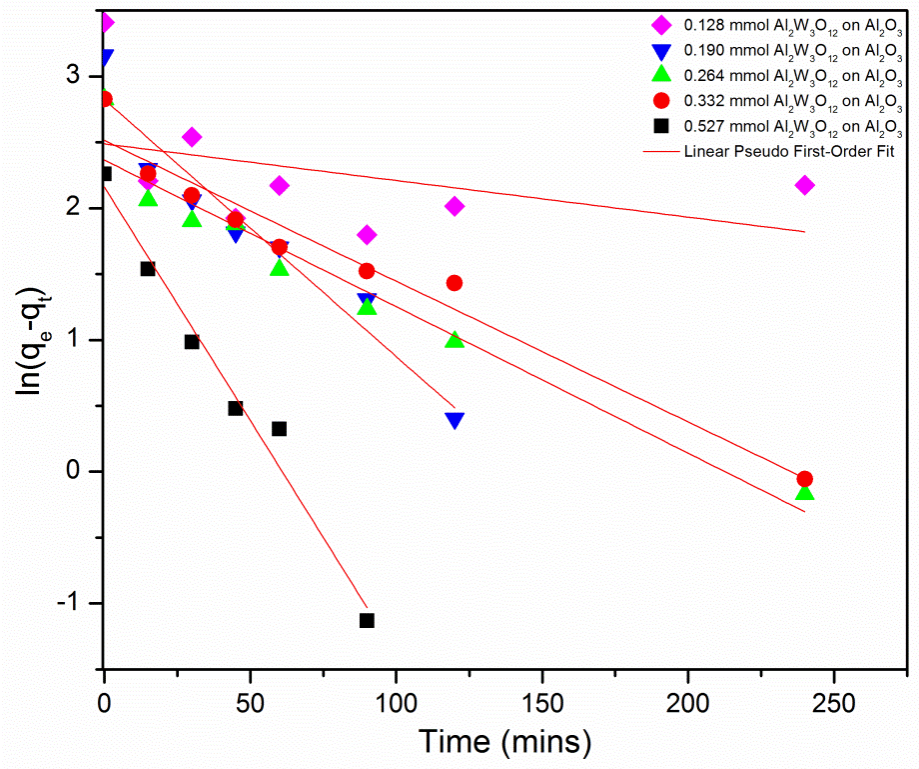

Figure 9: Linear Pseudo First-Order Plot for the Uptake of Ga^{3+} by $Al_2W_3O_{12}$ on Al_2O_3

Table 5: Data and Results for Linear Pseudo First-Order Fit of the Uptake of Ga^{3+} by $Al_2W_3O_{12}$ on Al_2O_3

$Al_2W_3O_{12}$ (mmol)	k_1 (min^{-1})	q_e (mg/g)	q_e (mg/g) (experimental)	R^2
0.128	2.78E-03	12.0	30.2	0.0428
0.190	1.95E-02	16.8	23.6	0.922
0.264	1.11E-02	10.7	16.9	0.933
0.332	1.07E-02	12.4	16.9	0.953
0.527	3.55E-02	8.68	9.57	0.975

Figure 10 shows the uptake of gallium by most of the supported materials fit the nonlinear model very well. Further, the equilibrium data correlates very well with the experimental data, with the exception of the lowest sorbent loading. This data, together with the data from the powder sorption processes, suggests this model is ideal for modeling this sorption process. It is also meritorious for providing rate constants with an understood physical meaning.

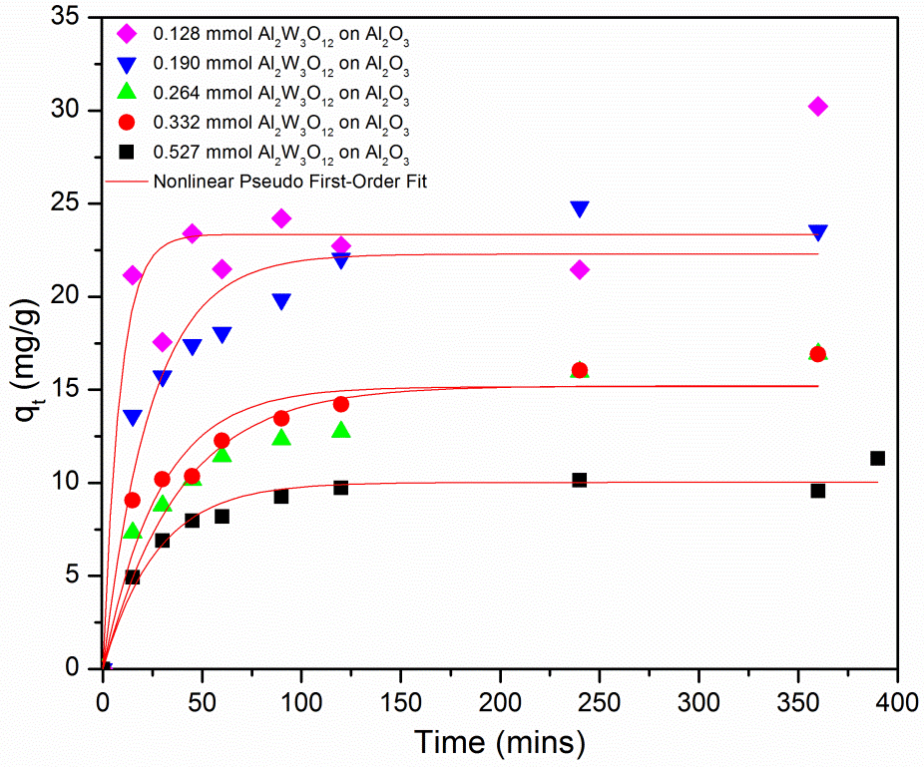

Figure 10: Nonlinear Pseudo First-Order Plot for the Uptake of Ga^{3+} by $Al_2W_3O_{12}$ on Al_2O_3

Table 6: Data and Results for Nonlinear Pseudo First-Order Fit of the Uptake of Ga^{3+} by $Al_2W_3O_{12}$ on Al_2O_3

$Al_2W_3O_{12}$ (mmol)	k_1 (min^{-1})	q_e (mg/g)	q_e (mg/g) (experimental)	R^2
0.128	1.19E-01	23.4	30.2	0.824
0.190	4.12E-02	22.3	23.6	0.922
0.264	3.51E-02	15.2	16.9	0.901
0.332	2.59E-02	15.2	16.9	0.914
0.527	3.68E-02	10.0	9.57	0.964

The sorption processes were also modeled using the pseudo second-order equations. Figure 11 shows the nonlinear pseudo second-order equation fits the sorption data very good as well and Table 7 shows nearly perfect correlation coefficients in some cases. Further, this model gives very good q_e predictions throughout the sorption process.

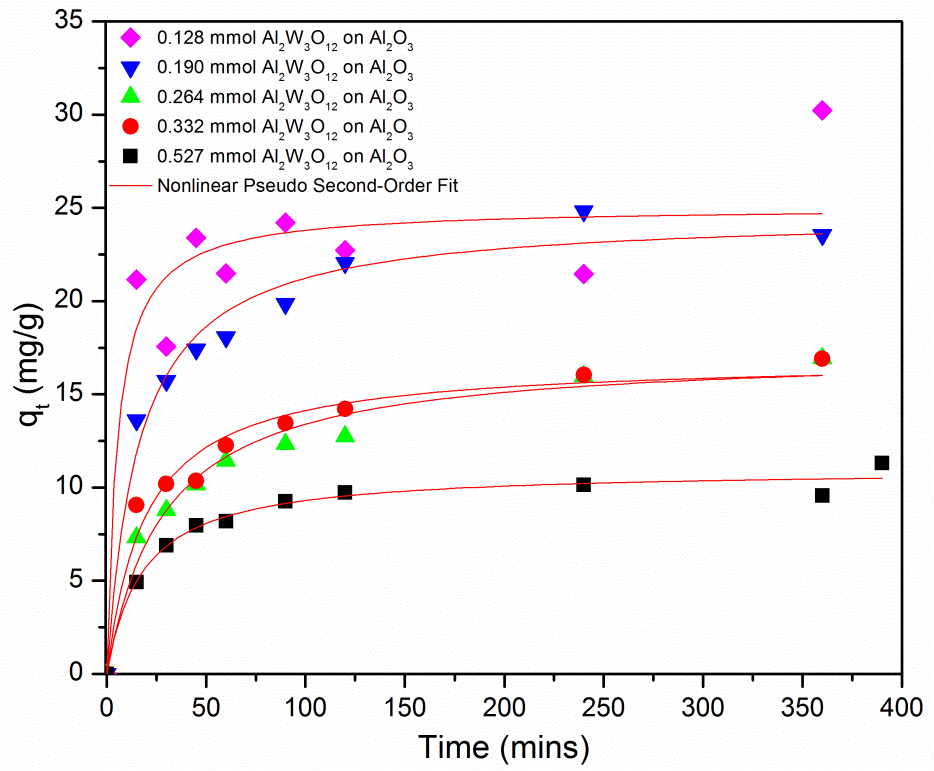

Figure 11: Nonlinear Pseudo Second-Order Plot for the Uptake of Ga^{3+} by $Al_2W_3O_{12}$ on Al_2O_3

Table 7: Data and Results for Nonlinear Pseudo Second-Order Fit of the Uptake of Ga^{3+} by $Al_2W_3O_{12}$ on Al_2O_3

$Al_2W_3O_{12}$ (mmol)	k_2 (g/mg min)	h (mg/g min)	q_e (mg/g)	q_e (mg/g) (experimental)	R^2
0.128	7.56E-03	4.74	25.0	30.2	0.980
0.190	2.50E-03	1.52	24.7	23.6	0.984
0.264	3.04E-03	0.866	16.9	16.9	0.997
0.332	1.98E-03	0.593	17.3	16.9	0.957
0.527	5.04E-03	0.608	11.0	9.6	0.998

The linear pseudo second-order model, depicted in Figure 12, gives the closest predicted q_e values throughout the entire sorbent loadings and highest R^2 values of all models, as summarized in Table 8. It is obvious this model gives the best correlations and prediction of equilibrium capacities; however the lack of a clear physical meaning for k_2 means this model is

only useful for predicting the equilibrium capacities, rather than giving meaningful kinetic parameters.

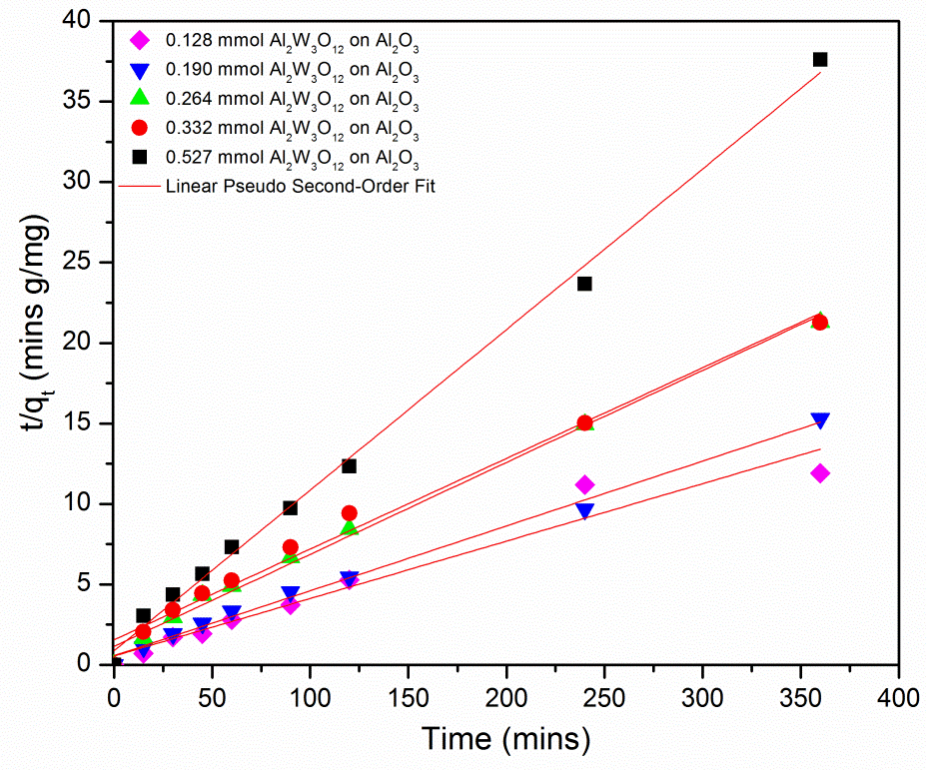

Figure 12: Linear Pseudo Second-Order Plot for the Uptake of Ga^{3+} by $Al_2W_3O_{12}$ on Al_2O_3

Table 8: Data and Results for Linear Pseudo Second-Order Fit of the Uptake of Ga^{3+} by $Al_2W_3O_{12}$ on Al_2O_3

$Al_2W_3O_{12}$ (mmol)	k_2 (g/mg min)	h (mg/g min)	q_e (mg/g)	q_e (mg/g) (experimental)	R^2
0.128	2.31E-03	1.82	28.0	30.2	0.946
0.190	2.83E-03	1.74	24.8	23.6	0.994
0.264	2.84E-03	0.869	17.5	16.9	0.993
0.332	2.04E-03	0.641	17.7	16.9	0.985
0.527	1.13E-02	1.14	10.0	9.6	0.996

The data from the two different sorbents suggests that the nonlinear pseudo first-order equation is best for modeling this sorption process. From this, we can then compare the kinetic

rates of the two different materials. Figure 13 shows the sorption half-life of the analyte when treated with similar amounts of sorbent. The data suggests that by supporting the material, the sorption half-life is not improved for higher mass loadings, likely due to the diffusion of liquid into the porous alumina medium. The only downfall to the supported material, however, is the apparent loss of material from the support.

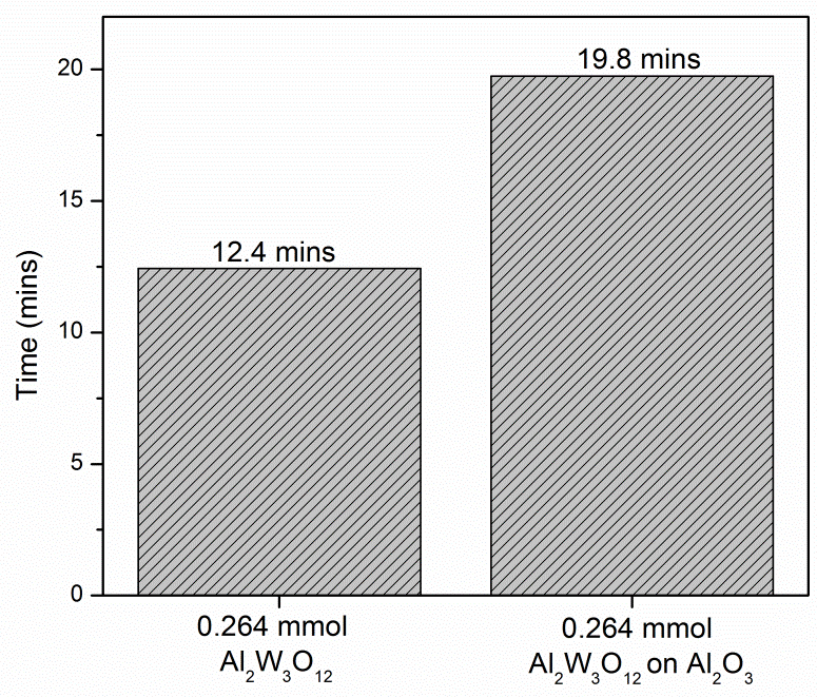

Figure 13: Sorption Half-Life for the Different Forms of $Al_2W_3O_{12}$

Treatment of Wastewaters

To determine if the sorbent could be implemented to recovery gallium from waste waters, the material was used to treat an effluent from the semi-conductor industry containing 52.6 ppm Ga^{3+}, among unknown concentrations of other analytes. A sample of 10.5 g of the solution was treated with 0.130 g of $Al_2W_3O_{12}$ powder. The solution was allowed to react for two weeks, reducing the concentration of Ga^{3+} to 22.3 ppm.

Conclusion:

Aluminum tungstate was shown to be an attractive candidate for the recovery of gallium from aqueous systems, including industrial effluents. Further studies should determine the capacities of both the powder and supported materials. Also, a study should focus on determining the optimum conditions for the recovery of Ga^{3+} from semi-conductor waste and applied to effluents like Bayer liquors. Moreover, the material should be tested for its ability to recovery other M^{3+} ions, including the more expensive rare earth metals. Finally, a method should be determined for recovery of Ga^{3+} and recycling the sorbent.

References:

1. J. M. Schoenung and J. P. Clark, Gallium Demand for Electronic Devices. *JOM* **1987,** *39* (6), 36-38.

2. D. E. Carter, H. V. Aposhian, and A. J. Gandolfi, The metabolism of inorganic arsenic oxides, gallium arsenide, and arsine: a toxicochemical review. *Toxicology and Applied Pharmacology* **2003,** *193* (3), 309-334.

3. O. Font, X. Querol, R. Juan, R. Casado, C. R. Ruiz, Á. López-Soler, P. Coca, and F. G. Peña, Recovery of gallium and vanadium from gasification fly ash. *Journal of Hazardous Materials* **2007,** *139* (3), 413-423.

4. B. Gutiérrez, C. Pazos, and J. Coca, Recovery of Gallium from Coal Fly Ash by a Dual Reactive Extraction Process. *Waste Management & Research* **1997,** *15* (4), 371-382.

5. P. A. Riveros, Recovery of gallium from Bayer liquors with an amidoxime resin. *Hydrometallurgy* **1990,** *25* (1), 1-18.

6. Z. Zhao, Y. Yang, Y. Xiao, and Y. Fan, Recovery of gallium from Bayer liquor: A review. *Hydrometallurgy* **2012,** *125–126* (0), 115-124.

7. U. S. Suryavanshi and S. R. Shukla, Adsorption of Ga(III) on Oxidized Coir. *Industrial & Engineering Chemistry Research* **2008,** *48* (2), 870-876.

8. P. Selvi, M. Ramasami, M. H. P. Samuel, P. Adaikkalam, and G. N. Srinivasan, Recovery of Gallium from Bayer Liquor Using Chelating Resins in Fixed-Bed Columns. *Industrial & Engineering Chemistry Research* **2004,** *43* (9), 2216-2221.

9. H. Albusaidi and A. W. Apblett, Adsorption and Separation of Uranium Using Tungsten Oxides. In *Environmental Issues and Waste Management Technologies in the Materials and Nuclear Industries XII*, John Wiley & Sons, Inc.: 2009; pp 39-46.

10. A. W. Apblett, B. P. Kiran, and M. Chehbouni, Molybdenum-Oxide Based Sorbants for Toxic Metals. *Ceramic Transactions* **2006,** *176*, 15-23.

11. K. N. Barber and A. W. Apblett, Green Process for Recovery of Copper. *Ceramic Transactions* **2009,** *207*, 171-175.

12. M. Chehbouni, H. Al-Busaidi, and A. W. Apblett, Green Process for Uranium Separations Utilizing Molybdenum Trioxide. In *Nuclear Energy and the Environment*, American Chemical Society: 2010; Vol. 1046, pp 155-167.

13. B. P. Kiran and A. W. Apblett, Process for Selective Removal and Concentration of Actinides and Heavy Metals from Water. *Ceramic Transactions* **2004,** *155*, 371-380.

14. B. P. Kiran, A. W. Apblett, and M. M. Chehbouni, Selective Absorption of Heavy Metals and Radionuclides from Water in a Direct-to-Ceramic Process. *Ceramic Transactions* **2003,** *143*, 385-394.

15. S. Lagergren, Zur theorie der sogenannten adsorption gelöster stoffe. Kungliga Svenska Vetenskapsakademiens. *Handlingar* **1898,** *24* (4), 1-39.

16. S. Azizian, Kinetic models of sorption: a theoretical analysis. *Journal of Colloid and Interface Science* **2004,** *276*, 47–52.

17. K. V. Kumar, Linear and non-linear regression analysis for the sorption kinetics of methylene blue onto activated carbon. *Journal of Hazardous Materials B* **2006,** *137*, 1538-1544.

18. Y. S. Ho and G. McKay, Pseudo-second order model for sorption processes. *Process Biochemistry* **1999,** *34*, 451-465.

CHAPTER VIII

LEAD UPTAKE BY MOLYBDENUM TRIOXIDE

Introduction:

Increasing concern about the effect of lead and other heavy metals on humans and aquatic ecosystems, along with increasing economic concerns, has led to growing interest for the development of materials for mitigation of heavy-metals. [1-10] Lead has been deemed a cancer causing agent and has also been noted to be toxic to the renal, cardiovascular, nervous, and reproductive systems.[11-17] Since children have a greater rate of intestinal absorption and retention of lead, thus they are more vulnerable to lead exposure, which has been directly correlated to the lowering of IQs.[18-20] Human exposure to lead typically is correlated with lead plumbing materials or lead-based paints, but has also been linked to lead containing soils.[21-22] Lead exposure has also been associated with the release of airborne particulates from industrial or waste elimination emissions and fallout from decades of leaded gasoline emissions.[3,21] The World Health Organization (WHO) and the Environmental Protection Agency (EPA) maximum contaminant levels for Pb^{2+} in drinking water are 10 μg/L and 15 μg/L, respectively.[23-24] Heavy metals can also occur from natural sources, with pollution typically being caused from the leaching from minerals. Furthermore, the rapid development of industries, such as metal plating facilities, mining operations, fertilizer industries, etc., have often directly introduced heavy metal

wastewaters into the environment, especially in developing countries. Unlike organic contaminants, heavy metals are not biodegradable and tend to accumulate in living organisms.[25]

Current metal mitigation technologies have progressed due the required acceptable contaminant limits many industries face. Thus, materials specifically targeting lead have been extensively studied, via a very broad range of processes including chemical precipitation,[5, 8] adsorption,[9, 26] solvent extraction,[27-29] ultrafiltration,[30-31] and ion exchange.[6-7, 32] Many of the materials for these types of applications have short falls due to low capacity, poor selectivity, lack of effectiveness, high cost, or a combination of these. Permeable reactive barriers (Figure 1), particularly are promising for ground water remediation, due to their facile implementation and retrieval route, especially if the sorbent is placed on a larger substrate.[33] An equal benefit of the complexation of persistent heavy metals is the ability for the sorbent to be recycled with limited byproducts, allowing for the contaminant and substrate to be easily separated. The Apblett group has previously shown the ability to remediate Pb^{2+} with a very high capacity using commercially available MoO_3 under reflux conditions in an acetate buffer.[34] Further, we have highlighted the very high reactivity of a nanometric suspension of MoO_3 with Pb^{2+} as presented in Chapter III.[35] The present study, however, is aimed at determining the reactivity of commercially available bulk-MoO_3 towards Pb^{2+} under ambient conditions without the presence of a buffer. Further, this study presents the use of MoO_3 on a high-surface area catalyst support as a target material for facile implementation in reactive barrier-type applications. The kinetics and molar capacities were studied and the materials were characterized for their identities post-treatment.

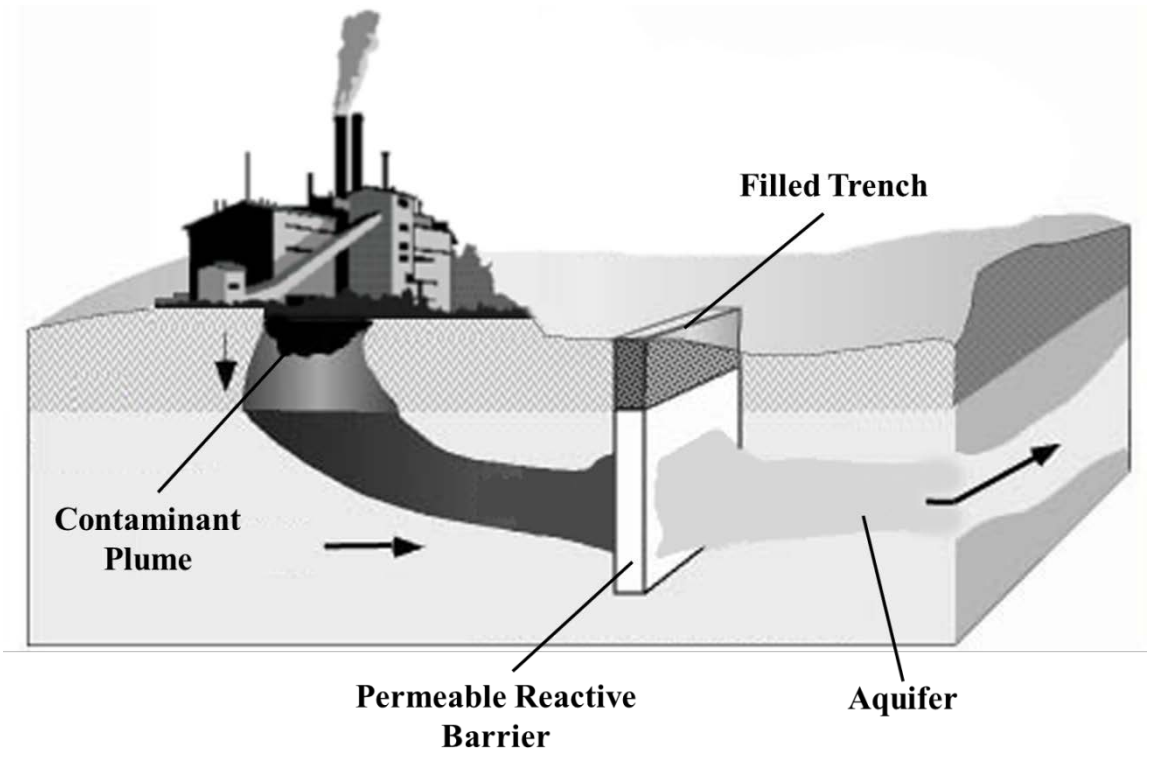

Figure 1: Permeable Reactive Barrier

Experimental:

All chemicals (reagent grade or higher) were used as received without further purification. The water used was purified by reverse osmosis followed by ion exchange. Lead nitrate, $Pb(NO_3)_2$ (Sigma-Aldrich), was used to prepare the lead stock solution with a concentration of approximately 100 mg/L. The concentrations of the stock and treated solutions were determined using a Varian GTA120/AA240Z graphite furnace atomic absorption spectrometer (GFAAS) equipped with an auto sampler. A 100 mg/L Pb^{2+} standard (BDH ARISTAR) was used to prepare the standard solutions used for analysis. Aliquots of the treated samples were taken at regular time intervals and diluted to the appropriate concentrations with a 1% HNO_3 solution, made using trace metal grade HNO_3 from Mallinckrodt. The commercially available molybdenum trioxide was used as the bulk reagent for sorption was received from Alfa-

Aesar. High surface area Al_2O_3 catalyst supports were obtained from Alfa-Aesar and used to support MoO_3 from the thermal decomposition of impregnated ammonium molybdate ($(NH_4)_6Mo_7O_{24}$) from the Alfa-Aesar Chemical company.

The Raman spectrum of the material at capacity was recorded on a Nicolet NXR 9610 Raman spectrometer. The surface areas were measured by N_2 physisorption and recorded using a NOVA Quantachrome 1200 BET. Scanning electron micrographs of the solids before and after treatment were also recorded using a FEI Quanta 600 field emission gun environmental scanning electron microscope. The X-ray powder diffraction (XRD) patterns of the sorbents at capacity were obtained on a Bruker D8-A25-Advance with a LynxEye detector.

Synthesis of Supported MoO_3

The high surface area Al_2O_3 supports were vacuum-impregnated by introducing a 35% by weight solution of ammonium molybdate to the supports *in vacuo*. The supports were held under vacuum for roughly 24 hours. When removed from the vacuum pump, the supports were rinsed with 50 mL of deionized water, to remove any excess material on the surface, and were then dried *in vacuo.* Once dry, the supports were transferred to a ceramic crucible and were heated to 500 °C, well over the decomposition temperature of ammonium molybdate to ensure the formation of MoO_3.[36] The pellets were held for 8 hours at 500 °C and were then cooled to room temperature. The mass of the resulting material indicated a loading of the support with 9.01% molybdenum trioxide by weight.

Results and Discussion:

Sorption Kinetics Using Bulk-MoO_3

The sorption uptake curve (Figure 2) depicts the sorption of lead by different amounts of molybdenum trioxide. The uptake curves depict a process in which sorption is initially very fast and then starts to slow as the reaction approaches an equilibrium state. The lower sorbent loading

experiments reach their respective equilibrium states later than the higher loadings. With sufficient sorbent, the sorption process continued at a slow rate until the entirety of the analyte was removed below the instrument detection limit of roughly 0.5 ppb. Determination of the kinetic rate is an integral aspect of determining if a sorbent can be used industrial applications. The kinetic uptake of Pb^{2+} was modeled by both the commonly used pseudo first and second-order models processes.

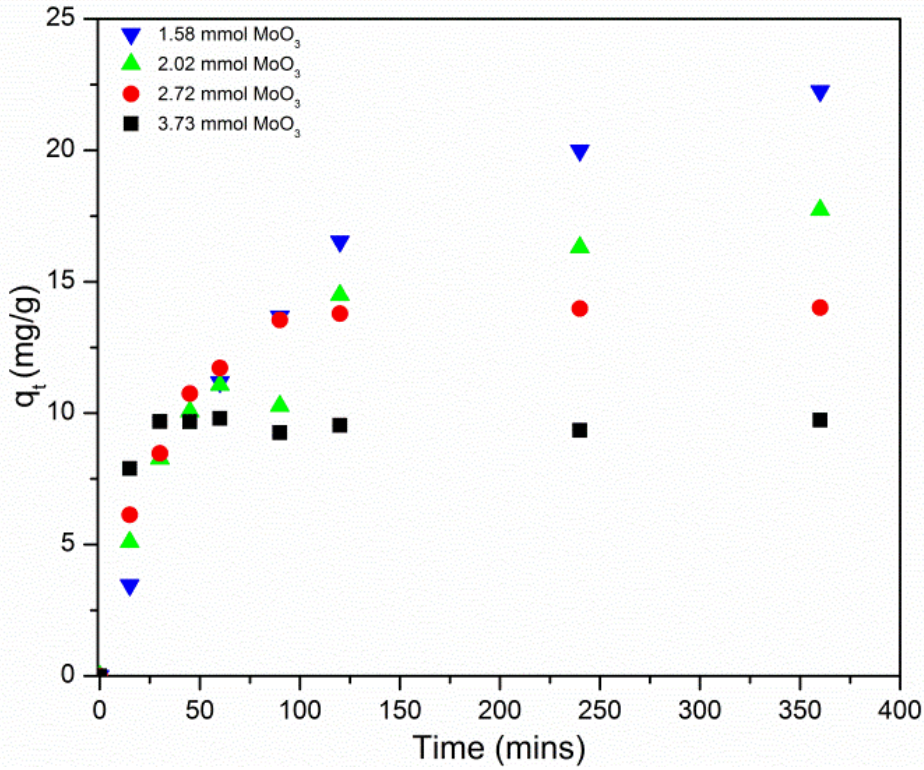

Figure 2: Sorption Uptake Curve of Pb^{2+} on Bulk-MoO_3

The pseudo first-order rate expression described by Lagergren (Equation 1) is an exponential function where q_t is the amount of the analyte sorbed at time t, k_1 is the rate constant of the pseudo first-order sorption process, and q_e is the amount of analyte sorbed at equilibrium.[37] Further, the natural log of Equation 1, yields a linear function (Equation 2) that gives the values of k_1 and q_e from the slope and intercept, respectively, of a plot of $\ln(q_e-q_t)$ vs. time.

$$q_t = q_e(1 - e^{-k_1 t})$$

Equation 1: The Nonlinear Pseudo First-Order Equation

$$\ln(q_e - q_t) = \ln(q_e) - k_1 t$$

Equation 2: The Linearized Formula for Pseudo First-Order Kinetics

Figure 3 shows that the linear pseudo first-order kinetic model for the bulk-MoO_3 does not apply throughout the various sorbent loadings. Although, the linear pseudo first-order does a fairly good job modeling the sorption process, it fails in the case of the largest sorbent loading, as is evident from the correlation coefficient (R^2) values listed in Table 1. The estimated q_e values, calculated from the equation, have a good agreement with the experimental values at the lowest mass loading, but as the sorbent is increased the model consistently underestimates the q_e values, with the error increasing as the sorbent mass increases. The deviation from linearity at larger sorbent loadings is likely due to the similar concentrations of lead ions and reactions sites on the sorbent.[38]

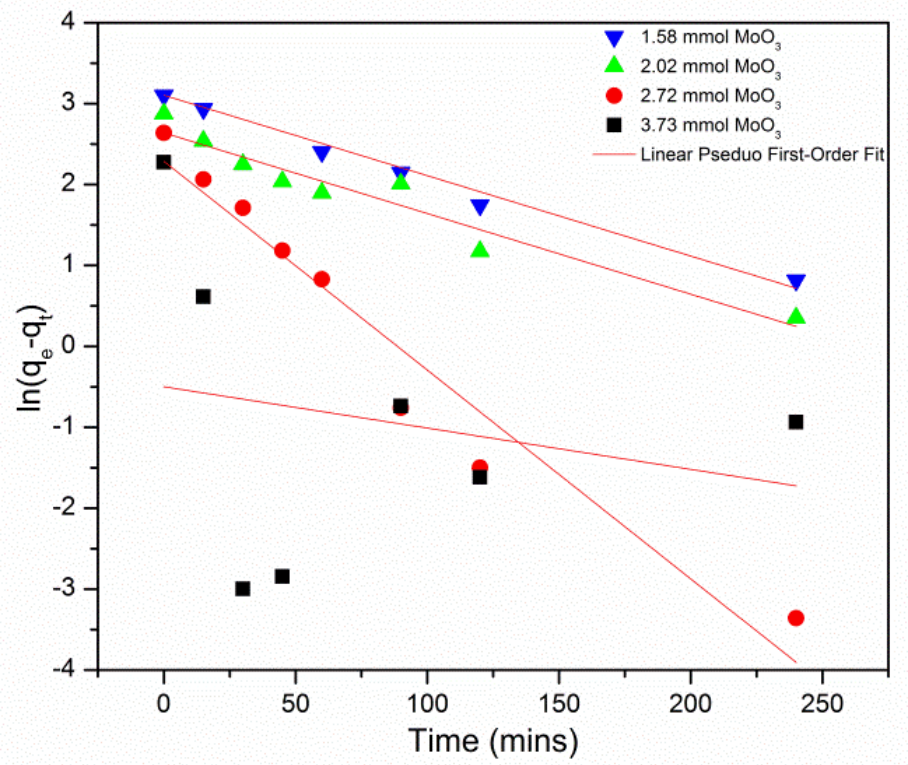

Figure 3: Linear Pseudo First-Order Plot for Bulk-MoO_3 Uptake of Pb^{2+}

Table 1: Data and Results for Linear Pseudo First-Order Fitting

MoO_3 (mmol)	k_1 (min^{-1})	q_e (mg/g)	q_e (mg/g) (experimental)	R^2
1.58	9.94E-03	22.3	22.3	0.975
2.03	9.97E-03	14.0	17.7	0.930
2.72	2.58E-02	9.85	14.0	0.940
3.73	5.10E-03	1.65	9.73	0.134

It has been suggested that modeling sorption processes using the nonlinear pseudo first-order model can provide vastly improved results.[39] The nonlinear pseudo first-order equation (Equation 1) was used to fit the experimental data, and the results are presented in Figure 4. The data are fitted well by the nonlinear equation, as indicated by the correlation coefficients in Table 2. Further, the model's prediction of q_e is in excellent agreement with the experimental values

with only a slight underestimation. These results are in good agreement with the hypothesis that the nonlinear method is far superior in modeling this sorption process than the linear method.

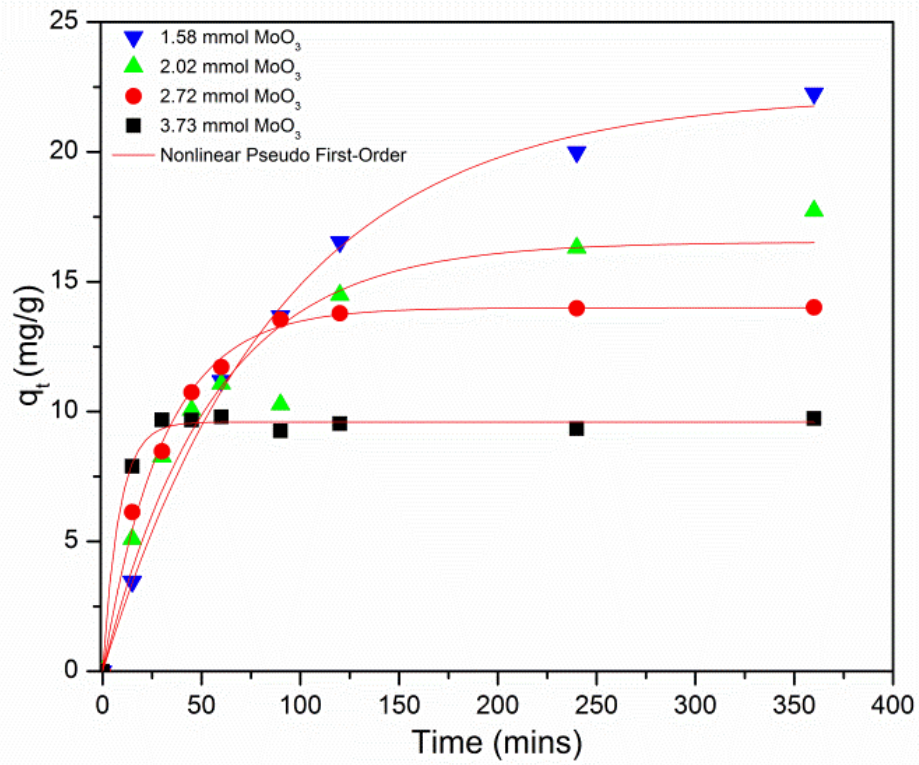

Figure 4: Nonlinear Pseudo First-Order Curve for Bulk-MoO_3 Uptake of Pb^{2+}

Table 2: Data and Results for Nonlinear Pseudo First-Order Uptake of Lead by Bulk-MoO_3

MoO_3 (mmol)	k_1 (min^{-1})	q_e (mg/g)	q_e (mg/g) (experimental)	R^2
1.58	1.11E-02	22.2	22.3	0.997
2.03	1.82E-02	16.5	17.7	0.933
2.72	3.30E-02	14.0	14.0	0.995
3.73	1.20E-01	9.60	9.73	0.994

Ho and McKay proposed a pseudo second-order kinetic model represented by the Equation 3, where k_2 is the rate constant of the pseudo second-order sorption process, with the units g mg^{-1} min^{-1}.[40] The equation can be further simplified to Equation 4, by substituting h in place of $k_2q_e^2$, where h can be considered to be the initial sorption rate, as t/q_t approaches 0. The

slope and the intercept of the plot of t/q_t versus t gives the values of the constants q_e and h, respectively.[38] Using the value of q_e and h, the rate constant (k_2) can be obtained.

$$\frac{t}{q_t} = \frac{1}{k_2 q_e^2} + \frac{1}{q_e} t$$

Equation 3: The Linearized Pseudo Second-Order Rate Equation

$$\frac{t}{q_t} = \frac{1}{h} + \frac{1}{q_e} t$$

Equation 4: The linearized Initial Rate Pseudo Second-Order Equation

The linear pseudo second-order plot for the sorption of lead onto molybdenum trioxide, Figure 5, shows a very good linear fit to the data. The results of the fitting are provided in Table 3. All of the experiments fit the linear pseudo second-order model much better than the linear pseudo first-order model, with very high linear regression correlation coefficient (R^2) values. The calculated q_e values are in close agreement with the experimental data, although the model overestimates the values in every case but the highest sorbent loading where qe is underestimated by a very small amount. The pseudo second-order rate constants (k_2) display a correlation with respect to the varying amount of sorbent, as the amount increases the rate increases. However, the units of the pseudo second-order rate constant make the physical significance of rate constant very vague.

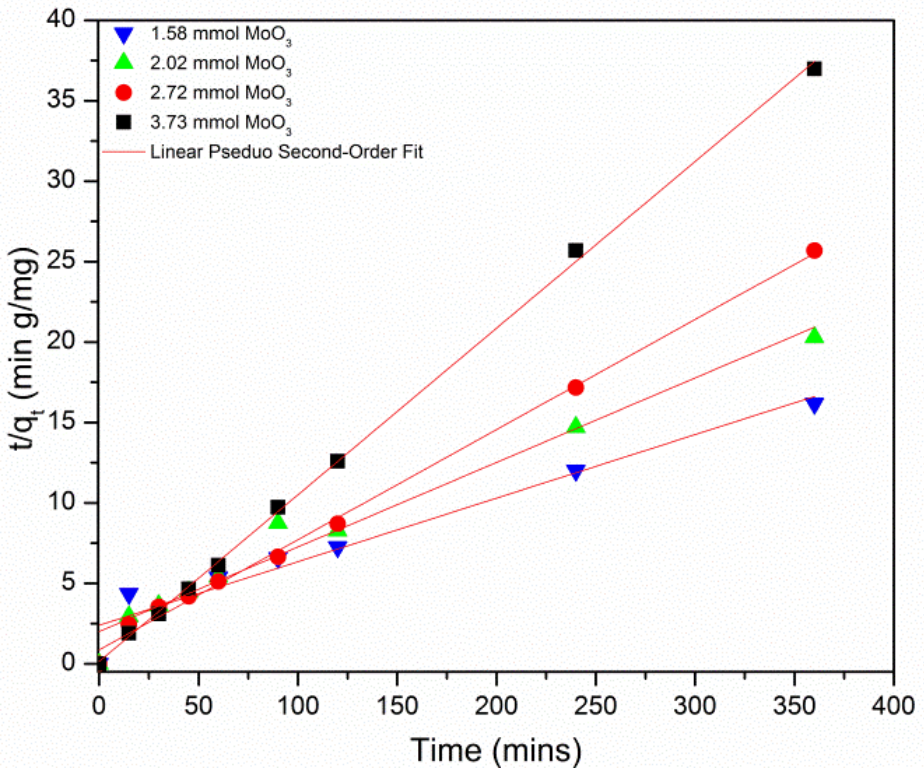

Figure 5: Linear Pseudo Second-Order Curves for the Uptake of Pb^{2+} by Bulk-MoO_3

Table 3: Data and Results for the Linear Pseudo Second-Order Modeling of Lead Uptake by Bulk-MoO_3

MoO_3 (mmol)	k_2 (g/mg min)	h (mg/g min)	q_e (mg/g)	q_e (mg/g) (experimental)	R^2
1.58	6.52E-04	0.417	25.3	22.3	0.999
2.03	1.37E-03	0.498	19.0	17.7	0.996
2.72	5.43E-03	1.16	14.6	14.0	0.970
3.73	7.44E-02	6.93	9.65	9.73	0.974

Previously, the nonlinear pseudo second-order equation (Equation 5) was used to effectively model the sorption process of methylene blue on activated carbon.[39] Figure 6 shows the plotted data fitted with the nonlinear pseudo second-order model with relatively good accuracy. Table 4 shows that the correlation coefficients for the nonlinear method are very high (R^2>0.96), similar to the linear model, suggesting that this method is also appropriate for

modeling this process. Similar to the linear method, the kinetic parameters of the nonlinear pseudo second-order appear to have little physical meaning. However, the equilibrium concentration values from the model are, in fact, higher in every case than the experimental values, and as the sorbent loading decreases, this trend is amplified.

$$q_t = \frac{k_2 q_e^2 t}{1 + k_2 q_e t}$$

Equation 5: The Nonlinear Pseudo Second-Order Equation

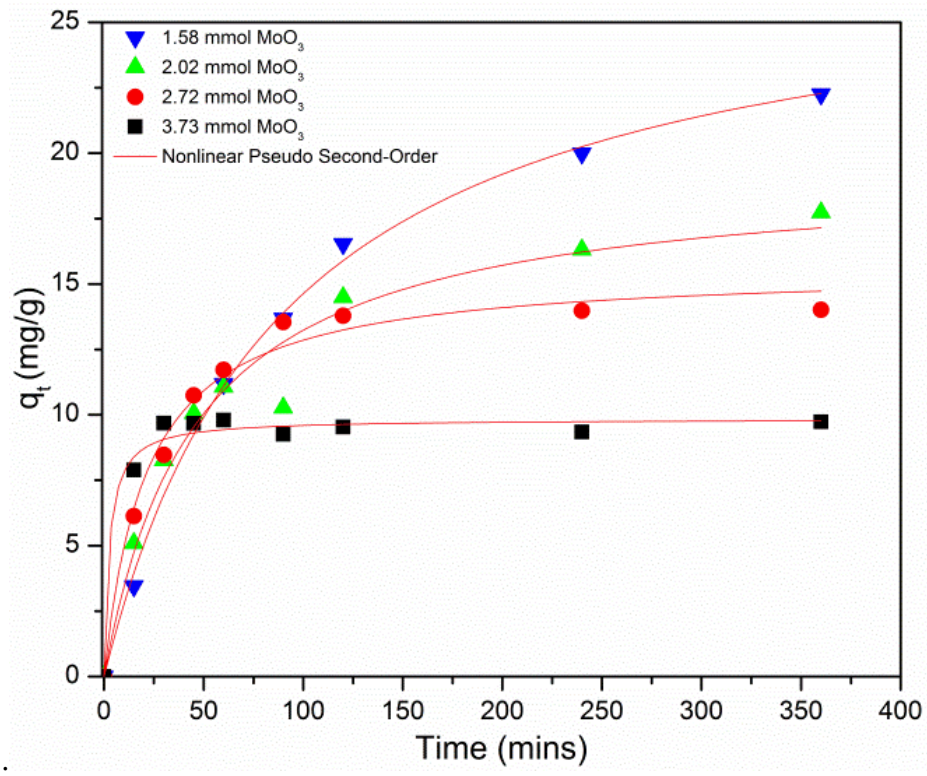

Figure 6: Nonlinear Pseudo Second-Order Curve for the Uptake of Pb^{2+}Bulk-MoO_3

Table 4: Data and Results for the Nonlinear Pseudo Second-Order Fit for the Uptake of Pb^{2+} by Bulk-MoO_3

MoO_3 (mmol)	k_2 (g/mg min)	h (mg/g min)	q_e (mg/g)	q_e (mg/g) (experimental)	R^2
1.58	3.96E-04	0.308	27.9	22.3	0.998
2.03	1.12E-03	0.419	19.3	17.7	0.964
2.72	3.00E-03	0.730	15.6	14.0	0.985
3.73	3.93E-02	3.80	9.84	9.73	0.983

The data presented suggests that the nonlinear pseudo first-order model is the best-suited model for the sorption of Pb^{2+} on bulk-MoO_3. This is due not only to the predicted q_e values, but also for the clear physical meaning of the pseudo first-order rate constant.

Sorption Kinetics for the Al_2O_3 Supported-MoO_3

By supporting the MoO_3 on the high surface area Al_2O_3 substrate, the surface area was improved from that of the bulk-MoO_3. The latter had a surface area of 0.7 $m^2\ g^{-1}$, while that of the supported material was 181 $m^2\ g^{-1}$. The impregnation method produced a product with 9.01% MoO_3 on the Al_2O_3 support. The sorption uptake curves (Figure 7) depict the sorption process where equilibrium was reached at roughly 60 minutes for all of the mass loadings. Furthermore, the equilibrium sorption capacities were improved in every case using the supported the material. However, the real advantage to using the supported-MoO_3, as opposed to the powder materials, is the facile implementation and retrieval of the supported material.

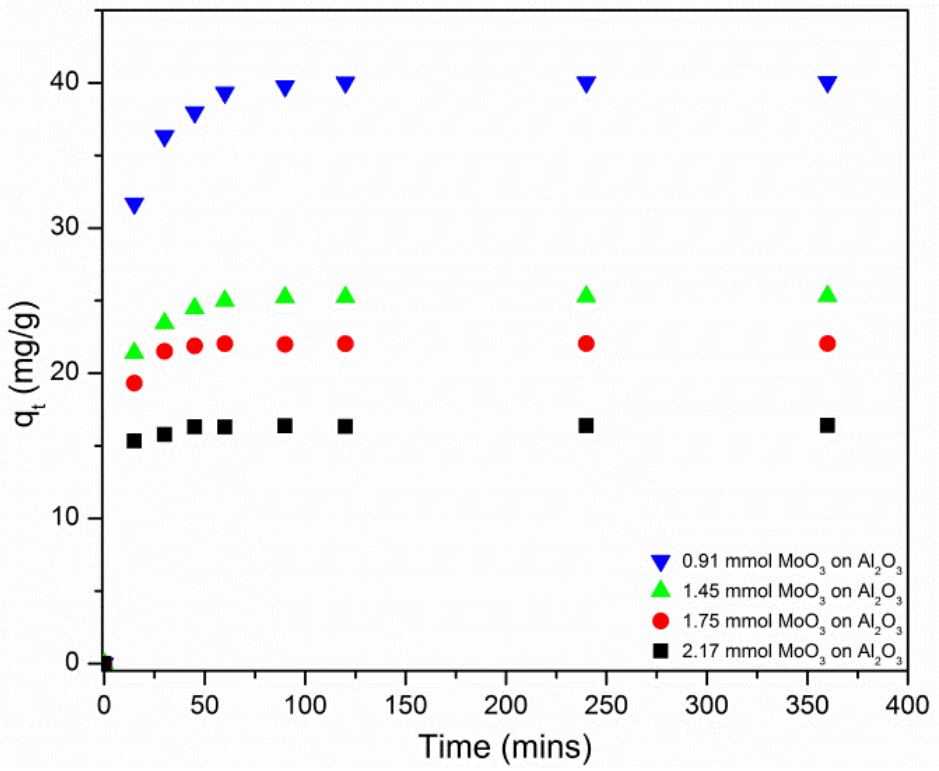

Figure 7: Sorption Uptake Curve for Pb^{2+} by the Al_2O_3 Supported-MoO_3

Interestingly, the linear pseudo first-order model, which gave decent correlations for the bulk-MoO_3, gave very poor data for the supported materials (Figure 8). Further, the model gave much lower prediction for q_e than was observed experimentally (Table 5). This data, coupled with the bulk-MoO_3 data suggests this model is not adequate for this sorption process.

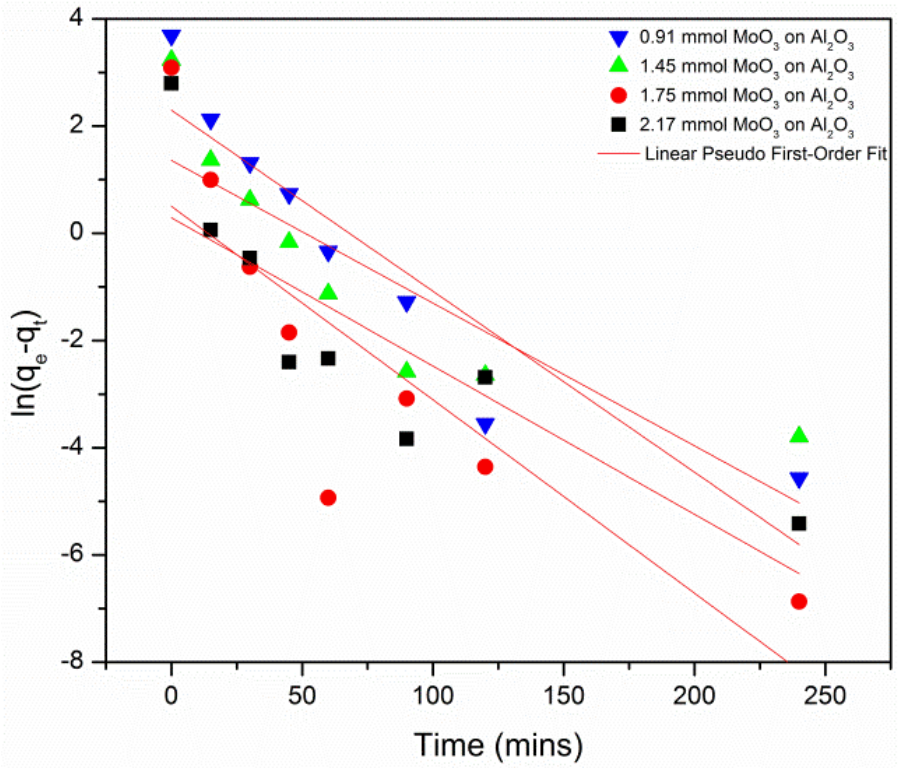

Figure 8: Linear Pseudo First-Order Fit for the Uptake of Pb^{2+} by Al_2O_3 Supported-MoO_3

Table 5: Data for the Linear Pseudo First-Order Fit for the Al_2O_3 Uptake of Pb^{2+} by Supported-MoO_3

MoO_3 (mmol)	k_1 (min^{-1})	q_e (mg/g)	q_e (mg/g) (experimental)	R^2
0.914	3.38E-02	9.94	40.0	0.842
1.45	2.66E-02	3.90	25.3	0.725
1.75	3.61E-02	1.65	22.0	0.675
2.17	2.77E-02	1.34	16.4	0.663

Similar to the bulk-MoO_3, Figure 9 shows the supported material fit the nonlinear model very well. Further, the correlation coefficients in every case are greater than 0.99 (Table 6), suggesting an almost perfect fit to the data. Also, in every case, the model gives very slight underestimation for the predicted values of q_e, as compared to what was observed experimentally. This data, together with the data from the bulk-MoO_3 sorption process, suggests this model is

ideal for modeling this sorption process. It is also meritorious for providing rate constants with an understood physical meaning.

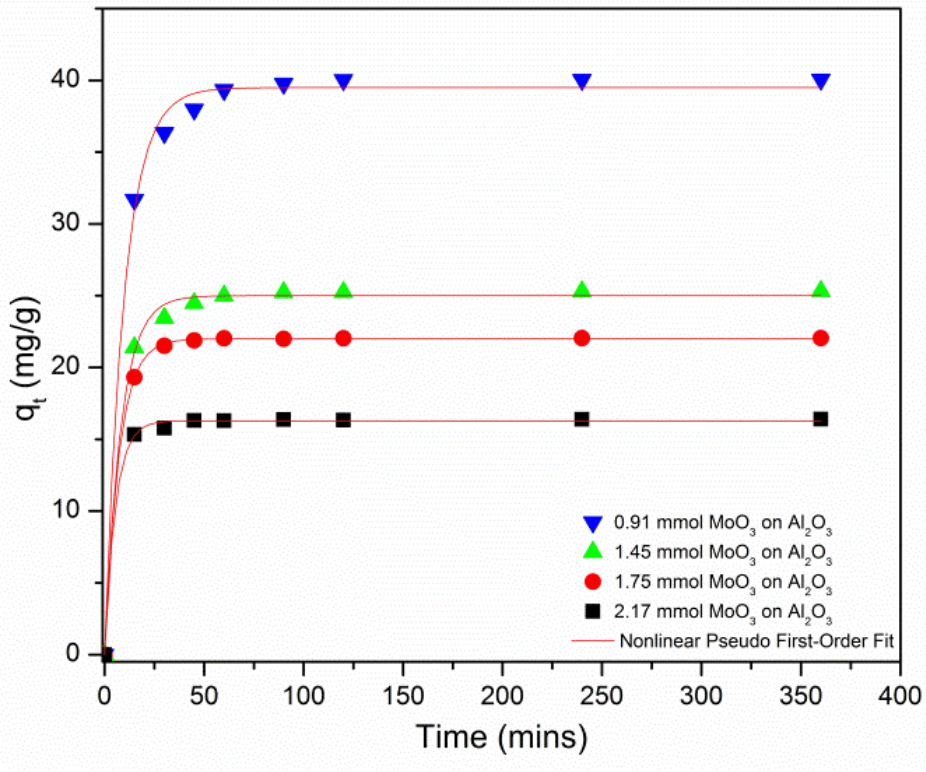

Figure 9: Nonlinear Pseudo First-Order Fit for the Uptake of Pb^{2+} by Al_2O_3 Supported-MoO_3

Table 6: Data and Results for the Nonlinear Pseudo First-Order Fit of the Uptake of Pb^{2+} by Al_2O_3 Supported-MoO_3

MoO_3 (mmol)	k_1 (min^{-1})	q_e (mg/g)	q_e (mg/g) (experimental)	R^2
0.914	1.02E-01	39.5	40.0	0.996
1.45	1.23E-01	25.0	25.3	0.997
1.75	1.40E-01	22.0	22.0	1.000
2.17	1.86E-01	16.3	16.4	0.999

For comparison purposes, the sorption processes were also modeled using the pseudo second-order equations. Figure 10 shows the nonlinear pseudo second-order equation fits the

sorption data very good as well and Table 7 shows perfect correlation coefficients. Further, this model gives almost perfect q_e predictions throughout the sorption process.

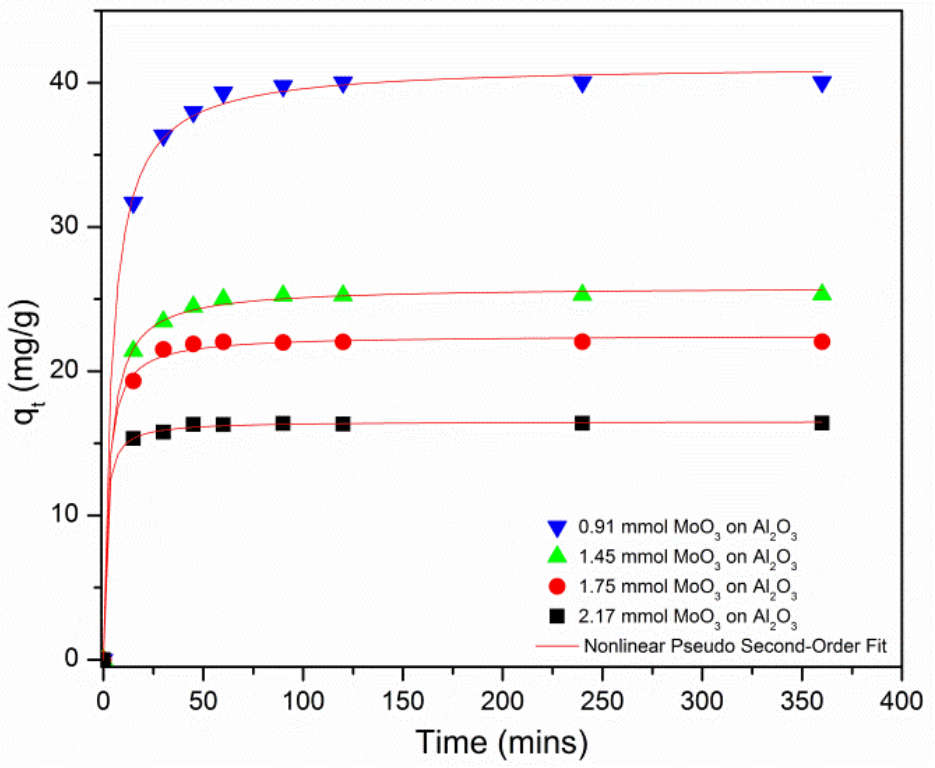

Figure 10: Nonlinear Pseudo Second-Order Fit for the Uptake of Pb^{2+} by Al_2O_3 Supported-MoO_3

Table 7: Data and Results for the Nonlinear Pseudo Second-Order Fit for the Uptake of Pb^{2+} by Al_2O_3 Supported-MoO_3

MoO_3 (mmol)	k_2 (g/mg min)	h (mg/g min)	q_e (mg/g)	q_e (mg/g) (experimental)	R^2
0.914	6.08E-03	9.28	39.1	40.0	0.998
1.45	1.30E-02	8.70	25.9	25.3	0.999
1.75	2.15E-02	10.9	22.5	22.0	0.998
2.17	5.24E-02	14.3	16.5	16.4	1.00

The linear pseudo second-order model, depicted in Figure 11, gives the closest predicted q_e values throughout the entire sorbent loadings. Further, the model gives flawless correlation coefficients for every single mass loading, listed in Table 8.

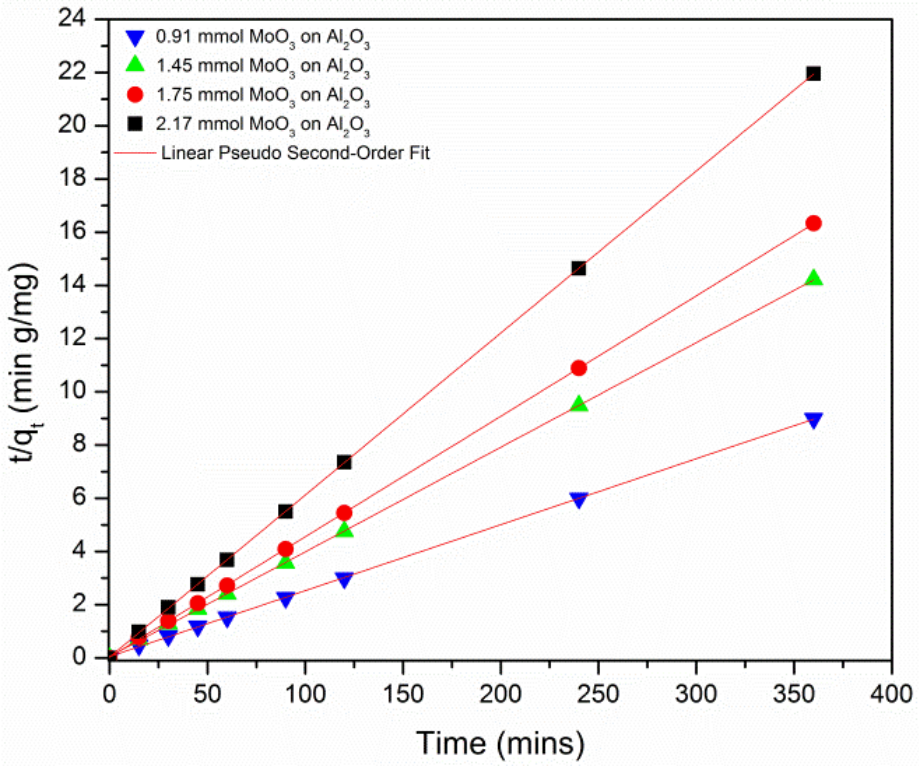

Figure 11: Linear Pseudo Second-Order Fit for the Uptake of Pb^{2+} by Al_2O_3 Supported-MoO_3

Table 8: Data for the Linear Pseudo Second-Order Fit for the Uptake of Pb^{2+} by Al_2O_3 Supported-MoO_3

MoO_3 (mmol)	k_2 (g/mg min)	h (mg/g min)	q_e (mg/g)	q_e (mg/g) (experimental)	R^2
0.914	1.22E-02	19.9	40.3	40.0	1.00
1.45	2.75E-02	17.8	25.4	25.3	1.00
1.75	7.07E-02	34.5	22.1	22.0	1.00
2.17	1.04E-01	28.0	16.4	16.4	1.00

It is obvious this model gives the best correlations and prediction of equilibrium capacities; however the lack of a clear physical meaning for k_2 means this model only useful for predicting the equilibrium capacities, rather than giving meaningful kinetic parameters.

The data from the two different sorbents suggests that the nonlinear pseudo first-order equation is ideal for modeling this sorption process. From this, we can then compare the kinetic rates of the two different materials. Figure 12 shows the sorption half-life of the analyte when treated with similar amounts of sorbent. The data suggests that by supporting the material, the sorption half-life can be improved roughly 10 fold, from 38 minutes to less than 4 minutes for the supported materials. The only downfall to the supported material, however, is the apparent loss of material from the support. That is, during the kinetic study, a white precipitate formed (Figure 13) that is likely due to the formation of $PbMoO_4$. This could be caused by the appreciable solubility of molybdenum trioxide (0.497 mg/L), which may be amplified by supporting the material.[41] Surprisingly precipitation formation did not occur during the capacity study. This may be due to the lead being in excess rather than the sorbent in these experiments.

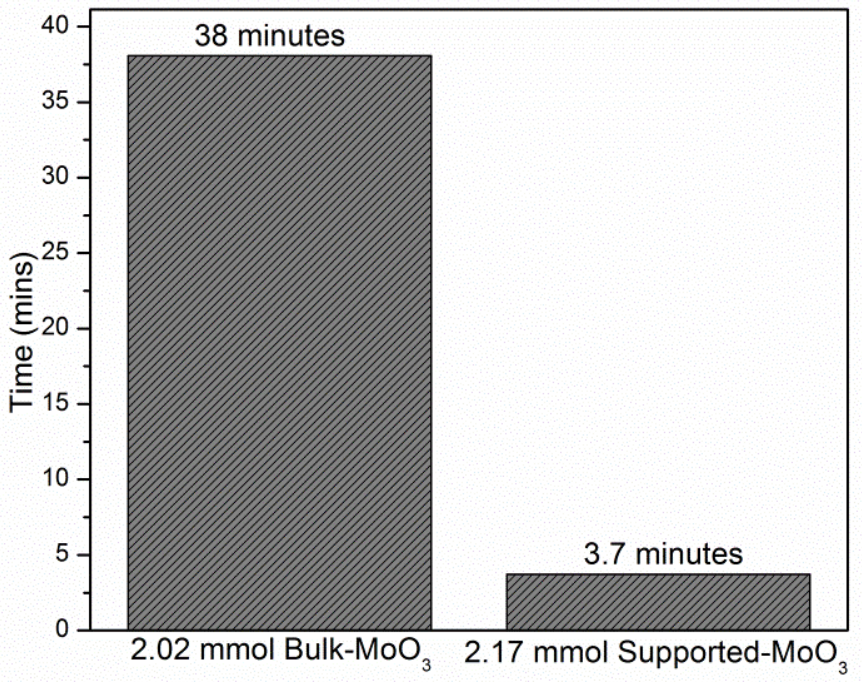

Figure 12: Sorption Half-Life for the Bulk-MoO_3 and the Alumina Supported MoO_3

Figure 13: Formation of a $PbMoO_4$ Precipitate after Only 15 Minutes in the Kinetic Study

Characterization of the Materials as Capacity

Each material was reacted with excess Pb^{2+} to determine the molar capacities for each material. The very low surface area bulk-MoO_3 had a molar sorption capacity of 16%, which was vastly improved, to 100%, by supporting the material, as summarized in Table 9. Further, it is

interesting to note the large drop in pH at the equilibrium point for the bulk-MoO_3, which is due to the reaction process described in Equation 6. This suggests that the sorption process for the bulk-MoO_3 could possibly be improved with the implementation of a buffer, as sorption capacity has been shown to be affected by pH.[42] The supported material does not suffer this large pH drop, suggesting there is some dissolution of Al_2O_3 during the course of this reaction. This phenomenon may also cause the observed delamination of the lead molybdate from the support.

Table 9: Summary of the Reaction Parameters for the Materials at Capacity

Material	Molar Sorption Capacity (%)	Surface Area (m^2/g)	Initial pH	Final pH
Bulk-MoO_3	16.0	0.7	3.9	0.9
Supported-MoO_3	100	181	3.9	3.1

$$MoO_3 + Pb^{2+} + H_2O \rightarrow PbMoO_4 + 2H^+$$

Equation 6: Schematic representation of the reaction of MoO_3 with Pb^{2+}

Both the bulk and supported-MoO_3 loaded to capacity with lead were characterized by X-ray powder diffraction. The XRD pattern for the bulk-MoO_3 that has been reacted with excess Pb^{2+} (Figure 14) shows that both unreacted MoO_3 and $PbMoO_4$ are present. On the other hand, the XRD pattern for the supported MoO_3 reacted with excess lead only contained peaks for $PbMoO_4$.

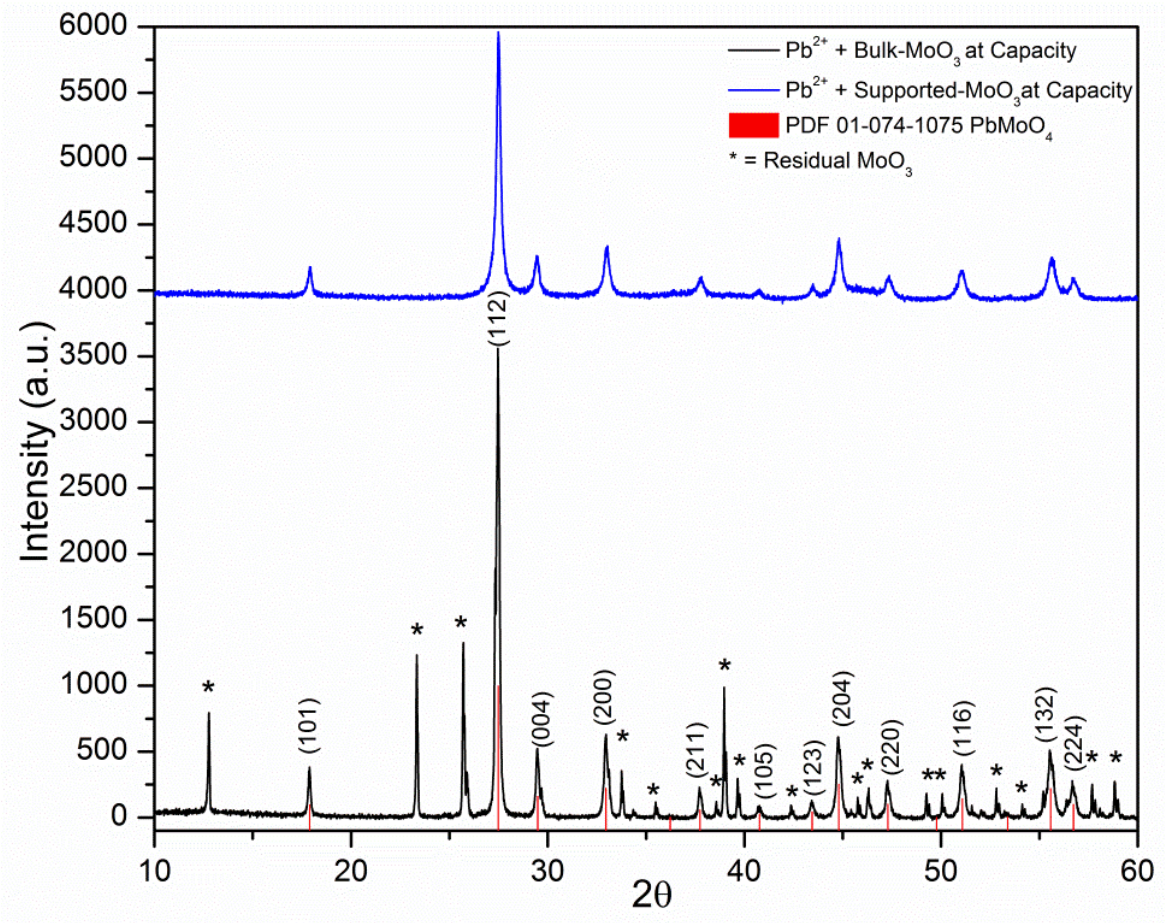

Figure 14: XRD Patterns for Sorbents Reacted with Excess Pb^{2+}

The bulk-MoO_3 was further characterized by Raman spectroscopy and scanning electron microscopy. The Raman spectrum (Figure 15) gave one peak characteristic of $PbMoO_4$ and the rest were characteristic of MoO_3. The peak at 868 cm^{-1} Figure 15 is characteristic of the $\nu_1(A_g)$ symmetric stretching band for the tetrahedral molybdate ion in $PbMoO_4$.[43] The peaks at 992, 819, 280, and 146 cm^{-1} are consistent with the previously reported Raman spectra of MoO_3.[44]

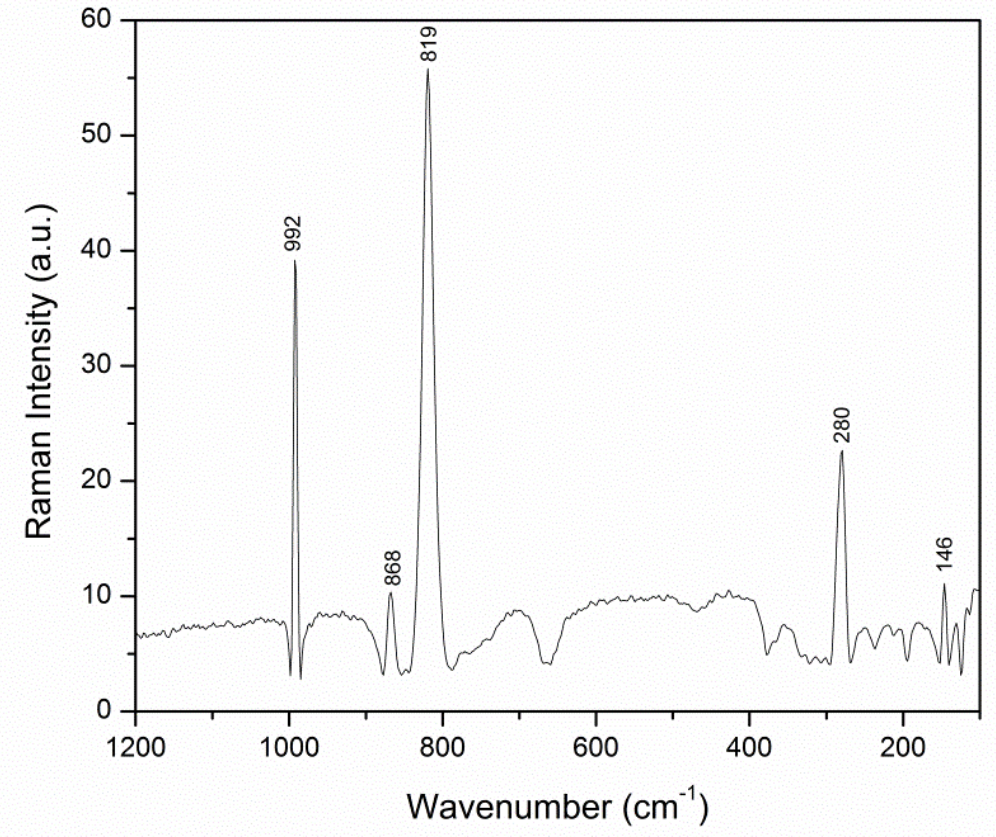

Figure 15: Raman Spectrum of MoO_3 Loaded to Capacity with Pb^{2+}

The SEM micrographs before and after reaction with lead are given in Figure 16. The images show a large morphological change at the surface upon exhaustive reaction with lead. The formation of the sharp-edged crystals on the surface of the material suggests the reaction proceeds by a dissolution-recrystallization reaction. The micrographs suggest that the reaction occurs exclusively at the surface (and may be surface limited) since there is no evidence of fragmentation or formation of unattached small $PbMoO_4$ crystals.

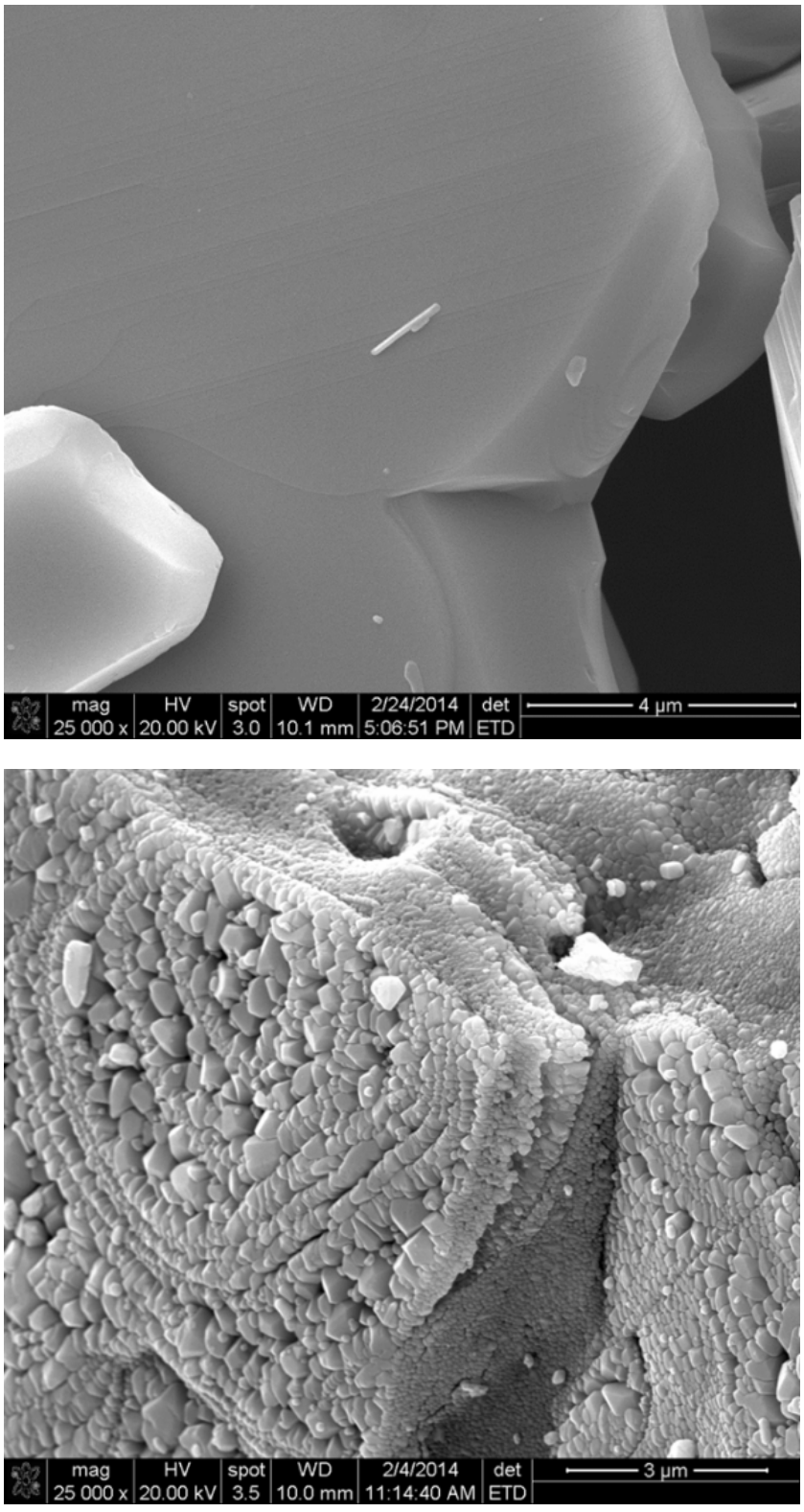

Figure 16: SEM Micrograph of the Starting Bulk-MoO_3 (top) and at Capacity (bottom)

Regeneration of the Spent Sorbent

To demonstrate the recyclability of the material, $PbMoO_4$ was synthesized by precipitating $Pb(NO_3)_2$ and $Na_2MoO_4 \cdot 2H_2O$ and then calcining the material at 600 °C. This material was characterized by XRD, showing that is was phase pure $PbMoO_4$. The regeneration-cycle (Figure 17) features a reaction of the spent material with excess 30% NH_4OH, yielding an insoluble lead hydroxide product. The solid was then filtered, separating the soluble molybdenum compound. The filtrate was dried and the produced powder was pyrolyzed at 550 °C, yielding MoO_3 with a 99% yield.

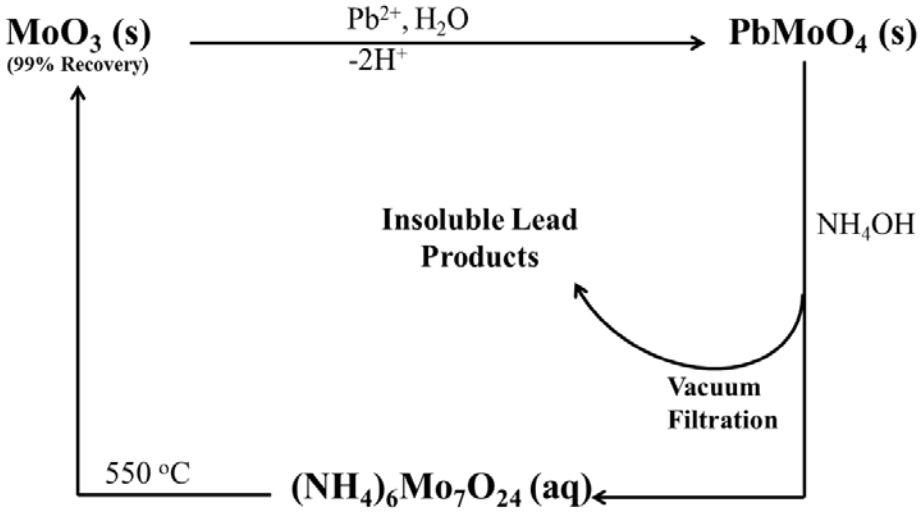

Figure 17: Green process for sorbent recovery

Conclusion:

Molybdenum trioxide was demonstrated to have a high affinity for aqueous lead. Furthermore, it was found that the rate and capacity can be increased by synthesizing the material on high surface area catalyst-supports. However, due to the appreciable solubility of MoO_3 (0.497 mg/L) this is likely not the best choice for remediation of potable water systems.[41] Further, due to this solubility, the supported-MoO_3 produced $PbMoO_4$ as a precipitate in the solution, rather than

on the surface of the support when the sorbent was in excess. Future study of this system could be aimed at characterizing the precipitate from the supported material, confirming that it is in fact $PbMoO_4$ and determining the particle size and morphology. The synthesized material could find use in catalysis and optics, among other applications. Further, the extent of the reaction should be studied in the presence of a buffer, to determine whether the pH or the surface area is the limiting factor of sorption capacity with this material. Finally, as research progress in the field of sorption kinetics, it would be useful to determine how novel models fit the presented data.

References:

1. J. E. Marcovecchio, S. E. Botte, and F. R. H., Heavy Metals, Major Metals, Trace Elements. In *Handbook of Water Analysis*, 2 ed.; Nollet, L. M., Ed. CRC Press: London, 2007.

2. P. A. Brown, S. A. Gill, and S. J. Allen, Metal removal from wastewater using peat. *Water Research* **2000,** *34* (16), 3907-3916.

3. T. Abdel-Fattah and K. B. Payne, Adsorption of divalent lead ions by zeolites and activated carbon: Effects of pH, temperature and ionic strength. *Journal of Environmental Science and Health Part A* **2004,** *227*, 2275-2291.

4. M. J. Baniamerian, S. E. Moradi, A. Noori, and H. Salahi, The effect of surface modification on heavy metal ion removal from water by carbon nanoporous adsorbent. *Applied Surface Science* **2009,** *256* (5), 1347-1354.

5. J. O. Esalah, M. E. Weber, and J. H. Vera, Removal of lead, cadmium and zinc from aqueous solutions by precipitation with sodium Di-(n-octyl) phosphinate. *The Canadian Journal of Chemical Engineering* **2000,** *78* (5), 948-954.

6. V. K. Gupta and I. Ali, Removal of lead and chromium from wastewater using bagasse fly ash—a sugar industry waste. *Journal of Colloid and Interface Science* **2004,** *271* (2), 321-328.

7. V. K. Gupta, M. Gupta, and S. Sharma, Process development for the removal of lead and chromium from aqueous solutions using red mud—an aluminium industry waste. *Water Research* **2001,** *35* (5), 1125-1134.

8. M. M. Matlock, B. S. Howerton, and D. A. Atwood, Chemical precipitation of lead from lead battery recycling plant wastewater. *Industrial & Engineering Chemistry Research* **2002,** *41* 6), 1579-1582.

9. R. M. McKenzie, The adsorption of lead and other heavy metals on oxides of manganese and iron. *Soil Research* **1980,** *18* (1), 61-73.

10. K. B. Payne and T. M. Abdel-Fattah, Adsorption of divalent lead ions by zeolites and activated carbon: Effects of pH, temperature, and ionic strength. *Journal of Environmental Science and Health A* **2004,** *39* (9), 2275-2291.

11. P. Wolff, Guidelines for Livestock Drinking-Water Quality in Dry Areas. *Tropenlandwirt* **1988,** *89*, 85-94.

12. P. J. Landrigan, Current issues in the epidemiology and toxicology of occupational exposure to lead. *Environmental Health Perspectives* **1990,** *89*, 61-66.

13. P. J. Landrigan, Strategies for epidemiologic studies of lead in bone in occupationally exposed populations. *Environmental Health Perspectives* **1991,** *91*, 81-86.

14. P. J. Landrigan and A. C. Todd, Lead Poisoning. *Western Journal of Medicine* **1994,** *161* (2), 153-159.

15. H. Needleman, Lead Poisoning. *Annual Review of Medicine* **2004,** *55* (1), 209-222.

16. S. Rehman, M. Adnan, N. Khalid, and L. Shaheen, Calcium Supplements: an Additional Source of Lead Contamination. *Biological Trace Element Research* **2011,** *143* (1), 178-187.

17. D. Rempel, The lead-exposed worker. *The Journal of the American Medical Association* **1989,** *262* (4), 532-534.

18. E. E. Ziegler, B. B. Edwards, R. L. Jensen, K. R. Mahaffey, and S. J. Fomon, Absorption and Retention of Lead by Infants. *Pediatric Research* **1978,** *12* (1).

19. Y. Finkelstein, M. E. Markowitz, and J. F. Rosen, Low-level lead-induced neurotoxicity in children: an update on central nervous system effects. *Brain Research Reviews* **1998,** *27* (2), 168-176.

20. Air Quality Criteria for Lead (EPA Report No. EA PA/600/8-83/028aF–dF). Environmental Protection Agency, Office of Health and Environmental Assessment: Research Triangle Park, 1986.

21. D. A. Burgoon, S. W. Rust, and K. A. Hogan, Relationships among lead levels in blood, dust, and soil. In *Lead Poisoning Exposure, Abatement, Regulation*, Breen, J. J., Stroup, C.R., Ed. Lewis Publishers Boca Raton, 1995; pp 255–264.

22. H. W. Mielke and P. L. Reagan, Soil is an important pathway of human lead exposure. *Environmental Health Perspectives* **1998,** *106*, 217-229.

23. Y. Sayato, Who Guidelines for Drinking-Water Quality. *Eisei Kagaku* **1989,** *35* (5), 307-312.

24. National Primary Drinking Water Regulations. Environmental Protection Agency: 2009; Vol. EPA 816-F-09-004, pp 1-6.

25. F. L. Fu and Q. Wang, Removal of heavy metal ions from wastewaters: A review. *Journal of Environmental Management* **2011,** *92* (3), 407-418.

26. Y.-S. Ho and G. McKay, Pseudo-second order model for sorption processes. *Process Biochemistry* **1999,** *34* (5), 451-465.

27. J. G. Dean, F. L. Bosqui, and K. H. Lanouette, Removing heavy metals from waste water. *Environmental Science & Technology* **1972,** *6* (6), 518-522.

28. K. Bang Mo, Membrane-based solvent extraction for selective removal and recovery of metals. *Journal of Membrane Science* **1984,** *21* (1), 5-19.

29. J. Pichtel and T. M. Pichtel, Comparison of solvents for ex situ removal of chromium and lead from contaminated soil. *Environmental Engineering Science* **1997,** *14* (2), 97-104.

30. F. Ferella, M. Prisciandaro, I. De Michelis, and F. Veglio, Removal of heavy metals by surfactant-enhanced ultrafiltration from wastewaters. *Desalination* **2007,** *207* (1), 125-133.

31. K. E. Geckeler and K. Volchek, Removal of hazardous substances from water using ultrafiltration in conjunction with soluble polymers. *Environmental Science & Technology* **1996,** *30* (3), 725-734.

32. M. Trgo, J. Perić, and N. V. Medvidović, A comparative study of ion exchange kinetics in zinc/lead—modified zeolite-clinoptilolite systems. *Journal of Hazardous Materials* **2006,** *136* (3), 938-945.

33. D. W. Blowes, C. J. Ptacek, S. G. Benner, C. W. T. McRae, T. A. Bennett, and R. W. Puls, Treatment of inorganic contaminants using permeable reactive barriers. *Journal of Contaminant Hydrology* **2000,** *45* (1–2), 123-137.

34. A. W. Apblett, B. P. Kiran, and M. Chehbouni, Molybdenum-Oxide Based Sorbants for Toxic Metals. *Ceramic Transactions* **2006,** *176*, 15-23.

35. C. K. Perkins, K. N. Barber, and A. W. Apblett, Direct conversion of a nanometric suspension of molybdenum trioxide into nanometric lead molybdate. *CrystEngComm* **2014**.

36. R. S. Mann and K. C. Khulbe, ESR study of MoO_3 obtained from the thermal decomposition of ammonium molybdate. *Bulletin of the Chemical Society of Japan* **1975,** *48* (3), 1021-1023.

37. S. Lagergren, Zur theorie der sogenannten adsorption gelöster stoffe. Kungliga Svenska Vetenskapsakademiens. *Handlingar* **1898,** *24* (4), 1-39.

38. S. Azizian, Kinetic models of sorption: a theoretical analysis. *Journal of Colloid and Interface Science* **2004,** *276*, 47–52.

39. K. V. Kumar, Linear and non-linear regression analysis for the sorption kinetics of methylene blue onto activated carbon. *Journal of Hazardous Materials B* **2006,** *137*, 1538-1544.

40. Y. S. Ho and G. McKay, Pseudo-second order model for sorption processes. *Process Biochemistry* **1999,** *34*, 451-465.

41. *The Merck Index: An Encyclopedia of Chemicals, Drugs, and Biologicals*. Wiley: 2006.

42. K. S. Smith, Metal sorption on mineral surfaces: An overview with examples relating to mineral deposits. *Reviews in Economic Geology* **1999,** *6A-B*, 161-182.

43. F. D. Hardcastle and I. E. Wachs, Determination of Molybdenum-Oxygen Bond Distances and Bond Orders by Raman Spectroscopy. *Journal of Raman Spectroscopy* **1990,** *21*, 683-691.

44. B. Windom, W. G. Sawyer, and D. Hahn, A Raman Spectroscopic Study of MoS2 and MoO3: Applications to Tribological Systems. *Tribology Letters* **2011,** *42* (3), 301-310.

CHAPTER IX

SORPTION OF LEAD BY TUNGSTEN TRIOXIDE

Introduction:

The dangers of lead have been discussed in Chapter VIII. The Apblett research group has previously demonstrated the attractiveness of using transition metal oxides as water remediation technologies.[1-7] More specifically, they have shown molybdenum trioxide's ability to react with Pb^{2+} in aqueous systems, with a very high capacity (110% by weight).[6, 8] However, due to molybdenum trioxide's slight solubility in water (addressed in Chapter VIII and Chapter III), it is possible that toxicity issues may make the use of MoO_3 unsuitable for the purification of drinking water. Due to the similarities between molybdenum and tungsten, it was proposed that insoluble tungsten trioxide would be an attractive alternative for an environmentally friendly process for lead mitigation.

Experimental:

All chemicals were ACS reagent grade or higher and were used without further purification. Water was purified by reverse osmosis and then deionized to a resistivity of 18 MΩ. Lead nitrate, $Pb(NO_3)_2$ (Sigma-Aldrich), was used to prepare the lead stock solution with a concentration of approximately 100 mg/L. The concentrations of the stock and treated solutions were determined using a Varian GTA120/AA240Z graphite furnace atomic absorption

spectrometer (GFAAS) equipped with an auto sampler. A 100 mg/L Pb^{2+} standard (BDH ARISTAR) was used to prepare the standard solutions used for analysis. Aliquots of the treated samples were taken at regular time intervals and diluted to the appropriate concentrations with a 1% HNO_3 solution, made using trace metal grade HNO_3 from Mallinckrodt.

Commercially available tungsten trioxide from Alfa-Aesar was used as the bulk reagent for sorption. Tungsten (VI) oxide nanopowder (<100 nm (BET)) was also a commercially available product that was purchased from Aldrich Chemical Company. High surface area Al_2O_3 catalyst supports were obtained from Alfa-Aesar and were used to support WO_3 from the thermal decomposition of impregnated ammonium tungstate ($(NH_4)_6W_{12}O_{39}$), also from Alfa-Aesar. The H_2O_2 and H_2WO_4 used for the synthesis of the mesoporous material were received from Alfa-Aesar and the Brij-56 ($C_{16}H_{33}(OCH_2CH_2)_nOH$, $n \sim 10$) used was received from the Spectrum chemical company.

The Raman spectra of the materials reacted with excess lead were recorded on a Nicolet NXR 9610 Raman spectrometer. The surface areas were measured by N_2 physisorption using a NOVA Quantachrome 1200 BET. Scanning electron micrographs of the solids before and after treatment were recorded using a FEI Quanta 600 field emission gun environmental scanning electron microscope. The X-ray powder diffraction (XRD) patterns of the sorbents at capacity were obtained on a Bruker D8-A25-Advance equipped with a LynxEye detector.

Synthesis of Supported WO_3

The high surface area Al_2O_3 supports were vacuum-impregnated by introducing a 40 weight percent solution of ammonium tungstate to the supports *in vacuo*. The supports were held under vacuum for roughly 24 hours. The support pellets were then rinsed with 50 mL of deionized water, to remove excess material on the surface and following this they were dried *in*

vacuo. Once dry, the pellets were transferred to a ceramic crucible and were calcined at 500 °C for 8 hours in a muffle-furnace.

Synthesis of Mesoporous WO_3

A previously reported method for making thermally stable mesoporous WO_3 thin films was adapted to prepare the mesoporous WO_3 used in this experiment.[9-10] The tungsten oxide precursor, peroxopolytungstic acid, was synthesized through the reaction of H_2WO_4 with hydrogen peroxide. A mass of 5.0 g of H_2WO_4 powder was dispersed in 20.0 g of deionized water, to which 35.0 g of 30% H_2O_2 was added. The reaction mixture was magnetically stirred at 40 ℃ overnight to produce a pale yellow solution. This solution was then dried at 40 ℃ in an oven to produce brightly colored yellow crystals. The original authors reported that 1.0 g of the crystals could be dissolved in a solution of 2.0 g deionized water and 1.0 g ethanol, but this could not be reproduced in this investigation. Therefore, the crystals were dissolved in a solution containing 5.0 g H_2O and 3.0 g of 30% H_2O_2 and 1.0 g of absolute ethanol. In a separate flask, the surfactant solution was prepared by dissolving 0.2 g of Brij-56 in a mixture of 1.5 g absolute ethanol and 2.5 g deionized water. Once the reactants were dissolved, the two flasks were mixed and the solution was allowed to evaporate. When the solvent was fully evaporated, the material was subjected to ethanolic soxhlet extraction to remove the organic surfactant without decreasing the surface area, yielding the mesoporous material. To determine the effect of an auxiliary templating agent, mesitylene was added to the surfactant solution before the solutions were combined. The solid thus produced was treated identically to the non-templated material.

Sorption Studies

The effect of sorbent dosage on reaction kinetics was investigated for each of the WO_3 materials by treating five different 50 mL solutions of 100 ppm Pb^{2+} while varying the amount of excess tungsten trioxide. The samples were agitated by a sample rotator, at a speed of 40 RPM, to eliminate the possibility of forming concentration gradients. Aliquots of each sample were taken

at regular time intervals, diluted with 1% HNO_3 to the appropriate concentration, and then analyzed by GFAAS. The reaction uptake curves were plotted using the sorption capacity at a given time (q_t) vs time (t). The sorption capacity was defined by Equation 1, where C_t is the concentration of analyte in the solution at time t, C_0 is the starting concentration, V is the volume of the analyte, and m is the mass of the sorbent.[11]

$$q_t = \frac{(C_0 - C_t)V}{m}$$

Equation 1: The sorption capacity equation

Molar capacity studies were also performed to determine the maximum uptake of lead by the WO_3 sorbents. Roughly 0.6 g of each of the WO_3 solids was used to treat solutions containing excess Pb^{2+}. Each of the materials were allowed to react with lead for roughly one month and the solutions were analyzed to determine the amount removed. Further, all of the solids were characterized by XRD, Raman spectroscopy, and scanning electron microscopy.

Results and Discussion:

Sorption Kinetics Using Nano-WO_3

The BET surface area of the nano-WO_3 was measured, to be 7.5 m^2 g^{-1}. The sorption uptake curves (Figure 1) depicts the sorption isotherm of lead uptake onto differing amounts of the nano-tungsten trioxide. The uptake curves depicts a process in which sorption is initially very fast and starts to slow as the reaction approaches an equilibrium state around 100 minutes for 0.743 mmol nano-WO_3 and roughly 50 minutes when the highest amount of sorbent is used (2.23 mmol WO_3). The sorption process continued at a slow rate until the concentration of the analyte fell below the instrument detection limit of roughly 0.5 ppb.

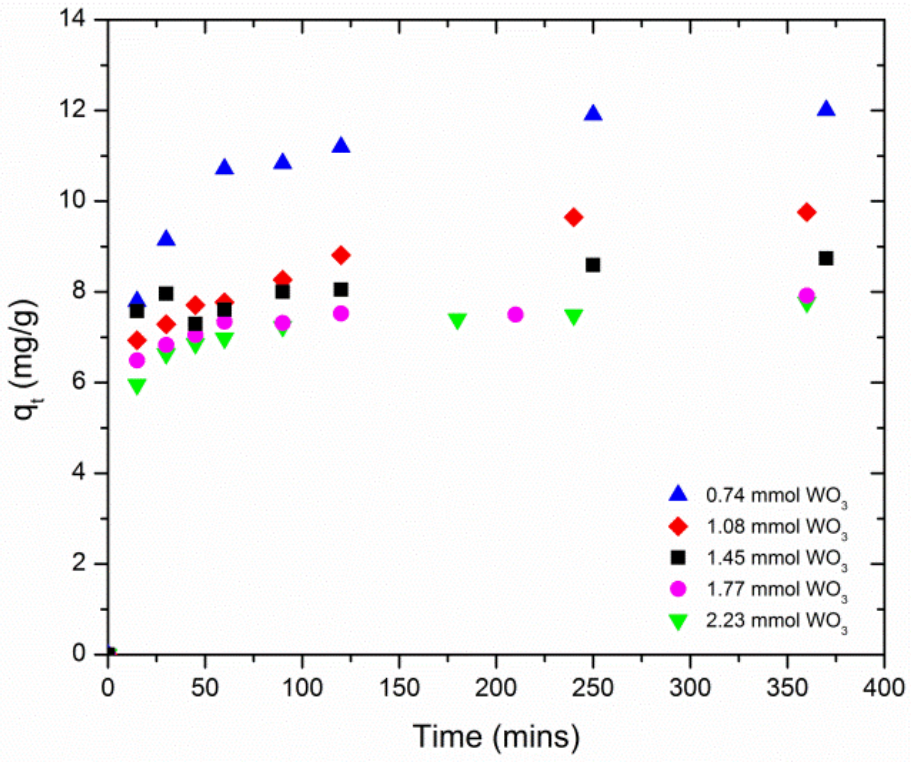

Figure 1: Sorption Uptake Curves of Pb^{2+} on Nano-WO_3

Knowledge of the kinetics for the uptake of target contaminants is integral for determining the optimum operating conditions for full-scale batch processes. The kinetic sorption rate of lead by nanometric tungsten oxide is important for determining its effectiveness as a possible sorbent to be incorporated in commercial applications. The kinetics of the sorption processes were analyzed using both pseudo first-order and second-order models commonly used to model sorption processes.

Equation 2 shows the pseudo first-order rate expression described by Lagergren, where q_t is the amount of the analyte sorbed at time t, k_1 is the rate constant of the pseudo first-order sorption process, and q_e is the amount of analyte sorbed at equilibrium.[12]

$$q_t = q_e(1 - e^{-k_1 t})$$

Equation 2: The Nonlinear Pseudo First-Order Equation

By taking the natural log of Equation 2, the values of k_1 and q_e can be determined from the linear pseudo first order plot using Equation 3. The linear plot of $\ln(q_e-q_t)$ vs. time gives the values of k_1 and q_e from the slope and intercept, respectively. Figure 3 shows that the linear pseudo first-order kinetic model for the nano-WO_3 does not apply throughout the various sorbent loadings. As the sorbent mass was increased, the data exhibits a large deviation from linearity, as evident from the correlation coefficient (R^2) values listed in Table 1. Furthermore, the estimated values of q_e calculated from the equation differ substantially from those measured experimentally, owing to the fact this sorption process cannot be satisfactorily described by the linear pseudo first-order model. The discrepancy is most likely due to the similar concentrations of lead ions and the reaction sites on the sorbent.[13]

$$\ln(q_e - q_t) = \ln(q_e) - k_1 t$$

Equation 3: The Linearized Formula for Pseudo First-Order Kinetics

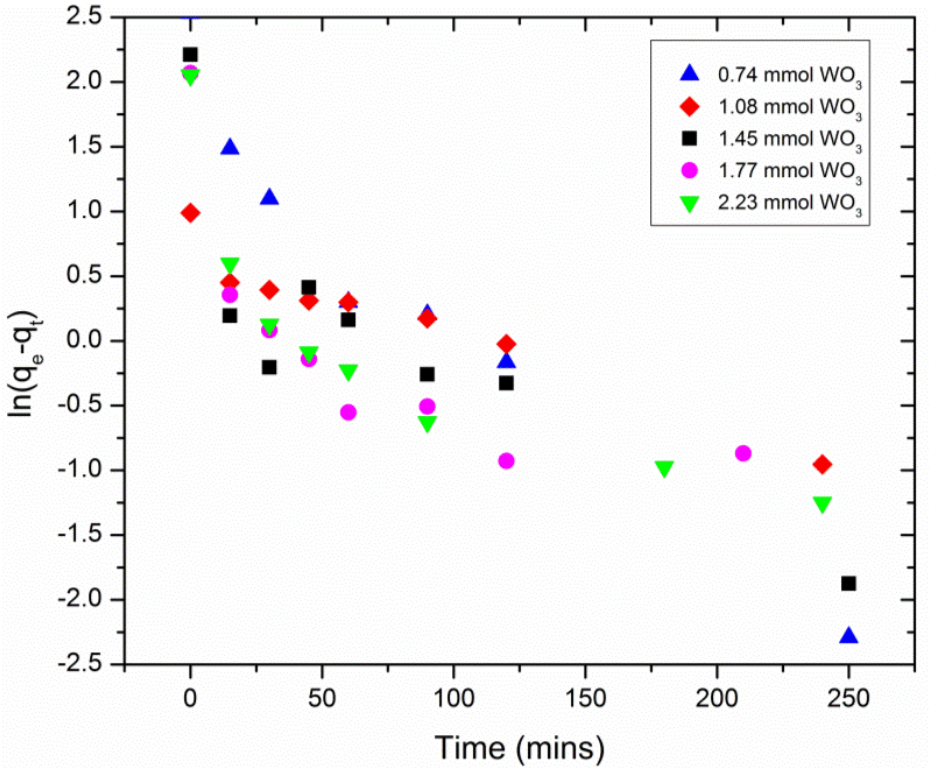

Figure 2: Linear Pseudo First-Order Plot for the Uptake of Pb^{2+} By Nano-WO_3 Uptake

Table 1: Data and Results for the Linear Pseudo First-Order Uptake of Pb^{2+} by Nano-WO_3

WO_3 (mmol)	k_1 (min^{-1})	q_e (mg/g)	q_e (mg/g) (experimental)	R^2
0.743	1.70E-02	6.26	12.6	0.939
1.08	1.59E-02	5.27	9.76	0.936
1.45	8.80E-03	2.54	9.13	0.703
1.77	1.03E-02	1.96	7.92	0.525
2.23	1.00E-02	2.17	7.77	0.671

It has been shown that modeling sorption processes using the nonlinear pseudo first-order model was much more appropriate for modeling the sorption of methylene blue on activated carbon using the nonlinear pseudo first-order equation (Equation 2). [14] Figure 3 shows the plotted uptake curves fitted with the nonlinear pseudo first-order equation, which depicts the model underestimating q_e in all cases. However, Table 2 shows the correlation coefficients for the

nonlinear method are much higher than the linear model and the q_e values are relatively close, suggesting that this method is far superior to the linearized model for this process.

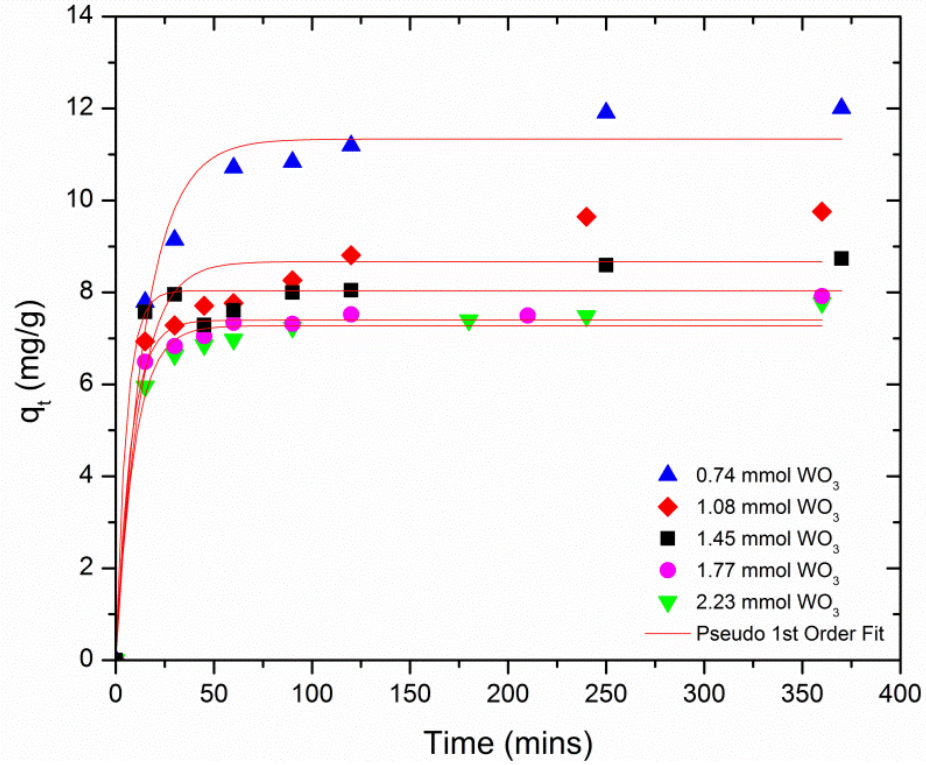

Figure 3: Nonlinear Pseudo First-Order Curves for the Uptake of Pb^{2+} by Nano-WO_3

Table 2: Data and Results for the Nonlinear Pseudo First-Order Uptake of Pb^{2+} by Nano-WO_3

WO_3 (mmol)	k_1 (min^{-1})	q_e (mg/g)	q_e (mg/g) (experimental)	R^2
0.743	6.71E-02	11.3	12.6	0.979
1.08	8.59E-02	8.67	9.76	0.923
1.45	1.88E-01	8.04	9.13	0.970
1.77	1.30E-01	7.40	7.92	0.986
2.23	1.05E-01	7.27	7.77	0.984

Ho and McKay proposed a pseudo-second order kinetic model represented by Equation 4. In this equation, k_2 is the rate constant of the pseudo second-order sorption process, with the units g mg^{-1} min^{-1}. [15] Equation 4 can be further simplified to Equation 3, by substituting h in place

of $k_2 q_e^2$, where h can be considered as the initial sorption rate, as t/q_t approaches 0. The slope and the intercept of the plot of t/q_t versus t give the values of the constants q_e and h, respectively.[13] Using the value of q_e (the slope) and h (the intercept), the rate constant (k_2) can be obtained.

$$\frac{t}{q_t} = \frac{1}{k_2 q_e^2} + \frac{1}{q_e} t$$

Equation 4: The Linearized Pseudo Second-Order Rate Equation

$$\frac{t}{q_t} = \frac{1}{h} + \frac{1}{q_e} t$$

Equation 5: The linearized Initial Rate Pseudo Second-Order Equation

Figure 4 shows the linear pseudo second-order plot for the sorption of lead using nanometric tungsten trioxide. The results show all of the samples fit the linear pseudo second-order model much better than that of the linear pseudo first-order model. The linear regression correlation coefficient (R^2) values for this model are very high (R^2>0.99) and the calculated q_e values are in very close agreement with the experimental data, while only slightly overestimating the values throughout the series. However, the pseudo second-order rate constant (k_2) does not display a correlation with respect to the differing amounts of solid used nor does the initial sorption rate (h). While the linear pseudo second-order model fits the present data very well, there is little physical significance that can be extrapolated from the kinetic results due to the dependence of the rate constant on both the concentrations of the sorbent and analyte.

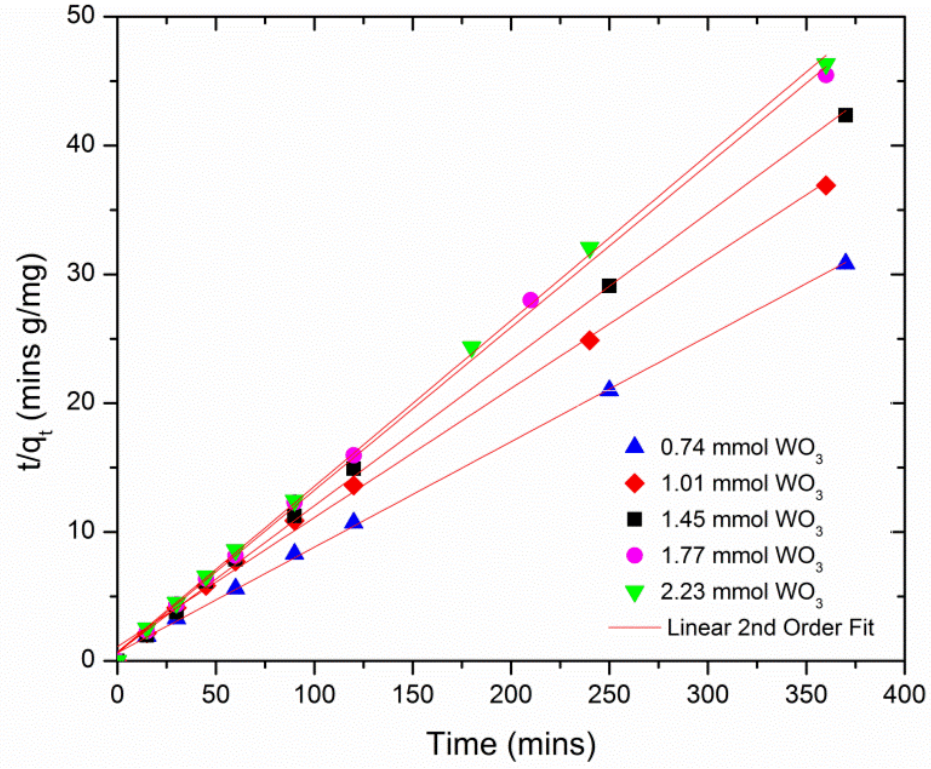

Figure 4: Linear Pseudo Second-Order Curves for the Uptake of Pb^{2+} by Nano-WO_3

Table 3: Data and Results for the Linear Pseudo Second-Order Uptake of Pb^{2+} by Nano-WO_3

WO_3 (mmol)	k_2 (g/mg min)	h (mg/g min)	q_e (mg/g)	q_e (mg/g) (experimental)	R^2
0.743	1.20E-02	1.95	12.8	12.6	0.999
1.08	1.11E-02	1.10	9.98	9.76	0.998
1.45	1.83E-02	1.55	9.20	9.13	0.999
1.77	3.17E-02	1.99	7.91	7.92	0.999
2.23	2.42E-02	1.46	7.78	7.77	0.999

The nonlinear pseudo second-order equation (Equation 6) was also used to effectively model the sorption process of methylene blue on activated carbon.[14] Figure 5 shows the experimental data fit the nonlinear pseudo second-order model with relatively good accuracy. Table 4 shows the correlation coefficients for the nonlinear method are very high (R^2>0.97), similar to the linear model, suggesting that this method is also appropriate for modeling this

process. As was the case for the linear pseudo second order model, the kinetic parameters appear to have little physical meaning. The equilibrium concentration values from the model are lower than the experimental values and have larger deviations than the values predicted by the linear pseudo second-order model. From the data presented, it suggests that the linear pseudo second-order model is the best-suited model for the sorption of Pb^{2+} on the nanometric-WO_3.

$$q_t = \frac{k_2 q_e^2 t}{1 + k_2 q_e t}$$

Equation 6: The Nonlinear Pseudo Second-Order Equation

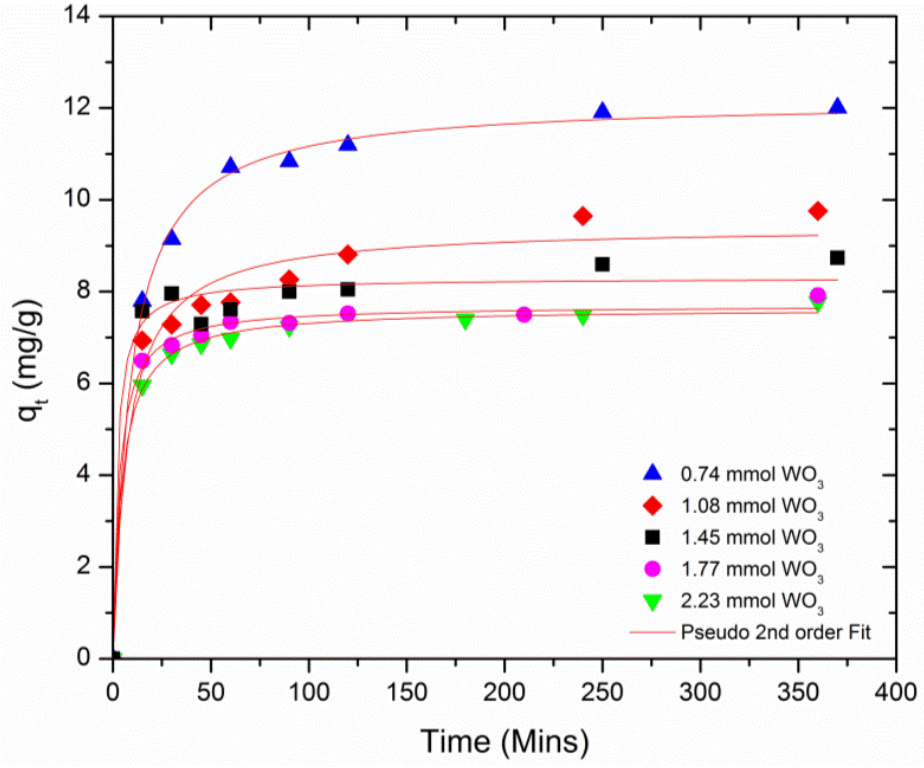

Figure 5: Nonlinear Pseudo Second-Order Curves for the Uptake of Pb^{2+} by Nano-WO_3

Table 4: Data and Results for the Nonlinear Pseudo Second-Order Uptake of Pb^{2+} by Nano-WO_3

WO_3 (mmol)	k_2 (g/mg min)	h (mg/g min)	q_e (mg/g)	q_e (mg/g) (experimental)	R^2
0.743	9.12E-03	1.35	12.2	12.6	0.998
1.08	1.41E-02	1.25	9.42	10.6	0.991
1.45	5.96E-02	4.10	8.30	9.13	0.979
1.77	4.06E-02	2.41	7.70	7.92	0.996
2.23	2.89E-02	1.69	7.64	7.77	0.998

Sorption Kinetics using Bulk-WO_3

The sorption uptake curves for the bulk-WO_3 are presented in Figure 6. The sorption curves depict a very poor sorption process in which the majority of the uptake of Pb^{2+} occurred within the first 15 minutes. Furthermore, the sorption capacities of the bulk materials were very low. The low affinity for sorption is likely due to the low surface area of the bulk-WO_3 of 1.0 m^2 g^{-1}.

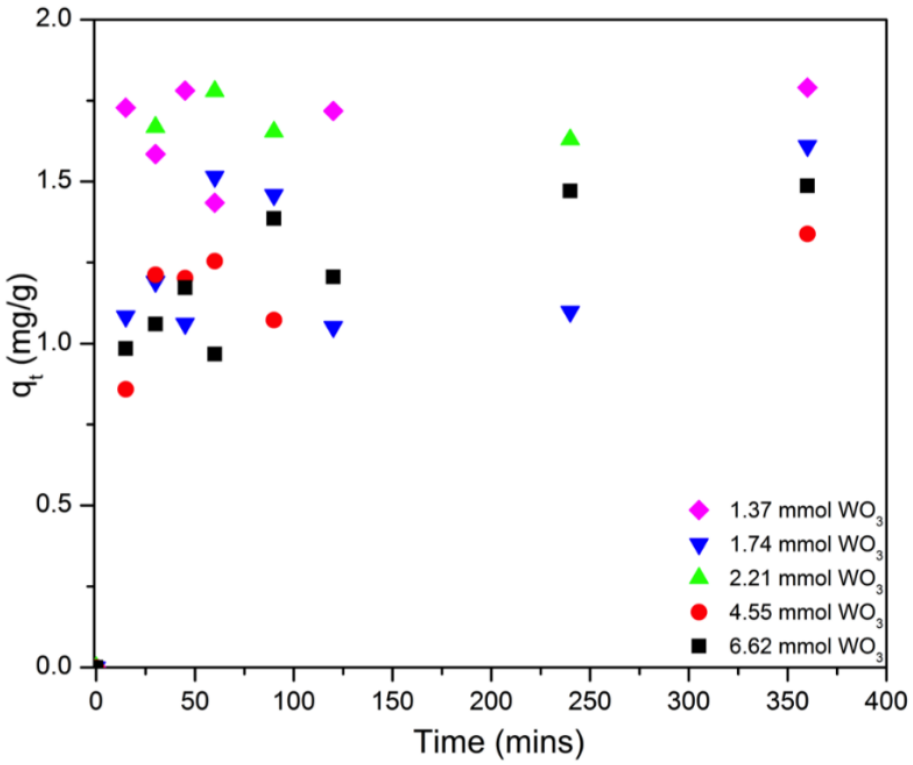

Figure 6: Sorption Uptake Curves for Pb^{2+} with Bulk-WO_3

Similar to the nano-WO_3, the linear pseudo first-order model did not fit the data from the bulk-WO_3 uptake. In fact, the linear correlation coefficients were zero in most cases, thus the linear pseudo first-order plot and data are not presented herein. However, the nonlinear pseudo first-order model was able to be used to model the sorption (Figure 6), albeit with poor correlation coefficients for two of the sorbent loadings (the 1.37 and 2.21 mmol treatments). This is most likely due to the low affinity of the material to sorb lead. Further, the large deviations from the fit are likely due to the low q_t values.

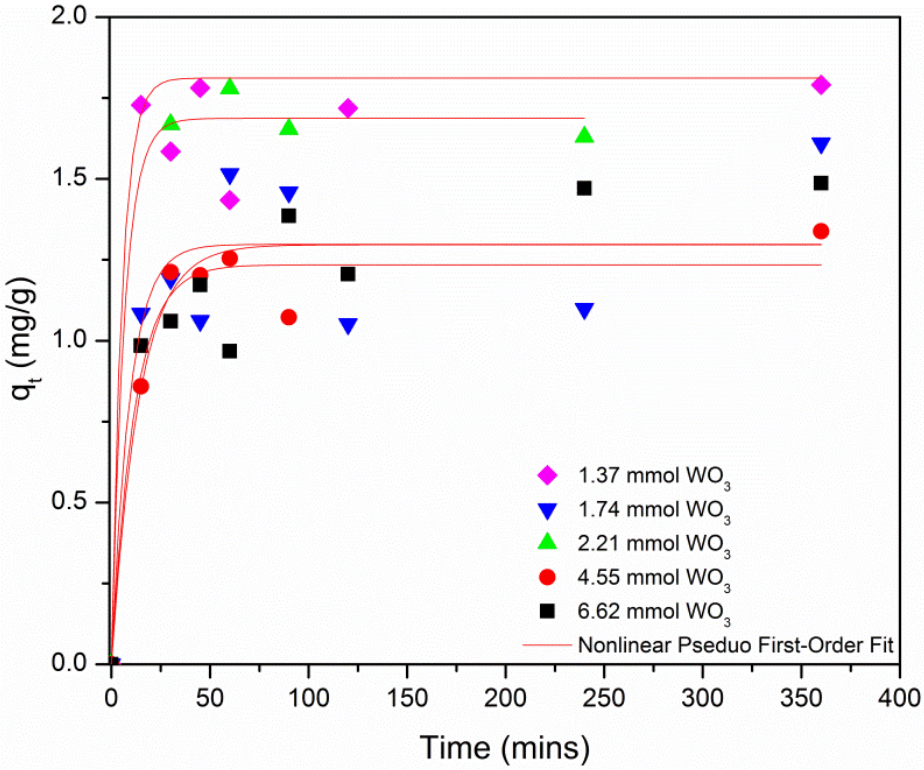

Figure 7: Nonlinear Pseudo First-Order Fit of the Uptake Curves of Pb^{2+} by Bulk-WO_3

Table 5: Data and Results for the Nonlinear Pseudo First-Order Uptake of Pb^{2+} by Bulk-WO_3

WO_3 (mmol)	k_1 (min^{-1})	q_e (mg/g)	q_e (mg/g) (experimental)	R^2
1.37	6.71E-02	1.81	1.79	0.765
1.74	8.59E-02	1.69	1.61	0.992
2.21	1.88E-01	1.30	1.54	0.789
4.55	1.30E-01	1.23	1.34	0.959
6.62	1.05E-01	1.29	1.49	0.852

Figure 8 shows the bulk material also had a similar fit for the nonlinear pseudo second-order model, with low correlation coefficients in most cases (Table 6). Moreover, the 2.21 mmol samples uptake was unable to be modeled by the function as the fit failed to converge. Again this is likely due to the materials low affinity for Pb^{2+}, thus this model should not be used to model this sorption process.

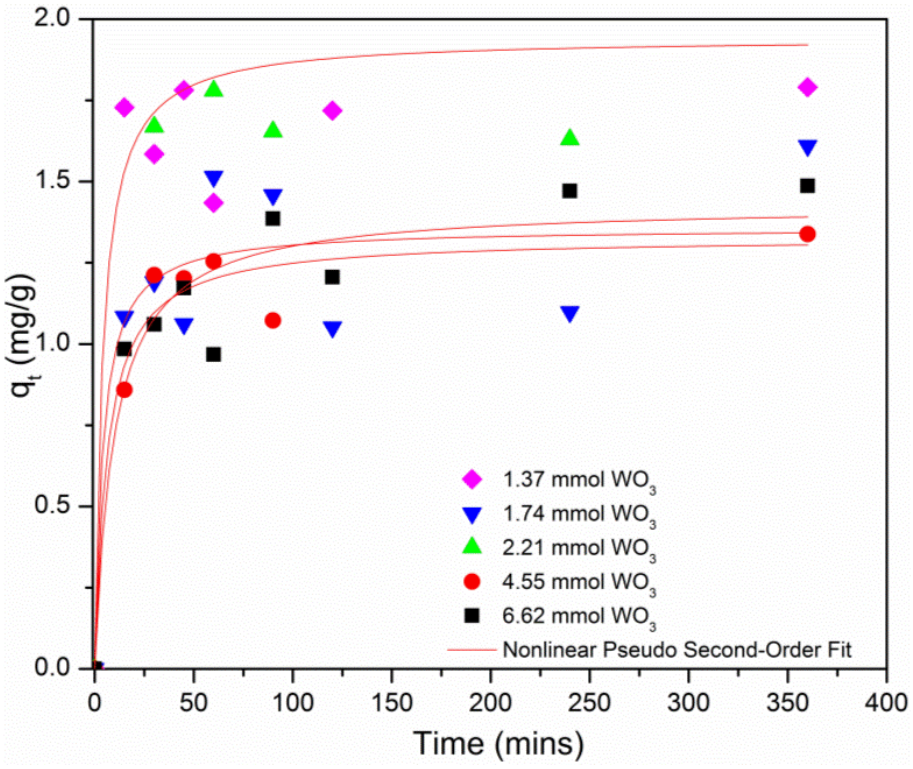

Figure 8: Nonlinear Pseudo Second-Order Fit of the Uptake of Pb^{2+} by Bulk-WO_3

Table 6: Data and Results for the Nonlinear Pseudo Second-Order Uptake of Pb^{2+} by Bulk-WO_3

WO_3 (mmol)	k_2 (g/mg min)	h (mg/g min)	q_e (mg/g)	q_e (mg/g) (experimental)	R^2
1.37	1.28E-01	0.484	1.94	1.79	0.793
1.74	1.82E-01	0.335	1.36	1.61	0.798
2.21	***Did not converge***			1.54	N/A
4.55	1.19E-01	0.210	1.33	1.34	0.951
6.62	7.17E-02	0.146	1.43	1.49	0.913

Lastly, the bulk-WO_3 was modeled using the linear pseudo second-order model (Figure 9) with relatively good fits in every case (Table 7). The slopes from Figure 9 are proportional to the inverse of the equilibrium capacity, q_e^{-1}, thus it was expected the highest mass loading (6.62 mmol) would have the highest slope. However, this result does not match what was observed experimentally, which is also likely due to the low affinity for the analyte.

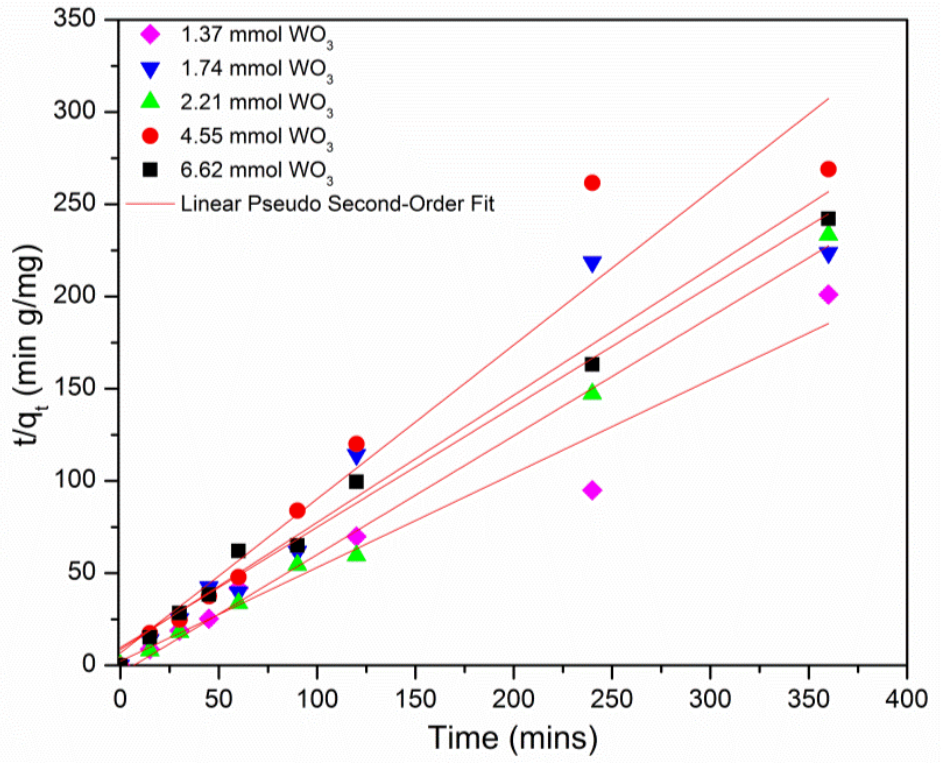

Figure 9: Linear Pseudo Second-Order Curve for the Uptake of Pb^{2+} by Bulk-WO_3

Table 7: Data and Results for the Linear Pseudo Second-Order Uptake of Pb^{2+} by Bulk-WO_3

WO_3 (mmol)	k_2 (g/mg min)	h (mg/g min)	q_e (mg/g)	q_e (mg/g) (experimental)	R^2
1.37	1.13E-01	0.437	1.97	1.79	0.953
1.74	9.53E-02	0.230	1.55	1.61	0.993
2.21	5.54E-02	0.117	1.45	1.54	0.923
4.55	1.03E-01	0.148	1.20	1.34	0.934
6.62	4.44E-02	0.104	1.53	1.49	0.960

Sorption Kinetics for Mesoporous-WO_3

The surface area of the mesoporous-WO_3 was vastly improved compared to the two commercially available products, to a value of 115 m^2 g^{-1}. By using the auxiliary templating agent, the surface area was improved to a value of 135 m^2 g^{-1}, although it was not used in this study. The sorption uptake curves (Figure 10) depicts an extremely fast sorption process in which the majority of the Pb^{2+} was removed within the first 15 minutes. For the highest loading, 0.260 mmol, the sorption capacity was reached in roughly 10 minutes, where the lowest mass loading, 0.093 mmol, reached equilibrium somewhere between 50 and 125 minutes. The sorption capacities of the mesoporous materials were also very high, highlighting the material's high affinity for the analyte. Due to the high affinity for Pb^{2+}, the reactions were performed with only a small molar excess of WO_3 to Pb^{2+} (from 3 to 10 times) whereas the nano-WO_3 experiments used an excess range from 30-100 and the bulk-WO_3 experiments had an excess of 70-270 times. Furthermore, the sorption process was able to remove the concentration of Pb^{2+} from these solutions to below the instrumental detection limit of 0.5 ppb.

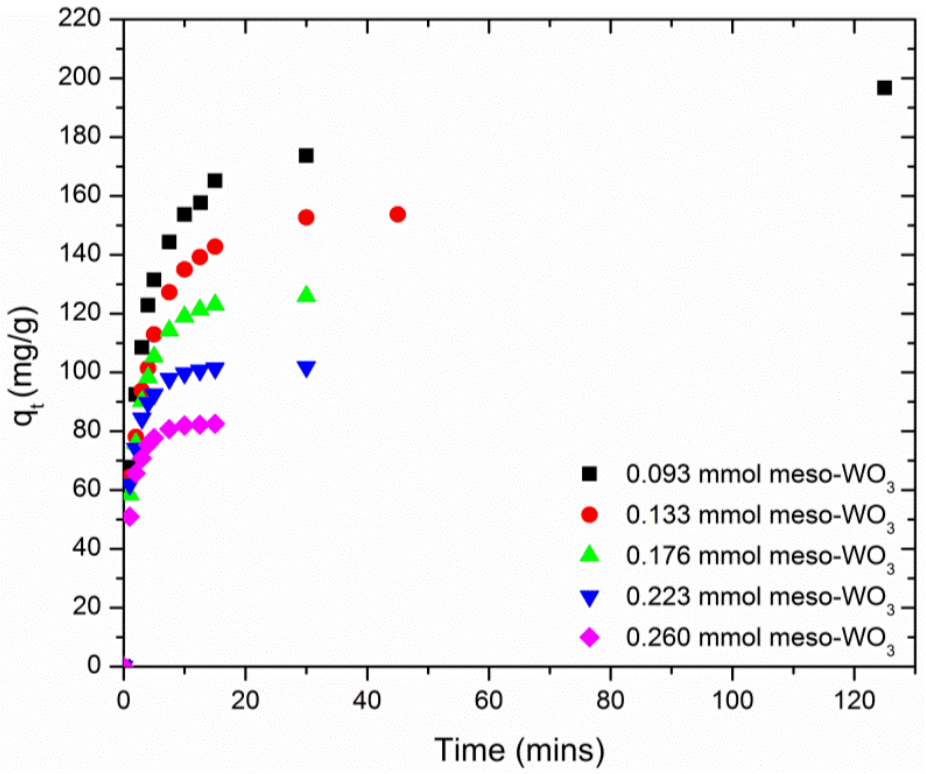

Figure 10: Uptake Curves for Mesoporous-WO_3 Sorption of Pb^{2+}

The results from the linear pseudo first-order model were better for the larger mass loadings. Figure 11 shows an obvious deviation from linearity for the lowest mass loading, corresponding to a lower correlation coefficient (R^2) summarized in Table 8. The experimental values of the equilibrium capacities were twice that of the predicted values from this model, suggesting it is not appropriate for modeling this process.

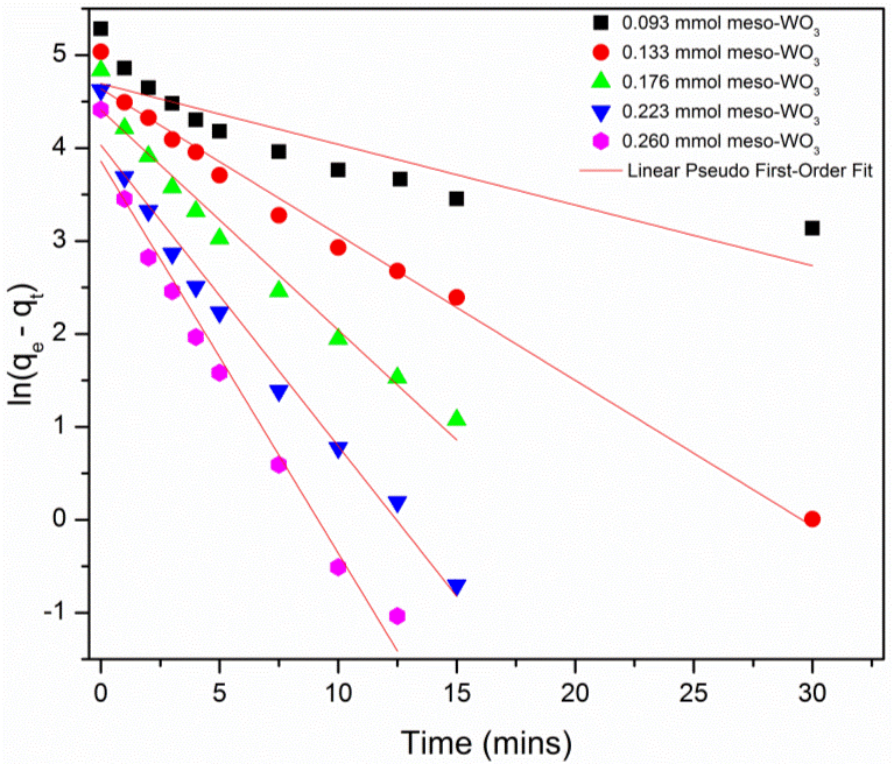

Figure 11: Linear Pseudo First-Order Fits for the Uptake of Pb^{2+} by Mesoporous-WO_3

Table 8: Data and Results for the Linear Pseudo First-Order Fit Uptake of Pb^{2+} by Mesoporous-WO_3

WO_3 (mmol)	k_1 (min^{-1})	q_e (mg/g)	q_e (mg/g) (experimental)	R^2
0.0927	6.53E-02	109	197	0.765
0.133	1.57E-01	103	154	0.985
0.180	2.37E-01	81.8	126	0.971
0.222	3.24E-01	56.3	102	0.974
0.267	4.22E-01	47.3	82.6	0.973

The nonlinear method, however, gave much more accurate results for the predicted q_e values, along with higher R^2 values (Table 9). Figure 12 shows the sorption uptake curves with the nonlinear pseudo first-order fits for each mass loading. From this, it is obvious that the nonlinear pseudo first-order method is much more appropriate for modeling this process. Notice,

however, the function underestimates the sorption capacity in every case, although only slightly for the higher sorbent loadings.

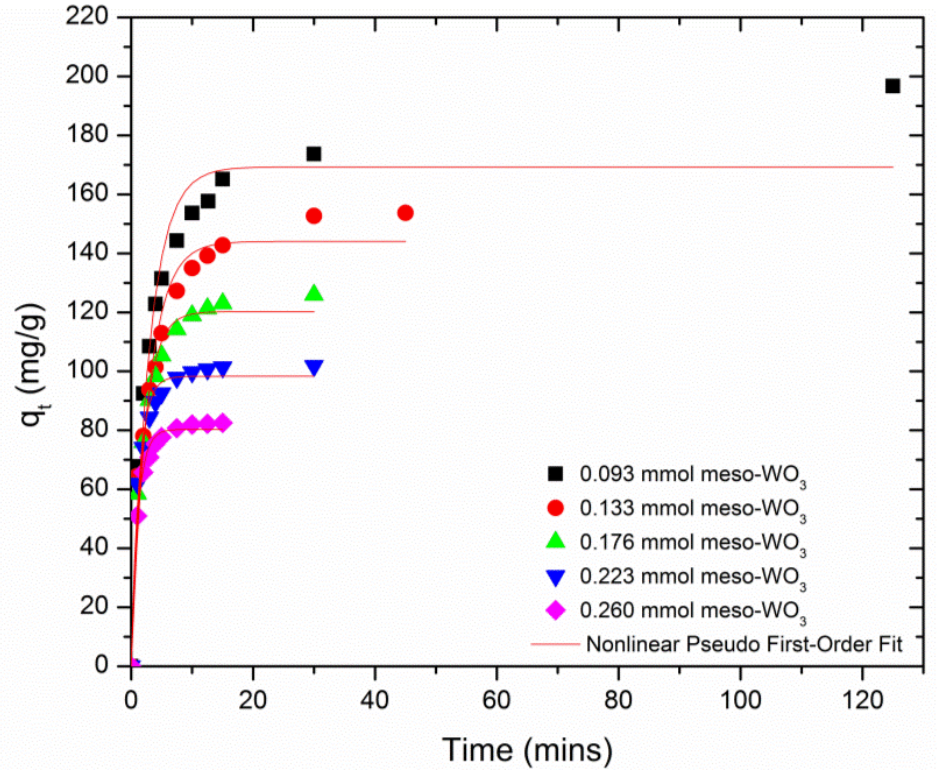

Figure 12: Nonlinear Pseudo First-Order Curves for the Uptake of Pb^{2+} by Mesoporous-WO_3

Table 9: Data and Results for the Nonlinear Pseudo First-Order Fit Uptake of Pb^{2+} by Mesoporous-WO_3

WO_3 (mmol)	k_1 (min^{-1})	q_e (mg/g)	q_e (mg/g) (experimental)	R^2
0.0927	3.42E-01	169	197	0.944
0.133	3.56E-01	144	154	0.958
0.180	4.94E-01	120	126	0.980
0.222	7.81E-01	98.3	102	0.979
0.267	8.89E-01	80.3	82.6	0.990

The sorption modeling using the pseudo second-order function, Figure 13, shows good fits throughout all the mass loadings, even for the lowest mass loading. Table 10 shows that the observed q_e values for this process are consistent with the predicted values from the function. Further, the R^2 values for this model all very high (R^2>0.99) suggesting this may be the best method for modeling this sorption process.

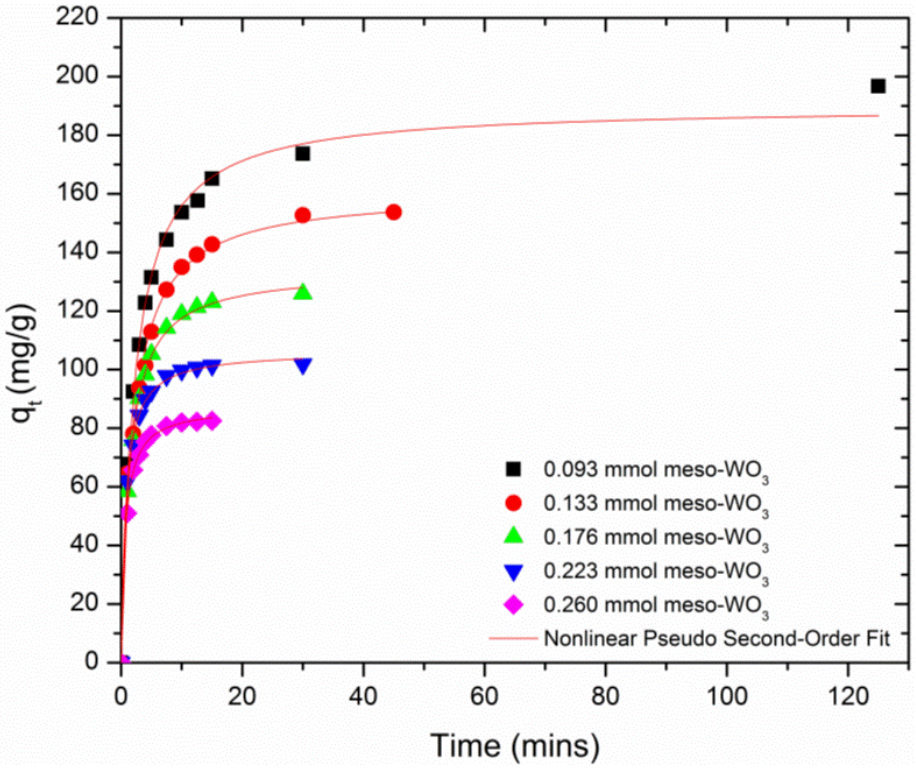

Figure 13: Nonlinear Pseudo Second-Order Curves for the Uptake of Pb^{2+} by Mesoporous-WO_3

Table 10: Data and Results for the Nonlinear Pseudo Second-Order Fit Uptake of Pb^{2+} by Mesoporous-WO_3

WO_3 (mmol)	k_2 (g/mg min)	h (mg/g min)	q_e (mg/g)	q_e (mg/g) (experimental)	R^2
0.0927	1.96E-03	78.2	200	197	1.00
0.133	2.45E-03	62.3	159	154	0.999
0.180	7.43E-03	126	130	126	0.999
0.222	1.85E-02	200	104	102	1.00
0.267	2.61E-02	189	85.0	82.6	0.999

Finally, the sorption process was modeled using the linear pseudo second-order model (Figure 14). The data from this model (Table 11) has almost perfect correlation coefficients and q_e values that are very close to the observed values, only slightly overestimating the values in each case.

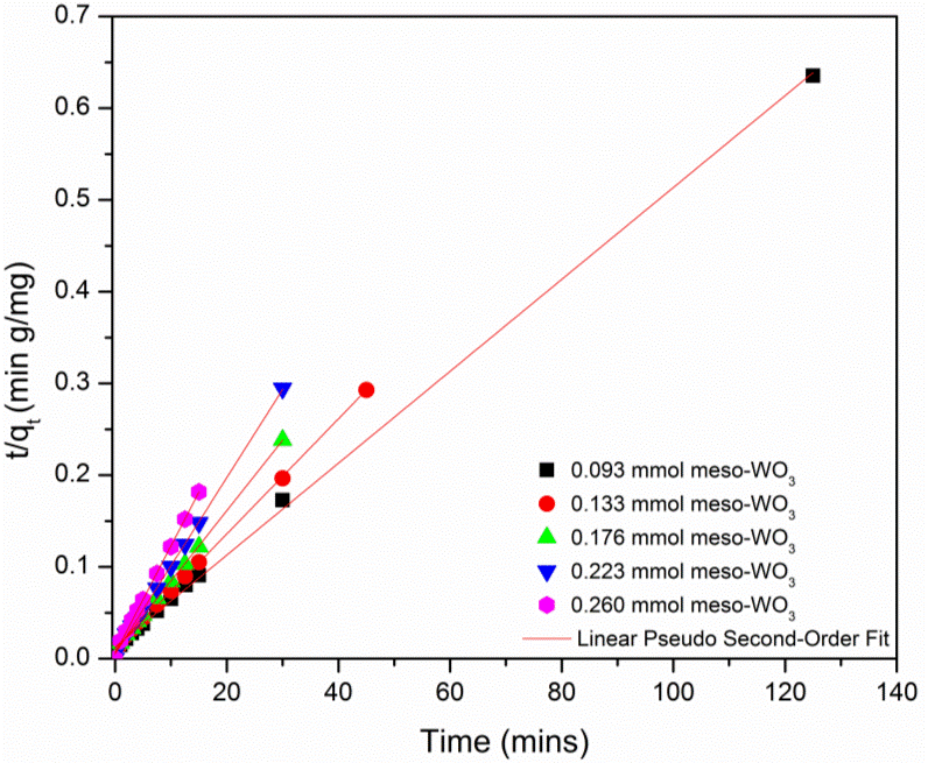

Figure 14: Linear Pseudo Second-Order Fit for the Uptake of Pb^{2+} by Mesoporous-WO_3

Table 11: Data and Results for the Linear Pseudo Second-Order Fit Uptake of Pb^{2+} by Mesoporous-WO_3

WO_3 (mmol)	k_2 (g/mg min)	h (mg/g min)	q_e (mg/g)	q_e (mg/g) (experimental)	R^2
0.0927	2.42E-03	87.25	190	197	0.993
0.133	3.12E-03	80.60	161	154	0.991
0.180	5.32E-03	95.59	134	126	0.998
0.222	1.23E-02	139.5	106	102	0.998
0.267	1.67E-02	127.8	87.4	82.6	0.999

Sorption Kinetics for the Al_2O_3 Supported-WO_3

By supporting the WO_3 on the high surface area Al_2O_3 substrate, the surface area was improved to 176 m^2 g^{-1}. The impregnation method produced a product containing 9.20% WO_3 by weight on the Al_2O_3 support. The sorption uptake curves (Figure 15) depicts the sorption process where the q_e was reached at roughly 120 minutes for the larger loadings and around 240 minutes for the smaller mass loadings. The equilibrium sorption capacities were higher than every material but the mesoporous-WO_3, although, the molar sorbent loadings were the same as that of the nano-WO_3. However, the advantage of using the supported-WO_3 as opposed to the powder materials is the ease of use in columns or in batch experiments without the need of filtration.

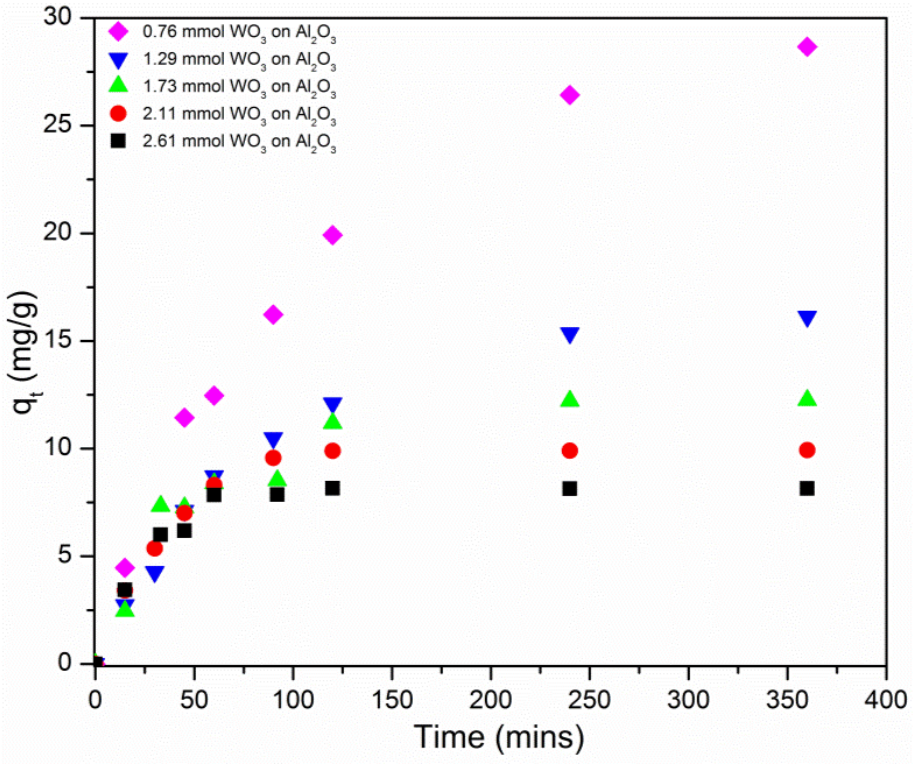

Figure 15: Uptake Curves for the Sorption of Pb^{2+} with Al_2O_3 Supported-WO_3

Interestingly, Figure 16 shows that the linear pseudo first-order equation gave good correlations to the data for 4 out of 5 of the sorbent loadings. Further, the model gave good q_e predictions for the lower mass loadings, but as the mass loadings increased the deviation increased (Table 12). This was not observed with any other material. Even though the model works well for the lower loadings, it is not sufficient for modeling the sorption process throughout all of the mass loadings.

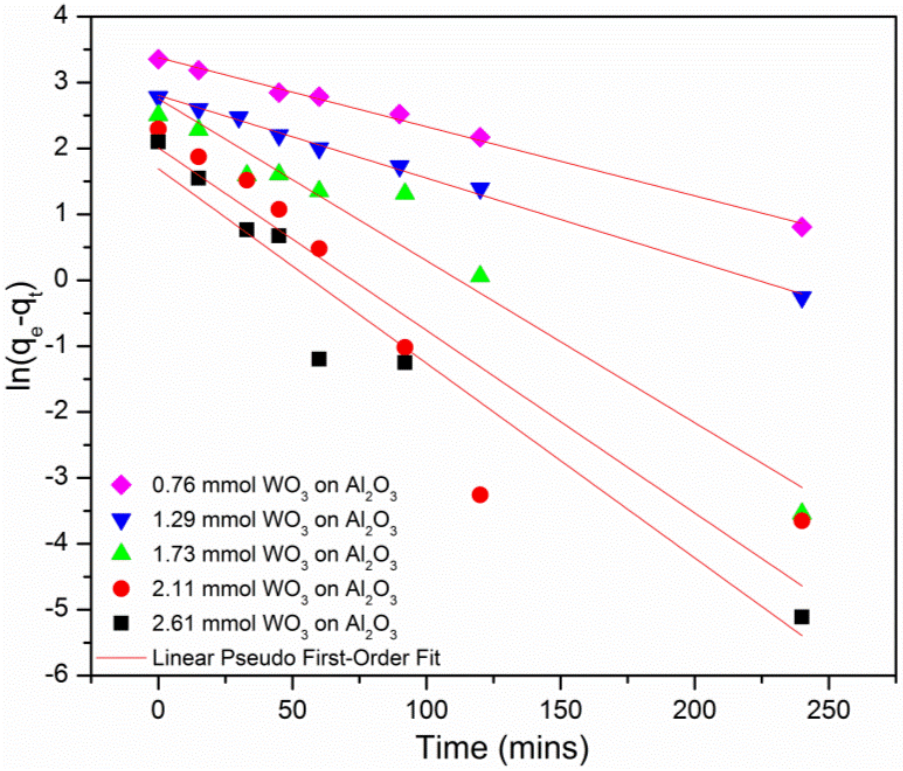

Figure 16: Linear Pseudo First-Order Fit for the Al_2O_3 Supported-WO_3 Uptake of Pb^{2+}

Table 12: Data and Results for the Linear Pseudo First-Order Fit of the Uptake of Pb^{2+} by WO_3 on Al_2O_3

WO_3 (mmol)	k_1 (min^{-1})	q_e (mg/g)	q_e (mg/g) (experimental)	R^2
0.756	1.05E-02	28.2	28.7	0.995
1.29	1.26E-02	16.5	16.1	0.996
1.73	2.46E-02	15.7	12.2	0.951
2.11	2.78E-02	7.46	9.93	0.831
2.61	2.95E-02	5.43	8.15	0.942

Figure 17 shows the sorption uptake curve fit with the nonlinear pseudo first-order model with very good accuracy. The model fits the data with very high R^2 values and q_e values that are very close the experimental values, summarized in Table 13.

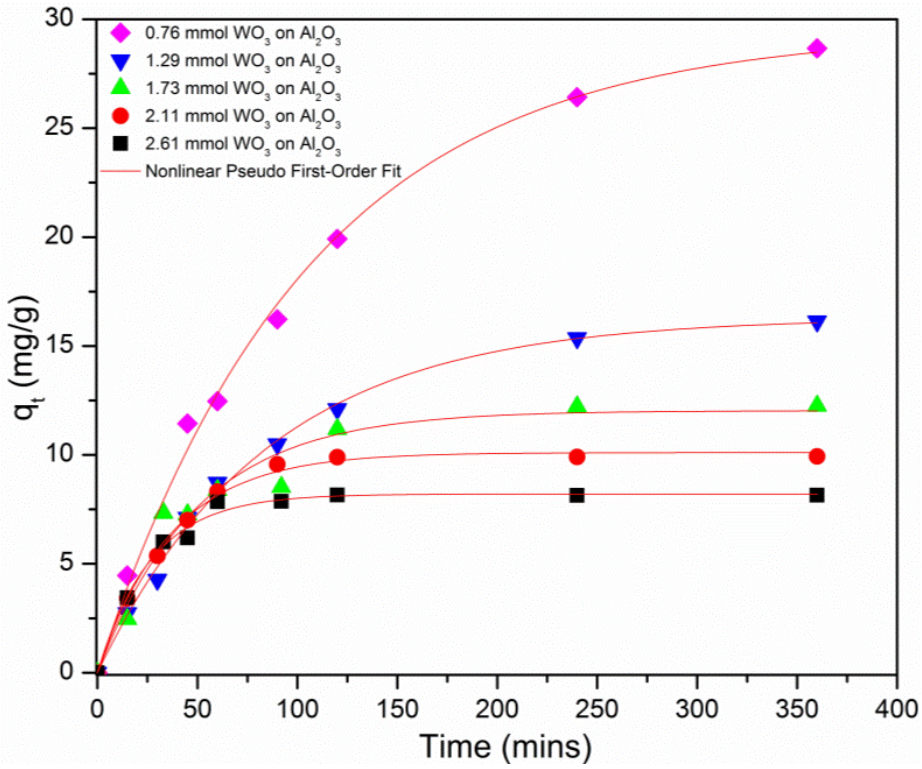

Figure 17: Nonlinear Pseudo First-Order Fit for the Al_2O_3 Supported-WO_3 Uptake of Pb^{2+}

Table 13: Data and Results for the Nonlinear Pseudo First-Order Fit of the Uptake of Pb^{2+} by WO_3 on Al_2O_3

WO_3 (mmol)	k_1 (min^{-1})	q_e (mg/g)	q_e (mg/g) (experimental)	R^2
0.756	9.51E-03	29.4	28.7	0.996
1.29	1.18E-02	16.3	16.1	0.996
1.73	2.00E-02	12.0	12.2	0.956
2.11	2.73E-02	10.1	9.93	0.996
2.61	3.74E-02	8.20	8.15	0.990

The nonlinear pseudo second-order equation fits the sorption data with very good accuracy as well. Figure 18 illustrates the fit of the function with very good correlation coefficients, as summarized in Table 14. However, the model actually overestimates the data in every case and by 30% in the case of the 0.76 mmol loading, thus the model does not satisfactorily describe the process as a whole.

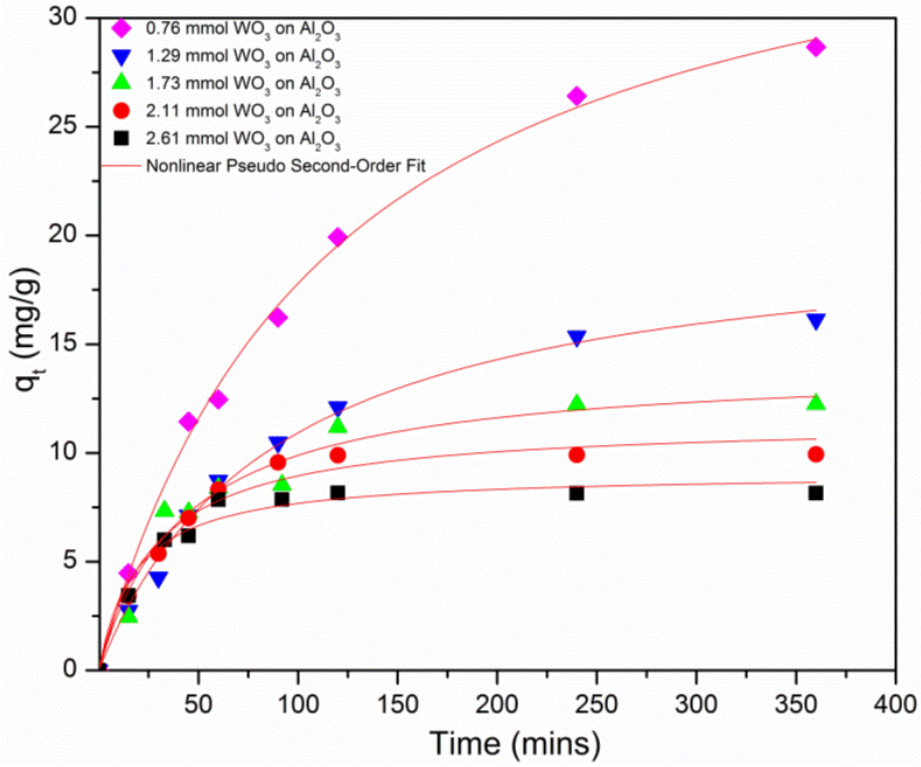

Figure 18: Nonlinear Pseudo Second-Order Fit for the Al_2O_3 Supported-WO_3 Uptake of Pb^{2+}

Table 14: Data and Results for the Nonlinear Pseudo First-Order Fit of the Uptake of Pb^{2+} by WO_3 on Al_2O_3

WO_3 (mmol)	k_2 (g/mg min)	h (mg/g min)	q_e (mg/g)	q_e (mg/g) (experimental)	R^2
0.756	2.26E-04	0.332	38.4	28.7	0.997
1.29	5.44E-04	0.232	20.7	16.1	0.993
1.73	1.67E-03	0.332	14.1	12.2	0.960
2.11	3.09E-03	0.407	11.5	9.93	0.970
2.61	6.03E-03	0.498	9.08	8.15	0.967

The linear pseudo second-order model depicted in Figure 19 also overestimates the q_e values throughout the mass loadings, similar to the nonlinear method; although the overestimations are not as drastic as the nonlinear method. Furthermore, the R^2 values are fairly

good throughout the mass loadings and get better as the sorbent loadings increase, as summarized in Table 15.

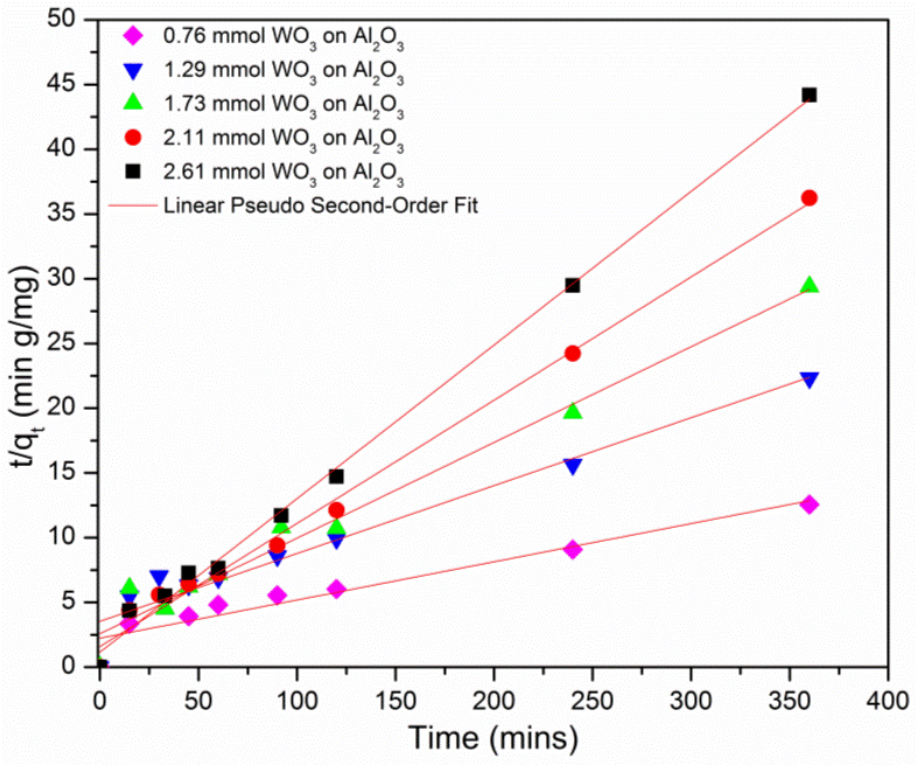

Figure 19: Linear Pseudo Second-Order Fit for the Al_2O_3 Supported-WO_3 Uptake of Pb^{2+}

Table 15: Data and Results for the Nonlinear Pseudo First-Order Fit of the Uptake of Pb^{2+} by WO_3 on Al_2O_3

WO_3 (mmol)	k_2 (g/mg min)	h (mg/g min)	q_e (mg/g)	q_e (mg/g) (experimental)	R^2
0.756	3.90E-04	0.448	33.9	28.7	0.920
1.29	7.75E-04	0.282	19.1	16.1	0.937
1.73	2.12E-03	0.388	13.5	12.2	0.972
2.11	5.71E-03	0.631	10.5	9.93	0.992
2.61	1.22E-02	0.867	8.43	8.15	0.998

Summary of Sorption Kinetics

From the presented data it is determined that the linear pseudo first-order model is not appropriate for modeling any of the sorption processes. Unfortunately the rate constants from the

pseudo second-order models do not have a clear physical meaning and are dependent on both the mass of the sorbent and the amount of analyte in the system. Due to the lack of physical meaning, it is practically impossible to compare the kinetic data from each of the materials using the pseudo second-order models. Furthermore, there has been concern about whether the linearity of the linear pseudo-order model is forced due to spurious correlations.[16]

The rate constants from the nonlinear first-order model, however, have a clear physical significance, allowing the different methods to be compared. To compare the effectiveness of each of the sorbents, the first-order half-lives are shown in Figure 20. Typically sorbent loadings under similar conditions are compared, which is done for the nano-WO_3 and supported-WO_3. Due to the rate at which of the mesoporous-WO_3 reacts with Pb^{2+}, the largest sorbent loading was only 0.267 mmol, thus this material could not be compared under the same conditions, however, this mass loading was plotted with the other two mass loadings of roughly three-times the amount. Furthermore, because of the extreme excess that the bulk-WO_3 needed to remove Pb^{2+} coupled with the fact that the sorption process did not seem to fit any model, the bulk material was not compared. The half-life of the supported material is largest, although this may be due to slow diffusion of the solution into the porous material. The mesoporous-WO_3 had the shortest half-life of all of the materials even though it was only roughly one-third of the mass loading of the other two samples, highlighting the very high reactivity of the mesoporous material for Pb^{2+}.

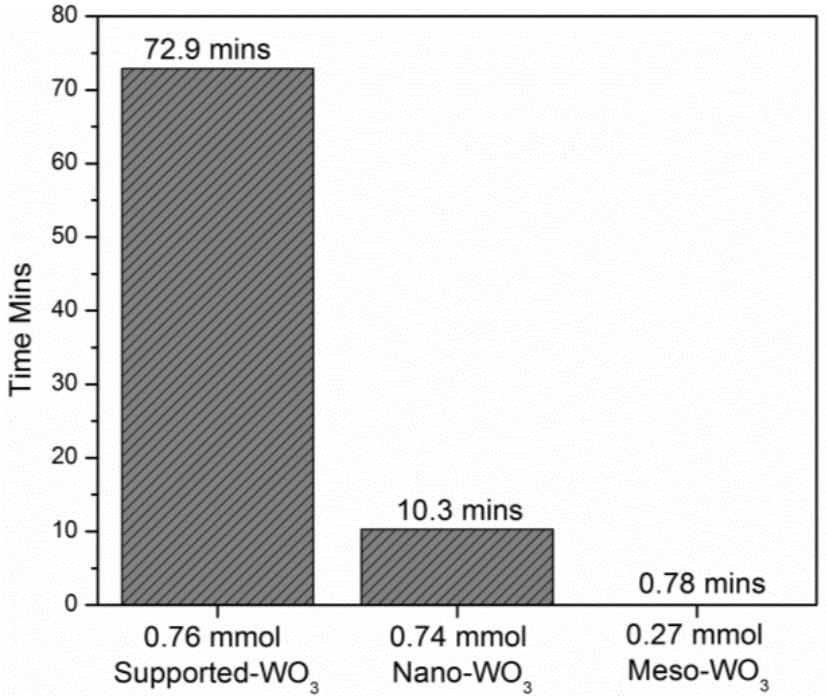

Figure 20: Comparison of the Half-Lives for the Materials

Characterization of the Materials as Capacity

Each material was reacted with excess Pb^{2+} to determine the molar capacities for each material. The spent materials from the capacity studies were characterized by XRD, Raman spectroscopy, and SEM to determine the state of the materials after the sorption process was complete, as summarized in Table 18. The pH of the 15,000 ppm Pb^{2+} solution before the treatments was 3.9, and become significantly more acidic in all cases except for the supported-WO_3. In the latter case the pH only dropped slightly, a likely consequence of reaction of Al_2O_3 with the generated acid. The drop in pH is due to the formation of $PbWO_4$ which produces two protons per formula unit, as summarized in Equation 7. The large drop in the pH could have possibly affected the sorption rate and capacity of the materials.[17] As expected, the increase of the sorption capacity showed a direct correlation to the increased surface area. However, even with the large improvement of the sorption capacity, none of the sorbents were completely exhausted.

Table 18: Summary of the Sorption Capacities

Material	Molar Sorption Capacity (%)	Surface Area ($m^2 g^{-1}$)	Initial pH	Final pH
Bulk-WO_3	2.0	1.0	3.9	1.6
Nano-WO_3	36.2	7.5	3.9	1.1
Mesoporous-WO_3	42.5	115	3.9	1.0
Supported-WO_3	58.9	176	3.9	3.1

$$WO_3 + Pb^{2+} + H_2O \rightarrow PbWO_4 + 2H^+$$

Equation 7: Schematic Representation of the Reaction of WO_3 with Pb^{2+}

The Raman spectrum of the nano-WO_3 loaded to capacity with lead, shown in Figure 21, gave characteristic stretches for both WO_3 and $PbWO_4$ in the stolzite phase. The symmetric stretching band, $\nu_1(A_g)$, for the tetrahedral tungstate ion in $PbWO_4$ appears at 902 cm^{-1}. The $\nu_2(A_g)$ vibration for stolzite was observed as a strong band at 325 cm^{-1}, however, the weak $\nu_2(B_g)$ band, normally at 356 cm^{-1} was not resolved in this spectrum.[18-20] The stretches observed at 802 and 716 cm^{-1} are consistent with the ν(O-W-O) vibration mode of WO_3. The weak stretching observed at 284 cm^{-1} is most likely consequence of the δ(O-W-O) band.[21]

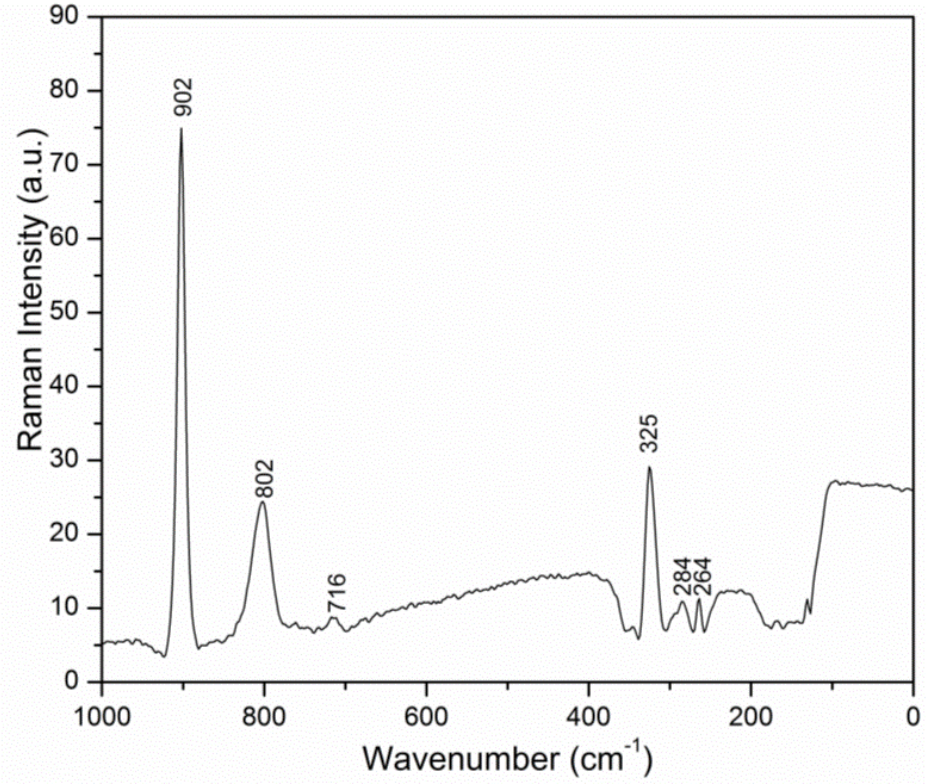

Figure 21: Raman of Nano-WO_3 with Pb^{2+}

Similarly, Figure 22 shows the formation of stolzite vibrations for the mesoporous material, although with the bands that were absent in the nano-WO_3 material are present in this spectrum. The symmetric stretching band, $\nu_1(A_g)$, for the tetrahedral tungstate ion in $PbWO_4$ appears at 905 cm^{-1}. The ν_3 stretch is split into two bands at 766 and 752 for the $\nu_3(B_g)$ and $\nu_3(E_g)$ bands, respectively. The $\nu_2(A_g)$ vibration for stolzite is observed as a strong band at 326 cm^{-1}, along with the weaker $\nu_2(B_g)$ band at 354 cm^{-1}. The band at 175 cm^{-1} is due to the ν(Pb-O) stretch of the $PbWO_4$. [18-20] A Raman spectrum of the supported materials could not be obtained due to of fluorescence from the Al_2O_3. Further, the Raman spectra of the lead-reacted bulk material could not be obtained due to the laser burning the sample.

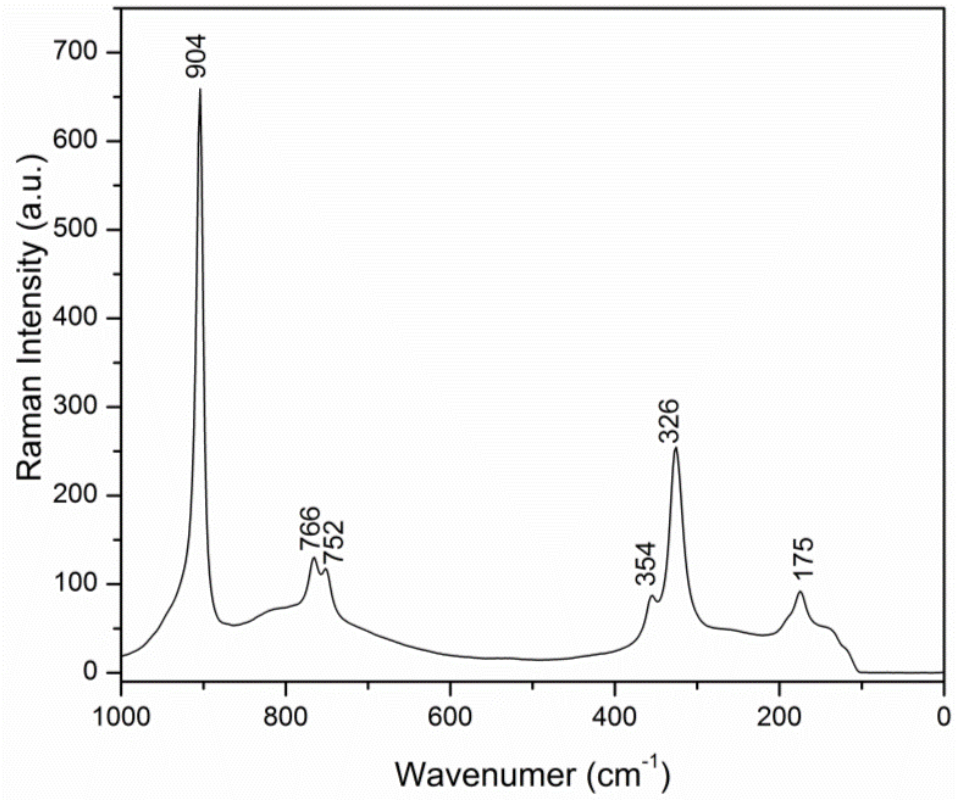

Figure 22: Raman Spectrum of Mesoporous WO_3 at Capacity

The stacked X-ray diffraction patterns (Figure 23) of the materials reacted with lead all show the formation of a crystalline stolzite ($PbWO_4$). The patterns of both the bulk and nanometric WO_3 sorbents show evidence of the parent WO_3 material, as expected since only 36% and 2% of the WO_3 in these samples, respectively, reacted to form $PbWO_4$. The materials were matched using PDF data from the International Centre for Diffraction Database. The XRDs of the mesoporous and supported WO_3 materials show the formation of crystalline stolzite phases, with no parent peaks. However, both of the starting materials were amorphous thus no parent peaks were expected nor were any observed for either material.

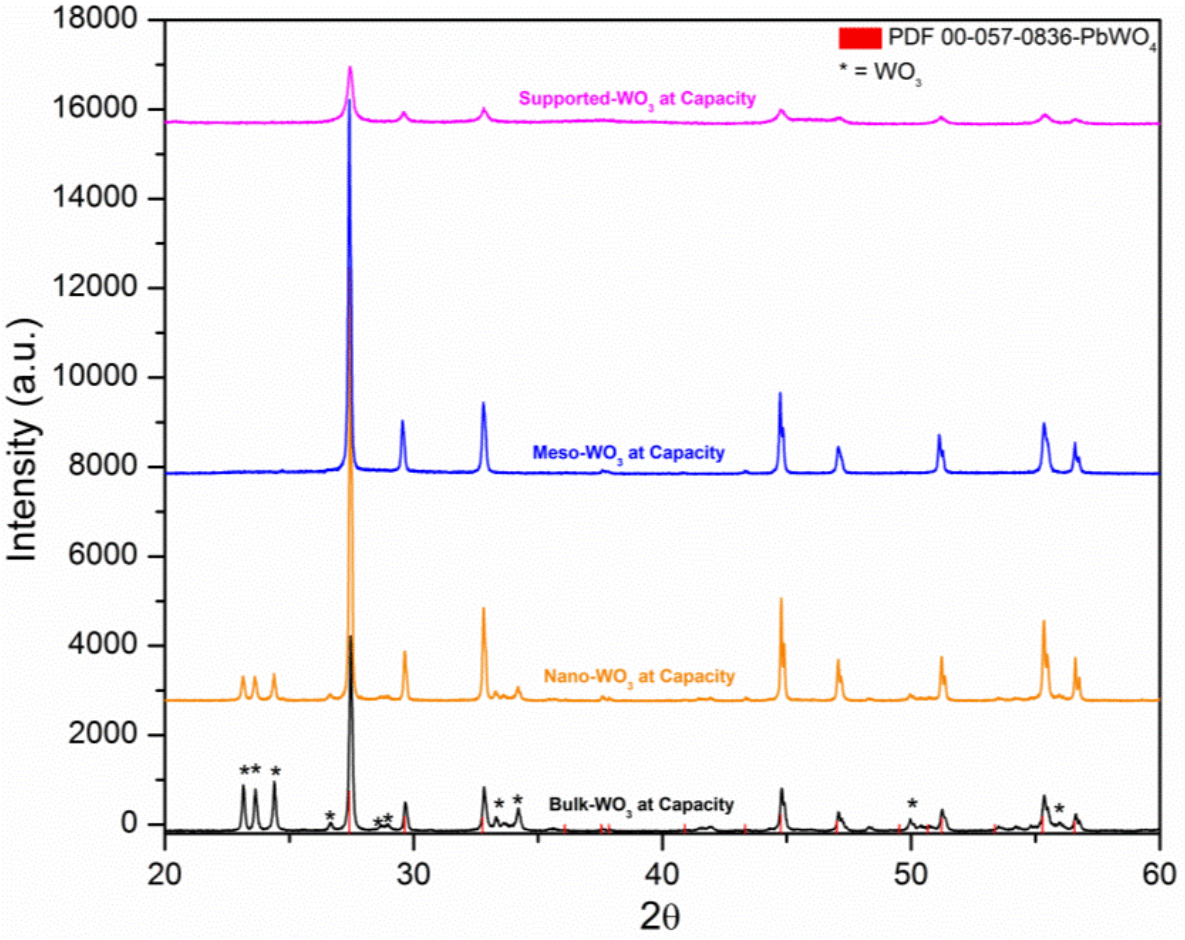

Figure 23: The Stacked XRD Spectra for the Materials at Capacity

The morphologies of the sorbents before and after sorption were characterized using scanning electron microscopy. The micrographs of the nano-WO_3 before treatment showed the material was comprised of globular and spherical aggregates of nanoparticles (Figure 24a), with aggregate diameters ranging from roughly 1 to 5 μm. Figure 24b gives a close up picture of the nanoparticles that make up the aggregates.

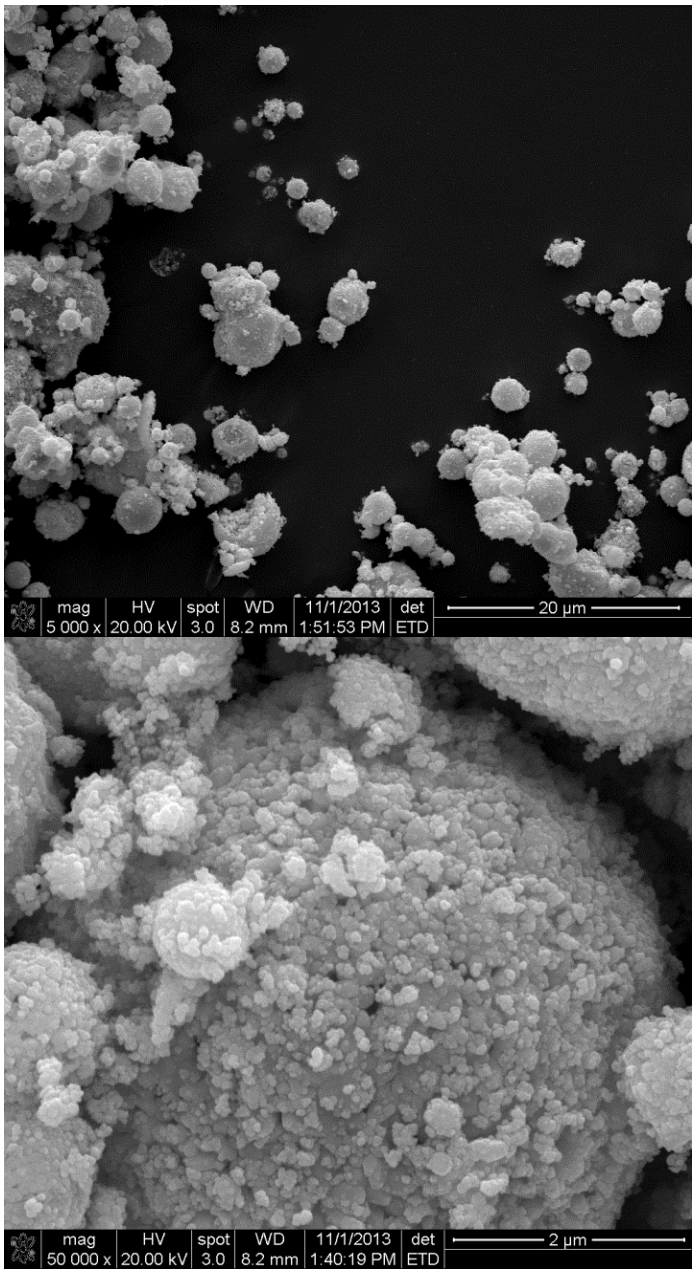

Figure 24: Electron Micrographs of Nano-WO_3 at (a) 5,000x and (b) 50,000x Magnification

However, the micrographs of the material at capacity (Figure 25) showed a major morphology change, from spherical aggregates to larger faceted particles including octahedrally-shaped particles. (Figure 25a). Furthermore, the micrograph at 50,000 x (Figure 25b) appears as though the newly formed particles are not larger aggregates of nanoparticles, but single monoliths

with nanoparticles decorating the surface. The newly formed material shows an obviously large size increase with an average diameter of particle of 3.93 ± 1.24 microns.

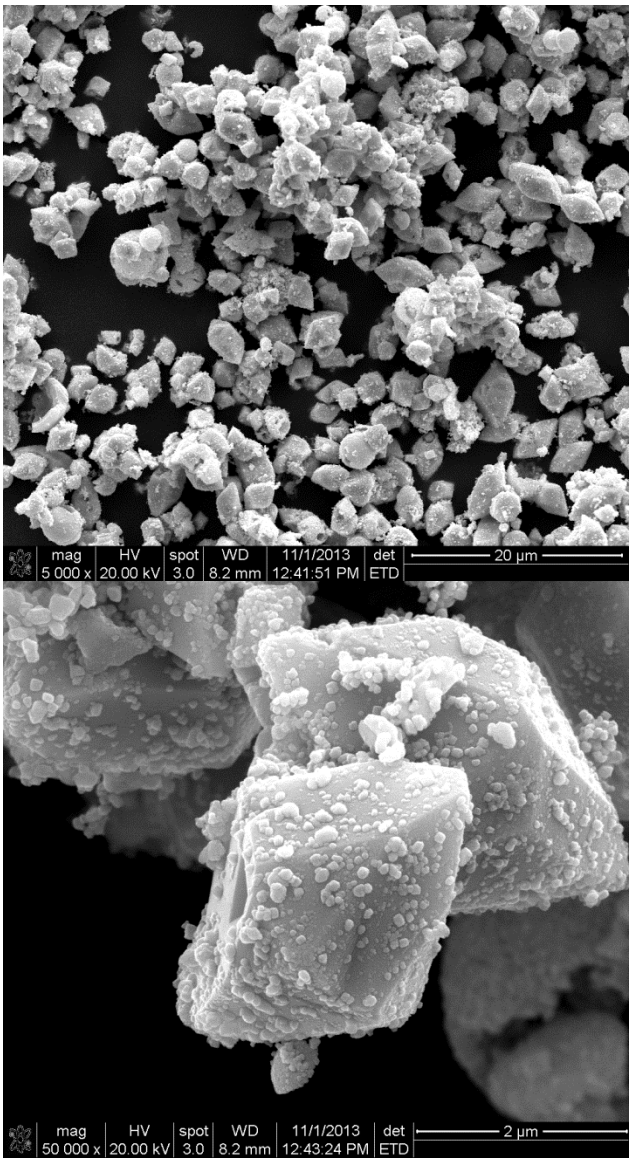

Figure 25: SEM Micrographs of the Material at Capacity at (a) 5,000x and (b) 50,000x Magnification

A similar motif is observed for all of the materials. Figure 26 shows SEM micrographs for the bulk-WO_3 before and after treatment of the Pb^{2+} solution. The micrograph shows a large

morphological change from large tabular particles to well-defined sharp-edged particles, of mostly octahedral shapes with sizes of roughly 795 ± 165 nm.

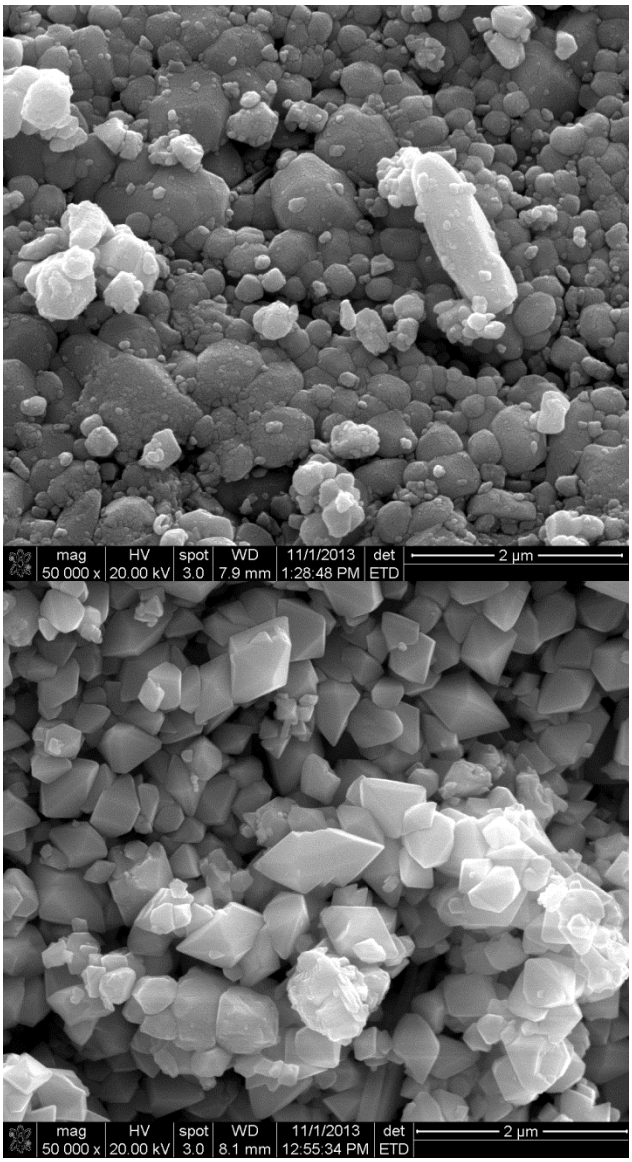

Figure 26: SEM Micrographs of the Bulk-WO_3 (a) Before and (b) After Reaction with Excess Pb^{2+}

Like the other two materials, the mesoporous-WO_3 material shows a large morphological change as well. Figure 27 shows the non-uniform mesoporous-WO_3 material before treatment and the large morphological change upon reaction with excess lead. Interestingly the newly

formed structures are mostly larger than those of the bulk-WO_3, with an average size of 1.06 ± 0.36 μm.

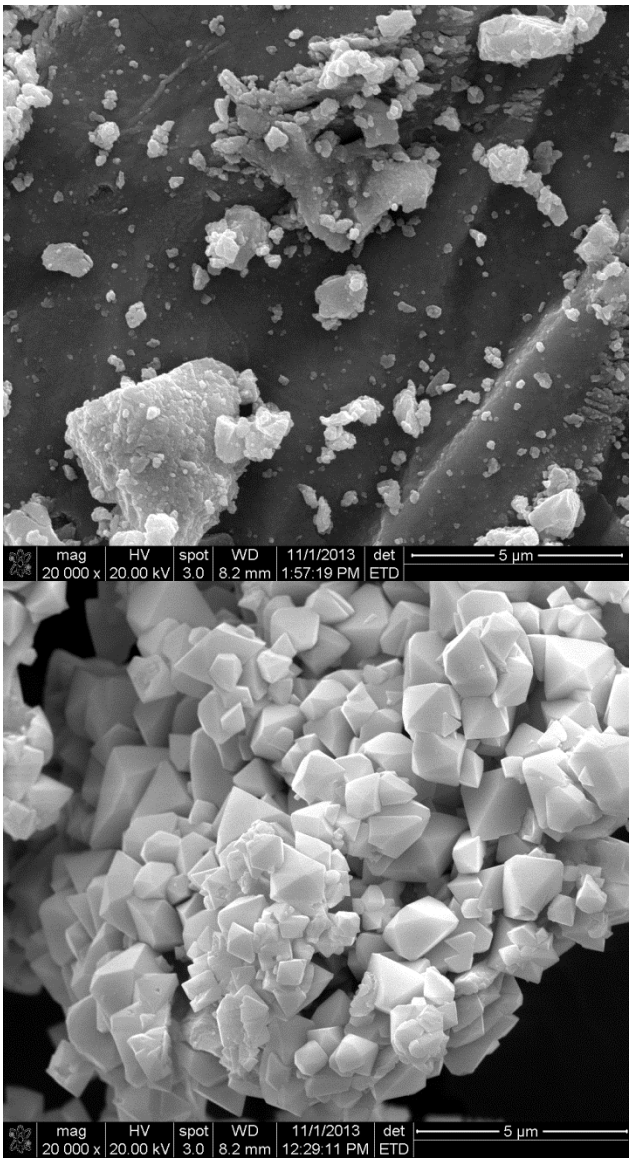

Figure 27: SEM Micrographs of the Mesoporous-WO_3 (a) Before and (b) After Reaction with Excess Pb^{2+}

Lastly, the surfaces of the high surface area supports were analyzed by SEM. The synthesized materials on the supports appear to consist as aggregates of nanoparticles, as

expected. Reaction with excess lead transforms these to large crystalline aggregates such as the dagger-like cluster shown in Figure 28 this is 5.8 μm on its longest axis.

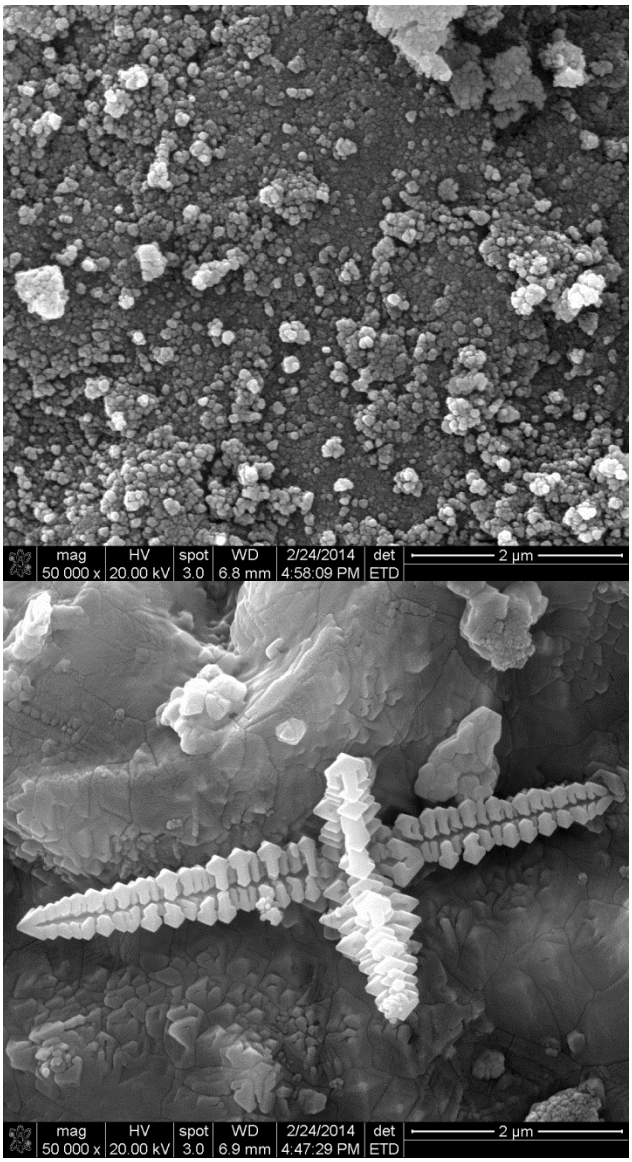

Figure 28: SEM Micrograph of the Supported-WO_3 (a) Before and (b) After Capacity

Clearly, the reaction of WO_3 with aqueous Pb^{2+} must involve intermediate species that have high mobility (either on the support surface or as aqueous ion pairs) that allow the material to migrate and crystallize as larger crystals and crystalline aggregates. The differences in crystal and aggregate shape for the $PbWO_4$ derived from the supported WO_3 verses the bulk, nano, and

mesoporous materials may arise from the high dispersion on the support surface, influence of the support, and differences in pH.

Green Process for Recovery of the Sorbents:

To show the ability for the material to be recycled, $PbWO_4$ was synthesized by a precipitation reaction of $Pb(NO_3)_2$ with $Na_2WO_4 \cdot 2H_2O$ followed by calcination of the precipitate at 600 °C. X-ray powder diffraction showed that the product was phase-pure $PbWO_4$. The regeneration-cycle (Figure 29) features a reaction of $PbWO_4$ with excess 30% NH_4OH, yielding an insoluble lead hydroxide product and a soluble ammonium tungstate that could readily be separated by filtration. The filtrate was evaporated to dryness and the resulting powder was pyrolyzed at 550 °C to generate a WO_3 in a 99% yield. Alternatively, to return to the tungstic acid material used for making the mesoporous material, one could simply react a mineral acid with the soluble ammonium tungstate, producing insoluble tungstic acid.

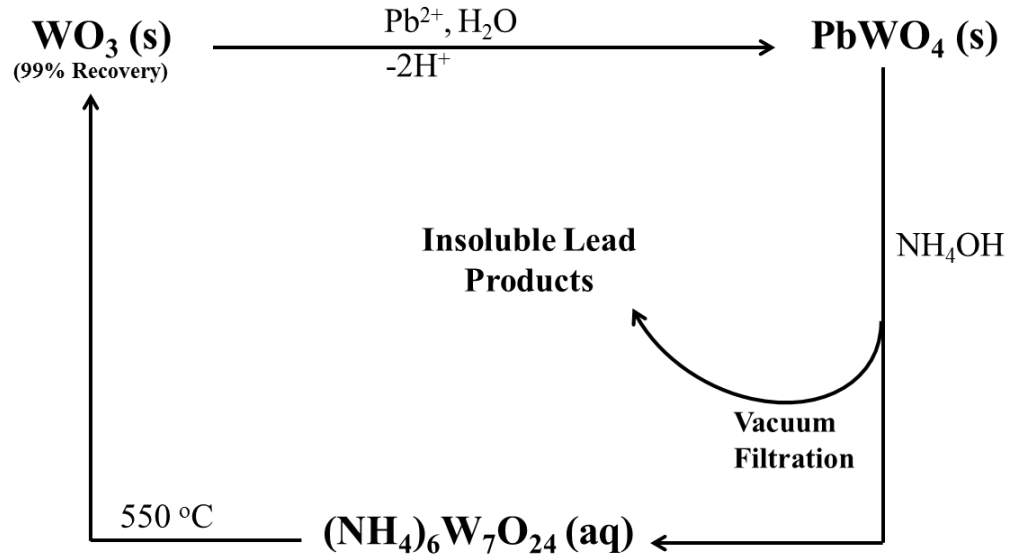

Figure 29: Cyclic-Green Process for Sorbent Recovery

Conclusion:

The results from this study show that tungsten trioxide is an attractive material for the remediation of aqueous lead. The study provides potential materials that could be rapidly incorporated into current treatment processes since two of the four materials are commercially available. Furthermore, this process is not only attractive due to the non-toxic nature of the starting material, but because the spent materials can be easily separated from the solution and recycled in a green fashion. Furthermore, by supporting WO_3, the sorption capacity was much improved compared to the commercially available products, but perhaps more importantly, the pellets are useful for preparation of water treatment columns of permeable reactive barriers. Furthermore, the supported material is much more readily separated from batch reactions than powder. Modeling of the sorption process gave reasonable results for both the linear and nonlinear pseudo-second order methods. The linear pseudo first-order model was not appropriate to model any of the sorption processes, while the nonlinear pseudo first-order model was much more effective. In all cases, the reactions produced $PbWO_4$ crystals with interesting morphologies. These had the stolzite structure as demonstrated by XRD and Raman spectroscopy. Mesoporous-WO_3 gave an extremely high rate of reaction compared to the other WO_3 materials and also gave the highest overall capacity for lead uptake of the powder starting materials. Further avenues of study for these materials would be to develop them for use in commercial applications. Also, solutions of different heavy metal contaminants should be treated to determine if the materials could be implemented in other heavy metal remediation processes. The mesoporous WO_3 using mesitylene as the auxiliary template should be studied to determine if the reactivity towards lead is improved.

References:

1. H. Albusaidi and A. W. Apblett, Adsorption and Separation of Uranium Using Tungsten Oxides. In *Environmental Issues and Waste Management Technologies in the Materials and Nuclear Industries XII*, John Wiley & Sons, Inc.: 2009; pp 39-46.

2. K. N. Barber and A. W. Apblett, Green Process for Recovery of Copper. *Ceramic Transactions* **2009,** *207*, 171-175.

3. C. Mohamed, A.-B. Hamed, and W. A. Allen, Green Process for Uranium Separations Utilizing Molybdenum Trioxide. In *Nuclear Energy and the Environment*, American Chemical Society: 2010; Vol. 1046, pp 155-167.

4. M. Chehbouni, H. Al-Busaidi, and A. W. Apblett, Green Process for Uranium Separations Utilizing Molybdenum Trioxide. In *Nuclear Energy and the Environment*, American Chemical Society: 2010; Vol. 1046, pp 155-167.

5. B. P. Kiran and A. W. Apblett, Process for Selective Removal and Concentration of Actinides and Heavy Metals from Water. *Ceramic Transactions* **2004,** *155*, 371-380.

6. B. P. Kiran, A. W. Apblett, and M. M. Chehbouni, Selective Absorption of Heavy Metals and Radionuclides from Water in a Direct-to-Ceramic Process. *Ceramic Transactions* **2003,** *143*, 385-394.

7. A. W. Apblett, B. P. Kiran, and M. Chehbouni, Molybdenum-Oxide Based Sorbants for Toxic Metals. *Ceramic Transactions* **2006,** *176*, 15-23.

8. C. K. Perkins, K. N. Barber, and A. W. Apblett, Direct conversion of a nanometric suspension of molybdenum trioxide into nanometric lead molybdate. *CrystEngComm* **2014,** *16* (14), 2869-2873.

9. W. Wang, Y. Pang, and S. B. Hodgson, On key factors for the fabrication of mesoporous tungsten oxide films from tungstic acid. *Journal of Sol-Gel Science and Technology* **2011,** *58* (1), 135-141.

10. W. Wang, Y. Pang, and S. N. B. Hodgson, XRD studies of thermally stable mesoporous tungsten oxide synthesised by a templated sol–gel process from tungstic acid precursor. *Microporous and Mesoporous Materials* **2009,** *121* (1–3), 121-128.

11. C. Dwivedi, S. K. Pathak, Manmohan Kumar, S. C. Tripathi, and a. P. N. Bajaj, Potassium cobalthexacyanoferrate–gel beads for cesium removal: kinetics and sorption studies. *RSC Advances* **2013,** *3*, 22102-22110.

12. S. Lagergren, Zur theorie der sogenannten adsorption gelöster stoffe. Kungliga Svenska Vetenskapsakademiens. *Handlingar* **1898,** *24* (4), 1-39.

13. S. Azizian, Kinetic models of sorption: a theoretical analysis. *Journal of Colloid and Interface Science* **2004,** *276*, 47–52.

14. K. V. Kumar, Linear and non-linear regression analysis for the sorption kinetics of methylene blue onto activated carbon. *Journal of Hazardous Materials B* **2006,** *137*, 1538-1544.

15. Y. S. Ho and G. McKay, Pseudo-second order model for sorption processes. *Process Biochemistry* **1999,** *34*, 451-465.

16. J.-Z. Zhang, Avoiding spurious correlation in analysis of chemical kinetic data. *Chemical Communications* **2011,** *47* (24), 6861-6863.

17. K. S. Smith, Metal sorption on mineral surfaces: An overview with examples relating to mineral deposits. *Reviews in Economic Geology* **1999,** *6A-B*, 161-182.

18. R. K. Khanna, W. S. Brower, B. R. Guscott, and E. R. Lippincott, Laser induced Raman spectra of some tungstates and molybdates *Journal of Research of the Notional Bureau af Standards - A* **1968,** *72A* (1), 81-84.

19. B. Ingham, S. V. Chong, and J. L. Tallon, Layered Tungsten Oxide-Based Organic−Inorganic Hybrid Materials: An Infrared and Raman Study. *The Journal of Physical Chemistry B* **2005,** *109* (11), 4936-4940.

20. S. Bastians, G. Crump, W. P. Griffith, and R. Withnall, Raspite and studtite: Raman spectra of two unique minerals. *Journal of Raman Spectroscopy* **2004,** *35* (8-9), 726-731.

21. M. F. Daniel, B. Desbat, J. C. Lassegues, B. Gerand, and M. Figlarz, Infrared and Raman study of WO_3 tungsten trioxides and WO_3, xH_2O tungsten trioxide hydrates. *Journal of Solid State Chemistry* **1987,** *67* (2), 235-247.

CHAPTER X

SORPTION OF HEAVY METALS BY NANOCRYSTALLINE CALCIUM TUNGSTATE

Introduction:

Copper is an essential trace-element essential for all life, but like all heavy metals it can be toxic in high concentrations. For example, excessive copper intake can result in accumulation in the liver, possibly producing gastrointestinal problems.[1] Since copper is widely used by industries, there are numerous potential sources for the introduction of copper into the environment. The typical sources of copper in industrial wastewaters include metal and electroplating, petroleum refining, fertilizer run-off, paper making, and mining. Concentrations of copper in wastewaters have been shown to reach values up to 1000 ppm. [2-4] The EPA has set the maximum concentration limit for the concentration of copper in drinking water to a value of 1.3 ppm.

There is also increasing interest in removing cadmium from drinking water due to the high toxicity threat to human health in small concentration. According to the World Health Organization guidelines, the permittable concentration of cadmium in drinking water is less than 3 ppb, while the EPA's action limit is set to 5 ppb. Chronic exposure to cadmium has variety of health related effects including lung insufficiency, bone lesions, cancer and hypertension, all primarily caused by cadmium's long half-life in most tissues, from 80 days in blood and 10-35

years in the kidney.[5-7] Drinking water contamination can stem from erosion and dissolution of naturally occurring ores. However, the major sources typically are from industrial processes such as electroplating, smelting, alloy manufacturing, pigments, nickel–cadmium battery production.[8-11] Further, the dangers associated with aqueous lead have previously been outlined in Chapter VIII.

The Apblett group has previously demonstrated the attractiveness of using transition metal oxides in water remediation technologies.[12-17] More specifically, this dissertation has highlighted the use of both molybdenum and tungsten trioxide for Pb^{2+} remediation. It was found, rather unexpectedly, that the addition of Ca^{2+} as a competing ion increased the sorption kinetics of a solution being treated with tungstic acid.[12] These results led to the proposal that insoluble scheelite ($CaWO_4$) would be an attractive material for use in an environmentally-friendly heavy metal mitigation process. This chapter accentuates the versatility of $CaWO_4$ to remove divalent transition metal from aqueous systems.

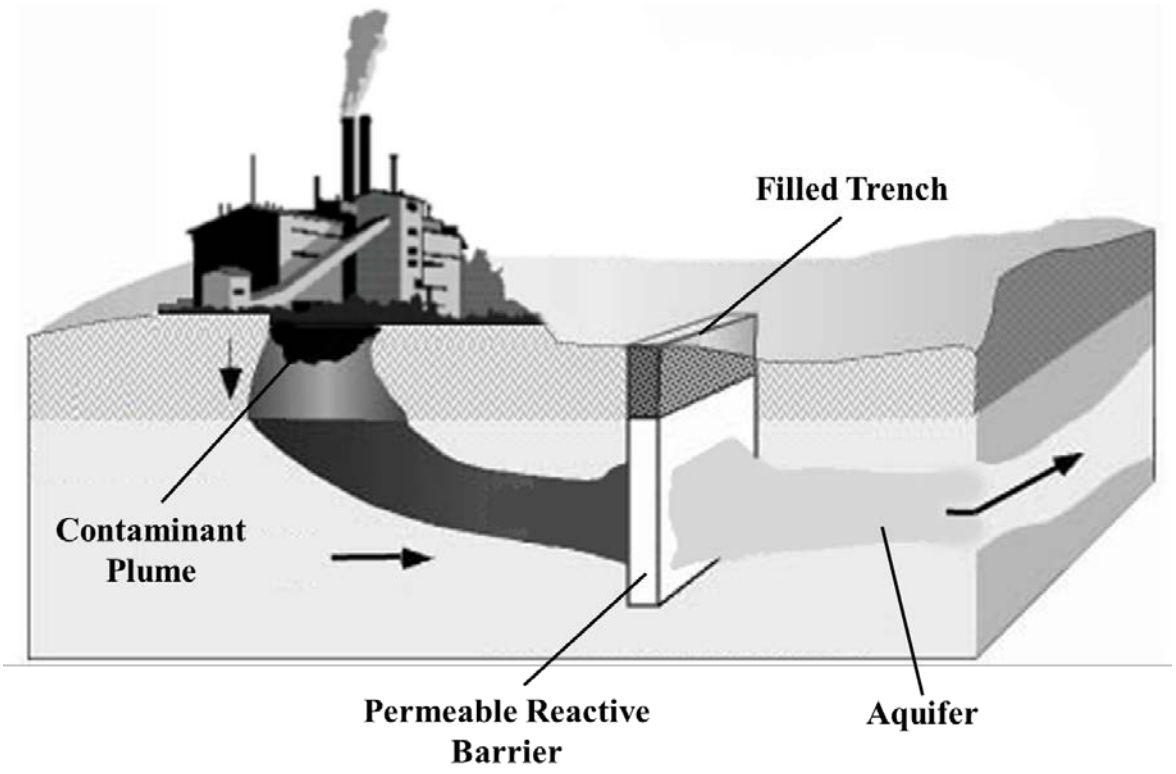

Figure 1: Permeable Reactive Barrier for Contamination Remediation

Experimental:

Materials

All chemicals (reagent grade or higher) were used as received without further purification, along with 18 MΩ ultra-pure water (Milli-Q Millipore). Tungstic acid, calcium D-gluconate, α-hydroxyisobutyric acid (98%), and the Al_2O_3 and SiO_2 high surface area catalyst supports were obtained from Alfa-Aesar. The lead nitrate, $Pb(NO_3)_2$ used to prepare the lead stock solution were received from Aldrich. The $Ca(OH)_2$ and NaOH used were obtained from Fisher Scientific. Trace metal HNO_3 used for sample acidification was obtained from Mallinckrodt. The heavy metal standards were purchased from BDH ARISTAR with concentrations of 100 ppm were used to prepare the standard solutions for calibration of the instrument. A 1000 mg/L Ca^{2+} standard used for flame absorption spectroscopy was obtained from Sherwood Scientific. Deuterated water from Aldrich was used for the liquid state NMR

spectroscopy experiment. Hydrochloric acid for the regeneration of H_2WO_4 was obtained from PHARMCO-AAPER.

Impregnation of supports

The high surface area alumina supports were vacuum-impregnated by introducing the calcium tungsten gluconate precursor solution to the supports *in vacuo*. The supports were held under vacuum for roughly 24 hours. They were then rinsed with 50 mL of deionized water, to prevent the any excess precursor to remain on the surface of the materials when calcined. Then supports were then dried in vacuum and then they were transferred to a ceramic crucible. They were then calcined at the decomposition temperature for 8 hours in a muffle-furnace.

Sorption studies

The sorption studies were performed using a 107 parts per million (ppm) solution of Pb^{2+}, that was prepared using $Pb(NO_3)_2$. The actual concentration of lead was determined by graphite furnace atomic absorption spectroscopy (GFAAS). The effect of sorbent dosage on reaction kinetics was determined by treating three approximately 50 mL solutions of 107 ppm Pb^{2+}, with varying amounts of excess calcium tungstate. Treating solutions of Cd^{2+} and Cu^{2+} were done in a similar fashion with concentration of 126 and 85.7 ppm, respectively.

All of the samples were agitated on a sample rotator, at a speed of 40 RPM, to eliminate the possibility of forming concentration gradients. Aliquots of each sample were taken at regular time intervals, diluted with a 1% trace-metal HNO_3 solution to the appropriate concentrations, and analyzed by GFAAS. The reaction uptake curves were plotted using the sorption capacity at a given time (q_t) vs time (t). The sorption capacity was defined by Equation 1, where C_t is the concentration of analyte in the solution at time t, C_0 is the starting concentration, V is the volume of the analyte, and m is the mass of the sorbent.

$$q_t = \frac{(C_0 - C_t)V}{m}$$

Equation 1: The Sorption Capacity Equation

At completion of the experiments, the solutions were analyzed for the concentration of calcium by flame atomic absorption spectroscopy using a Varian AA240FS flame atomic absorption spectrometer.

Characterization

The X-ray diffraction patterns for both the oxides before and after reactions with excess heavy metals were obtained using a Bruker D8-A25-Advance diffractometer equipped with a LynxEye detector. Fourier transformed infrared (FT-IR) spectroscopy was performed as a KBr pellet using a Nicolet Magna 750 IR spectrometer. The solutions from the capacity and kinetic studies were analyzed using a Varian GTA120/AA240Z graphite furnace atomic absorption spectrometer with an auto sampler. The concentration of Ca^{2+} in the treated solutions was determined using a Varian AA240FS flame atomic absorption spectrometer. The surface area of the starting material, $CaWO_4$, was measured by N_2 physisorption and was recorded using a NOVA Quantachrome 1200 BET. Scanning electron microscopy (SEM) was performed on the original material and the spent materials using a FEI Quanta 600 field emission gun environmental scanning electron microscope. The same materials were embedded and sectioned with a microtome and analyzed by transmission electron microscopy (TEM) using a JEOL JEM-2100 transmission electron microscope.

Results and Discussion:

The $CaWO_4$ used in these experiments was characterized in Chapter VIII. The highest surface area powder, from the methyl lactic acid precursor, was used in the sorption experiments for all analytes.

Sorption Kinetics for Pb^{2+}

The calcium tungstate produced from the α-hydroxyisobutyate precursor was used for the sorption kinetic studies because of its higher surface area. After addition of $CaWO_4$ to solutions of 107 ppm Pb^{2+}, the analyte concentrations were monitored via GFAAS. Figure 1 depicts the sorption uptake curves of lead onto varying amounts of calcium tungstate by plotting q_t verses time (from Equation 1**)**. The curves depict a process in which sorption is initially very fast and the starts to slow as the reaction approaches an equilibrium state around 120 minutes for 0.177 mmols $CaWO_4$ and roughly 15 minutes when the highest amount of sorbent is used (0.359 mmols $CaWO_4$). The sorption process continued until the entirety of the sorbate was removed below the instrument detection limit of roughly 0.5 ppb. The concentration of Ca^{2+} in the solution increased to roughly 20 ppm in every case.

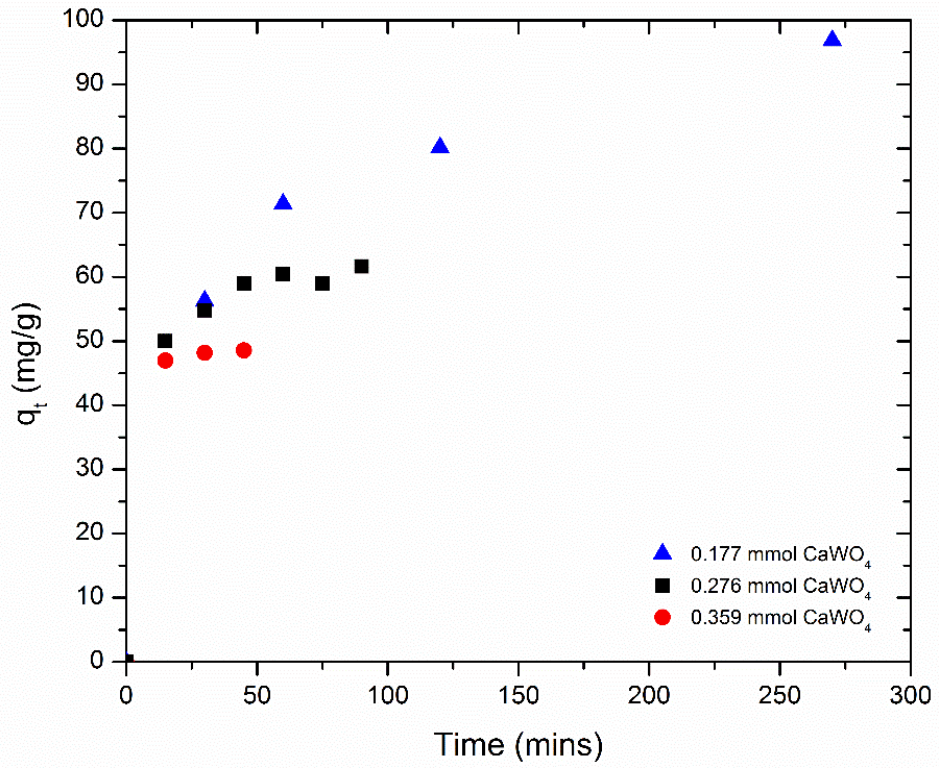

Figure 2: Sorption Uptake Curves of Pb^{2+} with Nanocrystalline $CaWO_4$

Modeling the kinetics for the uptake of heavy metal contaminants is important for determining the optimum operating conditions for industrial implementation. The kinetic sorption rate of lead by nanometric calcium tungstate determines its effectiveness for use in water treatment processes. Sorption kinetics can be analyzed using several different models, with both the pseudo first-order and pseudo second-order models being the most widely used. In this study, the nonlinear and linear pseudo first and pseudo second order functions were employed to model the sorption process.

The pseudo first-order rate expression (Equation 2) was first described by Lagergren in 1898, where k_1 is the kinetic rate constant for the pseudo first-order sorption process. The amount of analyte sorbed at any specific time (t) is represented by q_t and the amount of analyte sorbed at equilibrium is represented by q_e.[18]

$$q_t = q_e(1 - e^{-k_1 t})$$

Equation 2: The Nonlinear Pseudo First-Order Equation

To simplify Equation 2, the natural log was taken giving a linear equation represented by Equation 3. From this equation, the values of k_1 and q_e can be determined from the slope and y-intercept, respectively, of the linear pseudo first-order plot.

$$\ln(q_e - q_t) = \ln(q_e) - k_1 t$$

Equation 3: The Linearized Formula for Pseudo First-Order Equation

From the plot of the linear pseudo first-order kinetic fit (Figure 3), we can determine that the linear pseudo first-order model does not apply throughout the various sorbent loadings. At the lowest sorbent mass loading, the data exhibits the largest deviation from linearity, as evident from the correlation coefficient (R^2) values listed in Table 1. Furthermore, the estimated values of q_e calculated from the equation differ substantially from those measured experimentally, owing to the fact this sorption process cannot be satisfactorily modeled as a linear pseudo first-order process. It has been hypothesized that the linear pseudo first-order model fails as the concentration of the reaction sites become much greater than that of the concentration of the analyte.[19] Here, the opposite trend is observed for this data, with the lowest mass loading showing the largest deviation from linearity.

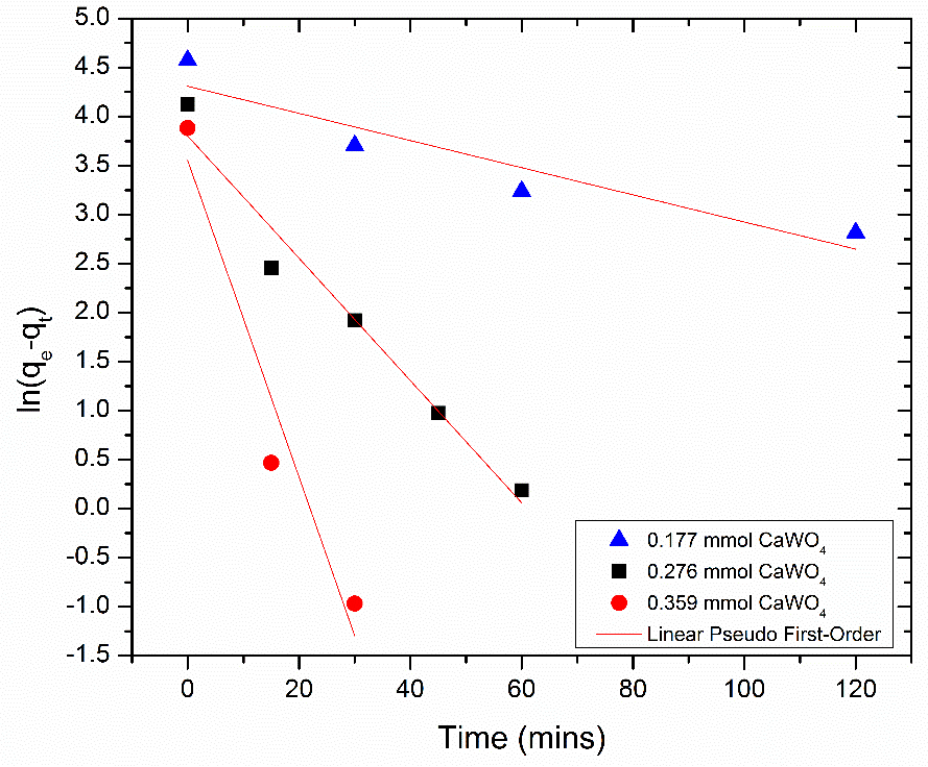

Figure 3: Linear Pseudo First-Order Fit for the Uptake of Pb^{2+} by Nanocrystalline $CaWO_4$

Table 1: The Kinetic Data for the Linear Pseudo First-Order Fit

$CaWO_4$ (mmol)	k_1 (min^{-1})	q_e (mg/g)	q_e (mg/g) (experimental)	R^2
0.177	1.39E-02	74.4	96.8	0.831
0.276	6.24E-02	44.8	61.6	0.958
0.359	1.62E-01	34.9	48.5	0.895

It has been suggested that the nonlinear pseudo first-order equation may be more appropriate to fit pseudo first-order sorption processes. This method was previously applied for the sorption of methylene blue on activated carbon and was shown to greatly outperformed the linear model.[20] Using the nonlinear pseudo first-order equation (Equation 2) to fit the data, nonlinear regression plots were made using Origin graphing software. The plotted nonlinear pseudo first-order model (Figure 4) shows this model underestimates the equilibrium capacities (q_e) in all cases. However, the kinetic parameters, summarized in Table 2, show correlation

coefficients for the nonlinear method that are much higher than the linear model, suggesting that this method is superior to the linearized model for this sorption process.

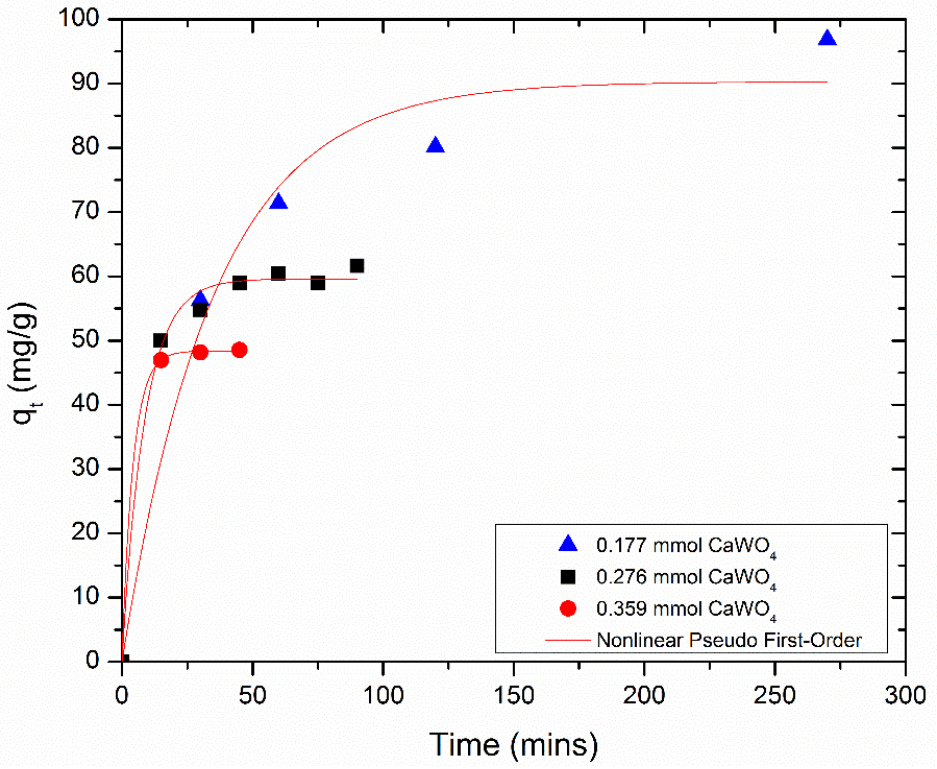

Figure 4: Nonlinear Pseudo First-Order Fit of the Sorption of Pb^{2+} by Nanocrystalline $CaWO_4$

Table 2: The Kinetic Data for the Nonlinear Pseudo First-Order Fit

$CaWO_4$ (mmol)	k_1 (min^{-1})	q_e (mg/g)	q_e (mg/g) (experimental)	R^2
0.177	2.85E-02	90.3	96.8	0.971
0.276	1.15E-01	59.6	61.6	0.994
0.359	2.34E-01	48.4	48.5	1.00

Ho and McKay proposed a pseudo-second order kinetic model represented by Equation 4, where k_2 is the rate constant of the pseudo second-order sorption process, with the units g mg^{-1} min^{-1}.[21]

$$\frac{t}{q_t} = \frac{1}{k_2 q_e^2} + \frac{1}{q_e} t$$

Equation 4: The Linearized Pseudo Second-Order Equation

By substituting h in place of $k_2 q_e^2$, Equation 4 can be further simplified, as represented in Equation 5. The variable h, in this equation, is defined as the initial sorption rate as t/q_t approaches 0. The linear plot of t/q_t versus t gives the constants q_e and h, from the slope and the intercept, respectively.[19] Using the value of q_e (the slope) and h (the intercept), the rate constant (k_2) can be obtained.

$$\frac{t}{q_t} = \frac{1}{h} + \frac{1}{q_e} t$$

Equation 5: The Linearized Initial Rate Pseudo Second-Order Equation

The linear pseudo second-order plot, Figure 5, shows that the linear pseudo second-order equation fits the data much better than the linear pseudo first-order equation. Linear regression of the functions gave very high correlation coefficient values (R^2>0.99). Furthermore, the calculated q_e values are in very close agreement with the experimental data, although the model slightly overestimates the values throughout the series (Table 3). The pseudo second-order rate constants (k_2) increase as the amount of sorbent is increased. This correlation is also observed in the initial sorption rate (h) data.

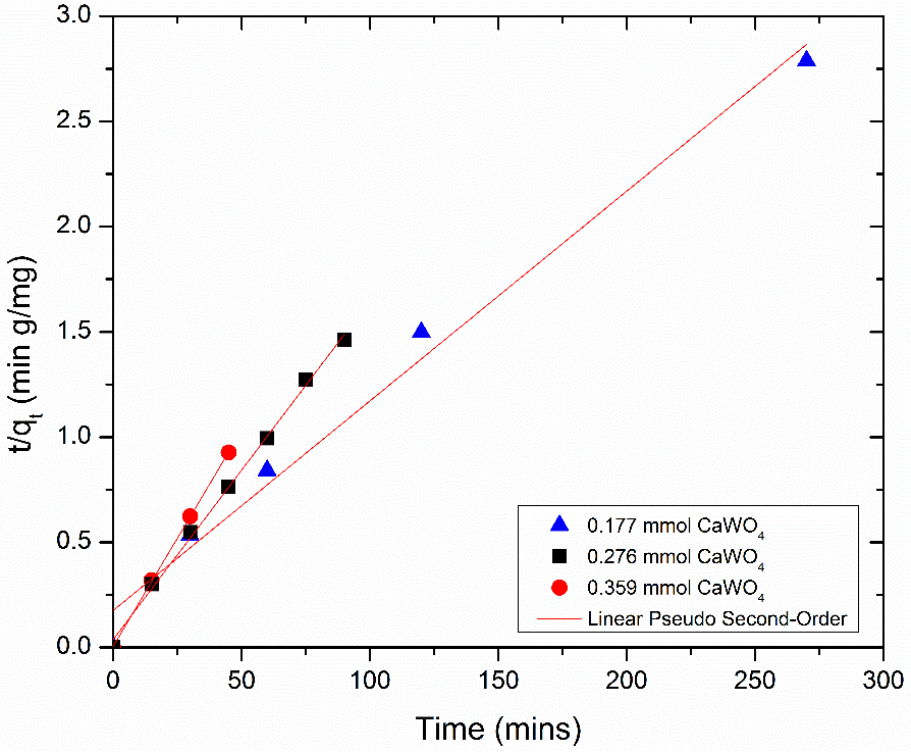

Figure 5: Linear Pseudo Second-Order Fit of the Sorption of Pb^{2+} by Nanocrystalline $CaWO_4$

Table 3: Kinetic Data from the Fit of the Linear Pseudo Second-Order Equation

$CaWO_4$ (mmol)	k_2 (g/mg min)	h (mg/g min)	q_e (mg/g)	q_e (mg/g) (experimental)	R^2
0.177	5.67E-04	5.70	100	96.8	0.999
0.276	7.05E-03	27.1	62.0	61.6	0.998
0.359	9.01E-02	213	48.6	48.5	0.999

The nonlinear pseudo second-order equation (Equation 6) was also shown to be a viable option to model the sorption process of methylene blue on activated carbon.[20]

$$q_t = \frac{k_2 q_e^2 t}{1 + k_2 q_e t}$$

Equation 6: The Nonlinear Pseudo Second-Order Equation

The nonlinear pseudo second-order function fit the data with relatively good accuracy (Figure 6). The kinetic values, summarized in Table 4, show the correlation coefficients for the nonlinear method are very high (R^2>0.97) similar to the linear model suggesting that this method

is also appropriate for modeling this process. As for the linear pseudo second-order model, the rate constants and initial rate values consistently increase with increasing sorbent loading. This model also slightly overestimates the equilibrium sorption capacity in every case. From the data presented, it suggests that both pseudo second-order models describe the sorption of Pb^{2+} by the nanometric-$CaWO_4$ very well. However, even though the models fit the present data very well, there is little physical meaning that can be extrapolated from the kinetic results, as the rate constants are dependent on the concentration of the analyte. Also, concern has been raised on the validity of the linear pseudo-second order equation to model sorption processes, due to spurious correlations.[22] However, the models could be employed to determine equilibrium capacities of the materials used in this system fairly accurately.

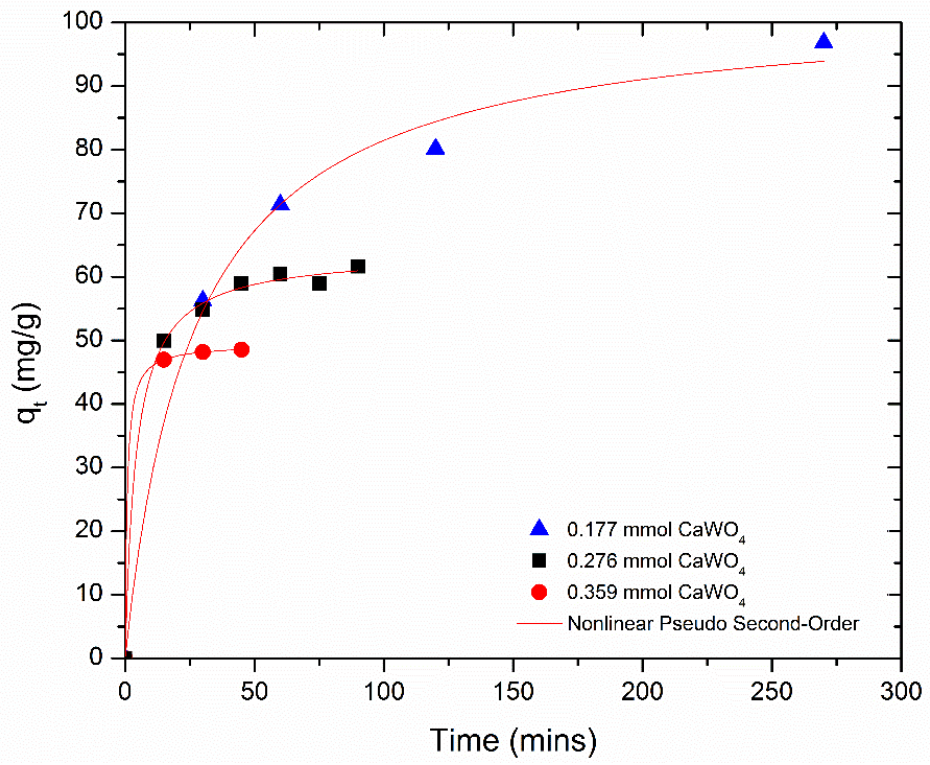

Figure 6: Linear Pseudo Second-Order Fit of the Sorption of Pb^{2+} by Nanocrystalline $CaWO_4$

Table 4: The Kinetic Data for the Nonlinear Pseudo Second-Order Fit

$CaWO_4$ (mmol)	k_2 (g/mg min)	h (mg/g min)	q_e (mg/g)	q_e (mg/g) (experimental)	R^2
0.177	3.63E-04	3.86	103	96.8	0.998
0.276	3.65E-03	14.9	63.8	61.6	0.991
0.359	2.59E-02	63.2	49.4	48.5	0.979

In order to prepare sorbent materials with possibly increased uptake kinetics and a form factor conducive for treatment of water in columns or permeable reactive barriers, $CaWO_4$ supported on high surface area silica pellets was prepared. To accomplish this, supports were impregnated using the D-gluconate single-source precursor solution and then calcined to produce $CaWO_4$ on the support. This improved the substrate's BET surface area from 24 to 131 m^2/g. It was hypothesized that improving the surface area of the substrate would also improve the reaction uptake kinetics. Thus, the SiO_2 supported $CaWO_4$ (with a 4.6% mass loading) were also analyzed for their sorption kinetics under the similar conditions as previously described. The sorption uptake curves, Figure 7, shows that the sorption equilibrium capacities are reached at close to 60 minutes for the two larger loadings and around 90 minutes for the lowest loading. The sorption process was modeled using all four models.

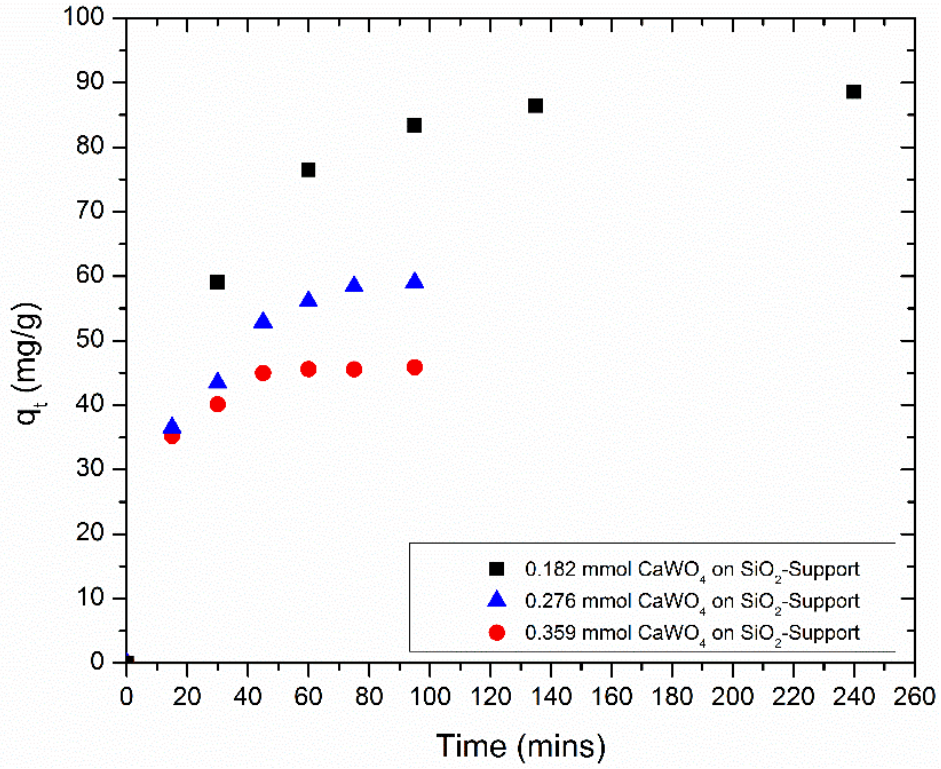

Figure 7: Sorption Uptake Curves of the Supported $CaWO_4$

The plot of the nonlinear pseudo first-order fit (Figure 8) shows that this model fits the data very well, with very high correlation coefficients (R^2>0.98) in all cases. The predicted equilibrium sorption capacities, summarized in Table 5, are in very close agreement to the experimental values. Furthermore, from this model the rate constants and reaction half-lives can be compared for the powder and supported materials.

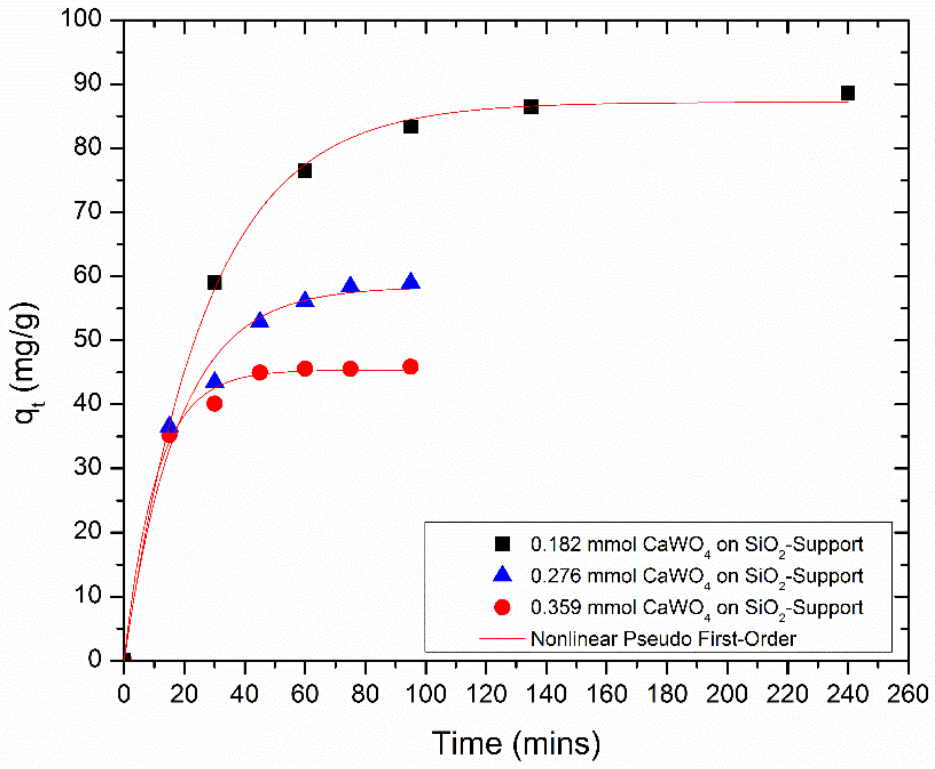

Figure 8: Nonlinear Pseudo First-Order Fit Using $CaWO_4$ on SiO_2 Supports

Table 5: Summary of Kinetic Data from Non-linear Pseudo First-Order Model for Uptake of Pb^{2+} by Supported $CaWO_4$

$CaWO_4$ (mmol)	k_1 (min^{-1})	q_e (mg/g)	q_e (mg/g) (experimental)	R^2
0.182	3.66E-02	90.3	88.6	0.999
0.276	5.51E-02	59.6	59.0	0.986
0.359	9.29E-02	48.4	45.9	0.994

The linear pseudo first-order model for the uptake of Pb^{2+} by the supported $CaWO_4$ (Figure 9) led to a similar conclusion as that for the $CaWO_4$ in powder form. The largest deviation from linearity is for the treatment with the least amount of pellets used. Also, the equilibrium capacity for Pb^{2+} is drastically overestimated for the 0.182 mmol case, predicting more than double that was observed experimentally. As noted with the powder, the linear pseudo first-order equation does not adequately describe the sorption process.

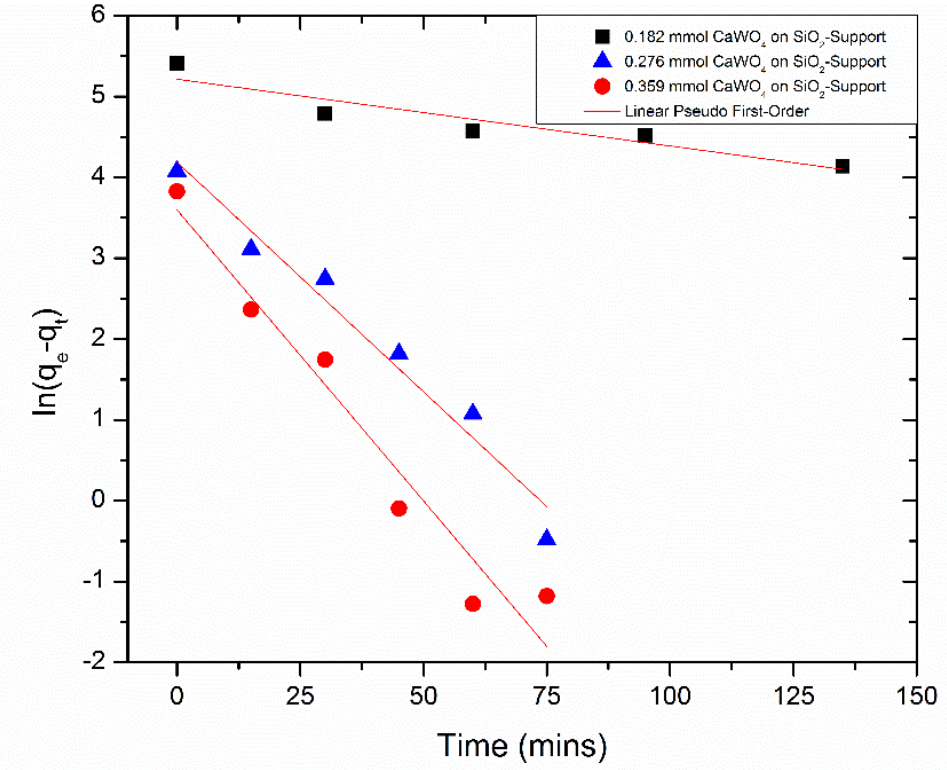

Figure 9: Linear Pseudo First-Order Fit of the Uptake of Pb^{2+} by $CaWO_4$ on SiO_2

Table 6: Data for the Linear Pseudo First-Order Fit for the Uptake of Pb^{2+} by $CaWO_4$ on SiO_2

$CaWO_4$ (mmol)	k_1 (min^{-1})	q_e (mg/g)	q_e (mg/g) (experimental)	R^2
0.182	8.26E-03	184	88.6	0.848
0.276	5.69E-02	66.0	59.0	0.960
0.359	7.20E-02	36.5	45.9	0.938

The linear pseudo second-order equation fits the data almost perfectly (Figure 10), with very high correlation coefficients (Table 7). The model also predicts the sorption equilibrium capacities with very good accuracy, only slightly over estimating in every case. However, the kinetic data suggest that the second highest mass loading has the slowest initial sorption rate.

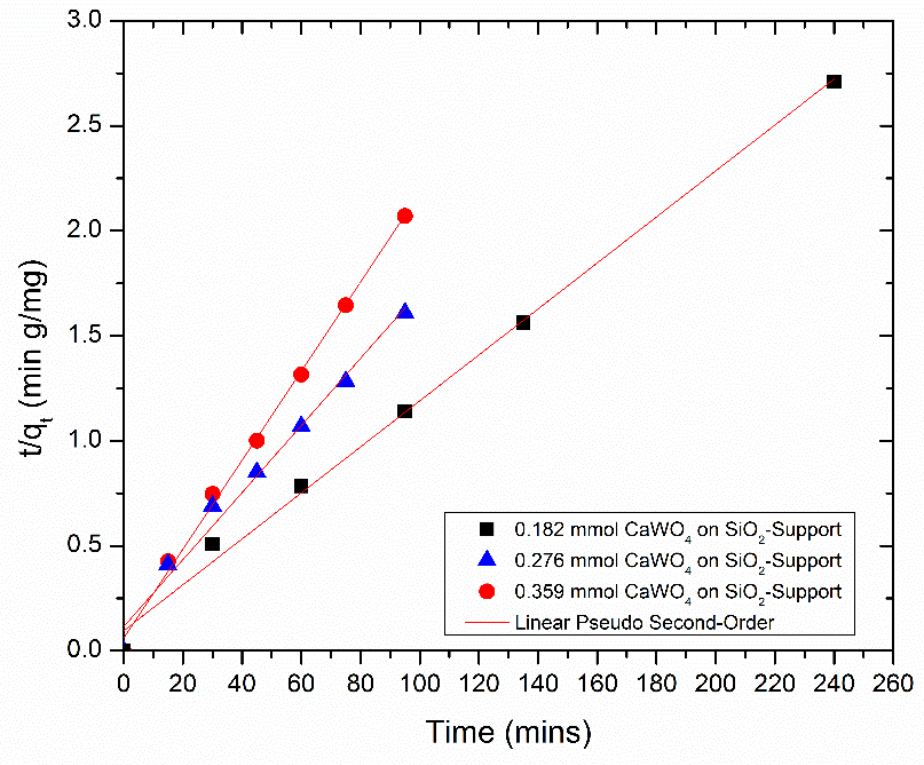

Figure 10: Linear Pseudo Second-Order Fit for Pb^{2+} Uptake by $CaWO_4$ on SiO_2

Table 7: Data for the Linear Pseudo Second-Order Fit for Pb^{2+} Uptake by $CaWO_4$ on SiO_2

$CaWO_4$ (mmol)	k_2 (g/mg min)	h (mg/g min)	q_e (mg/g)	q_e (mg/g) (experimental)	R^2
0.182	1.26E-03	10.5	91.3	88.6	0.995
0.276	2.22E-03	8.70	62.6	59.0	0.981
0.359	7.43E-03	16.5	47.2	45.9	0.996

The nonlinear pseudo second-order equation also fits the data almost perfectly (Figure 11), with nearly perfect correlation coefficients (Table 8). The model also predicts the sorption equilibrium capacities with fairly good accuracy, but it overestimates the equilibrium sorption capacity more than its linear counterpart does in every case. Moreover, both models, counterintuitively, suggests that second highest mass loading has the slowest initial sorption rate.

This result could be consequence of the limited physical meaning that may be extrapolated from the pseudo second-order model.

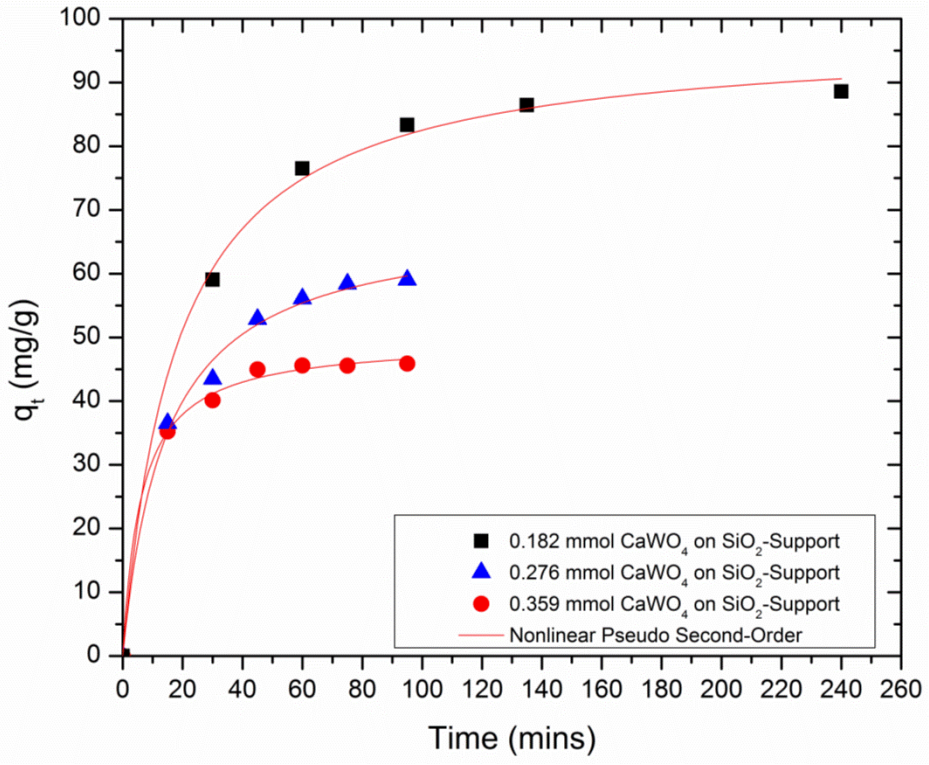

Figure 11: Nonlinear Pseudo Second-Order Fit for Pb^{2+} Uptake by $CaWO_4$ on SiO_2

Table 8: Data for the Nonlinear Pseudo Second-Order Fit for Pb^{2+} Uptake by $CaWO_4$ on SiO_2

$CaWO_4$ (mmol)	k_2 (g/mg min)	h (mg/g min)	q_e (mg/g)	q_e (mg/g) (experimental)	R^2
0.182	5.68E-04	5.40	97.4	88.6	0.997
0.276	1.01E-03	4.78	68.7	59.0	0.994
0.359	3.28E-03	8.07	49.6	45.9	0.997

Since the pseudo second-order models have limited physical meaning, the powder and supported data can best be compared using the pseudo first-order models. Since the linear pseudo first-order model failed to appropriately describe the sorption process for both materials, data from the nonlinear pseudo first-order models was selected for comparison. The original hypothesis that increasing the surface area by supporting the material would increase the rate of sorption was true in only one case. Figure 12 shows the comparison of the sorption half-lives,

calculated from the pseudo first-order rate constants. In only one case, the 0.177-0.182 mmol reactions, was the hypothesis met. This was most likely due to diffusion into the pellet interior being the rate-limiting factor for the porous-supported materials. This hypothesis is supported by the fact that the initial rate of reaction in the first 15 minutes is higher for the supported materials than it is for the powder.

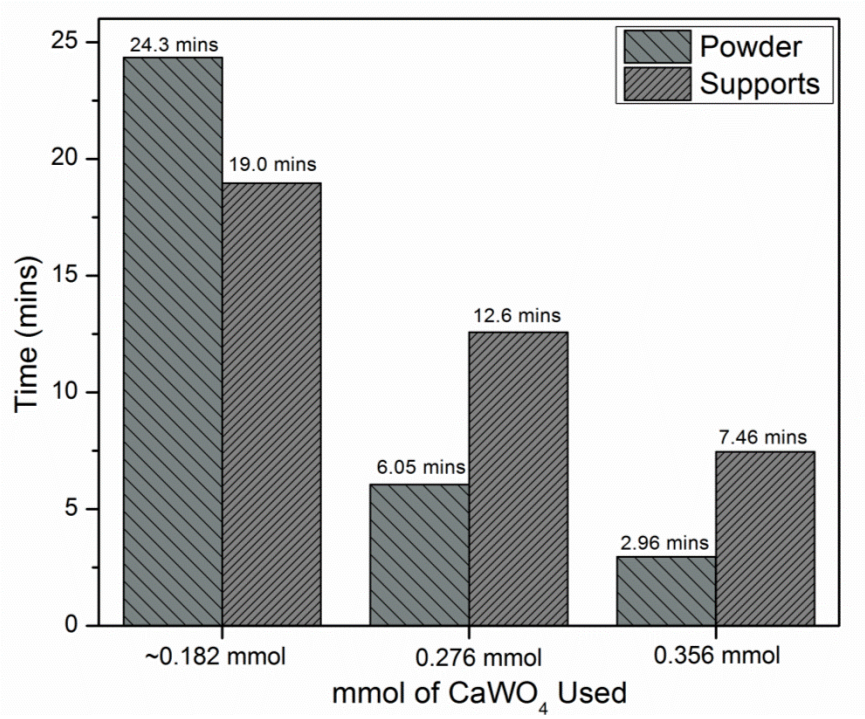

Figure 12: Comparison of Sorption Half-Lives for Pb^{2+}

Sorption Kinetics of Cd^{2+}

The sorption of Cd^{2+} by $CaWO_4$ was monitored in the same fashion as was previously described for Pb^{2+}. After the addition of the sorbents to roughly 50 mL solutions of 126 ppm Cd^{2+}, the analyte concentrations were monitored via GFAAS. Figure 13 portrays the sorption uptake curves of cadmium by five different amounts of calcium tungstate. The uptake curves illustrate a process in which sorption is initially very fast and starts to slow as the reaction approaches the equilibrium state. The sorption processes continued until the entirety of the analyte was removed below the instrument detection limit of roughly 0.3 ppb.

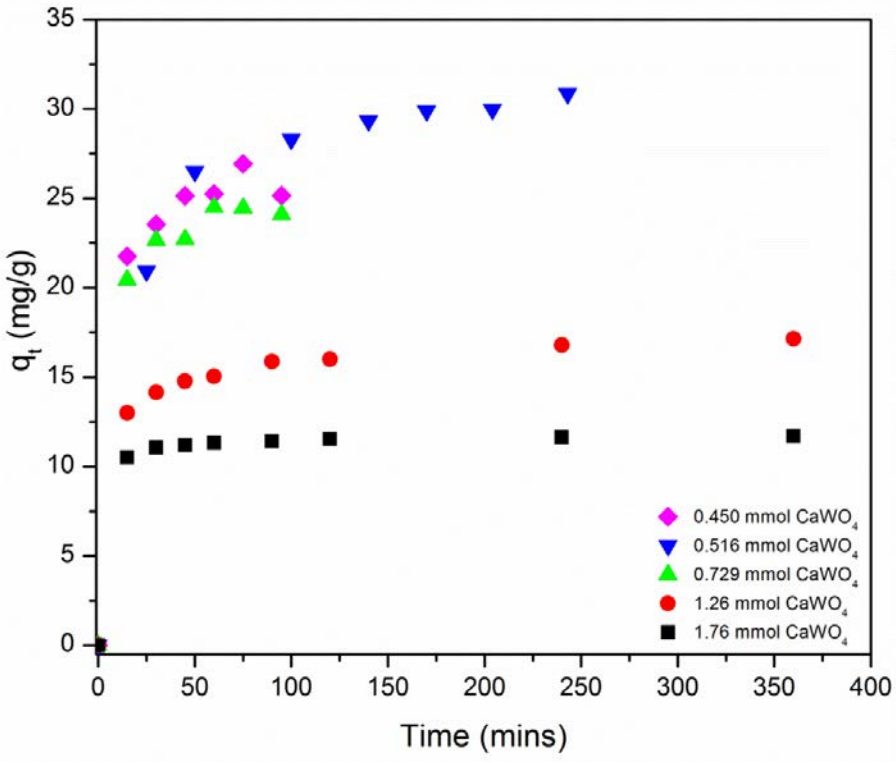

Figure 13: Sorption Uptake Curves for Cd^{2+} by Nanocrystalline $CaWO_4$

The plot of the nonlinear pseudo first-order fit in Figure 14 shows the model fits the data very well, with good correlation coefficients throughout the sorbent loadings. The predicted equilibrium sorption capacities, summarized in Table 9, are in fairly close agreement to the experimental values; however, the fit consistently underestimates these capacities.

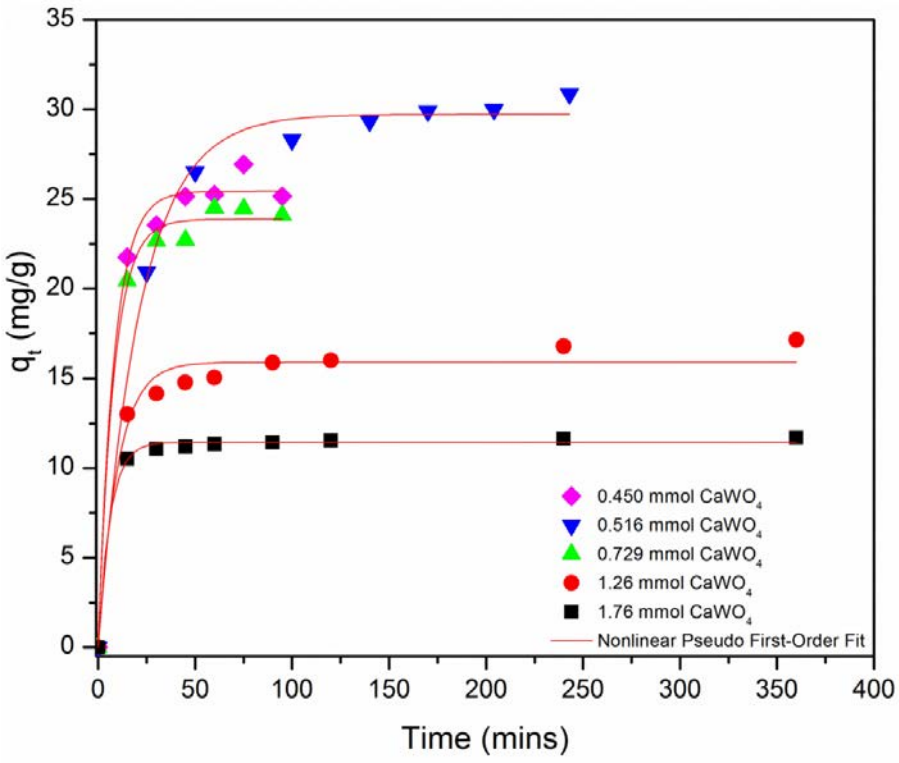

Figure 14: Nonlinear Pseudo First-Order Fit for the Sorption of Cd^{2+} by Nanocrystalline $CaWO_4$

Table 9: Data for the Nonlinear Pseudo First-Order Fit for Cd^{2+} Uptake by Nanocrystalline $CaWO_4$

$CaWO_4$ (mmol)	k_1 (min^{-1})	q_e (mg/g)	q_e (mg/g) (experimental)	R^2
0.450	4.70E-01	29.7	26.9	0.979
0.518	1.22E-01	25.4	30.9	0.923
0.729	1.24E-01	23.9	24.1	0.970
1.26	1.01E-01	15.9	17.2	0.986
1.76	1.64E-01	11.4	11.7	0.984

Figure 15 shows that linear pseudo first-order fit for the sorption of Cd^{2+}. It is obvious from the plotted data that the model does not fit the data very well. Further, from the data summarized in Table 10, the data fit with poor correlation coefficients in most cases and the equilibrium capacities were drastically underestimated throughout the sorbent loadings. This model fails to adequately describe this sorption process.

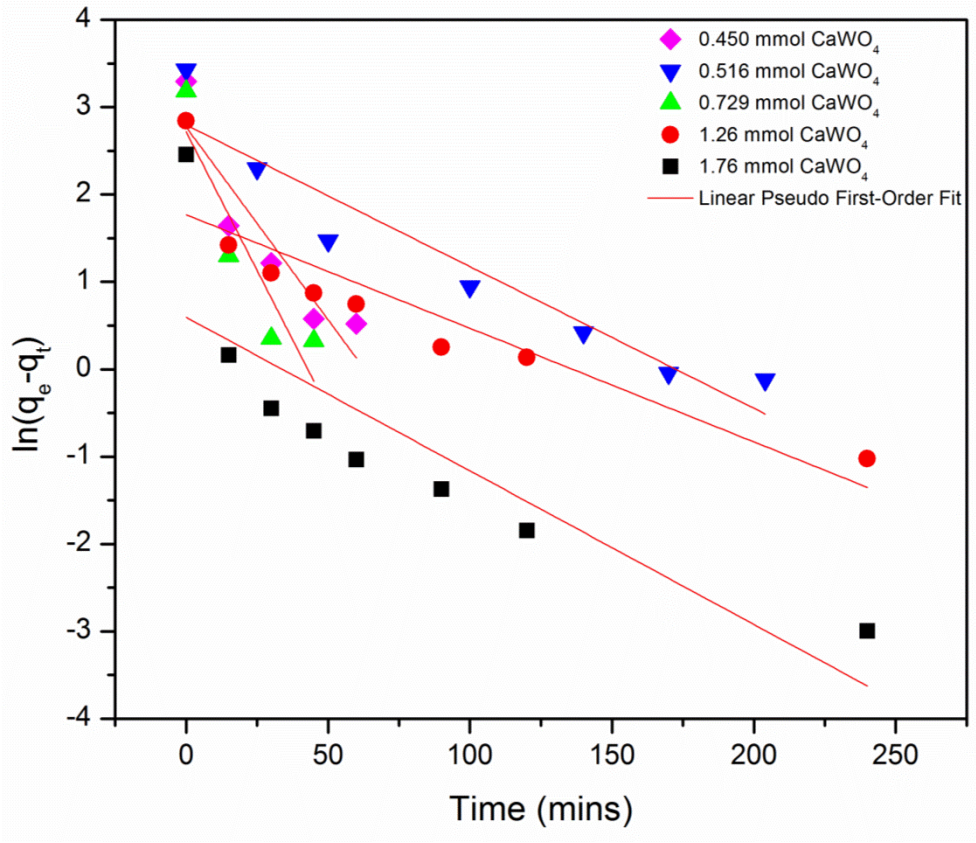

Figure 15: Linear Pseudo First-Order Fit for the Sorption of Cd^{2+} by Nanocrystalline $CaWO_4$

Table 10: Data for the Linear Pseudo First-Order Fit for Cd^{2+} Uptake by Nanocrystalline $CaWO_4$

$CaWO_4$ (mmol)	k_1 (min^{-1})	q_e (mg/g)	q_e (mg/g) (experimental)	R^2
0.450	4.41E-02	16.1	26.9	0.806
0.518	1.62E-02	16.4	30.9	0.895
0.729	6.35E-02	15.1	24.1	0.761
1.26	1.30E-02	5.87	17.2	0.780
1.76	1.76E-02	1.81	11.7	0.674

The nonlinear pseudo second-order model fit had a very good correlation to the data, shown in Figure 16. The data from the function summarized in Table 11 shows perfect R^2 values. Further, the predicted values for the equilibrium capacities are very close to the observed values

for the three highest mass loadings and gave acceptable results for the two lowest sorbent loadings.

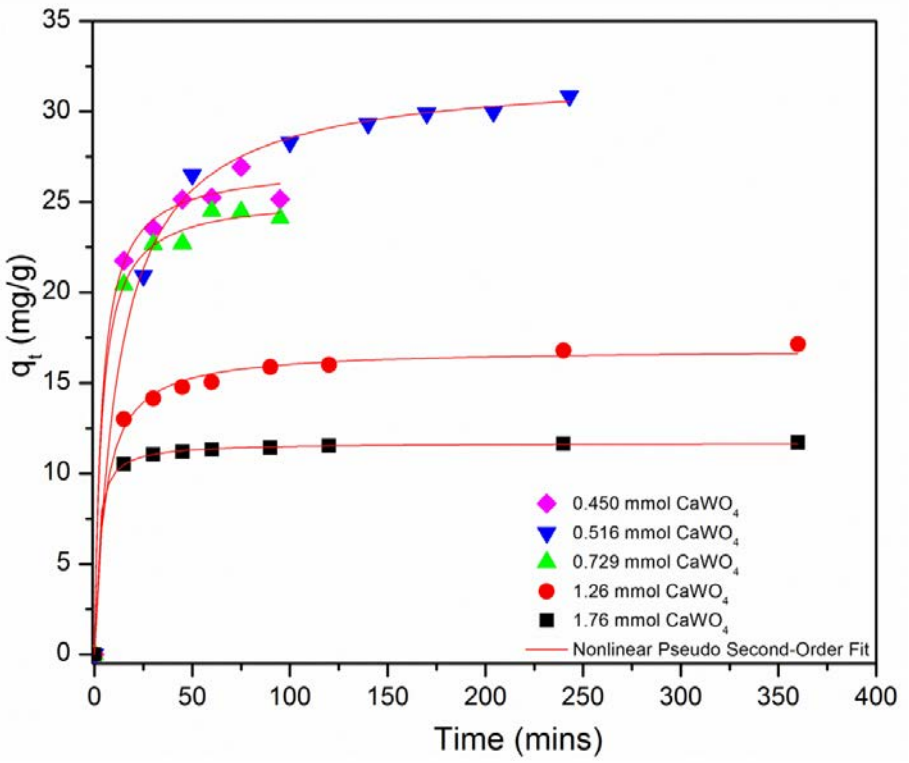

Figure 16: Nonlinear Pseudo Second-Order Fit for the Sorption of Cd^{2+} by Nanocrystalline $CaWO_4$

Table 11: Data for the Nonlinear Pseudo Second-Order Fit for Cd^{2+} Uptake by Nanocrystalline $CaWO_4$

$CaWO_4$ (mmol)	k_2 (g/mg min)	h (mg/g min)	q_e (mg/g)	q_e (mg/g) (experimental)	R^2
0.450	2.45E-03	2.54	32.2	26.9	0.998
0.518	9.87E-03	7.21	27.0	30.9	0.995
0.729	1.08E-02	6.96	25.3	24.1	0.997
1.26	1.14E-02	3.24	16.9	17.2	0.995
1.76	4.93E-02	6.74	11.7	11.7	1.00

Figure 17 shows the fit of the linear pseudo second-order model, which models the data for this sorption process flawlessly. Table 12 shows the data fit the equation with near perfect fits in every case, along with predicting the equilibrium capacities within 2% of the observed values.

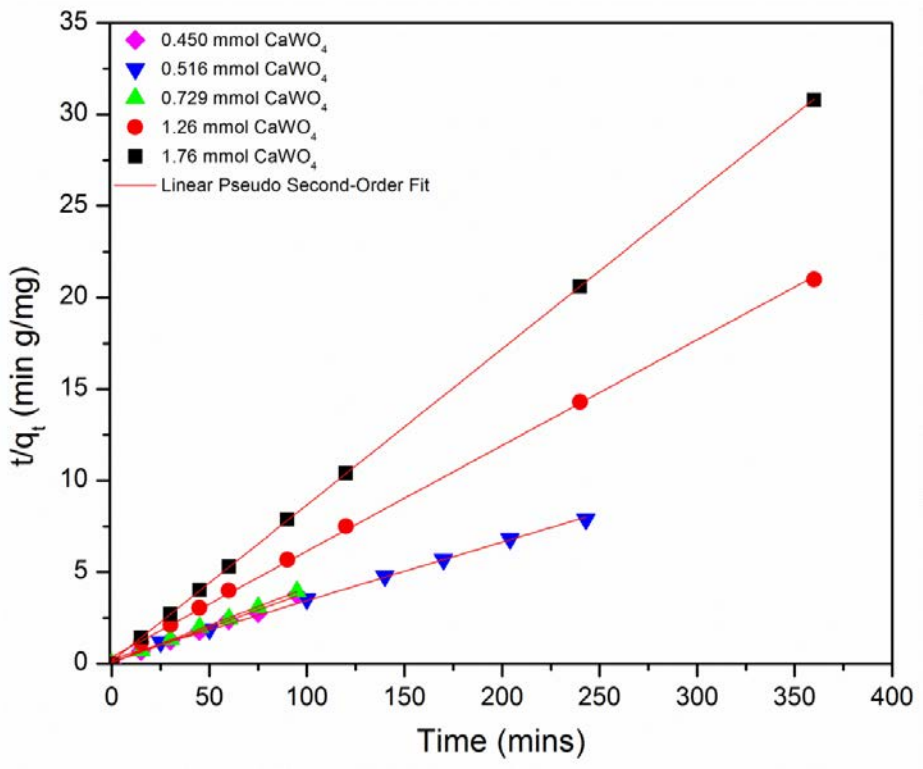

Figure 17: Linear Pseudo Second-Order Fit for the Sorption of Cd^{2+} by Nanocrystalline $CaWO_4$

Table 12: Data for the Linear Pseudo Second-Order Fit for Cd^{2+} Uptake by Nanocrystalline $CaWO_4$

$CaWO_4$ (mmol)	k_2 (g/mg min)	h (mg/g min)	q_e (mg/g)	q_e (mg/g) (experimental)	R^2
0.450	2.30E-02	15.7	26.1	26.9	0.995
0.518	4.08E-03	4.00	31.3	30.9	0.999
0.729	2.16E-02	13.2	24.7	24.1	0.999
1.26	9.01E-03	2.70	17.3	17.2	1.00
1.76	5.08E-02	6.99	11.7	11.7	1.00

Due to the higher mass loading on high surface area alumina, the alumina catalyst supports were impregnated using the calcium tungsten gluconate single-source precursor solution and calcined producing $CaWO_4$ on the support. The mass loading of the $CaWO_4$ was improved to 14.1% with a surface area of 178 m^2/g. The supported material was also analyzed for its ability to sorb aqueous Cd^{2+} in the same fashion as the nanocrystalline $CaWO_4$. Figure 14 shows the

sorption uptake curves with the sorption equilibrium capacities being reached from 120 to 240 minutes in most cases. This sorption process was also modeled using all four equations.

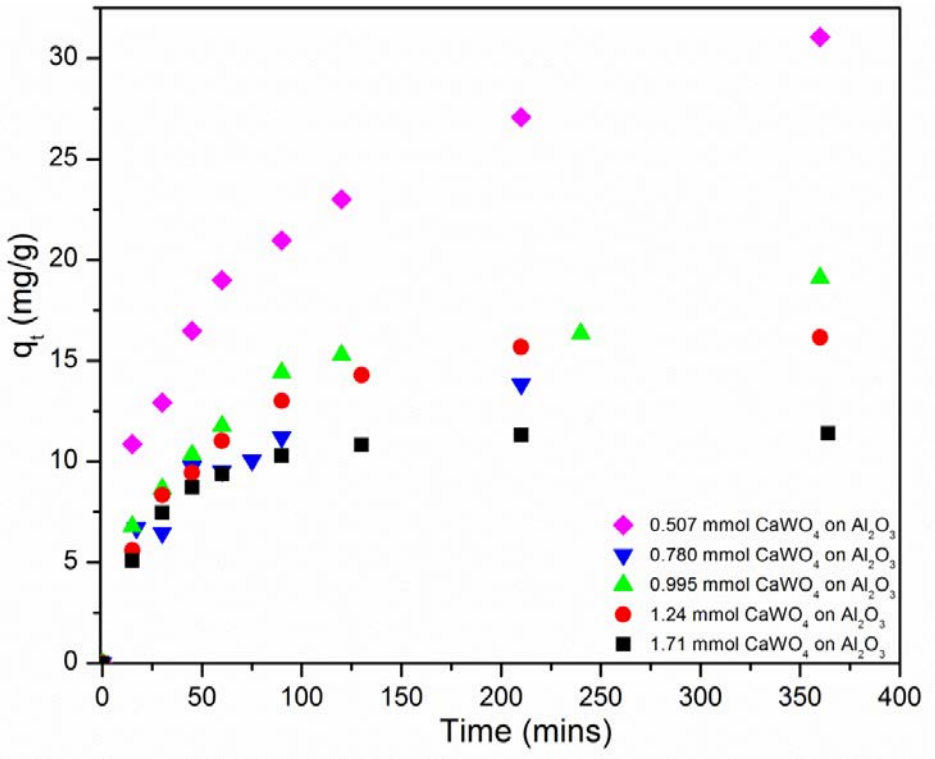

Figure 18: Sorption Uptake Curves of Cd^{2+} by $CaWO_4$ on Al_2O_3

The nonlinear pseudo first order model, in Figure 19, fit the sorption data well as summarized in Table 13. The equation, however, underestimated the equilibrium capacities in every case, and by roughly 20% for the 0.780, 0.995, and 1.24 mmol sorbent loadings.

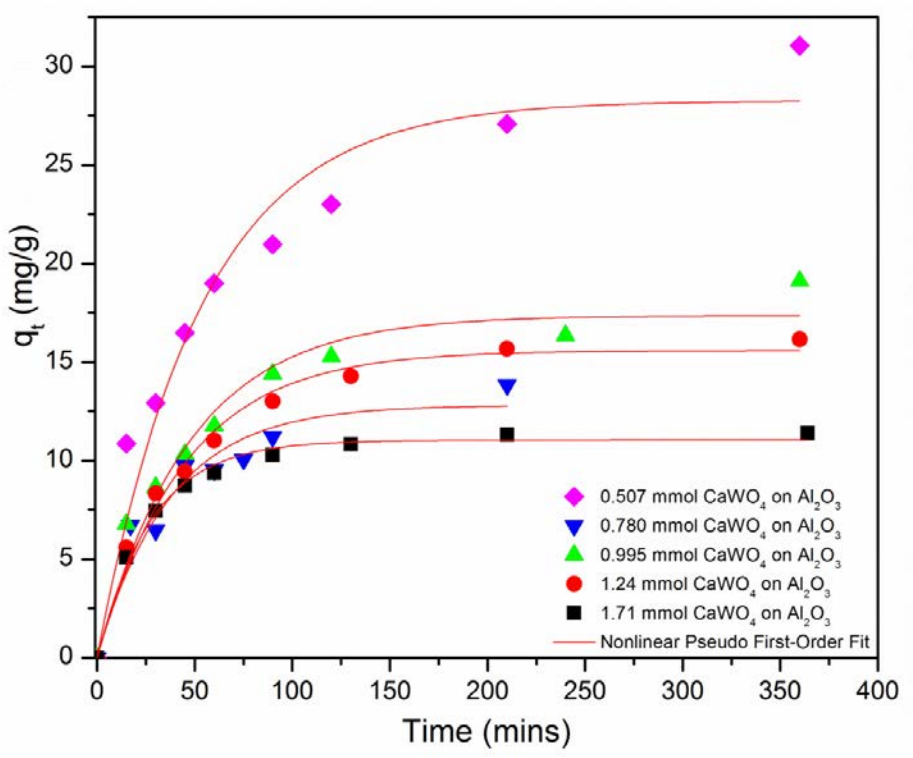

Figure 19: Nonlinear Pseudo Second-Order Fit for the Sorption of Cd^{2+} by $CaWO_4$ on Al_2O_3

Table 13: Data for the Nonlinear Pseudo Second-Order Fit for Cd^{2+} Uptake by $CaWO_4$ on Al_2O_3

$CaWO_4$ (mmol)	k_1 (min^{-1})	q_e (mg/g)	q_e (mg/g) (experimental)	R^2
0.507	1.87E-02	28.3	31.1	0.944
0.780	2.11E-02	17.4	22.2	0.959
0.995	2.23E-02	15.6	19.1	0.984
1.24	2.70E-02	12.8	16.2	0.923
1.71	3.62E-02	11.0	11.4	0.992

Figure 20 shows the linear pseudo first-order model, which again does not model the data in an acceptable fashion, albeit the model fits this data better than the data from the nanocrystalline powder. With this, the model still severely underestimates the equilibrium capacities of the materials.

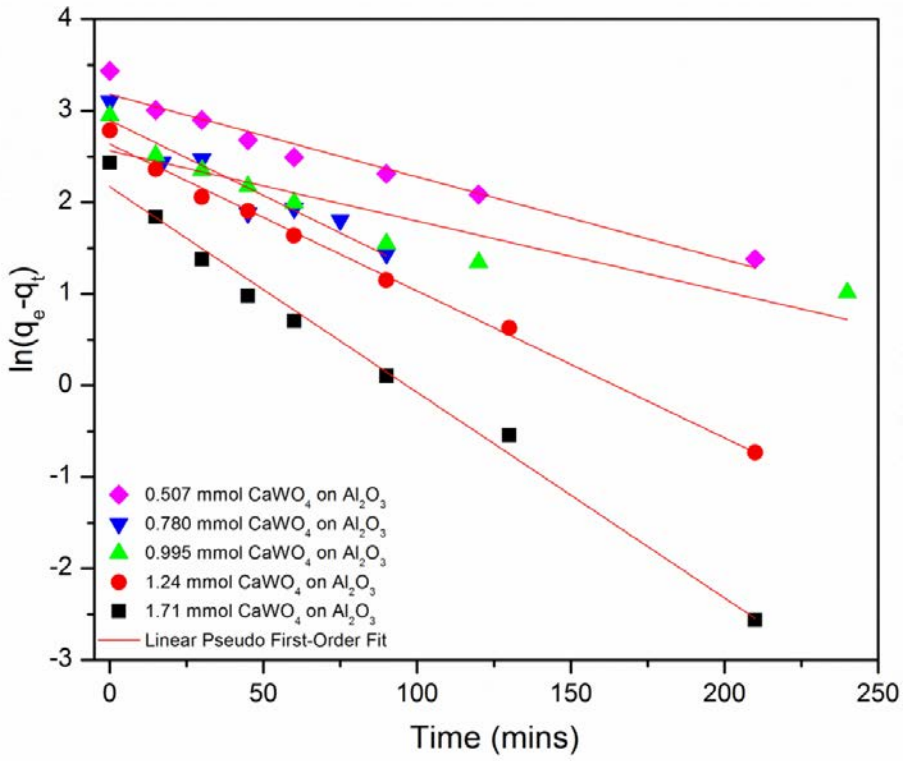

Figure 20: Linear Pseudo First-Order Fit for the Sorption of Cd^{2+} by $CaWO_4$ on Al_2O_3

Table 14: Data for the Linear Pseudo First-Order Fit for Cd^{2+} Uptake by $CaWO_4$ on Al_2O_3

$CaWO_4$ (mmol)	k_1 (min^{-1})	q_e (mg/g)	q_e (mg/g) (experimental)	R^2
0.507	9.02E-03	24.0	31.1	0.954
0.780	1.64E-02	18.1	22.2	0.886
0.995	7.68E-03	13.0	19.1	0.821
1.24	1.60E-02	14.0	16.2	0.994
1.71	2.24E-02	8.74	11.4	0.988

Figure 21 shows the fit of the nonlinear pseudo second-order equation fit for the sorption of Cd^{2+} by $CaWO_4$ on alumina. The fit has very good correlation coefficients and gives predicted q_e values that are fairly close to the values observed experimentally, summarized in Table 15. The initial sorption rates do not seem to have any correlation with the rate constant or the masses of the sorbents.

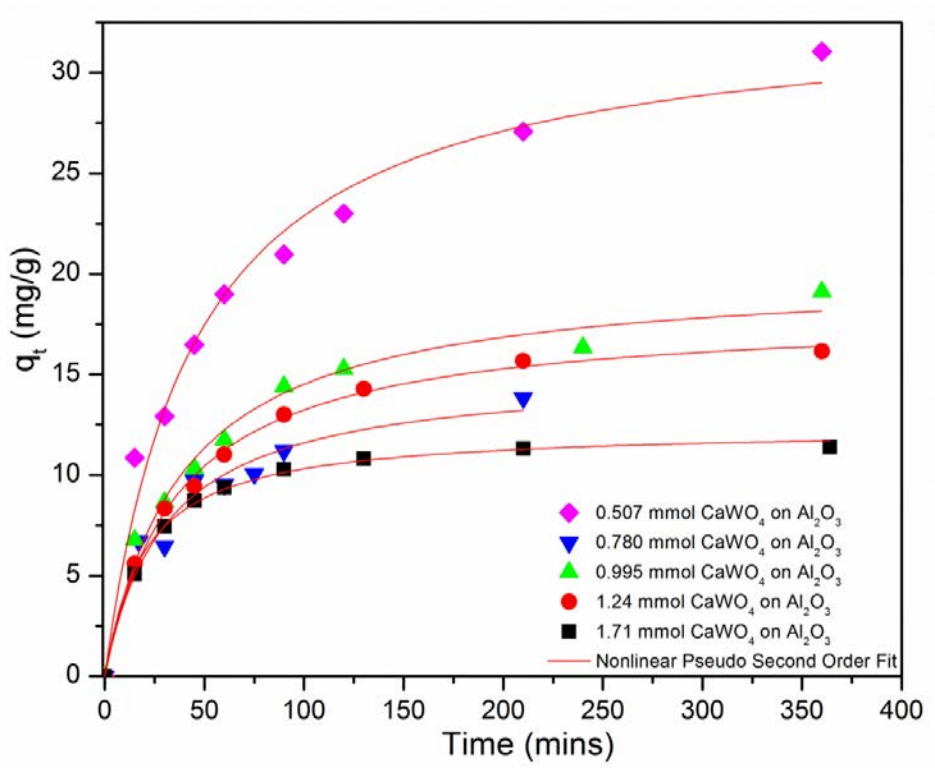

Figure 21: Nonlinear Pseudo Second-Order Fit for the Sorption of Cd^{2+} by $CaWO_4$ on Al_2O_3

Table 15: Data for the Nonlinear Pseudo Second-Order Fit for Cd^{2+} Uptake by $CaWO_4$ on Al_2O_3

$CaWO_4$ (mmol)	k_2 (g/mg min)	h (mg/g min)	q_e (mg/g)	q_e (mg/g) (experimental)	R^2
0.507	6.69E-04	0.738	33.2	31.1	0.980
0.780	1.29E-03	0.522	20.1	22.2	0.984
0.995	1.52E-03	0.496	18.1	19.1	0.997
1.24	2.16E-03	0.495	15.2	16.2	0.957
1.71	4.13E-03	0.629	12.3	11.4	0.998

The linear pseudo second-order equation also fits the sorption data very well, as pictured in Figure 22. The model predicts the equilibrium capacities with good accuracy throughout the mass loadings, with great correlation coefficients, as summarized in Table 16.

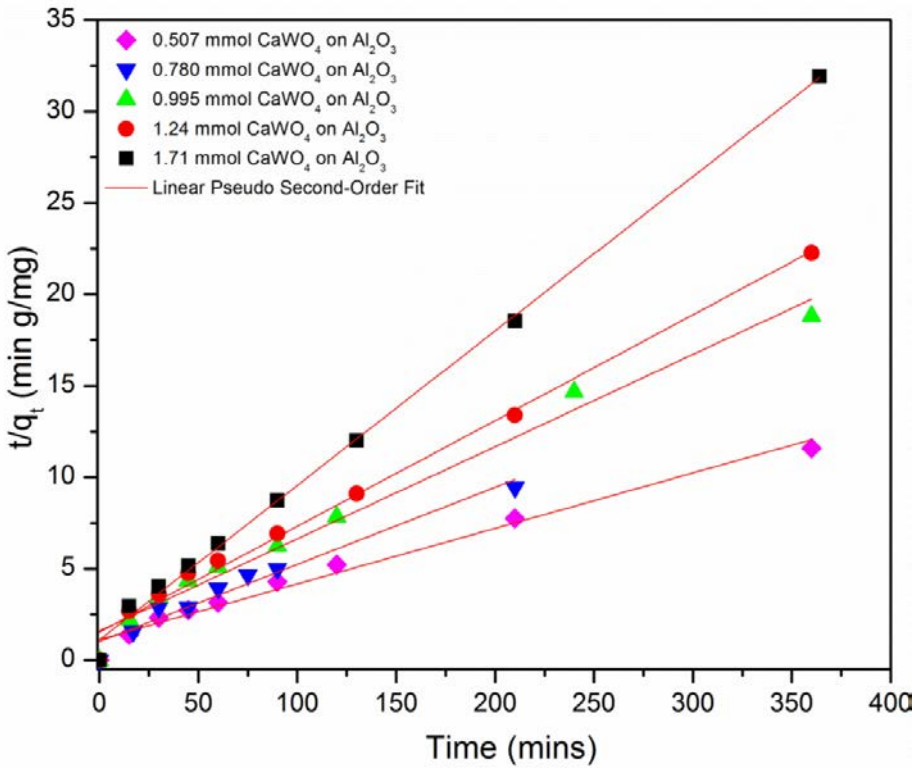

Figure 22: Nonlinear Pseudo Second-Order Fit for the Sorption of Cd^{2+} by $CaWO_4$ on Al_2O_3

Table 16: Data and Results for the Nonlinear Pseudo Second-Order Fit for the Uptake of Cd^{2+} by $CaWO_4$ on Al_2O_3

$CaWO_4$ (mmol)	k_2 (g/mg min)	h (mg/g min)	q_e (mg/g)	q_e (mg/g) (experimental)	R^2
0.507	8.12E-04	0.881	32.9	31.1	0.989
0.780	1.74E-03	0.979	23.7	22.2	0.982
0.995	1.60E-03	0.628	19.8	19.1	0.991
1.24	2.18E-03	0.652	17.3	16.2	0.996
1.71	6.38E-03	0.895	11.8	11.4	0.999

For the sorption of Cd^{2+} by $CaWO_4$, both the pseudo second-order models give very good results. However, due to their limited physical meanings, the powder and supported data can only be compared using the pseudo first-order models. Similar to the uptake of lead, the linear pseudo first-order model failed to appropriately describe the sorption processes. Thus the data from the nonlinear pseudo first-order models were compared yielding sorption half-lives. The half-life for the two lowest sorbent loadings is presented in Figure 23. The results show that the nanocrystalline $CaWO_4$ sample has a sorption half-life twice that of the supported material, which

again could be due to slow movement of the solution into the porous high surface area supports due to escaping air bubbles.

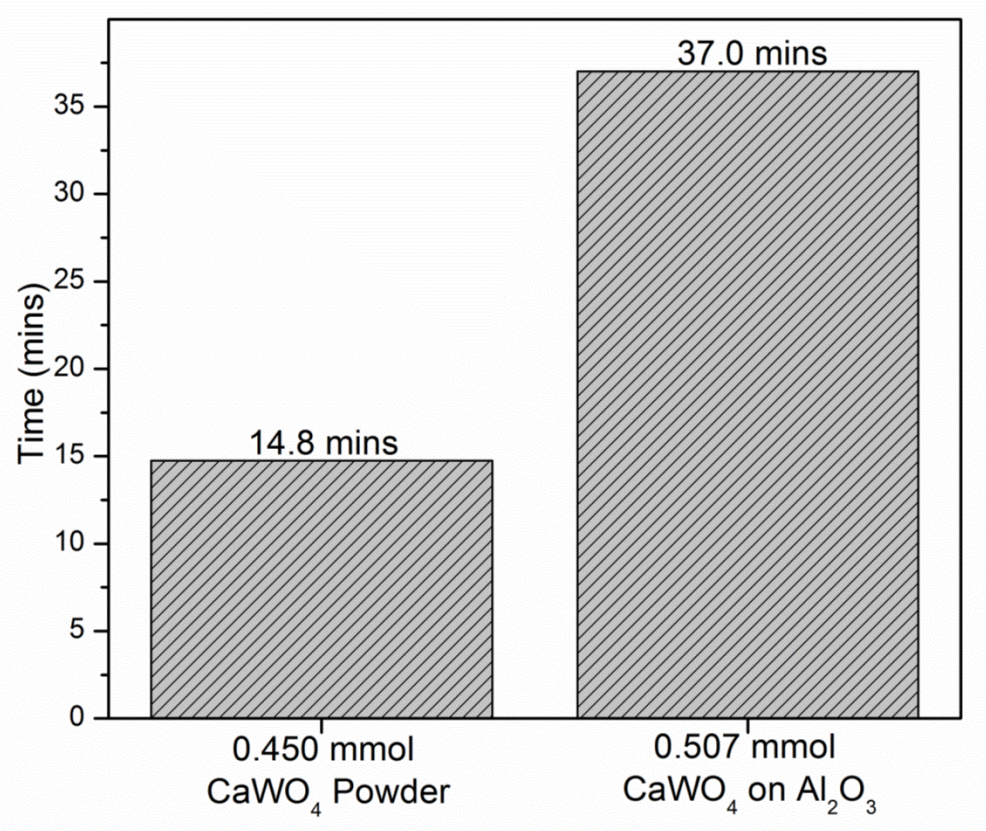

Figure 23: Sorption Half-Life for Cd^{2+} by CaWO4

Sorption Kinetics for Cu^{2+}

The sorption of Cu^{2+} by $CaWO_4$ was monitored in the same fashion previously described for the other two metals. After the addition of the sorbents to roughly 50 mL solutions of 85.7 ppm Cu^{2+}, the analyte concentrations were monitored via GFAAS. Figure 24 shows the sorption uptake curves of copper by five different amounts of calcium tungstate. The uptake curves depict a process in which sorption is initially very fast and starts to slow as the reaction approaches the equilibrium state. The sorption processes continued until the entirety of the analyte was removed below the instrument detection limit of roughly 0.2 ppb.

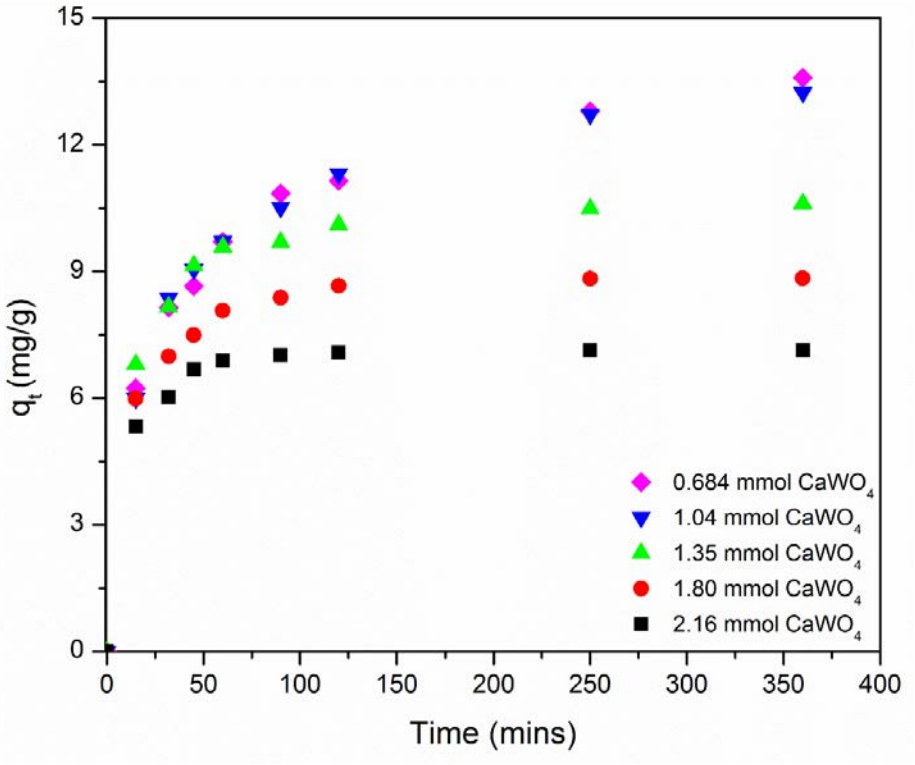

Figure 24: Sorption Uptake Curves for Cu^{2+} by $CaWO_4$

The fit of the nonlinear pseudo first-order equation, shown in Figure 25, shows a good correlation to the sorption uptake curves, giving high correlation coefficients. Further, this model gave very good predictions for sorption capacities throughout the sorbent loadings, within 10% of the experimental values summarized in Table 17.

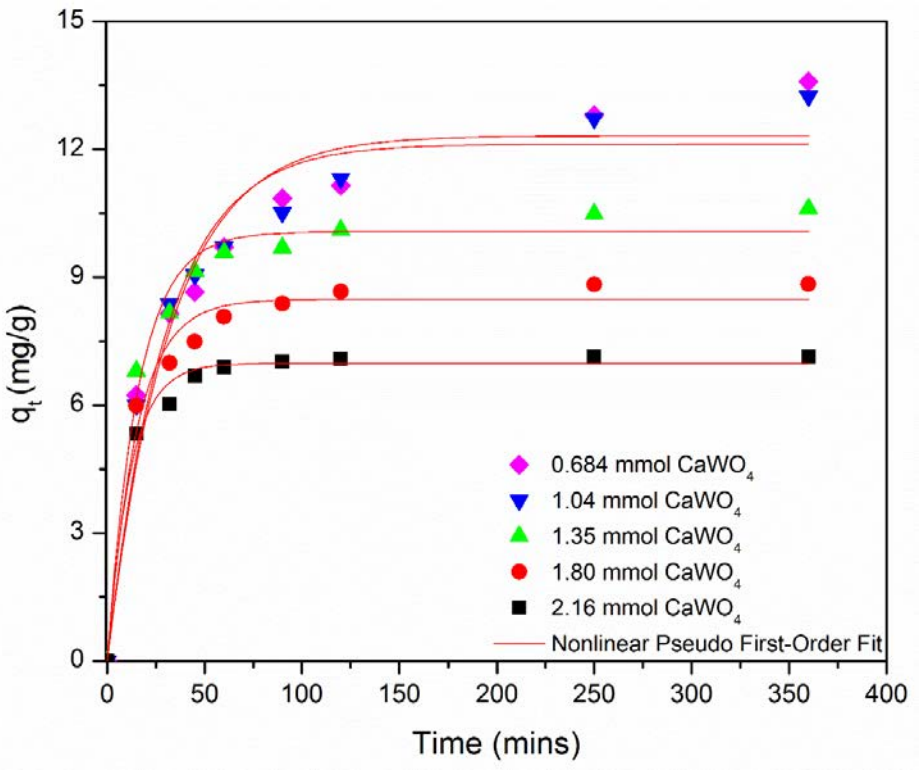

Figure 25: Nonlinear Pseudo First-Order Fit for the Sorption of Cu^{2+} by $CaWO_4$

Table 17: Data and Results for the Nonlinear Pseudo First-Order Fit for the Uptake of Cu^{2+} by $CaWO_4$

$CaWO_4$ (mmol)	k_1 (min^{-1})	q_e (mg/g)	q_e (mg/g) (experimental)	R^2
0.684	3.11E-02	12.3	13.6	0.941
1.04	3.34E-02	12.1	13.2	0.953
1.35	6.31E-02	10.1	10.6	0.981
1.80	6.70E-02	8.48	8.84	0.976
2.16	8.56E-02	6.98	7.14	0.989

The linear pseudo first-order model surprisingly fit the data rather well (Figure 26), with decent R^2 values, listed in Table 18. However, the predicted equilibrium capacities were severely underestimated, with some of the predicted capacities half of the observed values.

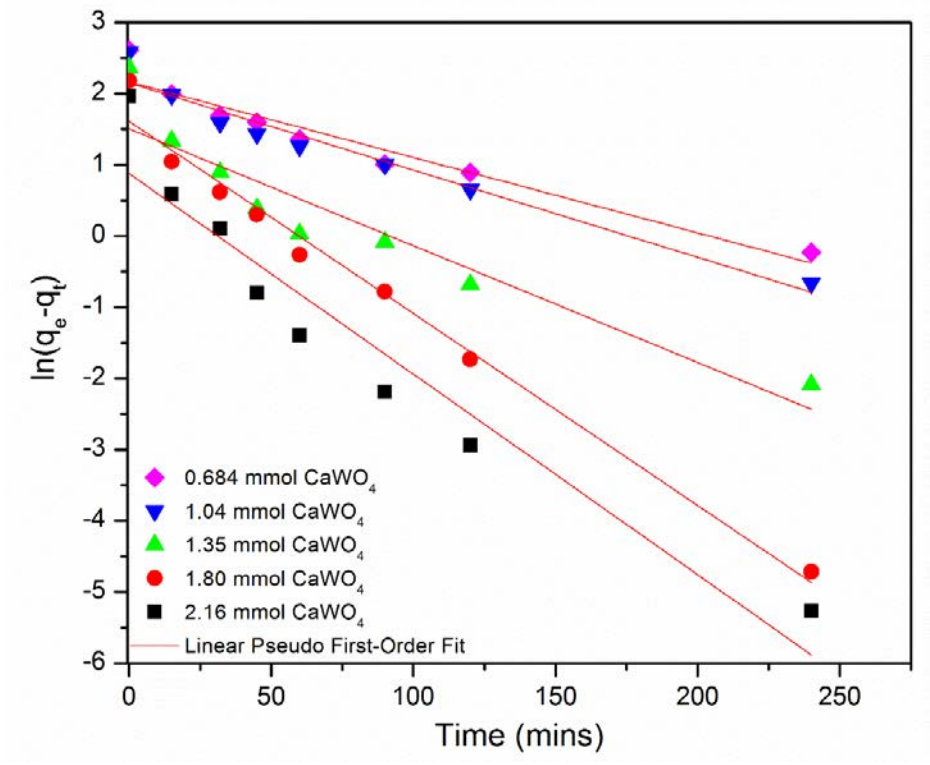

Figure 26: Linear Pseudo First-Order Fit for the Sorption of Cu^{2+} by $CaWO_4$

Table 18: Data and Results for the Linear Pseudo First-Order Fit for the Uptake of Cu^{2+} by $CaWO_4$

$CaWO_4$ (mmol)	k_1 (min^{-1})	q_e (mg/g)	q_e (mg/g) (experimental)	R^2
0.684	1.06E-02	8.70	13.6	0.926
1.04	1.22E-02	8.59	13.2	0.949
1.35	1.64E-02	4.51	10.6	0.878
1.80	2.70E-02	5.01	8.84	0.982
2.16	2.52E-02	2.41	7.14	0.916

The linear pseudo-second order model (Figure 27) fits the data with perfect correlation coefficients, as listed in Table 19. Further, the model gives excellent predictions of the equilibrium capacities, all within 3%.

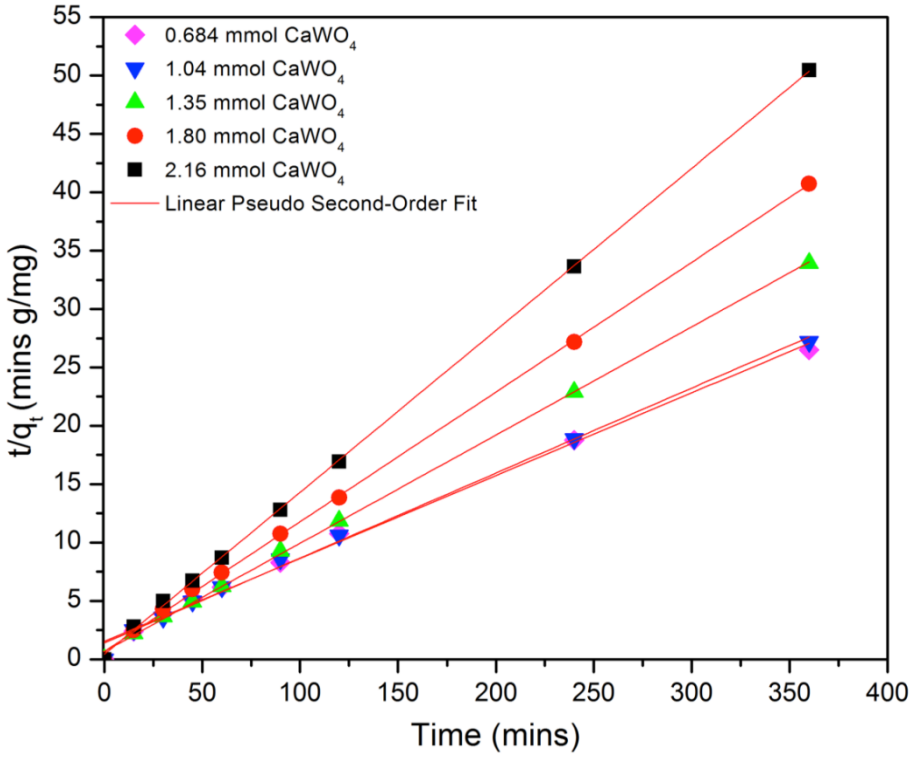

Figure 27: Linear Pseudo Second-Order Fit for the Sorption of Cu^{2+} by $CaWO_4$

Table 19: Data and Results for the Linear Pseudo First-Order Fit for the Uptake of Cu^{2+} by $CaWO_4$

$CaWO_4$ (mmol)	k_2 (g/mg min)	h (mg/g min)	q_e (mg/g)	q_e (mg/g) (experimental)	R^2
0.684	3.24E-03	0.645	14.1	13.6	0.992
1.04	3.80E-03	0.717	13.7	13.2	0.994
1.35	1.27E-02	1.48	10.8	10.6	0.999
1.80	1.83E-02	1.48	9.00	8.84	0.999
2.16	4.40E-02	2.29	7.21	7.14	1.00

High surface area catalyst supports with a mass loading of 9.65% and a surface area of 181 m^2/g were used to treat a Cu^{2+} solution with a concentration of 85.7 ppm. The supported material was also analyzed for its ability to sorb aqueous Cu^{2+} in the same fashion as the $CaWO_4$ powder. The sorption process was also modeled using all four pseudo order functions and analyzed for their fits and predictive abilities. Figure 28 shows the sorption uptake curves of Cu^{2+} by $CaWO_4$ on alumina.

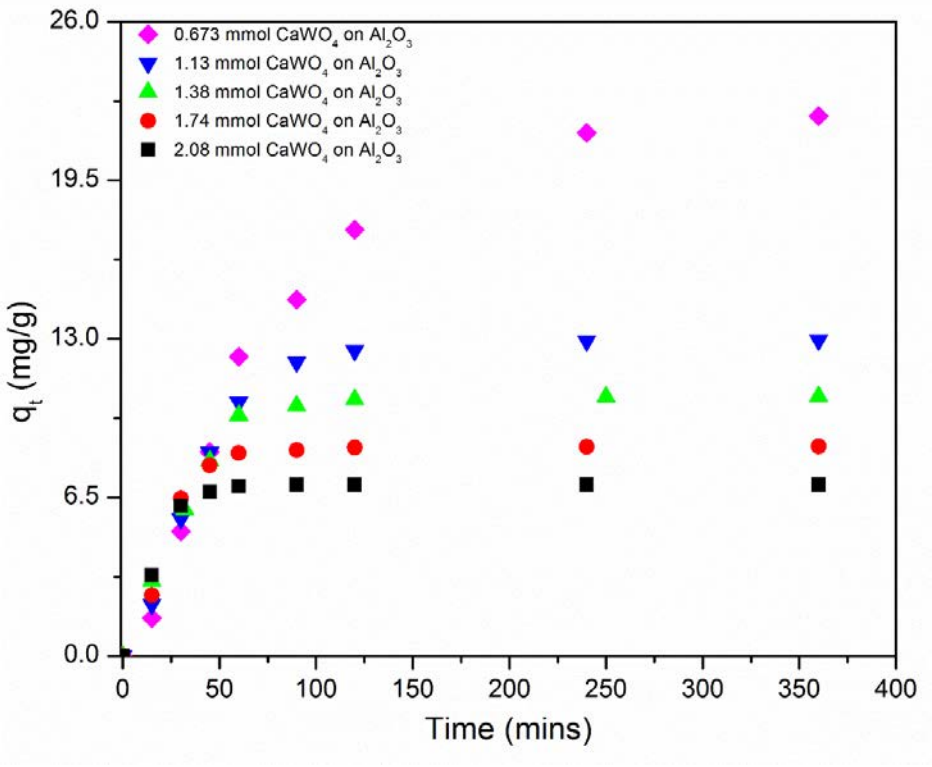

Figure 28: Sorption Uptake Curve of Cu^{2+} by $CaWO_4$ on Al_2O_3

The fit of the nonlinear pseudo first-order equation (Figure 29) showed a good correlation to the sorption uptake curve, giving high correlation coefficients. Further, this model gave very good sorption capacities predictions throughout the sorbent loadings, within 5% of the experimental values summarized in Table 21.

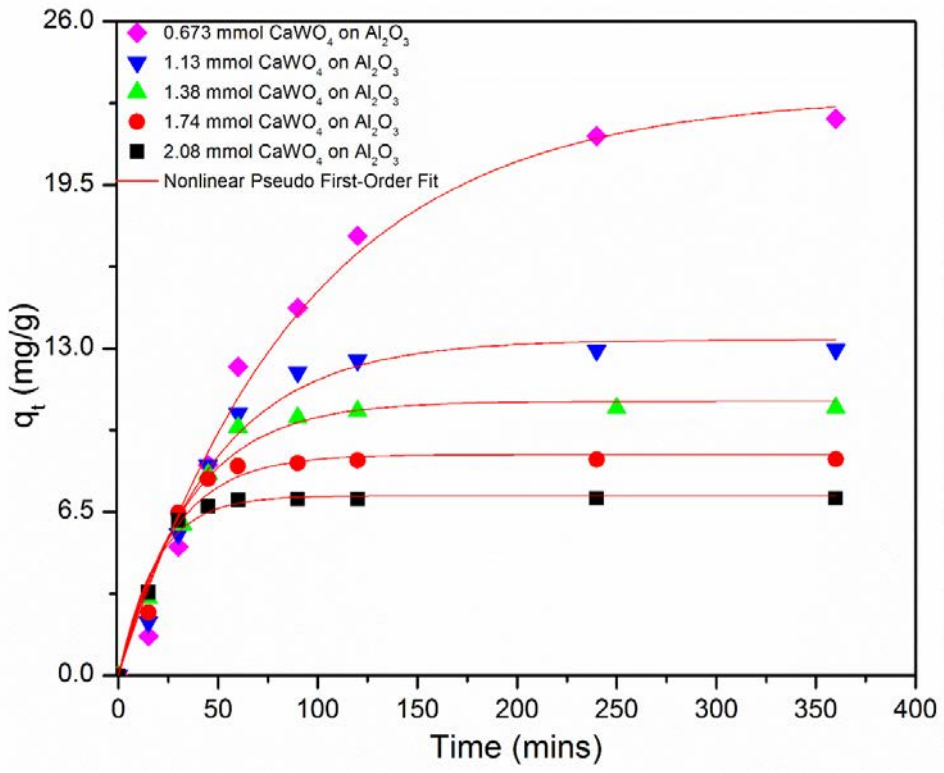

Figure 29: Nonlinear Pseudo First-Order Fit of the Uptake of Cu^{2+} by $CaWO_4$ on Al_2O_3

Table 20: Data from the Nonlinear Pseudo First-Order Fit of the Uptake of Cu^{2+} by $CaWO_4$ on Al_2O_3

$CaWO_4$ (mmol)	k_1 (min^{-1})	q_e (mg/g)	q_e (mg/g) (experimental)	R^2
0.673	1.08E-02	23.1	22.1	0.983
1.13	2.12E-02	13.3	12.9	0.975
1.38	2.84E-02	10.9	10.6	0.982
1.74	3.83E-02	8.78	8.59	0.962
2.08	5.31E-02	7.14	7.03	0.983

However, Figure 30 shows that the linear pseudo first-order model gave very poor results for the sorption data. Table 22 shows acceptable correlation coefficients for most of the process, but gave very poor results for the predicted sorption capacities. The poor results from this model are consistent for all of the sorption processes discussed in this chapter.

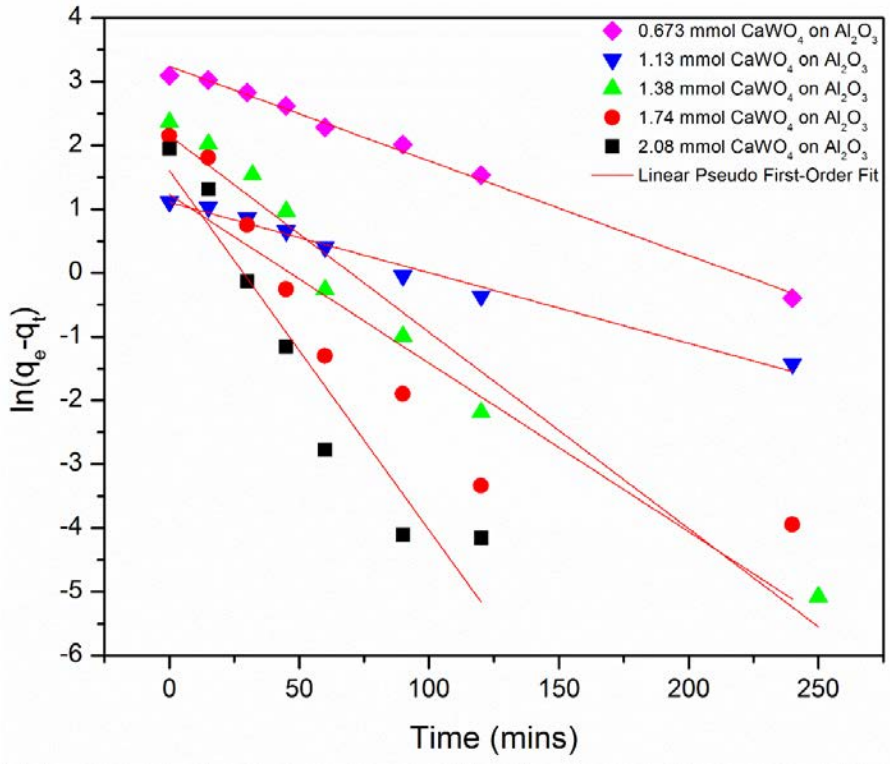

Figure 30: Linear Pseudo First-Order Fit of the Uptake of Cu^{2+} by $CaWO_4$ on Al_2O_3

Table 21: Data from the Linear Pseudo First-Order Fit of the Uptake of Cu^{2+} by $CaWO_4$ on Al_2O_3

$CaWO_4$ (mmol)	k_1 (min^{-1})	q_e (mg/g)	q_e (mg/g) (experimental)	R^2
0.673	1.48E-02	25.5	22.1	0.993
1.13	1.11E-02	3.03	12.9	0.982
1.38	3.08E-02	8.62	10.6	0.962
1.74	2.64E-02	3.42	8.59	0.782
2.08	5.64E-02	4.97	7.03	0.906

Figure 31 shows the nonlinear pseudo second-order equation fits the present data with decent R^2 values throughout the sorbent loadings, summarized in Table 23. The equilibrium capacities calculated from the sorption data from the equation, however, is overestimated in every case. This trend is most severe for the lowest mass loading, giving better results as the mass loading is increased.

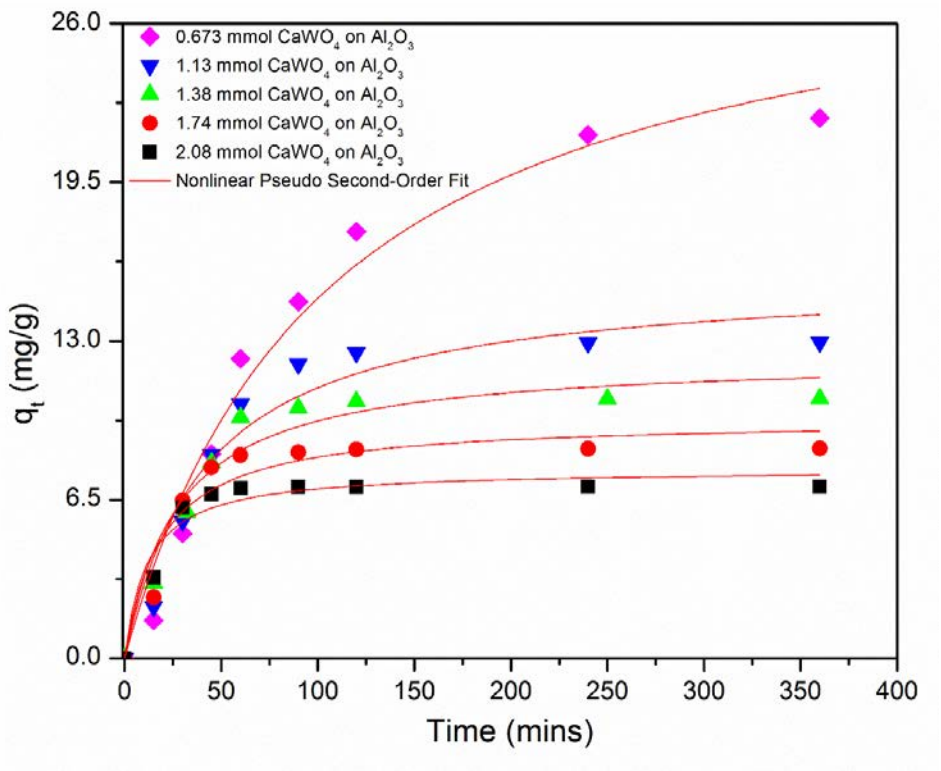

Figure 31: Nonlinear Pseudo Second-Order Fit of the Uptake of Cu^{2+} by $CaWO_4$ on Al_2O_3

Table 22: Data from the Nonlinear Pseudo Second-Order Fit of the Uptake of Cu^{2+} by $CaWO_4$ on Al_2O_3

$CaWO_4$ (mmol)	k_2 (g/mg min)	h (mg/g min)	q_e (mg/g)	q_e (mg/g) (experimental)	R^2
0.673	3.18E-04	0.29	30.1	22.1	0.971
1.13	1.52E-03	0.38	15.7	12.9	0.938
1.38	2.97E-03	0.45	12.4	10.6	0.943
1.74	5.39E-03	0.52	9.79	8.59	0.913
2.08	1.11E-02	0.67	7.74	7.03	0.944

Finally, the linear pseudo second-order model fit this process very well. Figure 32 shows that all of the data fit this function well, besides for the lowest mass loading, suggested by the kinetic data, summarized in Table 24. The data from this model shows very high R^2 values for four of the five sorbent loadings and the model gives good predictions for the q_e values for all of the samples besides the 0.673 mmol loading. Further, the linear model gives better q_e predictions than its nonlinear counterpart.

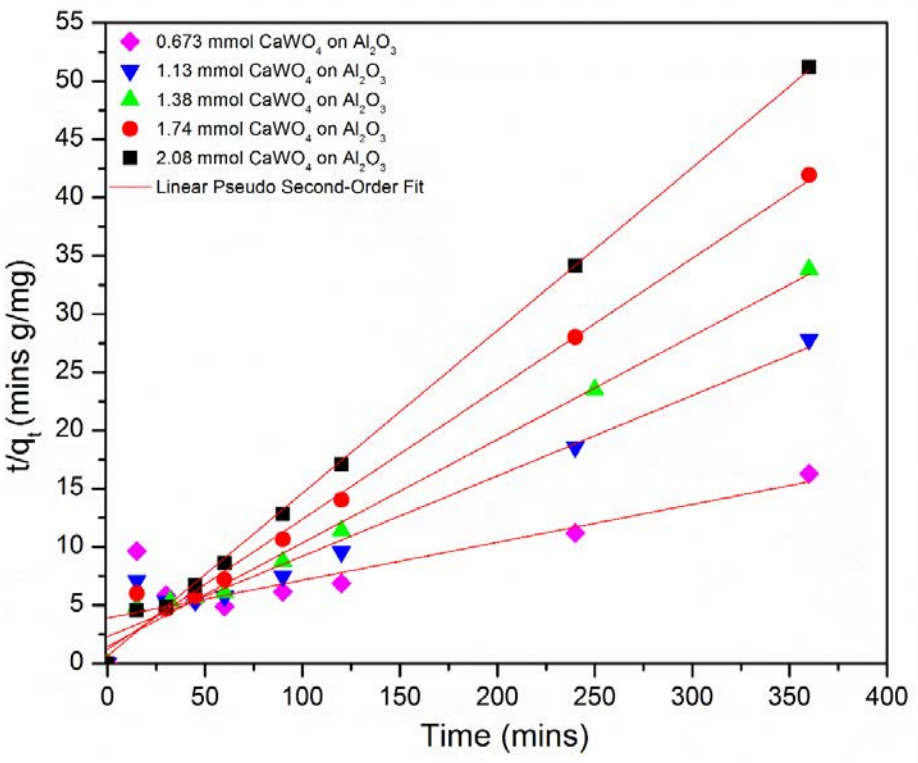

Figure 32 Linear Pseudo Second-Order Fit of the Uptake of Cu^{2+} by $CaWO_4$ on Al_2O_3

Table 23: Data from the Linear Pseudo Second-Order Fit of the Uptake of Cu^{2+} by $CaWO_4$ on Al_2O_3

$CaWO_4$ (mmol)	k_2 (g/mg min)	h (mg/g min)	q_e (mg/g)	q_e (mg/g) (experimental)	R^2
0.673	2.72E-04	0.26	30.7	22.1	0.681
1.13	2.06E-03	0.43	14.5	12.9	0.979
1.38	5.40E-03	0.69	11.3	10.6	0.995
1.74	1.04E-02	0.83	8.94	8.59	0.996
2.08	2.99E-02	1.53	7.16	7.03	0.998

For the sorption of Cu^{2+} by $CaWO_4$, both of the pseudo second-order models give very good results, similar to the sorption of the other two metals. Further, the linear pseudo first-order model also failed to appropriately describe the sorption processes for all of the heavy metal sorption processes. The nonlinear pseudo first-order data can be used to compare sorption half-lives for the sorption of copper. The half-life for the two lowest sorbent loadings is presented in Figure 33. The results show that the nanocrystalline sample reaches its sorption half-life more

than three times as fast as the supported material, which again could be due to slow infiltration of the solution into the porous high surface area supports.

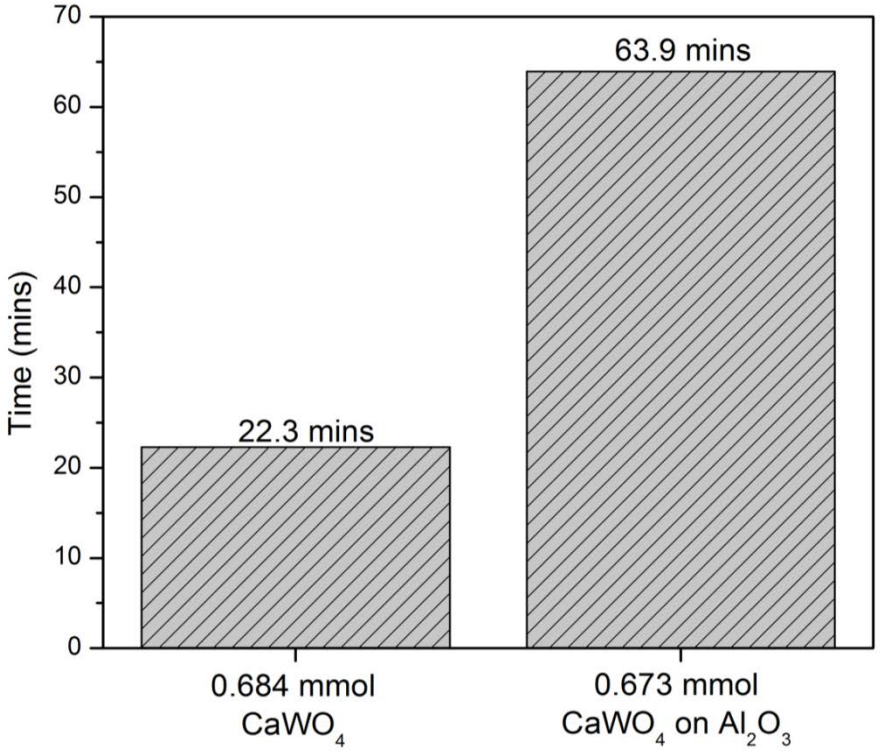

Figure 33: Sorption Half-Lives of Cu^{2+} for Nanocrystalline and Supported $CaWO_4$

Capacity and Characterization

The capacities of the materials for lead were determined by treating solutions with lead in a slight excess. A roughly 50 mL solution containing 15,000 ppm Pb^{2+} was treated with 0.960 g of $CaWO_4$. This provided a molar ratio of 1.05 to 1.00 of $CaWO_4$:Pb^{2+}. Upon completion, analytical measurements demonstrated that the $CaWO_4$ powder was able to remove roughly 70% of the lead from the solution. The material from this study was analyzed by TEM, SEM, XRD, and Raman spectroscopy.

The diffraction pattern (Figure 20) shows the formation of crystalline $PbWO_4$, (stolzite). As expected, due to capacity of only 70 mol % of lead, peaks from the parent material were also observed in the pattern. Since both materials adopt the scheelite-type structure, it is believed that sorption proceeds via an ion-exchange process. Furthermore, the absence of the metastable raspite

structure of $PbWO_4$ from the XRD supports the hypothesis of ion-exchange rather than a dissolution/reprecipitation reaction. It has been previously reported that under precipitation experiments, $PbWO_4$ crystallizes in both the stolzite and raspite phases.[23]

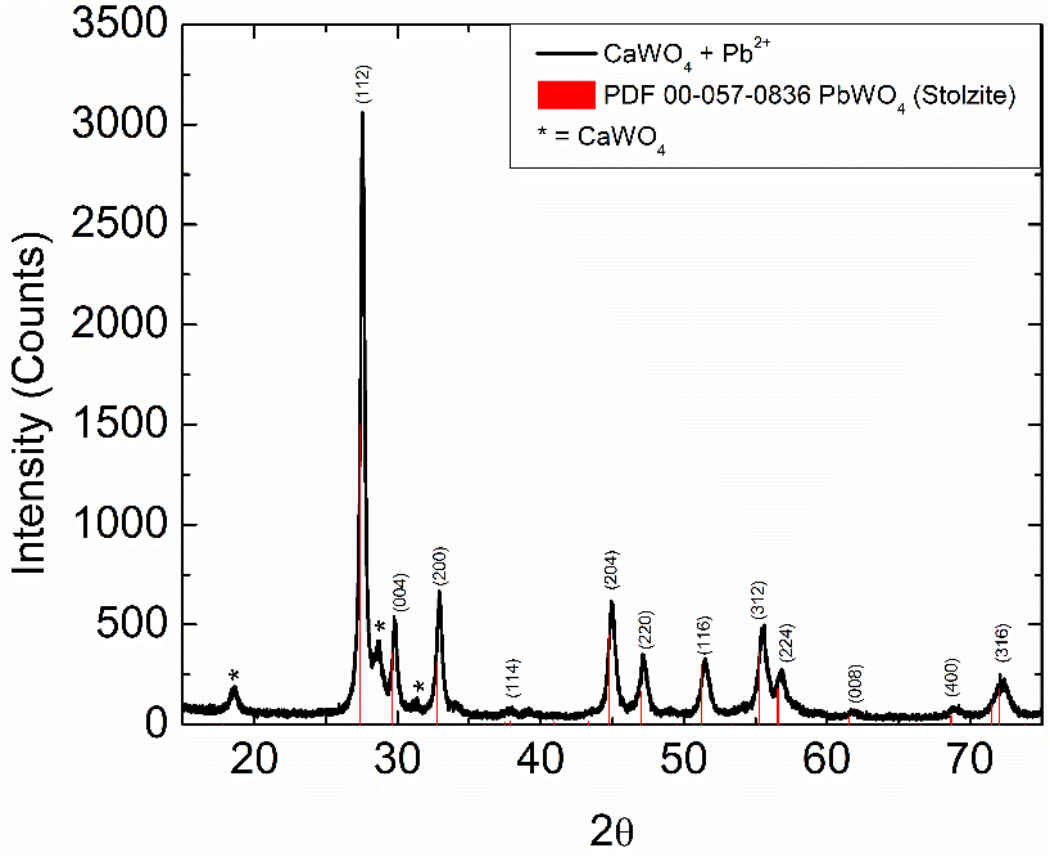

Figure 34: Diffraction Pattern of the $CaWO_4$ Material Saturated with Lead

The Raman spectrum (Figure 21) is consistent with the XRD results, showing only the appearance of new peaks that are characteristic of stolzite. Two small peaks are still present that are due to calcium tungstate at 835 and 398 cm^{-1}. These are, respectively, the ν_4 and ν_3 bands of the tetrahedral tungstate ions. The symmetric stretching band, $\nu_1(A_g)$, for the tetrahedral tungstate ion in $PbWO_4$ appears at 905 cm^{-1}. The ν_3 stretch is split into two bands at 765 and 752 cm^{-1} for the $\nu_3(B_g)$ and $\nu_3(E_g)$ bands, respectively. The $\nu_2(A_g)$ vibration for stolzite is observed as a strong band at 325 cm^{-1}, along with the weaker $\nu_2(B_g)$ band at 356 cm^{-1}. The band at 178 cm^{-1} is due to the ν(Pb-O) stretch of the $PbWO_4$.[24, 25, 26]

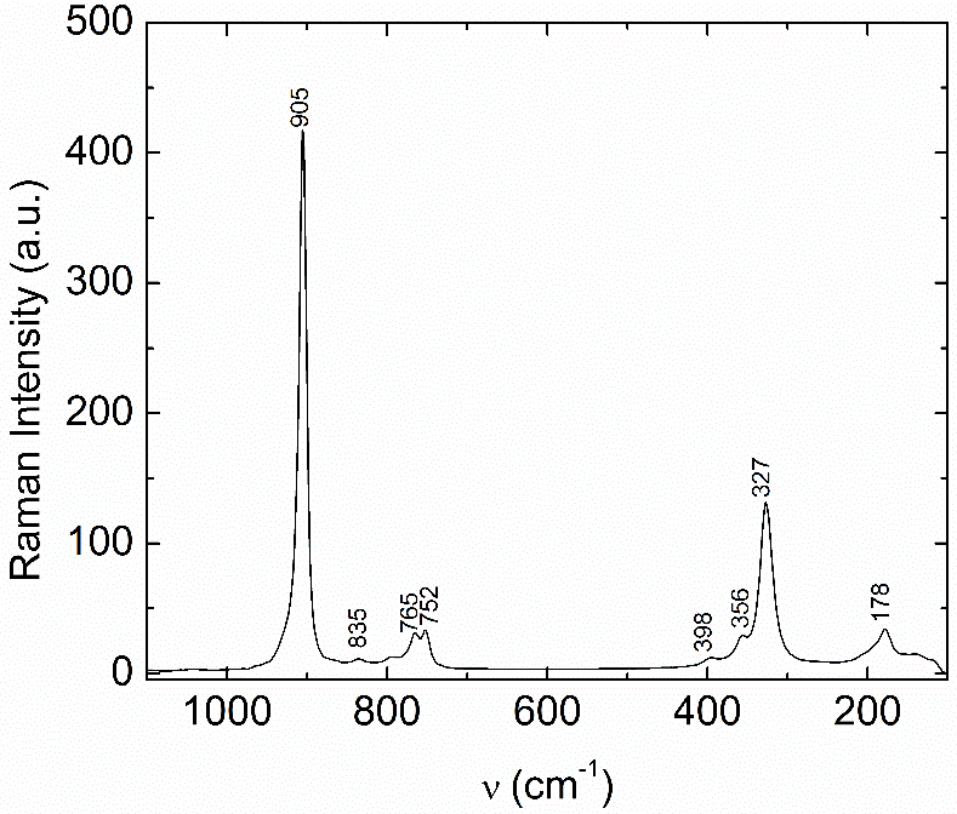

Figure 35: Raman Spectrum of the Material Saturated with Lead

The effect of lead uptake on the morphology of the tungstate particles was investigated by scanning electron microscopy. The micrographs (Figure 22) show there was no morphological changes upon sorption of lead. This provides further support for an ion exchange mechanism since it is reasonable that such a process would leave the morphology unchanged. Other mechanisms that would produce new $PbWO_4$ particles would be expected to change the morphology.[27, 28]

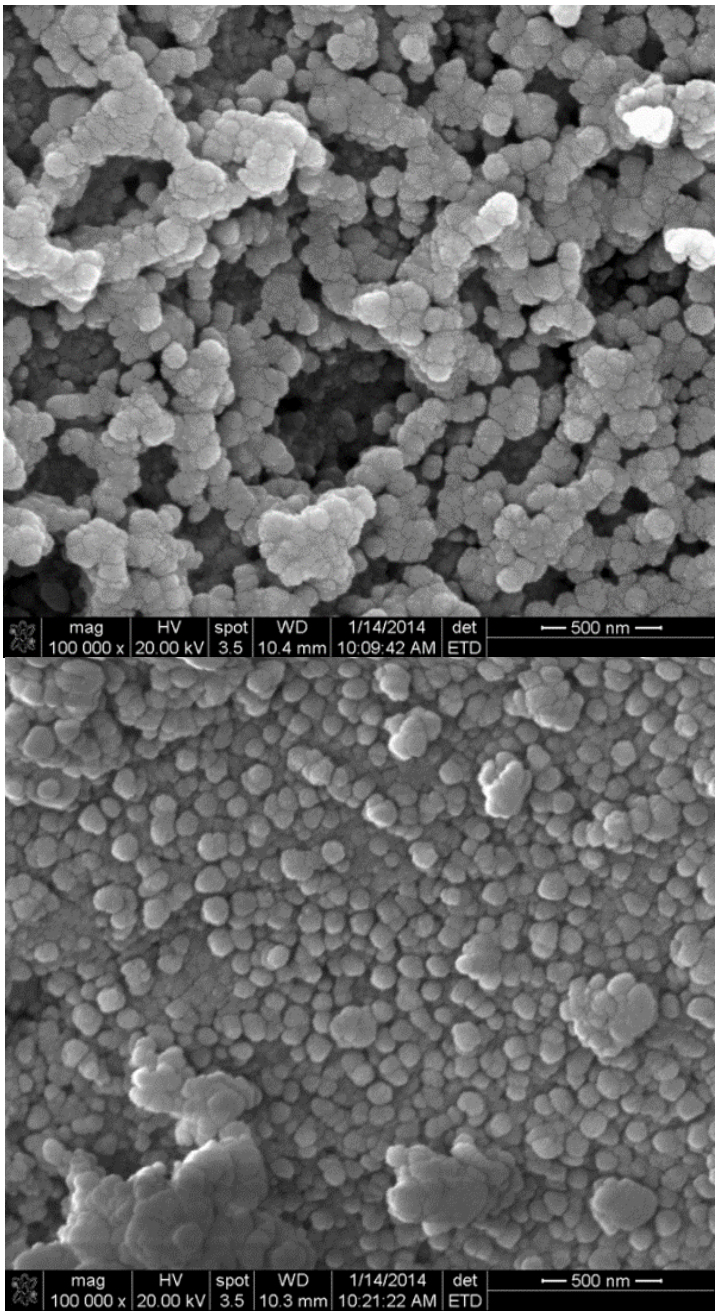

Figure 36: SEM micrographs of $CaWO_4$ (top) and $CaWO_4$ Reacted with Pb^{2+} (bottom)

Embedding and sectioning of these agglomerates with a microtome allowed their nanocrystalline nature to be imaged by transmission electron microscopy. The resulting micrographs clearly show tabular particles of $CaWO_4$ with an average size of 58 ± 24 nm. After reaction with lead, the morphology of the nanoparticles remained unchanged shown in Figure 37. The particle sizes of 42 ± 17 nm were well within the standard deviation of the starting materials

as well. Lattice fringes could be observed for a few of the particles of the lead treated material. These had spacing's that corresponded to the (001) and (110) planes of stolzite.

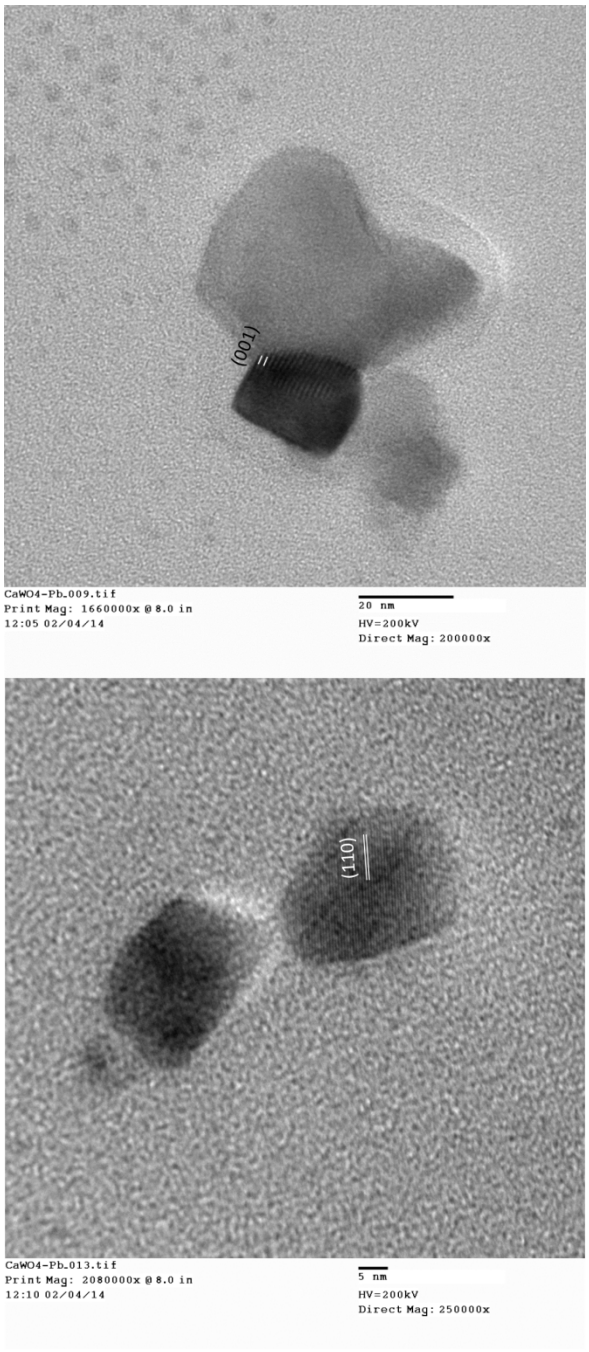

Figure 37: HRTEM of $CaWO_4$ Saturated with Lead

The capacity of the supported material was also determined to see if there was any effect on the extent of the reaction. Under similar reaction conditions as the powder, the supported

$CaWO_4$ was able to convert wholly to $PbWO_4$. The increased capacity likely results from the smaller particles of the supported material that allows penetration of the lead ions to the cores of the particles. X-ray diffraction showed the SiO_2 supported $CaWO_4$ and the lead treated material were both amorphous. By supporting $CaWO_4$ on high surface Al_2O_3 pellets, a slightly higher loading of 8.3% was achieved. Similar to the SiO_2 supported material, the Al_2O_3 supported $CaWO_4$ was fully converted to $PbWO_4$ when reacted with excess Pb^{2+}. XRD analysis of the $CaWO_4$ supported on Al_2O_3 also gave no indication of crystalline scheelite. Upon reaction with lead, the amorphous $CaWO_4$ was converted to crystalline stolzite (Figure 38).

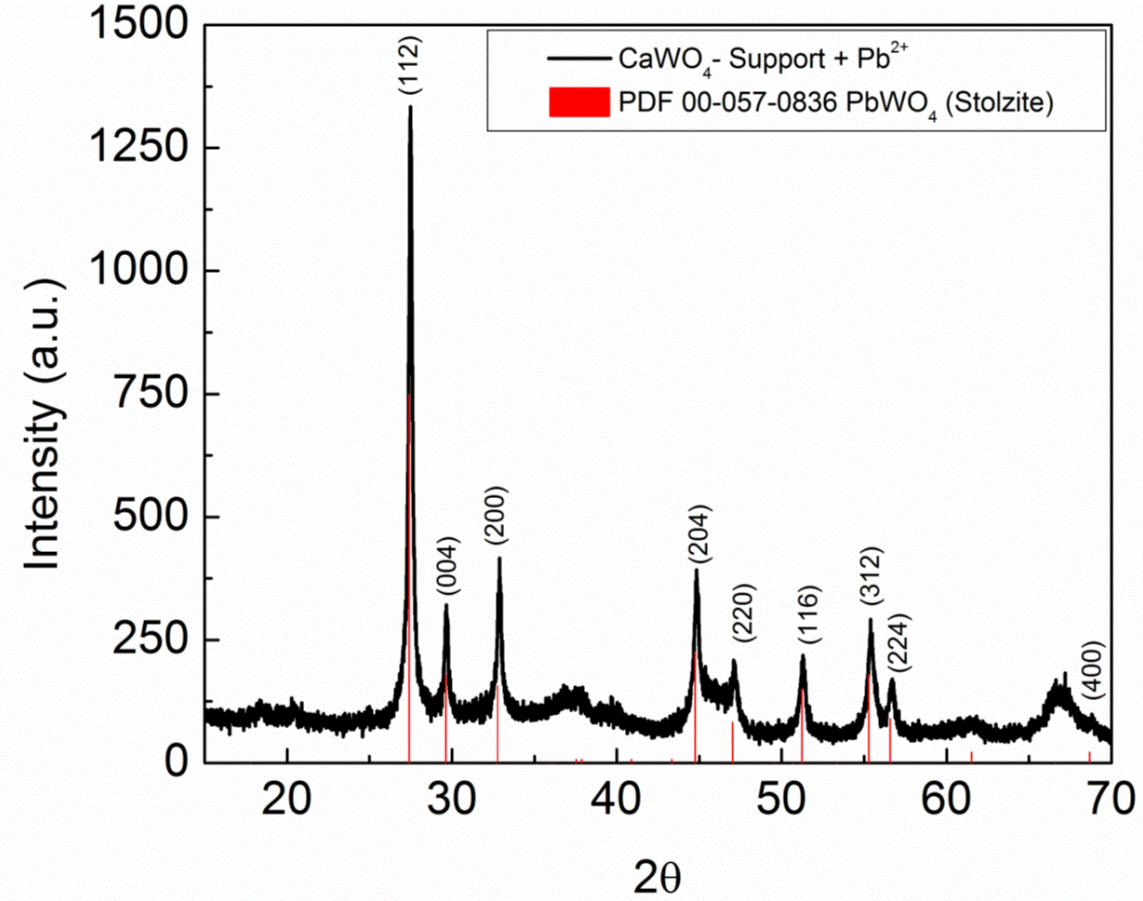

Figure 38: XRD of the Supported Material Saturated with Lead

The material used in the sorption process for Cd^{2+} was also characterized for the sorption capacities for both the nanocrystalline powder and the supported material. Both materials were reacted with excess Cd^{2+} and allowed to react for roughly one month. The nanocrystalline powder

had a 25.1% molar sorption capacity for cadmium, but by supporting the material, the sorption capacity was improved to 70.4%. These materials were also characterized by X-ray powder diffraction. However, neither material showed evidence of a crystalline phase for $CdWO_4$. The materials were also analyzed by scanning electron microscopy. The nanocrystalline powder showed no evidence of a morphology change, showed in Figure 39. The alumina supported material post treatment, however, only showed a markedly different morphology change forming plate like structures, shown in Figure 40.

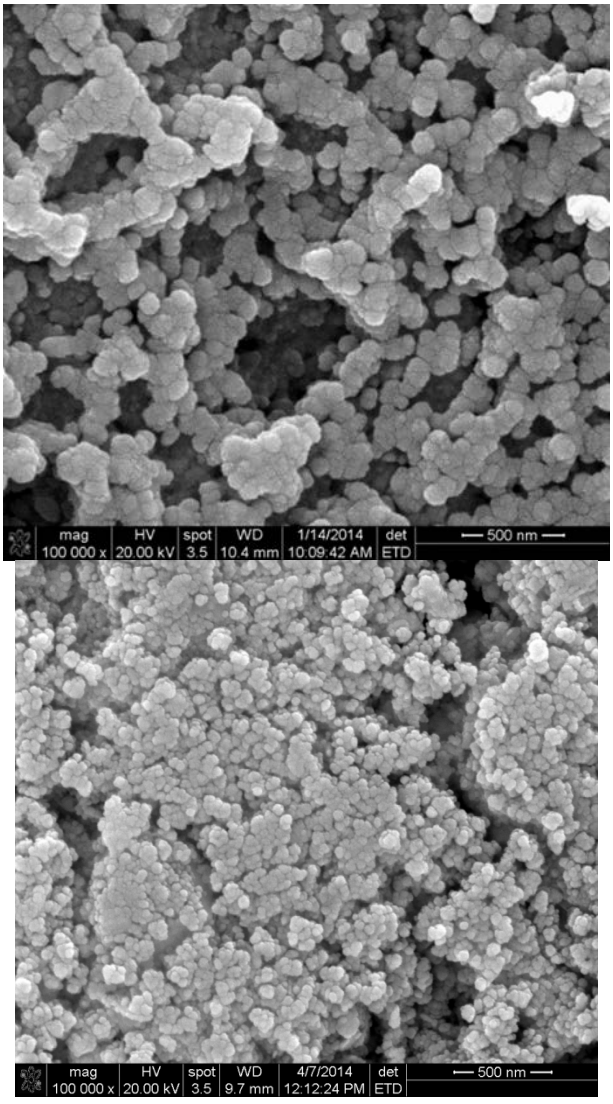

Figure 39: The Nanocrystalline $CaWO_4$ Before (top) and After Treatment (bottom) with Cd^{2+}

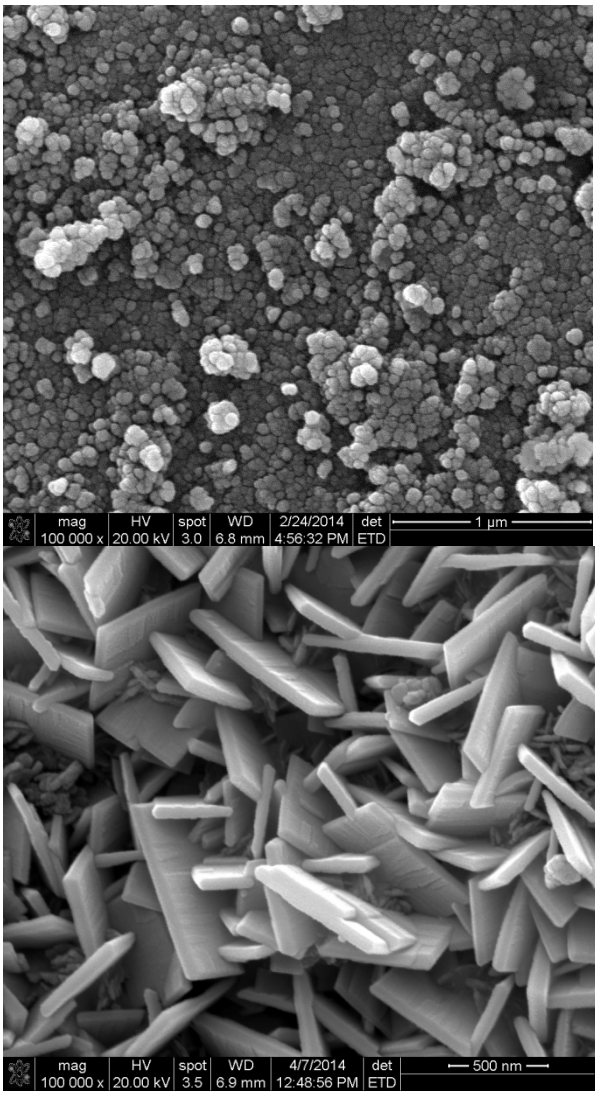

Figure 40: Morphology of the Supported $CaWO_4$ Before (top) and After Treatment (bottom) with Cd^{2+}

This process was repeated for one month for copper, allowing ample time for the sorption process to reach the sorption capacity. Unlike the other two materials, copper has a distinct color allowing for the reaction to be monitored in a qualitative fashion. Further, $Cu_3(WO_4)(OH)_2$ also has a distinct color. As Figure 41 shows, the nanocrystalline $CaWO_4$ used as the sorbent was turned to a pistachio-green color, indicative of the formation of $CuWO_4$. The molar sorption capacity for Cu^{2+} was 86.0%, much higher than both the metals presented in this chapter. Further, the material was characterized by powder XRD showing peaks consistent with both

calcium and copper tungstate hydroxide, shown in Figure 42. Further, the material before and after treatment was characterized by SEM, showing little to no morphology change post treatment, shown in Figure 43.

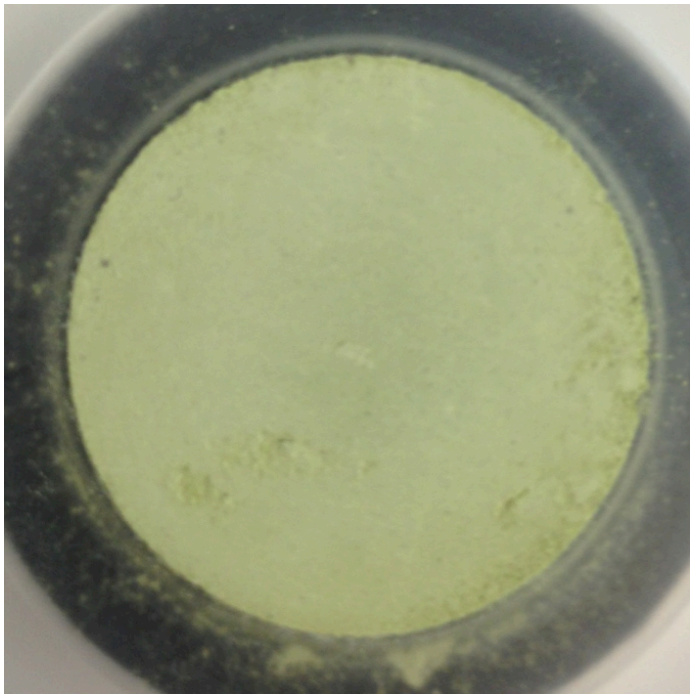

Figure 41: Nanocrystalline $CaWO_4$ Reacted with Cu^{2+}

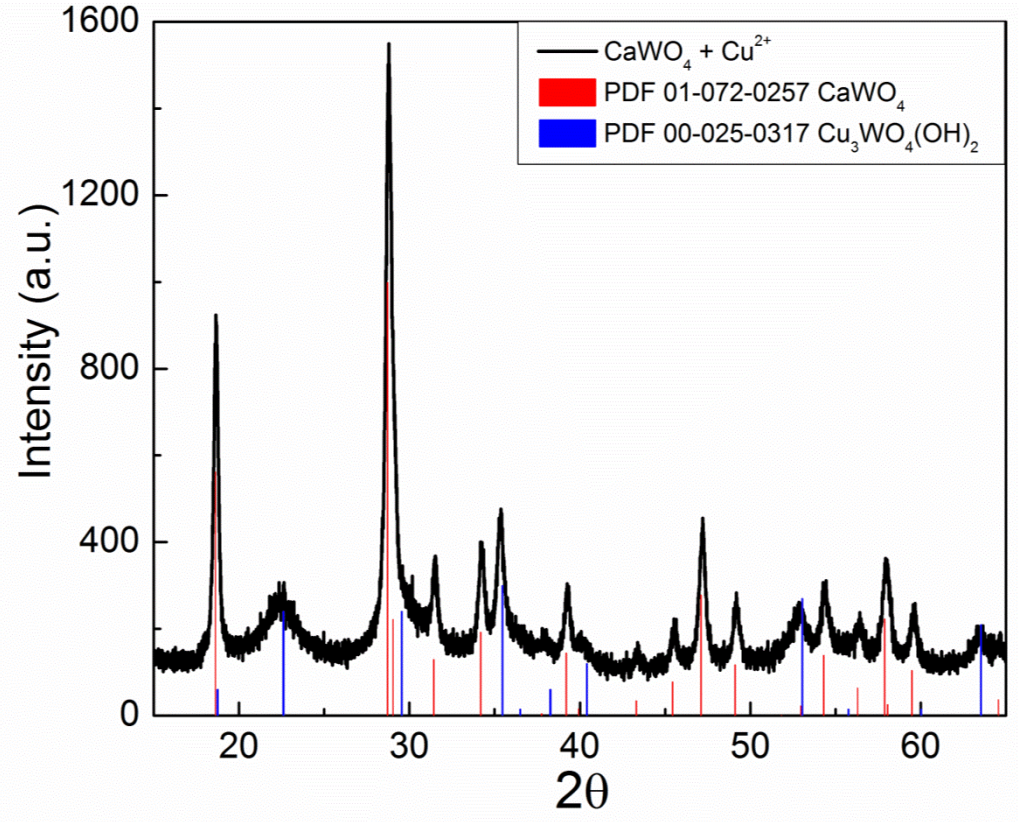

Figure 42: XRD of the Nanocrystalline $CaWO_4$ after Treatment of Excess Cu^{2+}

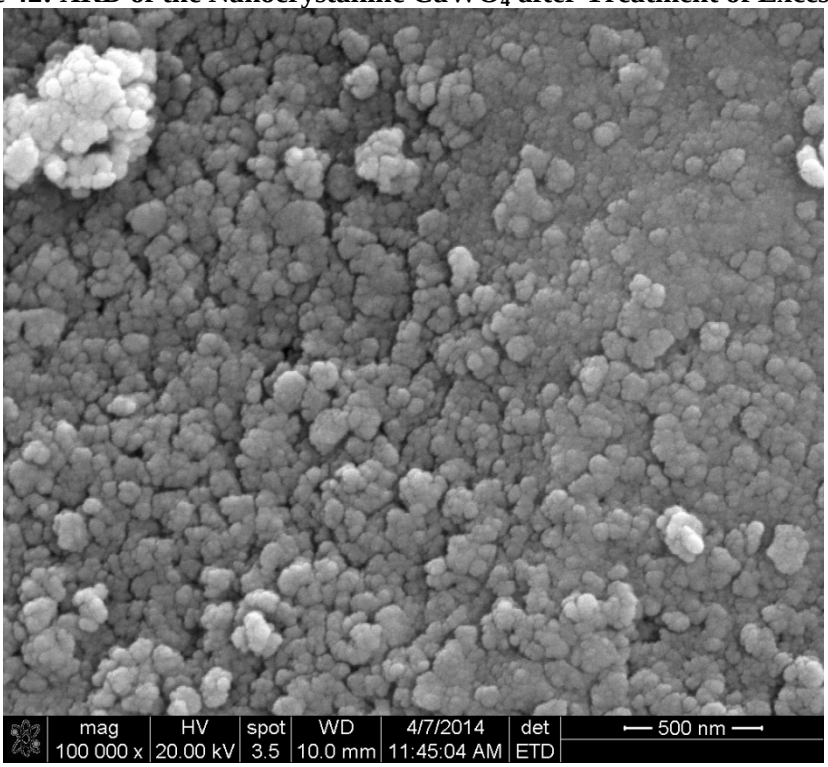

Figure 43: SEM of the Nanocrystalline Powder Reacted with Cu^{2+}

By supporting the material, the sorption capacity was further improved, being able to convert 100% to $CuWO_4$. The material on the high surface area support was light blue after treatment, instead of pistachio-green, as pictured in Figure 44. However, the XRD pattern showed the product was amorphous. Analysis by SEM also showed a product with little to no morphological change, pictured in Figure 45.

Figure 44: The Supported $CaWO_4$ after Treatment of Excess Cu^{2+}

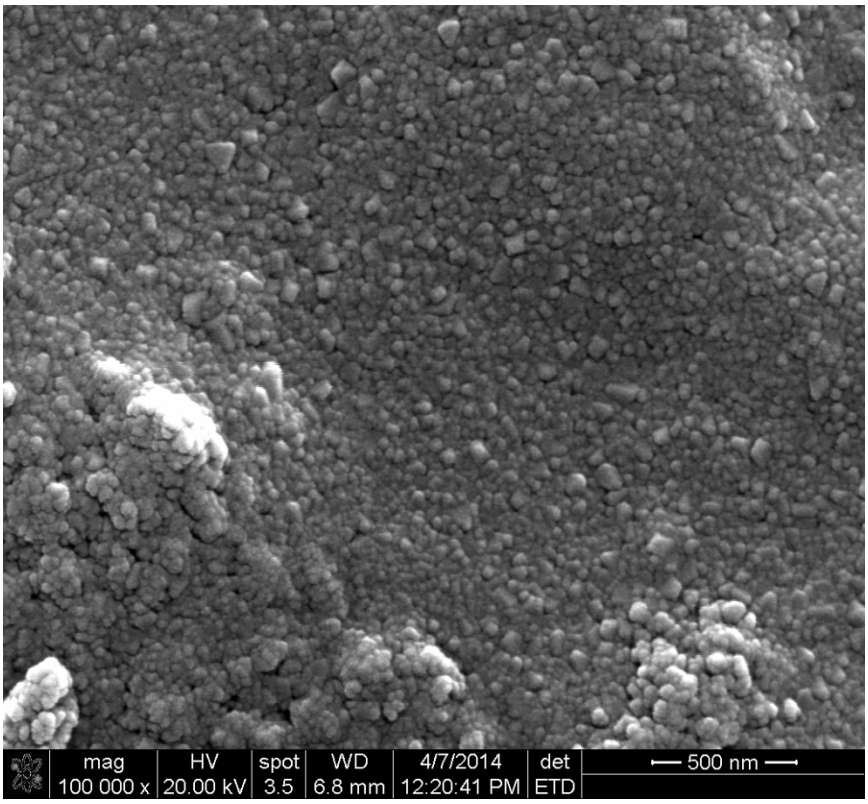

Figure 45: SEM of the Supported $CaWO_4$ Reacted with Cu^{2+}

Recovery of Materials

All of the heavy metal containing materials were able to be recovered and recycled in a cyclic and green process that only produced sodium chloride as a byproduct (Figure 45). For example, the reaction of $PbWO_4$ and aqueous NaOH, under stirring for roughly 24 hours produced an insoluble lead hydroxide product and aqueous sodium tungstate. The two products were separated by vacuum filtration. The filtrate was acidified with HCl, producing insoluble tungstic acid that was recovered in very high yields (98%). The tungstic acid was then converted to $CaWO_4$ by the already described method with a similar yield. When this process was repeated for $CuWO_4$, similar results were obtained, recovering the $Cu(OH)_2$ with a 99% yield. A similar process can be used for $CdWO_4$, where the NaOH is simply substituted for Na_2CO_3 to form insoluble $CdCO_3$.

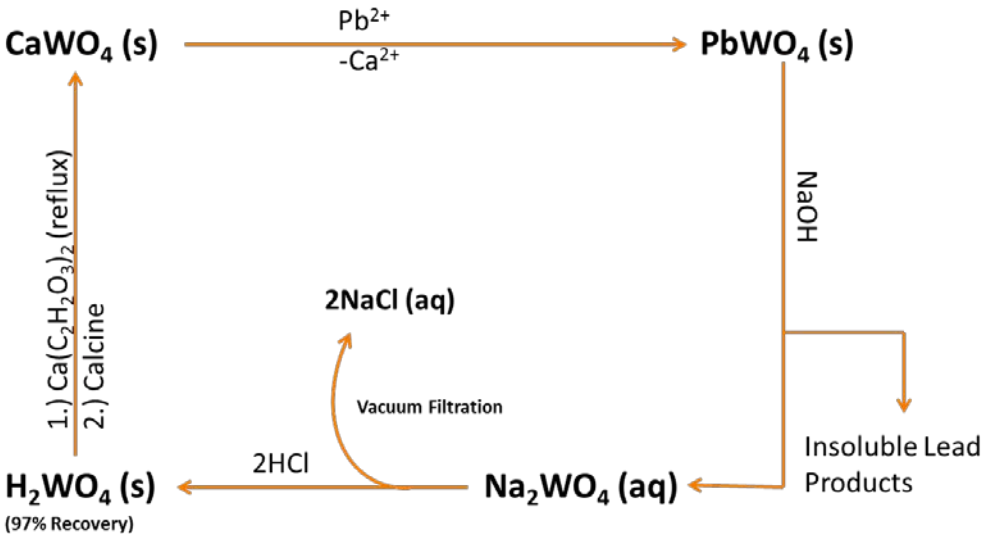

Figure 46: Cyclic Process for the Recovery for the Separation of Lead and Regeneration of $CaWO_4$

Implementation in Real World Samples

To determine if the material could be employed in real-world effluents, a simulated sample effluent of SunCor oil sand tailings was synthesized based on analytical data from the literature, summarized in Table 9 and was then treated.[29, 30] Two samples of the effluent of roughly 20 mL volume were treated with 0.439 mmols of $CaWO_4$ in the powder form and 0.494 mmols of $CaWO_4$ on the high surface area supports. Both solutions were sampled after 6 hours yielding concentrations of both Cu^{2+} and Pb^{2+} below the instrumental detection limit,

Table 24: Summary of the SunCor Mimic Before and After Treatment by Both the Powder and Supported Material[29]

Species	Initial Concentration (ppm)
Sodium	525
Calcium	25
Magnesium	12
Chloride	90
Bicarbonate	950
Sulfate	290
Ammonium	14
Copper	660
Arsenic	15
Lead	190

The positive results from the SunCor effluent remediation led to the treatment of consumer products. In September 2011, Consumer Reports published data that showed appreciable levels of lead in all 88 juices tested.[31] To mimic these results, a sample of grape juice was spiked to 75 ppb with lead, a five-time higher concentration than the EPA action limit for this toxic metal. A 225 mL sample of the spiked juice was treated using 0.466 mmols of supported-$CaWO_4$. Figure 26, shows that after only 15 minutes the concentration of lead in the solution dropped well below the EPA action limit and after 30 minutes the concentration had dropped below the instrument detection limit, while simultaneously fortifying the juice with calcium. The sorption process does not denature the juice, only slightly affecting the pH, dropping it from 3.2 to 3.1.

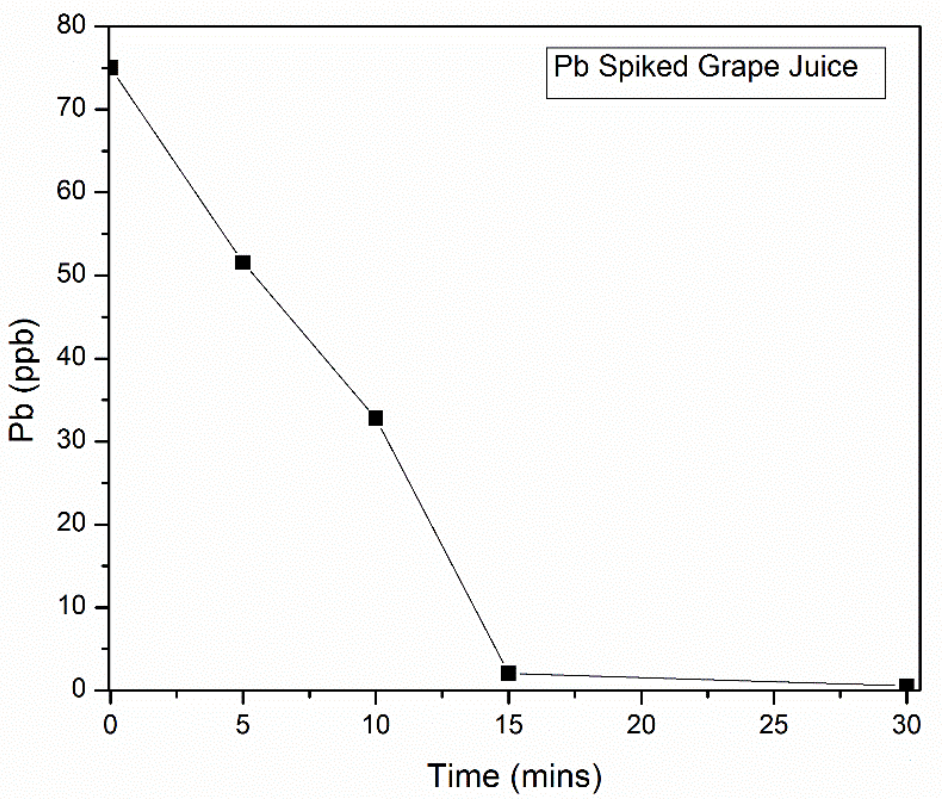

Figure 47: Treatment of Pb^{2+} Spiked Juice

Conclusion:

This study has shown that $CaWO_4$ is an attractive material for the remediation of aqueous heavy metals, with very fast reaction times and high sorption capacities via an ion-exchange process. Furthermore, this study describes a method for supporting $CaWO_4$ on high surface area catalyst supports providing a potential material to be rapidly incorporated into current treatment processes. It has also been shown that by supporting the material, it can be converted wholly from $CaWO_4$ to $PbWO_4$ and $CuWO_4$, where the material only has a roughly 70% sorption capacity for Cd^{2+}. The featured material is not only attractive due its non-toxic nature, but because the spent materials can be easily separated and regenerated in a green-fashion. Fitting the sorption process to several widely used kinetic models gave reasonable results. However, the nonlinear pseudo first-order method seems to not only describe the system accurately, but gives a rate constant with a clear physical meaning. It has also been shown the material has a high affinity for lead and

copper as suggested by the results of the treatment of industrial effluents. Moreover, the process described is a very effective and safe method for removing lead from juice and possibly other foodstuffs. Further research could apply this material to the recovery or remediation of other divalent metals. The material should also be subjected to other industrial effluents to determine its applicability to a wide range of waste streams.

References:

1. Environmental Health Criteria No. 200: Copper. In *International Programme on Chemical Safety*, World Health Organization: Geneva, 1998.

2. Y. Nuhoglu and E. Oguz, Removal of copper(II) from aqueous solutions by biosorption on the cone biomass of Thuja orientalis. *Process Biochemistry* **2003,** *38* (11), 1627-1631.

3. F. A. A. Al-Rub, M. H. El-Naas, I. Ashour, and M. Al-Marzouqi, Biosorption of copper on Chlorella vulgaris from single, binary and ternary metal aqueous solutions. *Process Biochemistry* **2006,** *41* (2), 457-464.

4. B. Yu, Y. Zhang, A. Shukla, S. S. Shukla, and K. L. Dorris, The removal of heavy metal from aqueous solutions by sawdust adsorption — removal of copper. *Journal of Hazardous Materials* **2000,** *80* (1–3), 33-42.

5. Y. C. Sharma, Economic Treatment of Cadmium(II)-Rich Hazardous Waste by Indigenous Material. *Journal of Colloid and Interface Science* **1995,** *173* (1), 66-70.

6. A. Bernard and R. Lauwerys, Cadmium in human population. In *Cadmium in the Environment*, Mislin, H.; Ravera, O., Eds. Birkhäuser Basel: 1986; Vol. 50, pp 114-123.

7. Cadmium. *In: Guidelines for drinking-water quality*. 3rd ed.; World Health Organization: Geneva, 2008; Vol. 1, pp 317-319.

8. J. Yin and H. W. Blanch, A bio-mimetic cadmium adsorbent: Design, synthesis, and characterization. *Biotechnology and Bioengineering* **1989,** *34* (2), 180-188.

9. D. Mohan and K. P. Singh, Single- and multi-component adsorption of cadmium and zinc using activated carbon derived from bagasse—an agricultural waste. *Water Research* **2002,** *36* (9), 2304-2318.

10. Y.-H. Li, S. Wang, Z. Luan, J. Ding, C. Xu, and D. Wu, Adsorption of cadmium(II) from aqueous solution by surface oxidized carbon nanotubes. *Carbon* **2003,** *41* (5), 1057-1062.

11. V. M. Fthenakis, Life cycle impact analysis of cadmium in CdTe PV production. *Renewable and Sustainable Energy Reviews* **2004,** *8* (4), 303-334.

12. H. Al-Busaidi and A. W. Apblett, Adsorption and Separation of Uranium Using Tungsten Oxides. In *Environmental Issues and Waste Management Technologies in the Materials and Nuclear Industries XII*, John Wiley & Sons, Inc.: 2009; pp 39-46.

13. K. N. Barber and A. W. Apblett, Green Process for Recovery of Copper. *Ceramic Transactions* **2009,** *207*, 171-175.

14. M. Chehbouni, H. Al-Busaidi, and A. W. Apblett, Green Process for Uranium Separations Utilizing Molybdenum Trioxide. In *Nuclear Energy and the Environment*, American Chemical Society: 2010; Vol. 1046, pp 155-167.

15. B. P. Kiran and A. W. Apblett, Process for Selective Removal and Concentration of Actinides and Heavy Metals from Water. *Ceramic Transactions* **2004,** *155*, 371-380.

16. B. P. Kiran, A. W. Apblett, and M. Chehbouni, Selective Absorption of Heavy Metals and Radionuclides from Water in a Direct-to-Ceramic Process. *Ceramic Transactions* **2003,** *143*, 385-394.

17. A. W. Apblett, B. P. Kiran, and M. Chehbouni, Molybdenum-Oxide Based Sorbants for Toxic Metals. *Ceramic Transactions* **2006,** *176*, 15-23.

18. S. Lagergren, Zur theorie der sogenannten adsorption gelöster stoffe. Kungliga Svenska Vetenskapsakademiens. *Handlingar* **1898,** *24* (4), 1-39.

19. S. Azizian, Kinetic models of sorption: a theoretical analysis. *Journal of Colloid and Interface Science* **2004,** *276*, 47–52.

20. K. V. Kumar, Linear and non-linear regression analysis for the sorption kinetics of methylene blue onto activated carbon. *Journal of Hazardous Materials B* **2006,** *137*, 1538-1544.

21. Y.-S. Ho and G. McKay, Pseudo-second order model for sorption processes. *Process Biochemistry* **1999,** *34* (5), 451-465.

22. J.-Z. Zhang, Avoiding spurious correlation in analysis of chemical kinetic data. *Chemical Communications* **2011,** *47* (24), 6861-6863.

23. X. Yang and J. Huang, Phase Transformation of Lead Tungstate at Normal Temperature from Tetragonal Structure to Monoclinic Structure. *Journal of the American Ceramic Society* **2012,** *95* (10), 3334-3338.

24. R. K. Khanna, W. S. Brower, B. R. Guscott, and E. R. Lippincott, Laser induced Raman spectra of some tungstates and molybdates. *Journal of Research of the Notional Bureau af Standards - A. Physics and Chemistry* **1967,** *72A* (1), 81-84.

25. B. Ingham, S. V. Chong, and J. L. Tallon, Layered Tungsten Oxide-Based Organic−Inorganic Hybrid Materials: An Infrared and Raman Study. *The Journal of Physical Chemistry B* **2005,** *109* (11), 4936-4940.

26. S. Bastians, G. Crump, W. P. Griffith, and R. Withnall, Raspite and studtite: Raman spectra of two unique minerals. *Journal of Raman Spectroscopy* **2004,** *35* (8-9), 726-731.

27. T. George, S. Joseph, A. Sunny, and S. Mathew, Fascinating morphologies of lead tungstate nanostructures by chimie douce approach. *Journal of Nanoparticle Research* **2008,** *10* (4), 567-575.

28. J. Yang, C. Lu, H. Su, J. Ma, H. Cheng, and L. Qi, Morphological and structural modulation of PbWO 4 crystals directed by dextrans. *Nanotechnology* **2008,** *19* (3), 035608.

29. A. Piquette, C. Cannon, and A. W. Apblett, Remediation of arsenic and lead with nanocrystalline zinc sulfide. *Nanotechnology* **2012,** *23* (29), 294014.

30. M. D. MacKinnon and A. Sethi, A comparison of the physical and chemical properties of the tailings ponds at the Syncrude and Suncor oil sands plants. In *Our Petroleum Future Conference*, Alberta Oil Sands Technology and Research Authority: Edmonton, Alberta, 1993.

31. Results of our apple juice and grape juice tests. *Consumer Reports* 2011.

CHAPTER XI

SORPTION OF RADIONUCLIDES BY NANOMETRIC CALCIUM TUNGSTATE

Introduction:

The need to provide solutions to the global energy crisis has renewed world-wide interest in nuclear power. However, the renaissance in nuclear power also renews serious environmental and health concerns due to highly dangerous radioactive waste. ^{90}Sr is one of the major heat producers and biohazards in nuclear wastes, thus making the removal of radioactive strontium an essential goal to reduce the risk of human exposure to radiation. Further, the remediation of radioactive strontium leads to considerable cost savings due to minimizing the storage space requirements for such materials that results from reduced heat generation.[1-3] Radioactive isotopes of strontium are among the most biologically hazardous radionuclides in nuclear waste due to their longevity and high concentrations.[4-5] If released into the environment, radioactive strontium becomes incorporated into the calcium pool. Radio-strontium is of particular importance among the fission products because of chemical and physical characteristics that result in comparatively high retention in the skeleton, due to the chemical similarity to calcium.[6-7] However, studies have suggested that the bone-seeking isotopes are most dangerous if exposed during a period of relatively active osteogenesis (i.e. puberty or healing of fractures), but not rapid turnover.[8-9]

Furthermore, due to the radiation leak at the Fukushima Daiichi nuclear power station, radioactive strontium has been discovered not only inside the evacuation zone of Fukushima, but also as far as 250 kilometers from the site itself. A recent report from Tokyo Electric Power showed concentrations of strontium-90 over 30 times that of the Japanese government's safety limit.[10-12] One of the pathways for radioactive strontium to enter the human body is through the principal pathway from soil to plant to cow's milk to humans.[7, 13] The dangers of uranium exposure have been previously covered in Chapter V.

A variety of techniques such as chemical precipitation, ion exchange, and evaporation are used for the treatment of aqueous waste systems. Polymer based ion-exchange materials have received much interest because of the simplicity of their application, despite their low capacity and mediocre selectivity. Inorganic ion-exchangers possess a number of advantages as sorbents for both UO_2^{2+} and Sr^{2+} over the conventional organic based ion-exchange resins, due to their thermal and chemical stabilities, higher exchange capacities, increased selectivities, and radiation stability.[1-2, 14]

The Apblett research group has previously demonstrated the usefulness of molybdenum hydrogen bronze removal of uranium from aqueous solutions and its potential use in a cyclic process for uranium recovery.[15-16] In Chapter V, the effectiveness of insoluble tungstic acid as a sorbent for aqueous uranyl ions was discussed. During experiments designed to determine the selectivity for uranium uptake over other environmentally common metals it was unexpectedly found, that the addition of Ca^{2+} as a competing ion increased the rate of uranium sorption by tungstic acid.[17] This result led to the hypothesis that calcium tungstate was an intermediate in the calcium-catalyzed uptake of uranyl ions, suggesting the use of $CaWO_4$ directly as an ion exchange material. Further, due to the similar chemistries of Ca^{2+} and Sr^{2+}, calcium tungstate is an attractive candidate of the sorption of the slightly larger cation, Sr^{2+}. The sorption kinetics for the uptake of Sr^{2+} and UO_2^{2+} were studied using $CaWO_4$ powder and $CaWO_4$ supported on

alumina. The molar sorption capacities of the materials and the ion exchange products were identified in this investigation.

Experimental:

Materials

All chemicals (reagent grade or higher) were used as received without further purification. Water was purified by reverse osmosis followed by deionization. The tungstic acid, $Sr(NO_3)_2$, calcium D-gluconate, α-hydroxyisobutyric acid (98%), and the Al_2O_3 high surface area catalyst supports were obtained from Alfa-Aesar. The $Ca(OH)_2$, $UO_2(NO_3)_2 \cdot 6H_2O$, and NaOH used were obtained from Fisher Scientific. Trace metal HNO_3 used for sample acidification was obtained from Mallinckrodt. The 1000 mg/L uranium standard was purchased from BDH ARISTAR. Hydrochloric acid for the regeneration of H_2WO_4 was obtained from PHARMCO-AAPER.

Characterization

The X-ray diffraction patterns for oxides before and after reaction with the target metal ions were obtained using a Bruker D8-A25-Advance diffractometer equipped with a LynxEye detector. Fourier transform infrared (FT-IR) spectroscopy was performed as a KBr pellet using a Nicolet Magna 750 IR spectrometer. Strontium concentrations were determined using a Varian GTA120/AA240Z graphite furnace atomic absorption spectrometer (GFAAS) equipped with an auto sampler and calibrated with a NIST-traceable standard. The concentration of UO_2^{2+} was determined using a PerkinElmer Optima 2100 DV inductively coupled plasma-atomic emission spectrometer equipped with an auto sampler and calibrated with a NIST-traceable standard. The surface areas of the starting materials were measured by N_2 physisorption using a NOVA Quantachrome 1200 BET instrument. Scanning electron microscopy (SEM) was performed using an FEI Quanta 600 field emission gun environmental scanning electron microscope.

Impregnation of Supports

The high surface area Al_2O_3 supports were vacuum-impregnated by introducing the calcium tungsten gluconate solution to the supports *in vacuo.* The supports were held under vacuum for roughly 24 hours and were then rinsed with 50 mL of deionized water to remove excess precursor on the surface of the supports, and were subsequently dried *in vacuo.* Once dry, the supports were transferred to a ceramic crucible and calcined at 600 °C and held for 8 hours in a muffle-furnace. The mass of the resulting materials indicated a loading of the support with 8.70% and 14.1% $CaWO_4$ by weight for the UO_2^{2+} and the Sr^{2+} experiments, respectively.

Sorption Studies

The UO_2^{2+} sorption studies were performed using a 142 parts per million (ppm) solution of uranyl. The Sr^{2+} was prepared using $Sr(NO_3)_2$ and had a concentration of 108 ppm that was determined by graphite furnace atomic absorption spectroscopy GFAAS spectroscopy. The effect of sorbent dosages on reaction kinetics, for both the powder and supports, were determined by treating four approximately 50 mL solutions of stock solutions for both UO_2^{2+} and Sr^{2+}, while only varying the amount of excess calcium tungstate. The treated solutions were also analyzed for the concentration of calcium by flame atomic absorption spectroscopy.

The samples were agitated by a sample rotator, at a speed of 40 RPM, to eliminate the possibility of forming concentration gradients. Aliquots of each sample were taken at regular time intervals, diluted with a 1% trace-metal HNO_3 solution to the appropriate concentrations, and analyzed by either GFAAS or ICP-AES. The reaction uptake curves were plotted using the sorption capacity at a given time (q_t) vs time (t). The sorption capacity, defined by Equation 1, was used to plot the uptake curves, where C_t is the concentration of analyte in the solution at time t, C_0 is the starting concentration, V is the volume of the analyte, and m is the mass of the sorbent.

$$q_t = \frac{(C_0 - C_t)V}{m}$$

Equation 1: The sorption capacity equation

Results and Discussion

The synthesis and characterization of the $CaWO_4$ used in these experiments was described Chapter VI. The highest surface area powder, from the methyl lactic acid precursor, was used in the sorption experiments for all analytes.

Sorption Kinetics for the Uptake of UO_2^{2+}

After addition of $CaWO_4$ to the stock solutions, the analyte concentrations were monitored via GFAAS for Sr^{2+} and ICP-AES for UO_2^{2+} over time. Figure 1 depicts the sorption uptake curves for uranyl by four different amounts of calcium tungstate by plotting q_t (from Equation 1) verses time. The uptake curves shows a process in which sorption is initially very fast and starts to slow as the reaction approaches an equilibrium state after 120 minutes for the two highest mass loadings and after 240 minutes for the two lowest. The sorption process continued until the concentration of the analyte dropped below the instrumental detection limit of roughly 50 ppb.

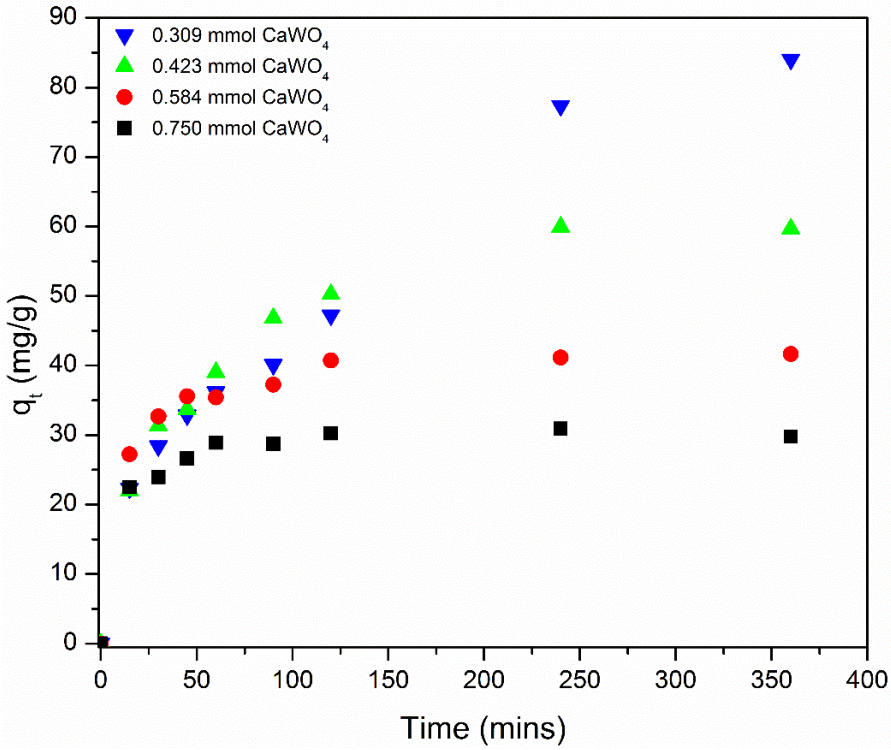

Figure 1: Uptake Curves for the Sorption of UO_2^{2+} by Nanocrystalline $CaWO_4$

In this study, the nonlinear and linear pseudo-order equations were employed to fit the data from the sorption processes. Equation 2 gives the pseudo first-order rate expression, first described by Lagergren in 1898, where k_1 is the kinetic rate constant for the pseudo first-order sorption process. The amount of analyte sorbed at any specific time (t) is represented by q_t and the amount of analyte sorbed at equilibrium is represented by q_e.[18]

$$q_t = q_e(1 - e^{-k_1 t})$$

Equation 2: The Nonlinear Pseudo First-Order Equation

To simplify Equation 2, the natural log can be taken giving a linear equation represented by Equation 3. From this equation, the values of k_1 and q_e can be determined from the slope and y-intercept, respectively, by plotting $\ln(q_e-q_t)$ vs time.

$$\ln(q_e - q_t) = \ln(q_e) - k_1 t$$

Equation 3: The Linearized Formula for Pseudo First-Order Kinetics

The plot of the linear pseudo first-order fit in Figure 2 shows that this model fits fairly well for the higher sorbent loading. However, we can determine that the linear pseudo first-order model does not apply throughout the various sorbent loadings as summarized by the correlation coefficient listed in Table 1. The sorption data from the lowest sorbent mass loading exhibits the largest deviation from linearity; however, the 0.584 mmol loading has the largest disparity between the calculated and experimentally observed equilibrium capacities. Furthermore, the estimated values of q_e calculated from the equation start to differ substantially from those measured experimentally as the sorbent mass is increased. This model does not satisfactorily describe this sorption process. This may be due to the larger excess of reaction sites created when the sorbent loadings are increased.[19]

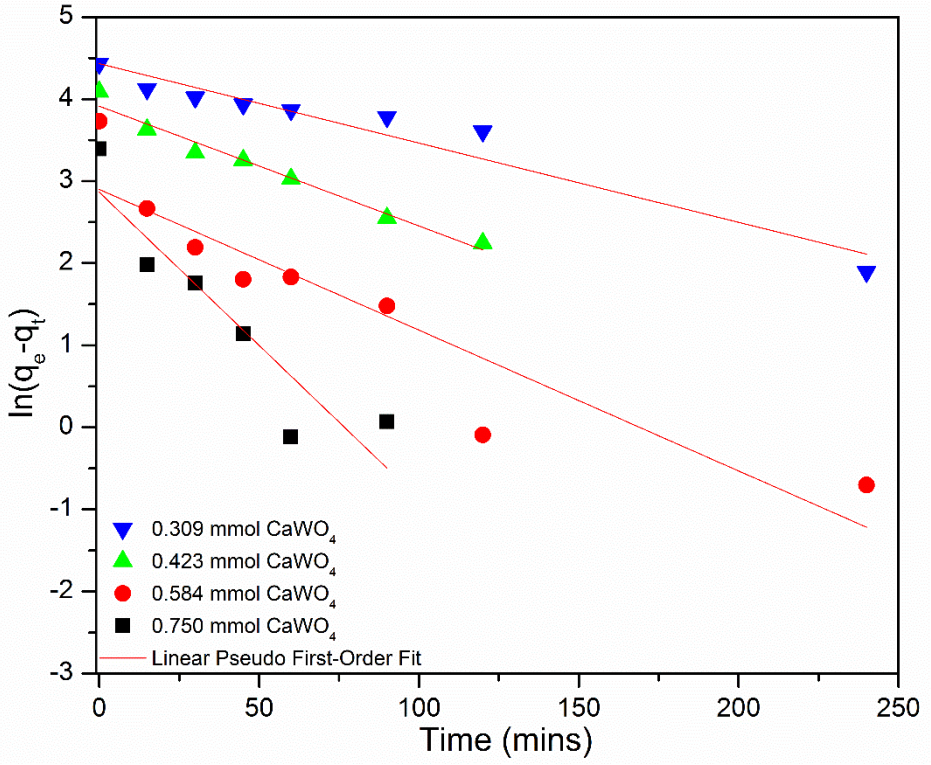

Figure 2: Linear Pseudo First-Order Fit for the Uptake of UO_2^{2+} by $CaWO_4$

Table 1: The Data and Results from the Linear Pseudo First-Order Fit

$CaWO_4$ (mmol)	k_1 (min^{-1})	q_e (mg/g)	q_e (mg/g) (experimental)	R^2
0.309	9.68E-03	84.2	84.0	0.929
0.424	1.46E-02	50.1	59.7	0.969
0.584	1.72E-02	18.2	41.6	0.838
0.750	3.74E-02	17.6	29.8	0.817

The nonlinear Lagergren equation has been used to model sorption processes, in some cases, giving better results.[20] Using the nonlinear pseudo first-order equation (Equation 2) to fit the data plotted by sorption capacity equation gave the fit featured in Figure 3. As the plot shows, this equation underestimates the equilibrium capacities (q_e) in all cases. However, the nonlinear equation fits the data with much more accuracy than the linear formula, yielding much more accurate predicted q_e values, summarized in Table 2. This equation is much more appropriate for

modeling the data from this sorption process, however, the predicted q_e values from the equation range from 85-90% of the experimental values.

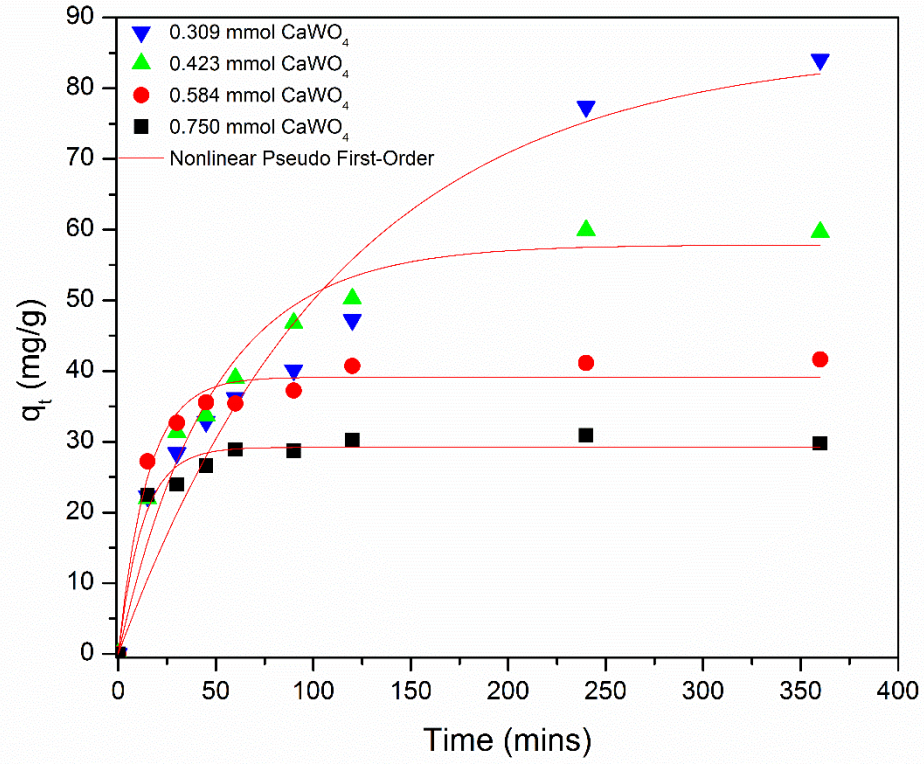

Figure 3: Nonlinear Pseudo First-Order Fit for the Uptake of UO_2^{2+} by $CaWO_4$

Table 2: The Data and Results from the Nonlinear Pseudo First-Order Fit

$CaWO_4$ (mmol)	k_1 (min^{-1})	q_e (mg/g)	q_e (mg/g) (experimental)	R^2
0.309	8.78E-03	75.5	84.0	0.924
0.424	2.12E-02	51.0	59.7	0.965
0.584	6.78E-02	34.5	41.6	0.970
0.750	7.99E-01	25.8	29.8	0.971

Ho and McKay's pseudo-second order kinetic model represented by Equation 4 was also used to fit the sorption data. In this equation, k_2 is the rate constant of the pseudo second-order sorption process, has the units g mg^{-1} min^{-1}.[21] By substituting *h* in place of $k_2q_e^2$, the equation can be further simplified as represented in Equation 5. The variable *h*, in this equation, can be

considered to be the initial sorption rate as t/q_t approaches 0. The linear plot of t/q_t versus t gives the constants q_e and h, from the slope and the intercept, respectively.[19] Using the value of q_e (the slope) and h (the intercept), the rate constant (k_2) can be obtained.

$$\frac{t}{q_t} = \frac{1}{k_2 q_e^2} + \frac{1}{q_e} t$$

Equation 4: The Linearized Pseudo Second-Order Rate Equation

$$\frac{t}{q_t} = \frac{1}{h} + \frac{1}{q_e} t$$

Equation 5: The Linearized Initial Pseudo Second-Order Rate Equation

The linear pseudo second-order plot, Figure 4, shows that this fits the data much better than the linear pseudo first-order equation, yielding very high correlation coefficients (R^2>0.94). The calculated equilibrium capacities are in very close agreement with the experimental data, and there is only a slight underestimation of the capacities of the three larger sorbent loadings, as summarized in Table 3. The pseudo second-order rate constants (k_2) and *h* are correlated to the sorbent loadings, as they increase with the amount of sorbent used.

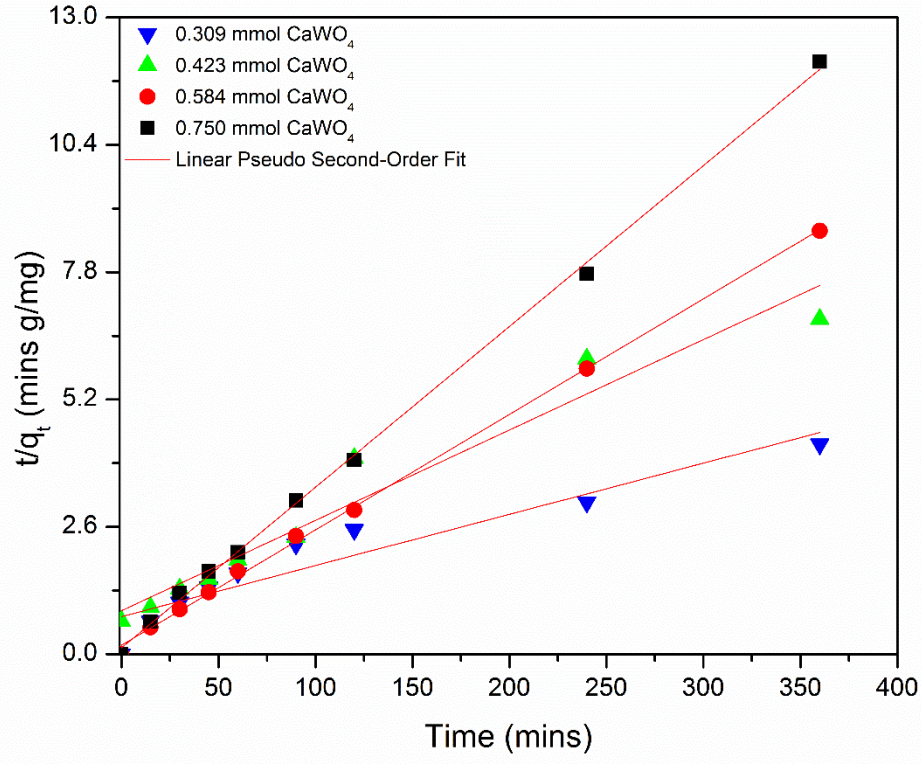

Figure 4: Linear Pseudo Second-Order Fit for the Uptake of UO_2^{2+} by $CaWO_4$

Table 3: The Data and Results from the Linear Pseudo Second-Order Fit

$CaWO_4$ (mmol)	k_2 (g/mg min)	h (mg/g min)	q_e (mg/g)	q_e (mg/g) (experimental)	R^2
0.309	1.61E-04	1.15	84.4	84.0	0.949
0.424	6.25E-04	2.01	56.8	59.7	0.988
0.584	3.47E-03	4.85	37.4	41.6	0.999
0.750	9.51E-03	6.86	26.9	29.8	0.999

The nonlinear pseudo second-order equation has also been shown to be a viable option for modeling sorption processes.[20] The nonlinear pseudo second-order function (Equation 6) fit the data with relatively good accuracy, depicted in Figure 5. The kinetic values, summarized in Table 4, show the correlation coefficients for the nonlinear method are very high (R^2>0.94) similar to the linear model suggesting that this method is also appropriate for modeling this process. Similar to the linear pseudo second-order model, the rate constants consistently increase with increasing sorbent loading. Further, this model gives a similar trend as the linear pseudo

second-order model when predicting the q_e values. From the data presented, it suggests that both pseudo second-order models describe the sorption of UO_2^{2+} on the nanometric-$CaWO_4$ very well. However, even though the models fit the experimental data very well, there is little physical meaning that can be extrapolated from the kinetic results. This is due to the nature of the pseudo second-order rate constant, which is dependent on the concentrations of the analyte and sorbent. Also, concern has been raised on the validity of the linear pseudo-second order equation to model sorption processes, due to spurious correlations, however, the presented data shows that the linear and nonlinear models perform with similar results.[22] The pseudo second-order models could be employed to determine equilibrium capacities of the materials used in this system fairly accurately. The nonlinear pseudo first-order equation gives fairly good results and kinetic parameters with clear physical meaning, thus should be used for modeling this process.

$$q_t = \frac{k_2 q_e^2 t}{1 + k_2 q_e t}$$

Equation 6: The Nonlinear Pseudo Second-Order Equation

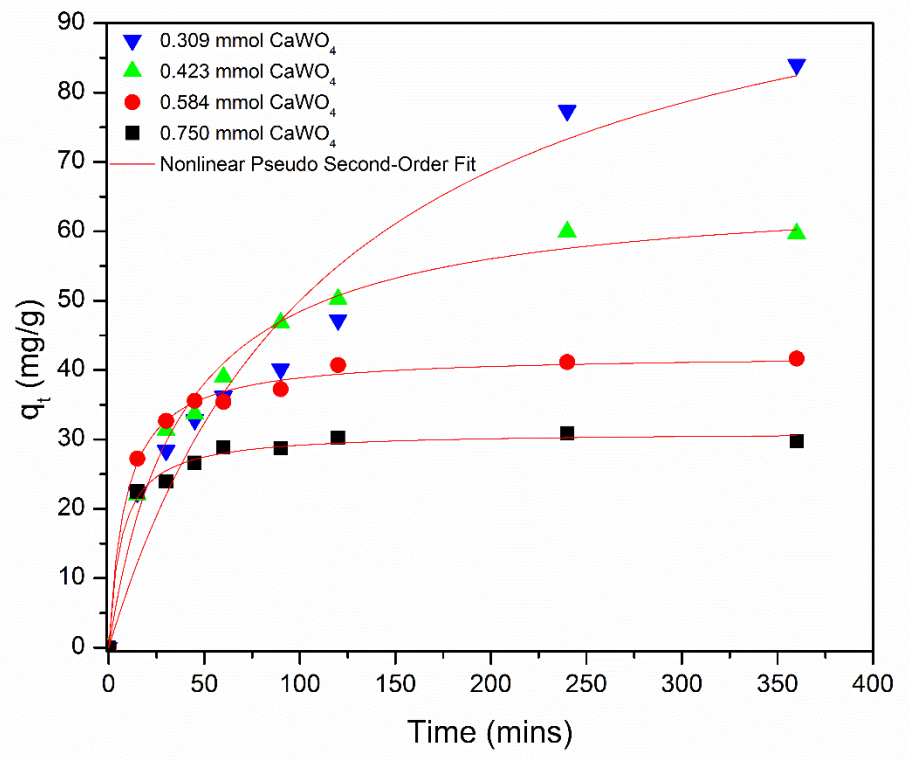

Figure 5: Nonlinear Pseudo Second-Order Fit for the Uptake of UO_2^{2+} by $CaWO_4$

Table 4: The Data and Results from the Nonlinear Pseudo Second-Order Fit

$CaWO_4$ (mmol)	k_2 (g/mg min)	h (mg/g min)	q_e (mg/g)	q_e (mg/g) (experimental)	R^2
0.309	8.65E-05	0.81	96.8	84.0	0.942
0.424	4.58E-04	1.57	58.6	59.7	0.989
0.584	3.05E-03	4.24	37.3	41.6	0.995
0.750	5.55E-03	4.17	27.4	29.8	0.991

In order to produce the sorbent in a more suitable form for water treatment, high surface area alumina catalyst supports where impregnated using the calcium tungsten gluconate single-source precursor solution and calcined to deposit $CaWO_4$ on the support. This improved the substrate's BET surface area from 24 to 181 m^2/g. It was hypothesized that improving the surface area of the substrate would also improve the reaction uptake kinetics. The supported material was reacted with UO_2^{2+} to determine its effectiveness as a sorbent. Figure 6 shows that the time for the sorption uptake curves to reach equilibrium increased with decreasing sorbent

loading. For example, the 0.942 mmol loading reached the equilibrium capacity at 30 minutes and the 0.604 mmol sorbent loading reached in 90 minutes. The sorption processes were modeled using all four models, discussed previously.

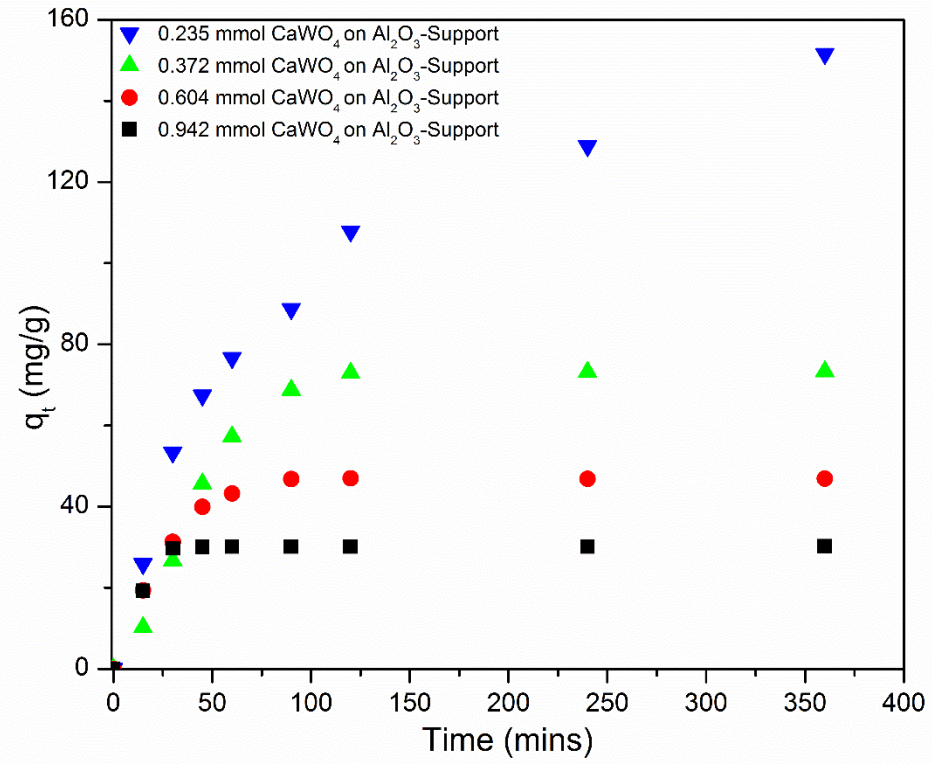

Figure 6: Sorption Uptake Curves of UO_2^{2+} with Al_2O_3 Supported $CaWO_4$

Figure 7 shows that the nonlinear pseudo first-order model fit the data with very good accuracy and with very high correlation coefficients (R^2>0.96) in all cases. The predicted equilibrium sorption capacities, summarized in Table 5, are in very close agreement to the experimental values. Furthermore, using this model allows the reaction half-lives to be easily determined and compared with the nanocrystalline $CaWO_4$.

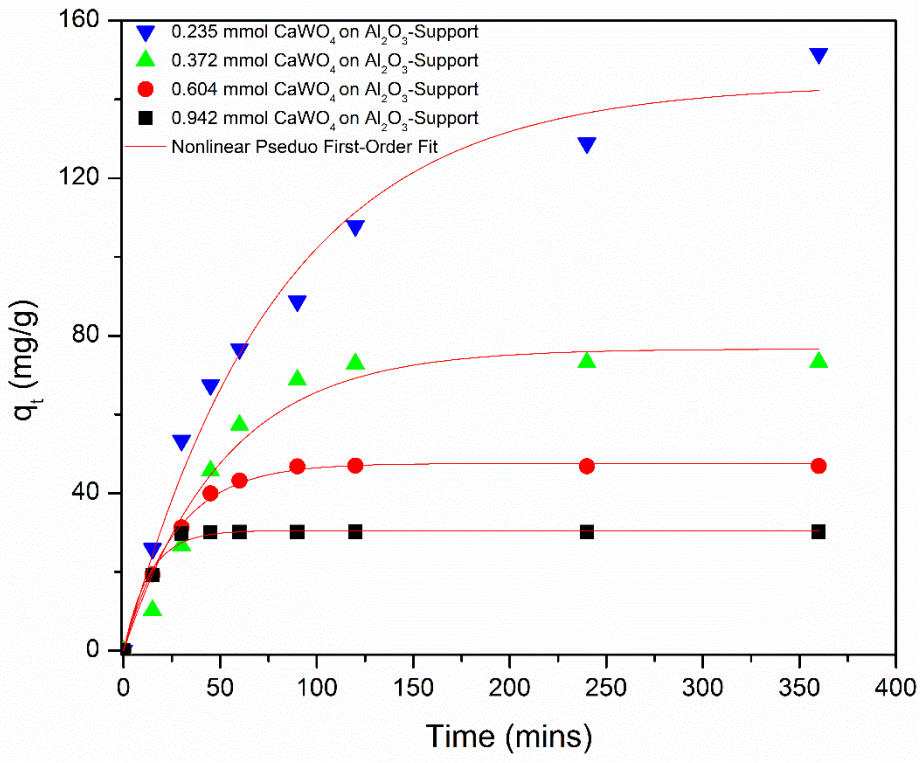

Figure 7: Nonlinear Pseudo First-Order Fit for the Uptake of UO_2^{2+} by Supported $CaWO_4$

Table 5: The Data and Results from the Nonlinear Pseudo First-Order Fit

$CaWO_4$ (mmol)	k_1 (min^{-1})	q_e (mg/g)	q_e (mg/g) (experimental)	R^2
0.235	1.24E-02	144	152	0.979
0.372	1.94E-02	76.7	73.3	0.962
0.604	3.74E-02	47.6	46.9	0.997
0.942	7.64E-02	30.5	30.2	0.988

The linear pseudo first-order equation showed in Figure 8 gives similar, albeit better, results as the nanocrystalline powder sorbent. Again, Table 6 shows the largest sorbent loading gave the largest deviation from the model, with a correlation coefficient of 0.331 for the 0.942 mmol loading. The largest deviation from linearity is for the treatment with the least amount of solid used. Furthermore, the q_e values from the model are drastically lower than observed for the

largest two mass loadings. As noted with the powder, the linear pseudo first-order equation does not adequately describe the sorption process.

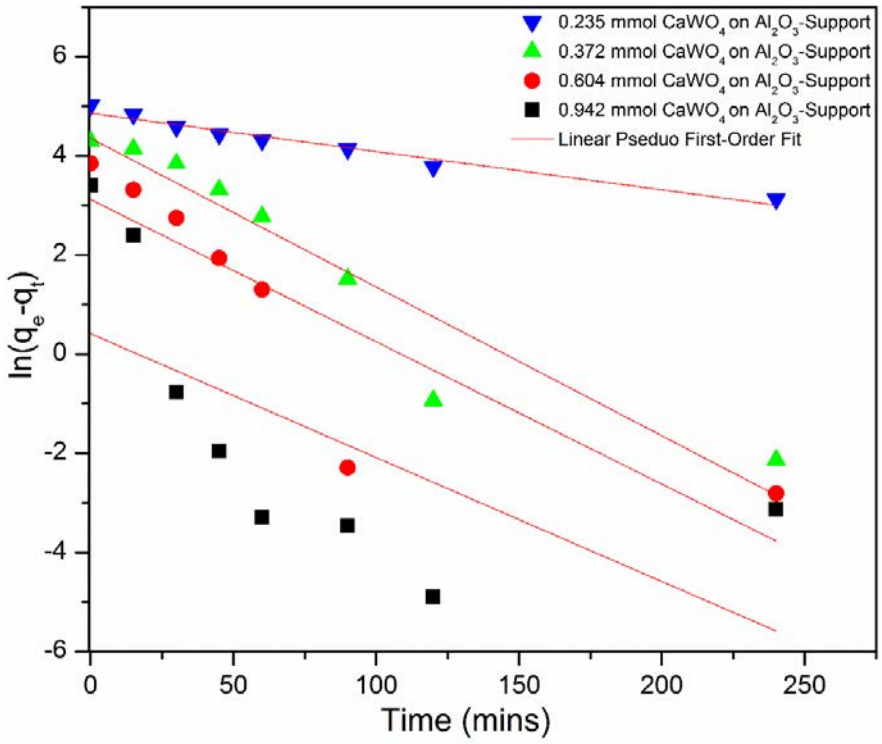

Figure 8: Linear Pseudo First-Order Fit for the Uptake of UO_2^{2+} by Supported $CaWO_4$

Table 6: The Data and Results from the Linear Pseudo First-Order Fit

$CaWO_4$ (mmol)	k_1 (min^{-1})	q_e (mg/g)	q_e (mg/g) (experimental)	R^2
0.235	7.72E-03	129	152	0.961
0.372	3.00E-02	77.8	73.3	0.895
0.604	2.87E-02	22.6	46.9	0.716
0.942	2.50E-02	1.51	30.2	0.331

The linear pseudo second-order equation fits the data almost perfectly (Figure 9), with very high correlation coefficients, listed in Table 7. The model predicts the equilibrium capacities of the two highest loadings with very good accuracy and gave reasonable results for the two lower loadings.

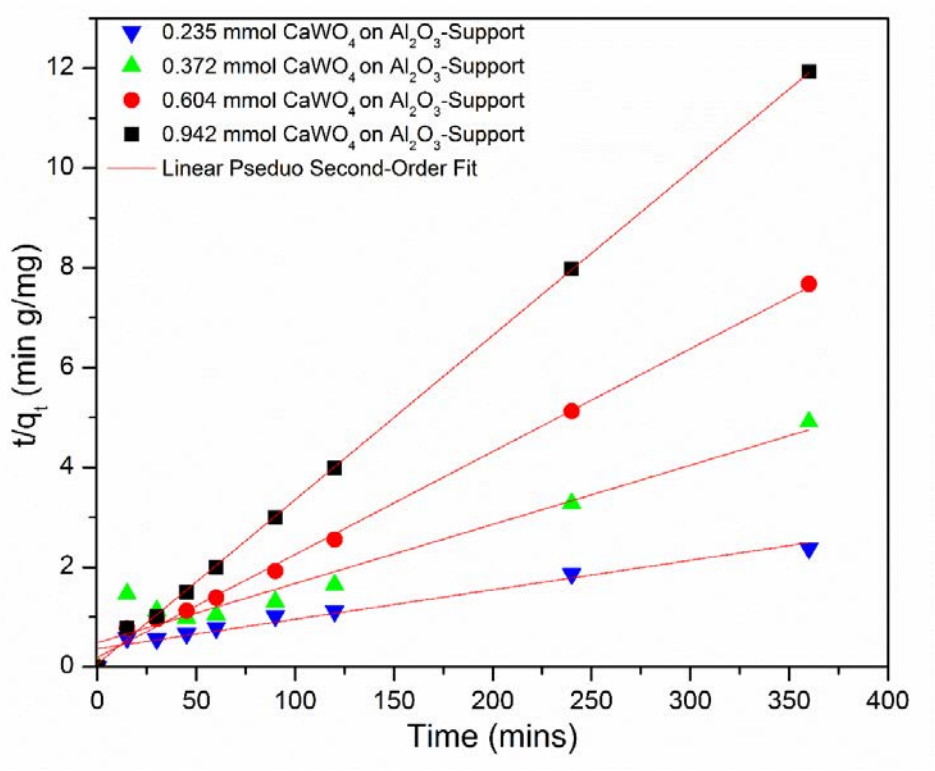

Figure 9: Linear Pseudo Second-Order Fit for the Uptake of UO_2^{2+} by Supported $CaWO_4$

Table 7: The Data and Results from the Linear Pseudo Second-Order Fit

$CaWO_4$ (mmol)	k_2 (g/mg min)	h (mg/g min)	q_e (mg/g)	q_e (mg/g) (experimental)	R^2
0.235	9.57E-05	2.74	169	152	0.948
0.372	2.88E-04	2.05	84.4	73.3	0.924
0.604	2.20E-03	5.18	48.5	46.9	0.996
0.942	1.79E-02	16.5	30.4	30.2	0.999

The nonlinear pseudo second-order equation gives very comparable results to the linear equation. Figure 10 shows the sorption data fitted with the nonlinear pseudo second-order equation. The results, listed in Table 8 are very similar to the linear model, however, the equilibrium capacities are overestimated in every case. Moreover, both models, counterintuitively, suggest that the second lowest mass loading has the slowest initial sorption rate. This result could be consequence of the limited physical meaning that may be extrapolated from the pseudo second-order model.

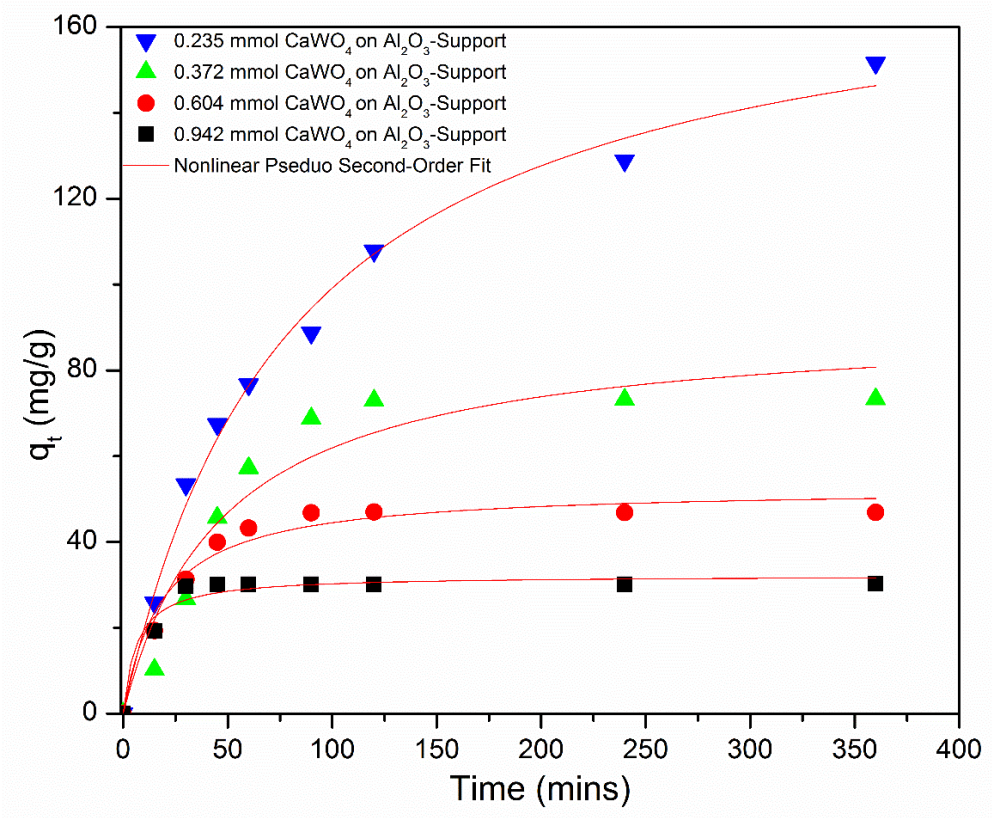

Figure 10: Nonlinear Pseudo Second-Order Fit for the Uptake of UO_2^{2+} by Supported $CaWO_4$

Table 8: The Data and Results from the Nonlinear Pseudo Second-Order Fit

$CaWO_4$ (mmol)	k_2 (g/mg min)	h (mg/g min)	q_e (mg/g)	q_e (mg/g) (experimental)	R^2
0.235	6.92E-05	2.22	179	152	0.992
0.372	2.30E-04	1.92	91.4	73.3	0.922
0.604	1.02E-03	2.85	52.7	46.9	0.967
0.942	4.82E-03	4.99	32.2	30.2	0.960

Since the pseudo second-order models have limited physical meaning, the powder and supported data can only be compared using the pseudo first-order models. However, since the linear pseudo first-order model failed to appropriately describe the sorption process for both materials, data from the nonlinear pseudo first-order models were compared. Figure 11 shows the comparison of the sorption half-lives for the lowest mass loadings for the nanocrystalline powder

and the supported materials. The supported material outperformed the nanocrystalline powder in the experiments with the lowest mass loading. However, this was not the case when comparing the two largest loadings, as diffusion of the solution into the porous media is likely the rate limiting factor for the supported materials. This was evident by out-gassing of air bubbles.

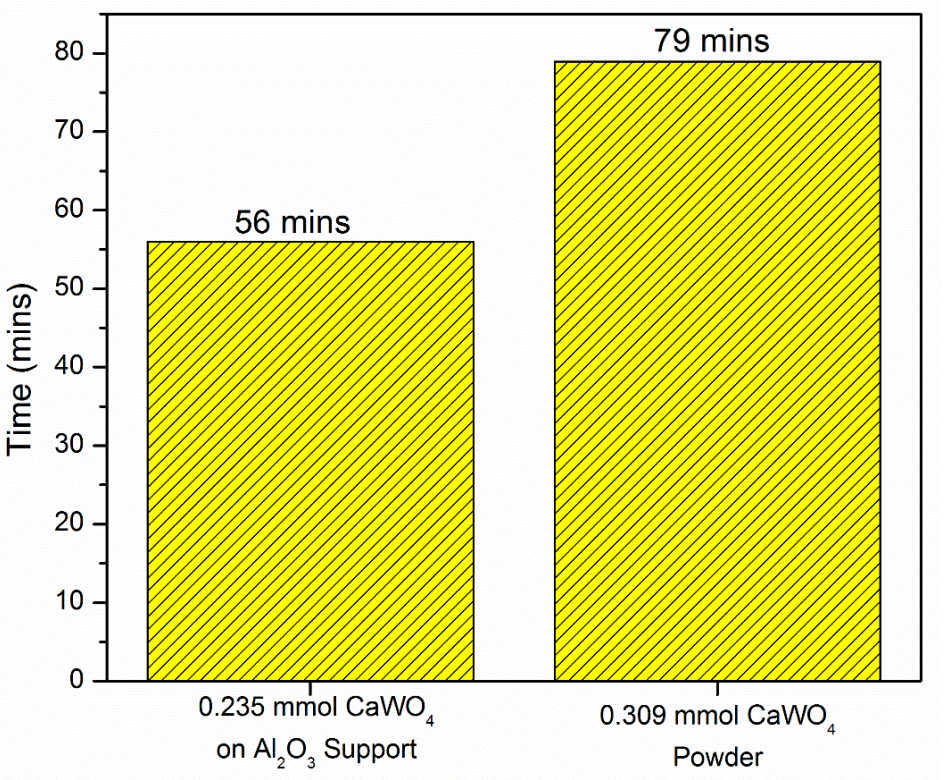

Figure 11: Comparison of Sorption Half-Lives of UO_2^{2+} for the Powder and Supported $CaWO_4$

Sorption Kinetics for the Uptake of Sr^{2+}

The sorption of Sr^{2+} by the $CaWO_4$ powder was studied in the same fashion as uranyl. The uptake curves in Figure 12 shows a process where sorption is initially very fast and starts to slow as the reaction approaches an equilibrium state around 15-30 minutes for the two highest mass loadings and 90 minutes for the 0.816 mmol loadings. The sorption process was followed until the analyte concentration dropped below the instrumental detection limit of roughly 1.5 ppb.

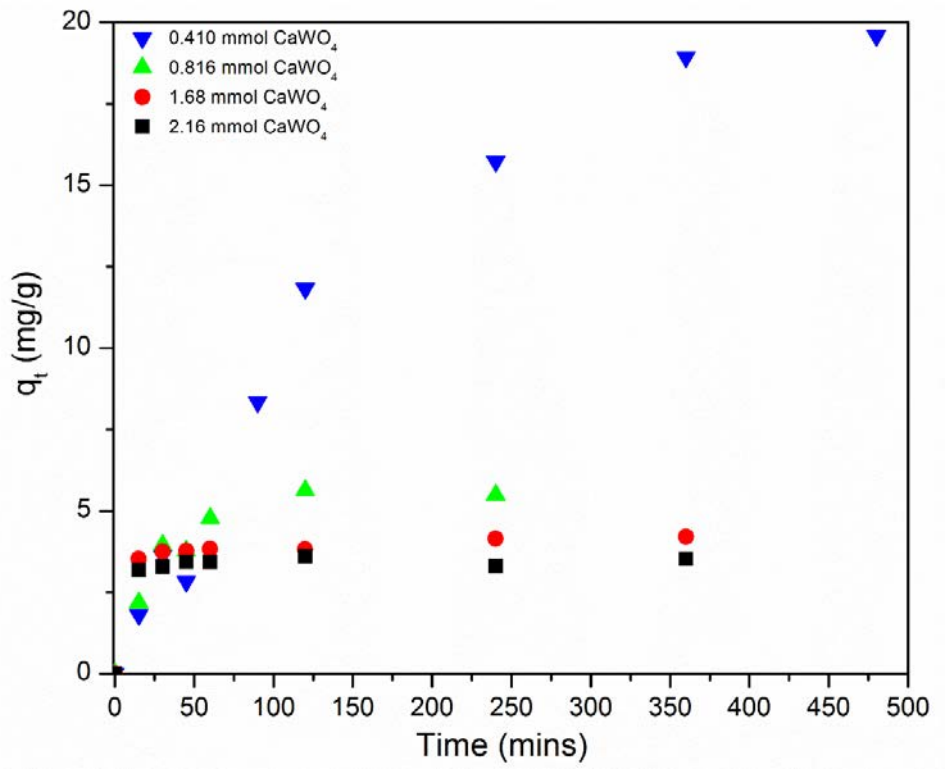

Figure 12: Sorption Uptake Curves of Sr^{2+} with Nanocrystalline $CaWO_4$

The plot of the nonlinear pseudo first-order fit in Figure 15 shows that this model fits the data very well and gives very high correlation coefficients (R^2>0.97) in all cases. The predicted equilibrium sorption capacities, summarized in Table 9, are in fairly close agreement to the experimental values. Furthermore, from this model the rate constants and reaction half-lives can be compared for the powder and supported materials.

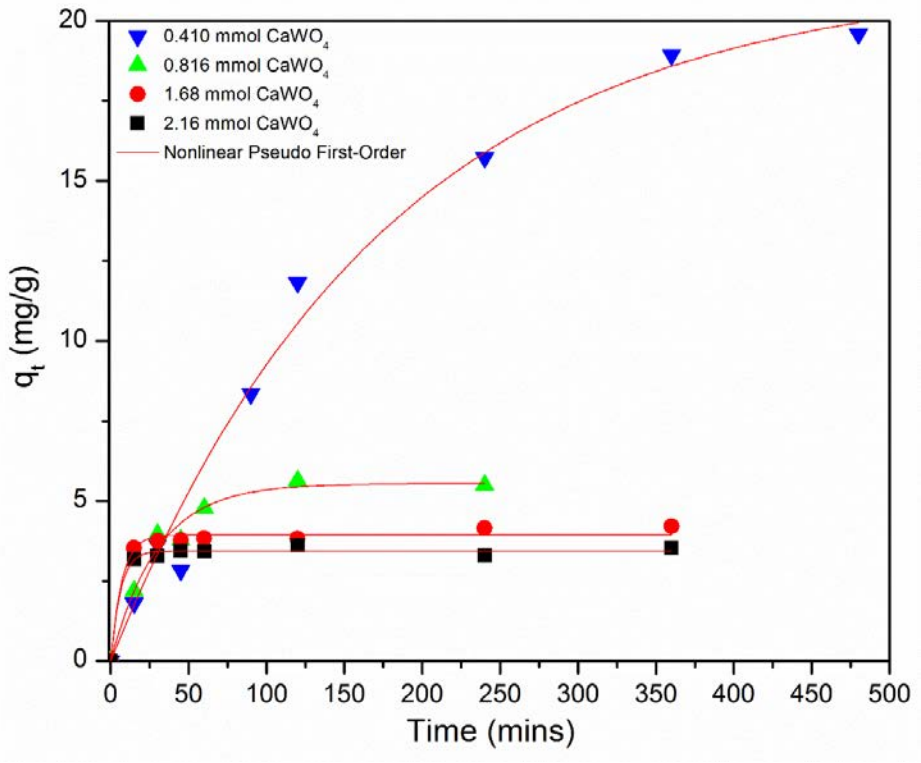

Figure 13: Nonlinear Pseudo First-Order Fit for the Uptake of Sr^{2+} by Nanocrystalline $CaWO_4$

Table 9: The Data and Results from the Nonlinear Pseudo First-Order Fit

$CaWO_4$ (mmol)	k_1 (min^{-1})	q_e (mg/g)	q_e (mg/g) (experimental)	R^2
0.410	5.68E-03	21.3	19.6	0.985
0.816	3.33E-02	5.54	5.49	0.974
1.68	1.44E-01	3.93	4.20	0.984
2.16	1.66E-01	3.44	3.62	0.991

The linear pseudo first-order model for the uptake of Sr^{2+} with $CaWO_4$ in Figure 14 gives similar results to the data from uranyl sorption. As the sorbent loading increases, so does the deviation from linearity and the inaccuracy of the predicted q_e values, as summarized in Table 10.

As noted from the uranyl study, the linear pseudo first-order equation does not adequately describe the sorption process.

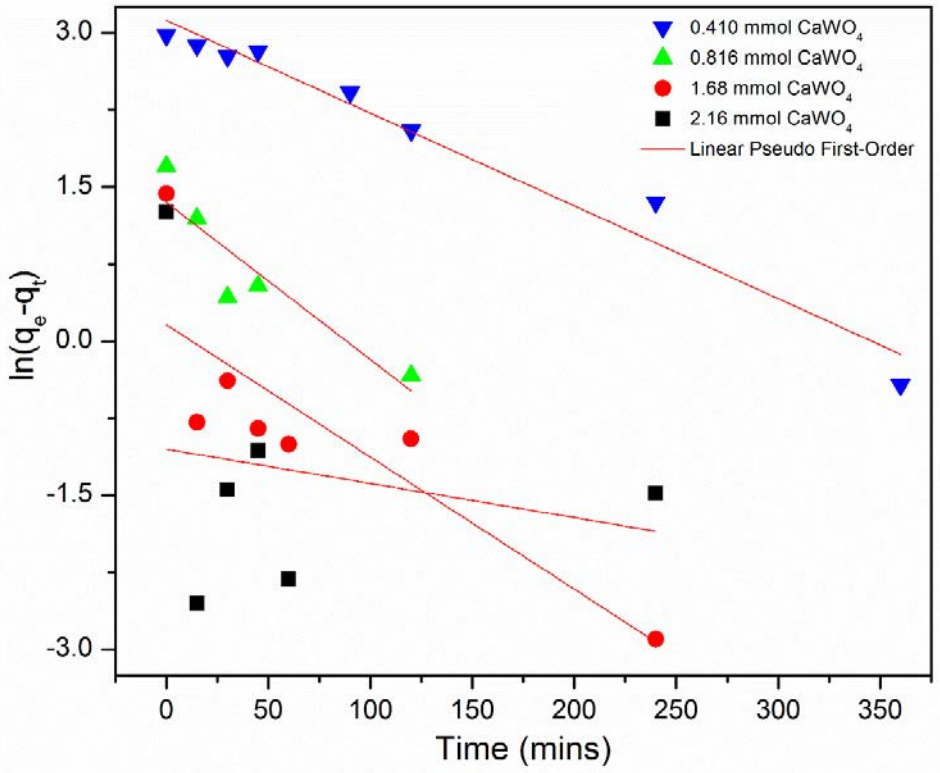

Figure 14: Linear Pseudo First-Order Fit for the Uptake of Sr^{2+} by Nanocrystalline $CaWO_4$

Table 10: The Data and Results from the Linear Pseudo First-Order Fit

$CaWO_4$ (mmol)	k_1 (min^{-1})	q_e (mg/g)	q_e (mg/g) (experimental)	R^2
0.410	9.02E-03	22.6	19.6	0.962
0.816	1.53E-02	3.85	5.49	0.789
1.68	1.29E-02	1.17	4.20	0.657
2.16	3.32E-03	0.35	3.62	0.192

The plotted linear pseudo second-order equation in Figure 15 fits the data almost perfectly for the three higher mass loadings. Table 11 shows the three higher mass loadings have very high correlation coefficients, while the lowest mass loading, 0.410 mmol, has an R^2=0.702. This is likely due to the low molar ratio of the sorbent to analyte (ratio of $CaWO_4$:Sr^{2+} of 6.67:1), leading to the concentration of reactive sites to be similar to the concentration the analyte,

suggesting the pseudo first-order model should be (and is) better suited.[19] The model predicts the sorption equilibrium capacities with good accuracy for three of the four cases. There is, however, only slight over estimations in two of the three cases, while the q_e value for the highest mass loading is slightly underestimated.

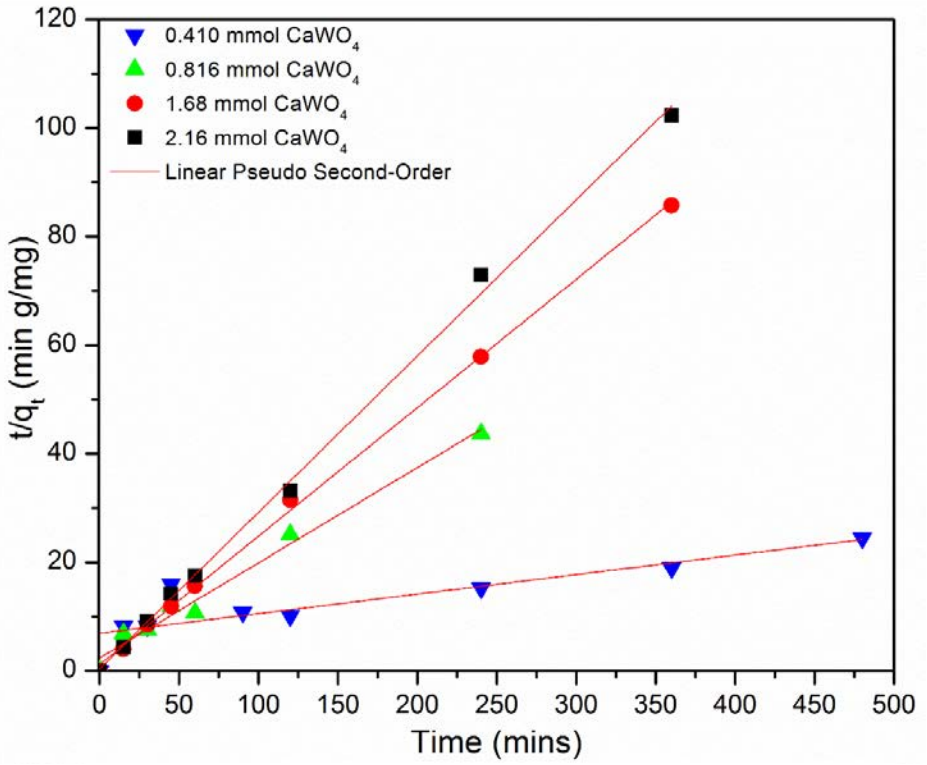

Figure 15: Linear Pseudo Second-Order Fit for the Uptake of Sr^{2+} by Nanocrystalline $CaWO_4$

Table 11: The Data and Results from the Linear Pseudo Second-Order Fit

$CaWO_4$ (mmol)	k_2 (g/mg min)	h (mg/g min)	q_e (mg/g)	q_e (mg/g) (experimental)	R^2
0.410	1.86E-04	0.144	27.8	19.6	0.702
0.816	1.32E-02	0.427	5.70	5.49	0.981
1.68	4.83E-02	0.862	4.22	4.20	0.999
2.16	2.20E-01	2.65	3.47	3.62	0.998

The nonlinear pseudo second-order equation fits the data almost perfectly (Figure 16), with very high correlation coefficients, listed in Table 12. As was the case for the linear method, the results for the lowest sorbent loading are much higher than observed experimentally. The model predicts the rest of the sorption equilibrium capacities with fairly good accuracy.

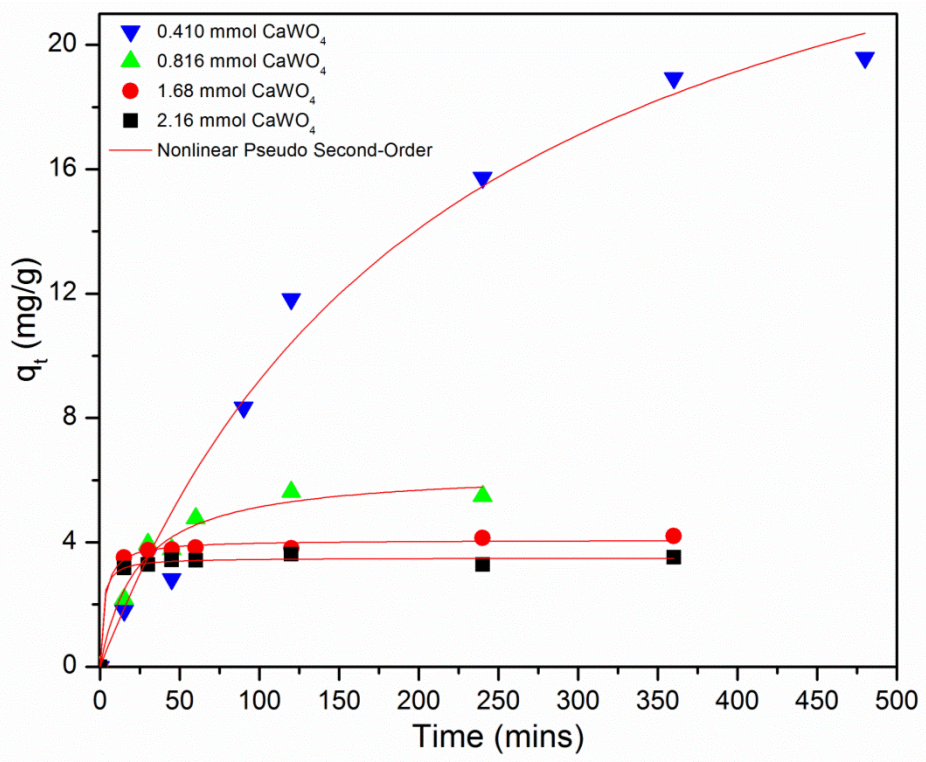

Figure 16: Nonlinear Pseudo Second-Order Fit for the Uptake of Sr^{2+} by Nanocrystalline $CaWO_4$

Table 12: The Data and Results from the Nonlinear Pseudo Second-Order Fit

$CaWO_4$ (mmol)	k_2 (g/mg min)	h (mg/g min)	q_e (mg/g)	q_e (mg/g) (experimental)	R^2
0.410	1.49E-04	0.133	29.9	19.6	0.981
0.816	6.73E-03	0.271	6.34	5.49	0.969
1.68	9.04E-02	1.50	4.08	4.20	0.993
2.16	1.86E-01	2.28	3.50	3.62	0.992

Comparing the results from the kinetic study using nanocrystalline $CaWO_4$ demonstrates that the nonlinear pseudo first order model is the best fit for this sorption process. Further, it is the only method that gives good results throughout the mass loadings, even for the 0.410 mmol loading which had very poor results when fit with the pseudo second-order models.

Supported calcium tungstate was also used as a sorbent for Sr^{2+} to determine its effectiveness as a sorbent. Figure 17 shows sorption uptake curves that indicate that the equilibrium capacities are reached later in every case than that of the nanocrystalline powder. For example, the highest mass loading reached the equilibrium capacity at roughly 90 minutes where a similar concentration of the nanocrystalline powder reached the equilibrium capacity at 15 minutes.

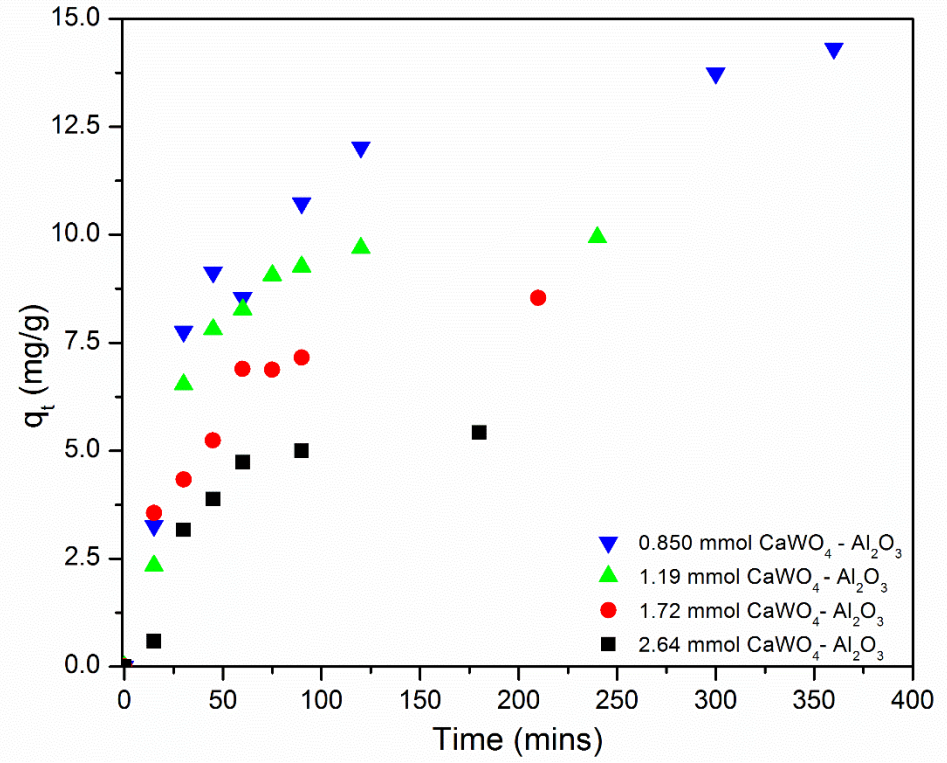

Figure 17: Sorption Uptake Curves of Sr^{2+} by Supported $CaWO_4$

Figure 18 shows that the nonlinear pseudo first-order model fits the data very well. The fit gave reasonable correlation coefficients, summarized in Table 13, that were greater than 0.93 in all cases. Furthermore, the predicted equilibrium sorption capacities are in close agreement with the experimental values. Interestingly, the k_1 values throughout the series are all very close, suggesting the sorption process was highly affected by the diffusion of air out of the porous substrate.

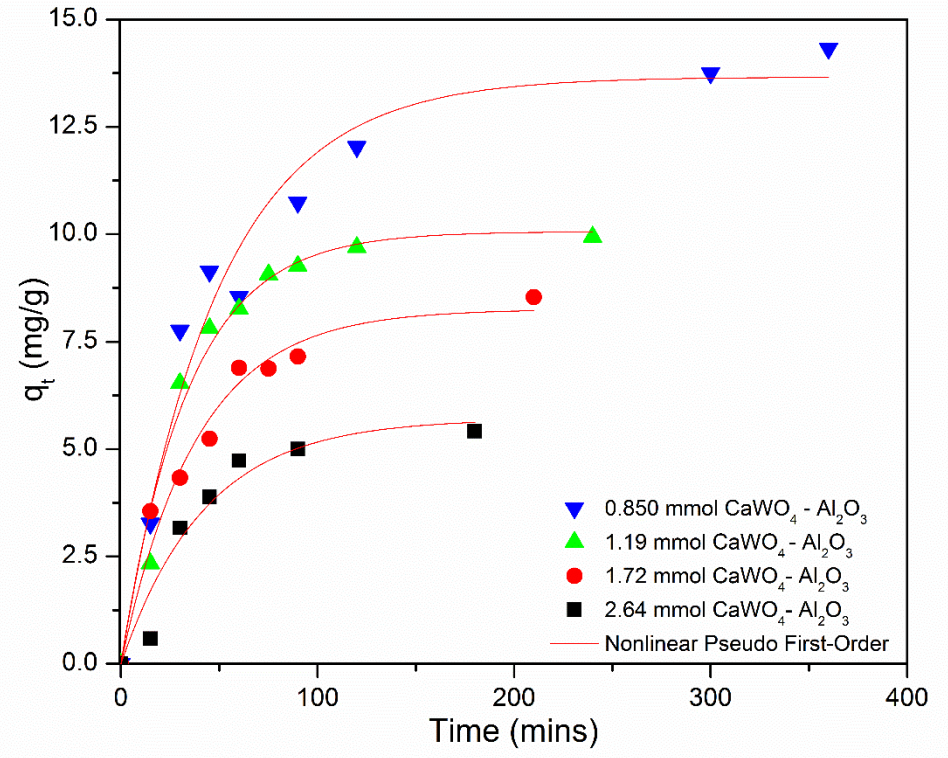

Figure 18: Nonlinear Pseudo First-Order Fit for the Uptake of Sr^{2+} by Supported $CaWO_4$

Table 13: The Data and Results from the Nonlinear Pseudo First-Order Fit

$CaWO_4$ (mmol)	k_1 (min^{-1})	q_e (mg/g)	q_e (mg/g) (experimental)	R^2
0.850	2.06E-02	13.7	14.3	0.964
1.19	2.62E-02	10.2	10.4	0.971
1.72	2.88E-02	8.25	8.53	0.968
2.64	2.92E-02	5.70	5.42	0.934

Interestingly, Figure 19 shows that the linear pseudo first-order model fit the data very well throughout the loadings. The model underestimates the equilibrium capacities throughout the series, but gave reasonable results summarized in Table 14. However, the data from the model suggests the 1.72 mmol loading has a lower rate constant than the 1.19 mmol loading.

The nonlinear model gives much more agreeable results, leading to the conclusion that the linear pseudo first-order equation is not an acceptable model for the data presented in this chapter.

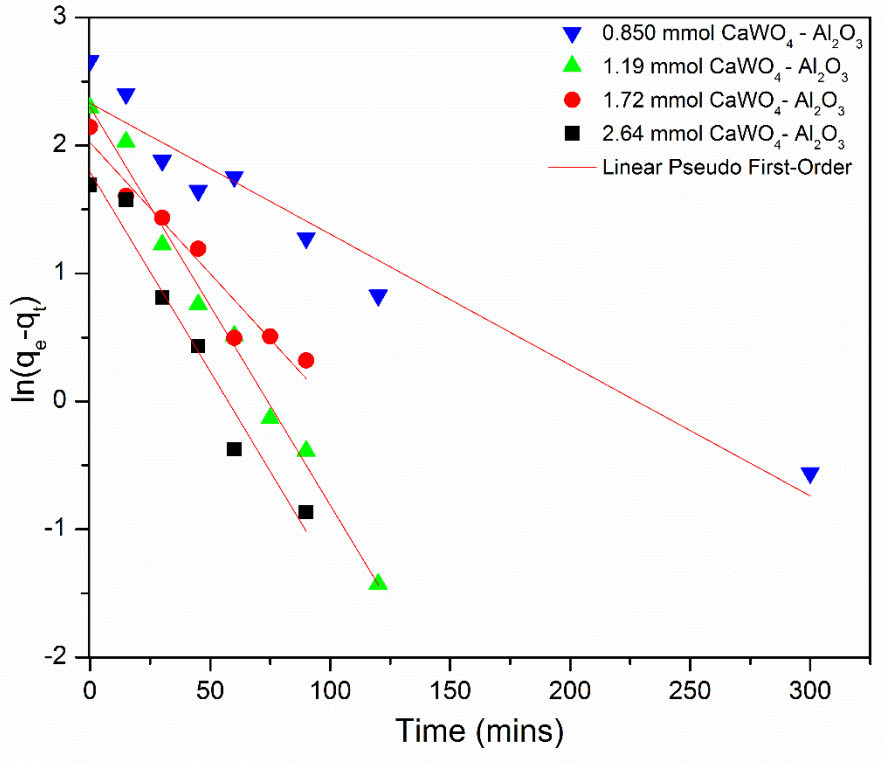

Figure 19: Linear Pseudo First-Order Fit for the Uptake of Sr^{2+} by Supported $CaWO_4$

Table 14: The Data and Results from the Linear Pseudo First-Order Fit

$CaWO_4$ (mmol)	k_1 (min^{-1})	q_e (mg/g)	q_e (mg/g) (experimental)	R^2
0.850	1.02E-02	10.28	14.3	0.941
1.19	3.11E-02	9.98	10.4	0.989
1.72	2.05E-02	7.55	8.53	0.938
2.64	3.12E-02	6.00	5.42	0.956

The linear pseudo second-order equation fits the data very well, with very high correlation coefficients, depicted in Figure 20. The model also gives fairly accurate predictions for the sorption equilibrium capacities, with a slight over estimation in each case summarized in Table 15.

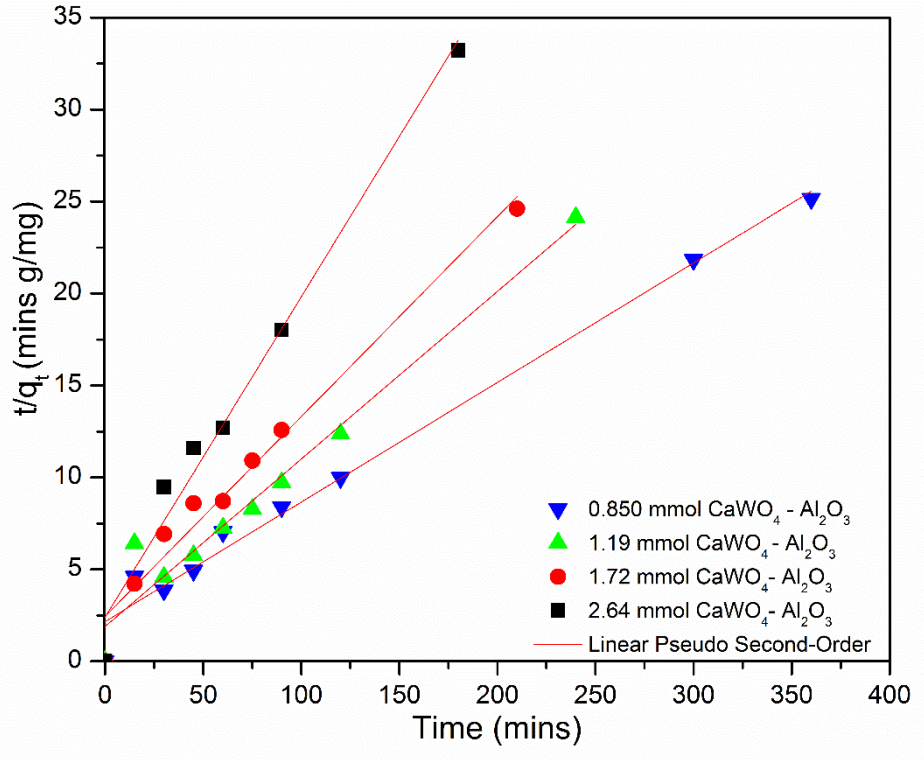

Figure 20: Linear Pseudo Second-Order Fit for the Uptake of Sr^{2+} by Supported $CaWO_4$

Table 15: The Data and Results from the Linear Pseudo Second-Order Fit

$CaWO_4$ (mmol)	k_2 (g/mg min)	h (mg/g min)	q_e (mg/g)	q_e (mg/g) (experimental)	R^2
0.850	1.96E-03	0.463	15.4	14.3	0.984
1.19	4.51E-03	0.544	11.0	10.4	0.955
1.72	4.90E-03	0.415	9.20	8.5	0.969
2.64	1.27E-02	0.417	5.74	5.42	0.977

Figure 21 shows the fit of nonlinear pseudo second-order equation, which gives similar results to the linear model. Further, this model does predict the sorption equilibrium capacities with fairly good accuracy, listed in Table 16, but the linear equation gives more reasonable results.

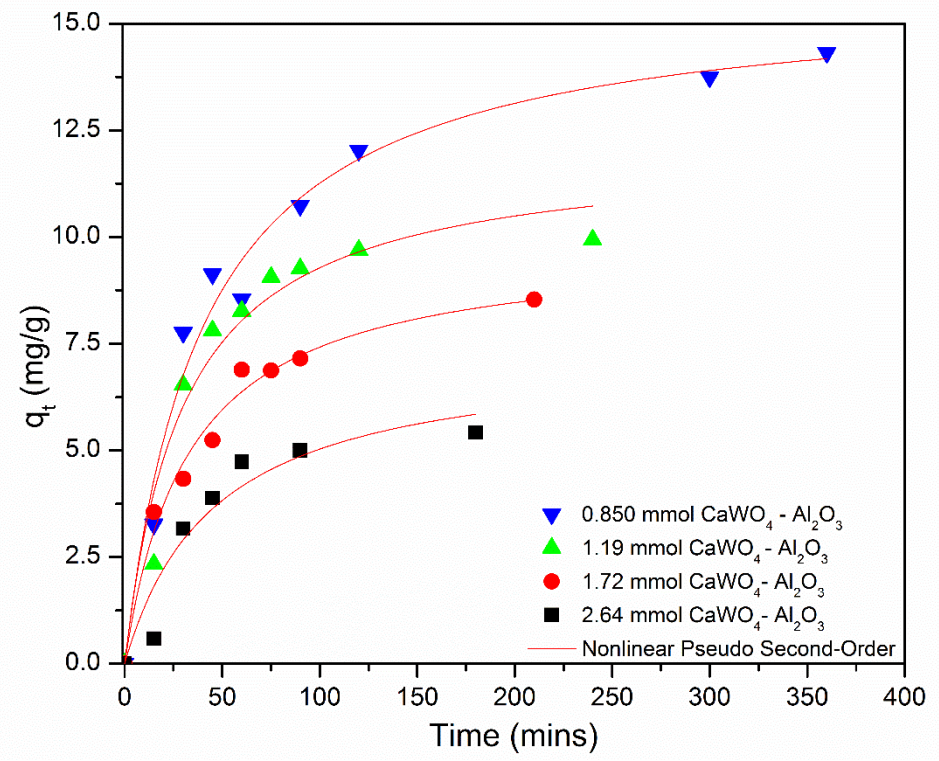

Figure 21: Nonlinear Pseudo Second-Order Fit for the Uptake of Sr^{2+} by Supported $CaWO_4$

Table 16: The Data and Results from the Nonlinear Pseudo Second-Order Fit

$CaWO_4$ (mmol)	k_2 (g/mg min)	h (mg/g min)	q_e (mg/g)	q_e (mg/g) (experimental)	R^2
0.850	1.59E-03	0.395	15.7	14.3	0.977
1.19	2.76E-03	0.402	12.1	10.4	0.950
1.72	3.11E-03	0.301	9.85	8.53	0.981
2.64	2.98E-03	0.160	7.33	5.42	0.908

Using the pseudo first-order rate constants of the powder and supported materials from the nonlinear model, the sorption half-lives can be calculated and compared. Figure 22 shows the comparison of the sorption half-lives for the lowest mass loadings for the supported material and the second lowest for the nanocrystalline powder. The nanocrystalline powder showed faster kinetics compared to the supported materials in every case. Again, this is likely do to diffusion of the liquid into the media being rate limiting.

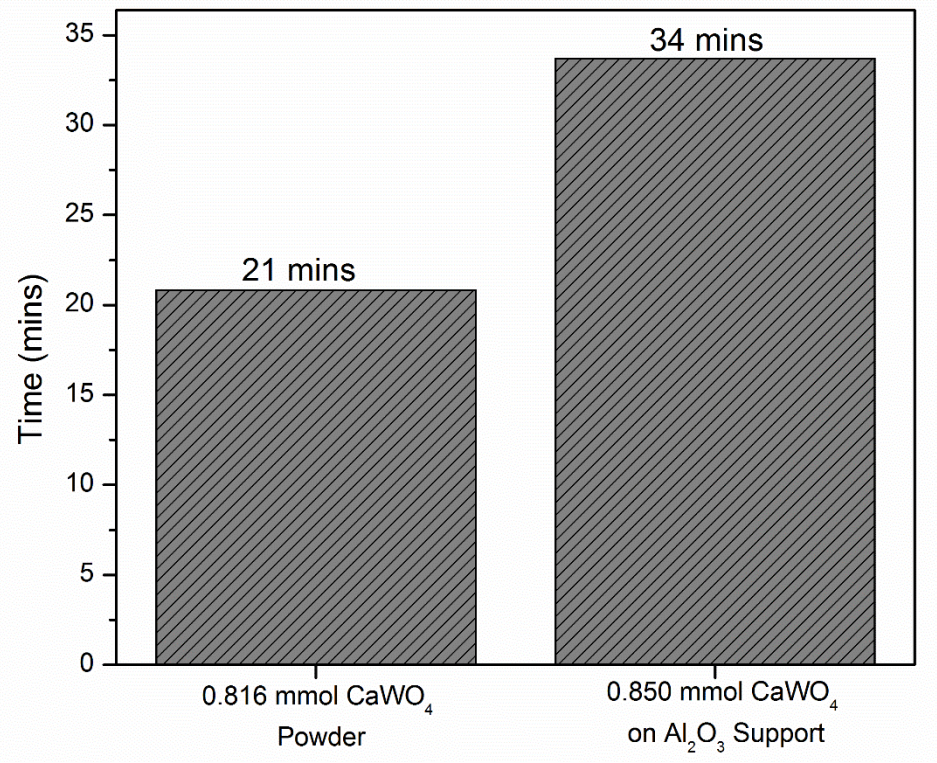

Figure 22: Comparison of Sorption Half-Lives of Sr^{2+} for the Powder and Supported $CaWO_4$

Capacity and Characterization

The capacities of the materials were determined by reacting the sorbents with excess uranium and strontium. A solution of roughly 50 mL of 19,500 ppm UO_2^{2+} was treated with 0.75 g of $CaWO_4$, a molar ratio of 1.5 to 1.0 respectively. The capacity experiment for Sr^{2+} was performed using a solution with a concentration of 6,500 ppm giving a molar ratio of 1.4 to 1.0. Upon completion, the $CaWO_4$ was able to remove roughly 55 mole percent of the uranyl from the solution. The same material had a sorption capacity of 35 mole percent for strontium under the same conditions. The material from this study was analyzed by SEM and X-ray powder diffraction. Both of the X-ray diffraction patterns showed no evidence of newly formed crystalline materials. Further, the material used to sorb Sr^{2+} showed little to no change of morphology, as evident by from the electron micrograph in shown in Figure 23. The material

from the reaction with excess UO_2^{2+} showed a slight morphology change, shown in Figure 24, with the particles showing flat-elongated agglomerated particles. These results make sense since the strontium can react via an ion exchange reaction but the large uranyl ion must react to produce a product where the $CaWO_4$ lattice is completely deconstructed. Therefore, a dissolution/reprecipitation process likely takes place that changes the morphology of the particles.

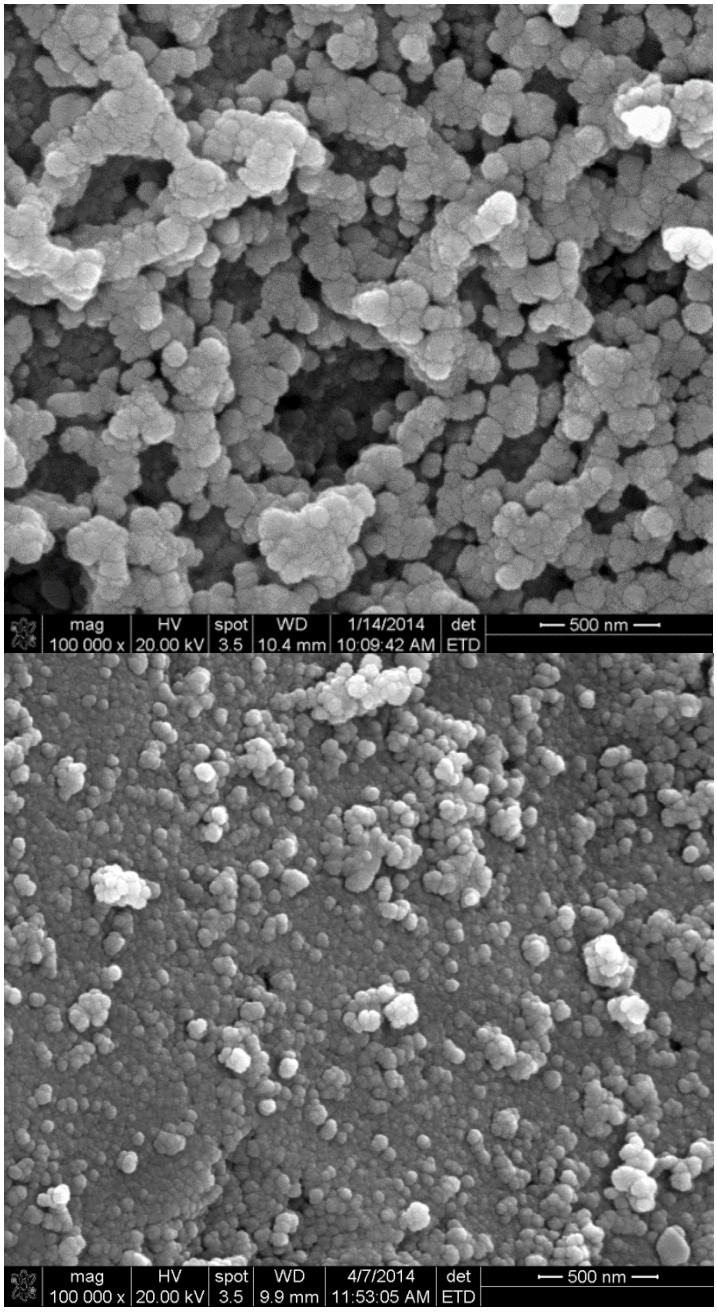

Figure 23: SEM of the $CaWO_4$ before (left) and after Treatment (right) of Excess Sr^{2+}

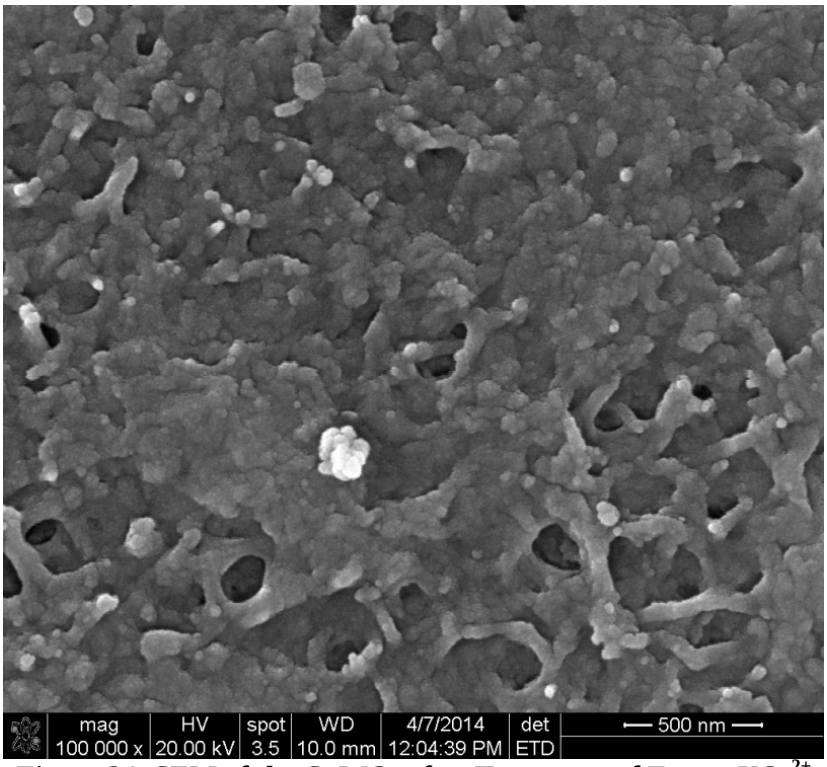

Figure 24: SEM of the $CaWO_4$ after Treatment of Excess UO_2^{2+}

The capacity of the supported material was also of interest to determine if there was any improvement on the extent of the reaction. Under similar reaction conditions as the powder, the supported $CaWO_4$ was reacted to complete exhaustion (100 mole percent) with UO_2^{2+} and to 85 mole percent when reacted with Sr^{2+}. The increased extent of the reactions is likely due to smaller particles in the supported material that permits the reactants to penetrate the core of the particles. Figure 25 shows the bright yellow pellets produced from the reaction of UO_2^{2+} with the supported $CaWO_4$. These pellets were characterized by XRD and the product was found to be amorphous. Further, the scanning electron micrographs of the material before and after treatment (Figure 26) showed little change. However, the supported material after the treatment of Sr^{2+} unexpectedly gave particles with a large morphology change, as depicted in Figure 27. The particles appear to be large pillar-like particles with flat tops. Unlike the reaction of the powder with strontium, the reaction of strontium appears to have formed novel particles by outgrowth of the product from the surface.

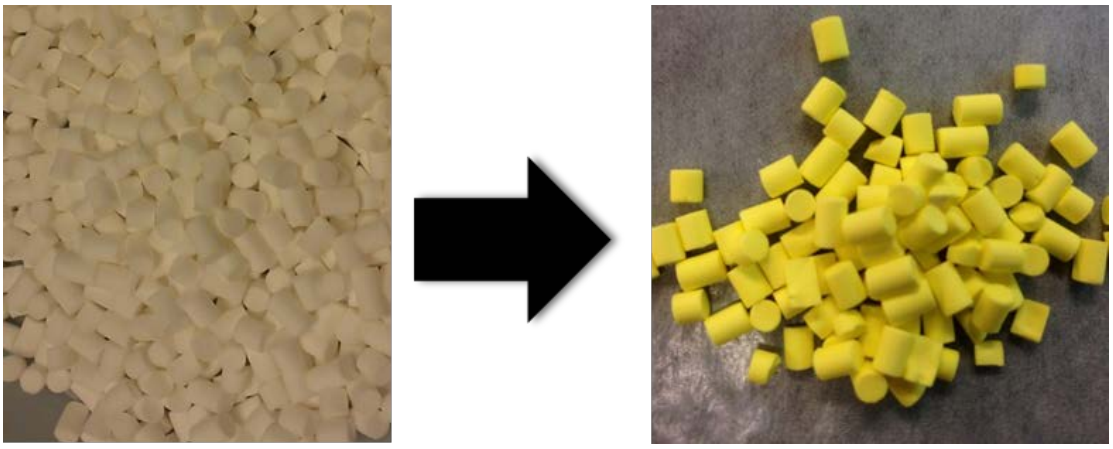

Figure 25: Production of a Brightly Yellow Colored Pellet from the Reaction of UO_2^{2+} with $CaWO_4$ on Alumina

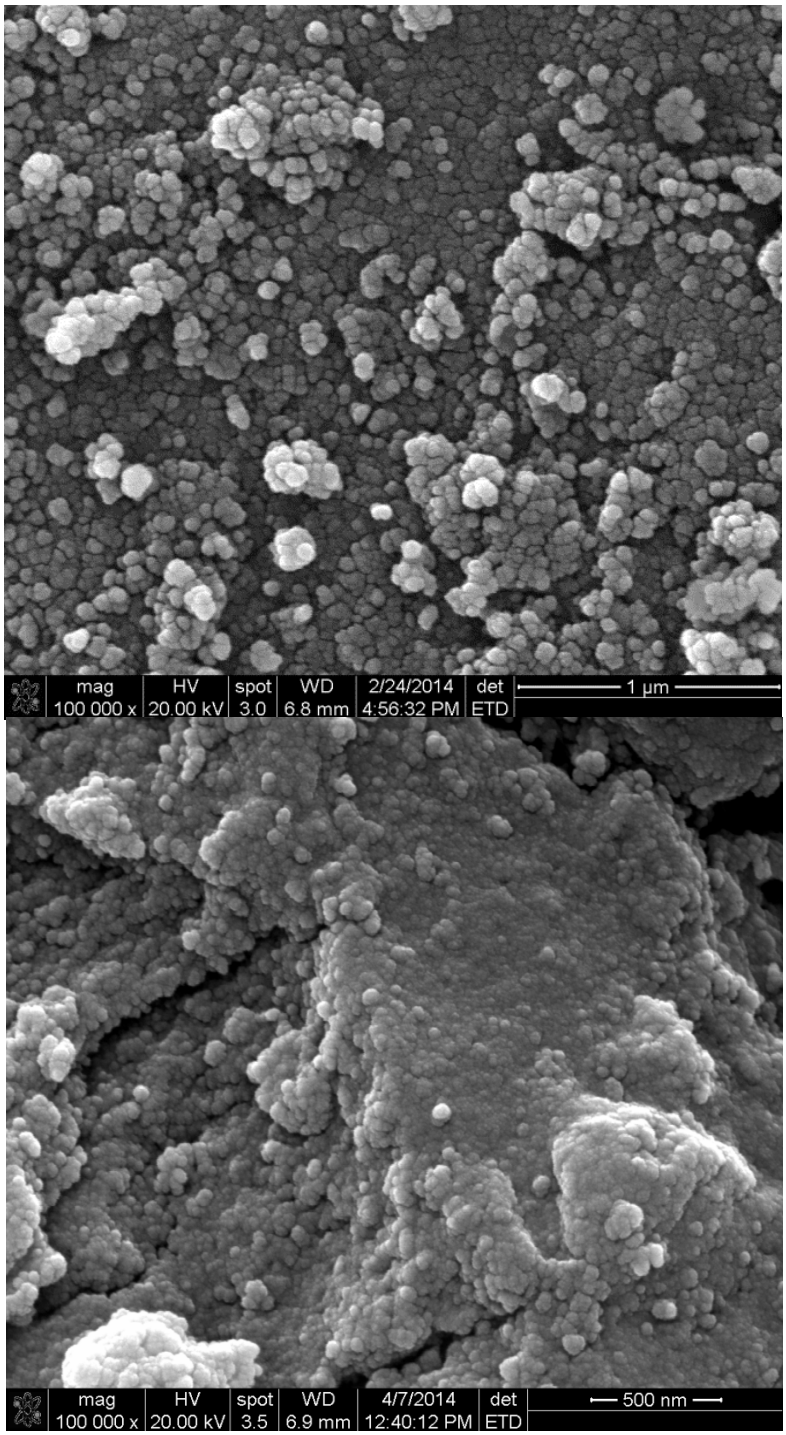

Figure 26: SEM Micrographs of the Supported $CaWO_4$ before (top) and after Treatment with Excess Uranyl (bottom)

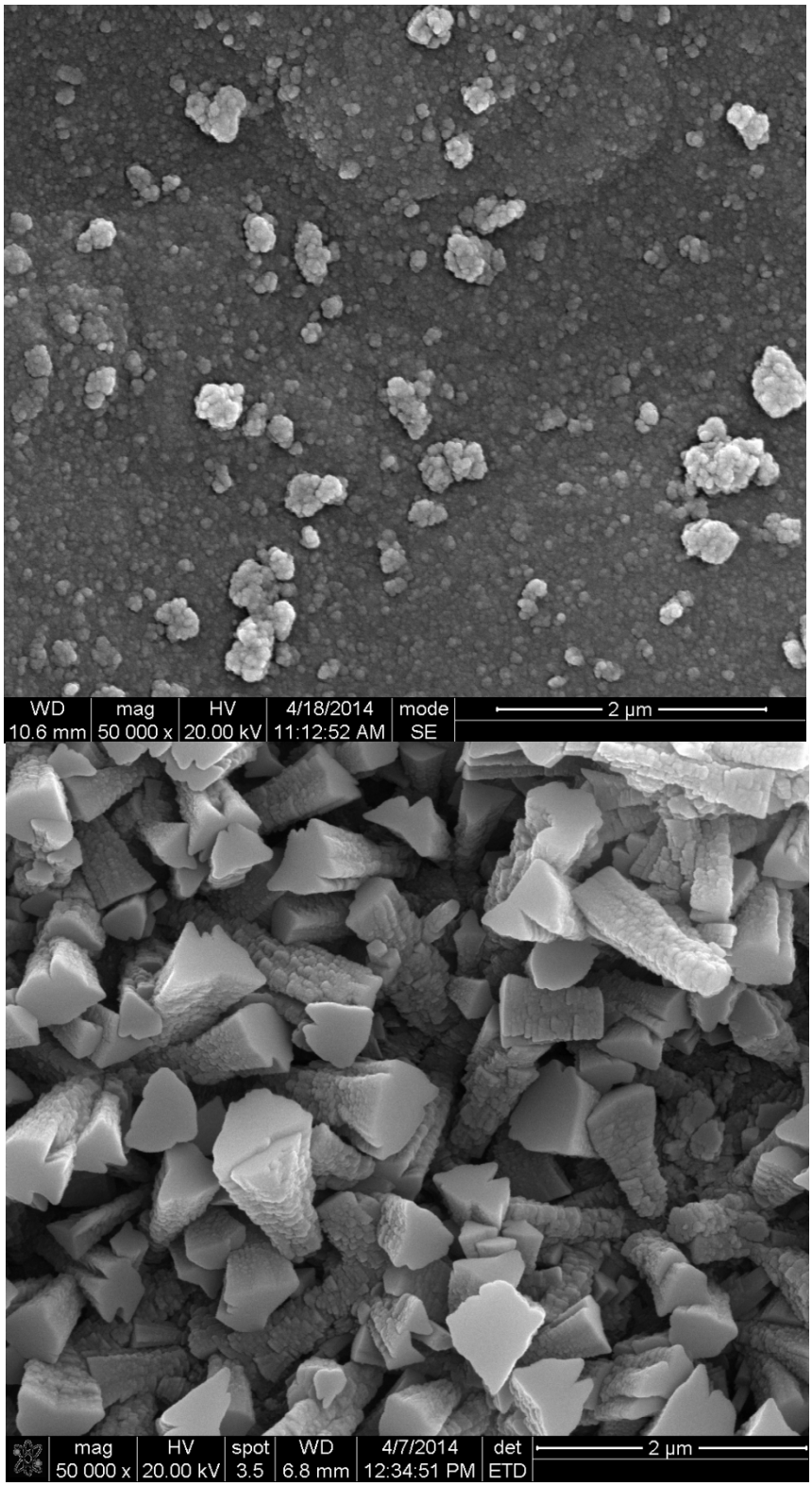

Figure 27: SEM of the Supported $CaWO_4$ (14.1%) before (top) and Reacted with Excess Sr^{2+} (bottom)

Recovery of Materials

As previously demonstrated, the spent materials can be easily recovered in a green fashion.[17] The spent materials were able to be recovered in a cyclic process by treating the post sorption materials with ammonium hydroxide, generating ammonium chloride as the only byproduct (Figure 28). The recovery process took roughly 24 hours with magnetic stirring, producing an insoluble uranium containing material called yellow cake and soluble ammonium tungstate. The two products were separated by vacuum filtration. The yellow cake can then be calcined and repurposed as uranium oxide (U_3O_8) with a very high yield. The filtrate was then acidified with HCl, producing insoluble tungstic acid recovered in very high yields (98%). From there, the tungstic acid was converted back to $CaWO_4$ with the same yield as the original preparation of calcium tungstate.

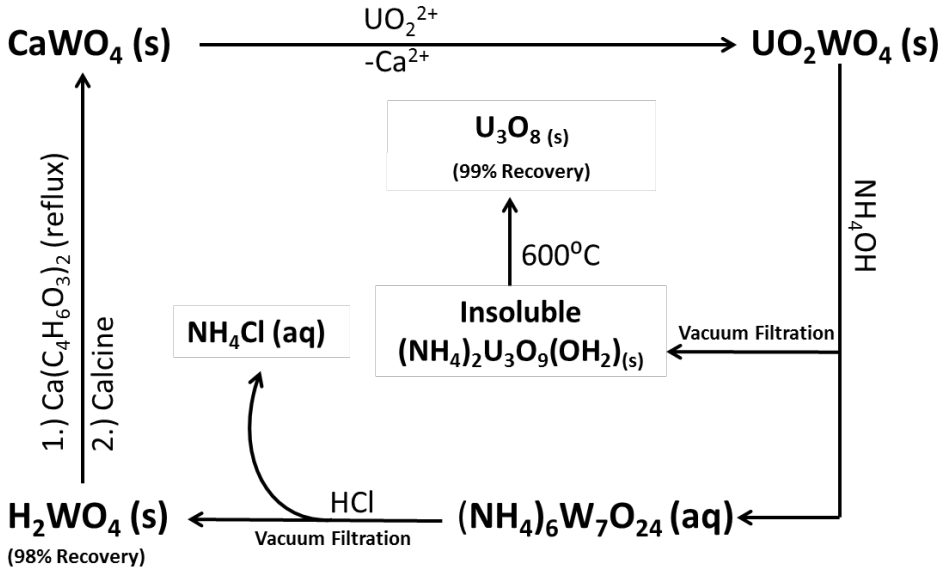

Figure 28: The Cyclic-Green Process for the Recovery of Uranium

Further, the $SrWO_4$ produced could also be recovered in a cyclic and green process that is outlined in Figure 29. By treating the spent material with Na_2CO_3 for roughly 72 hours under ambient conditions, insoluble $SrCO_3$ was produced along with soluble Na_2WO_4. The Na_2WO_4

solution was then treated with HCl, producing insoluble tungstic acid with a very high yield. The tungstic acid was then converted to $CaWO_4$ as previously described.

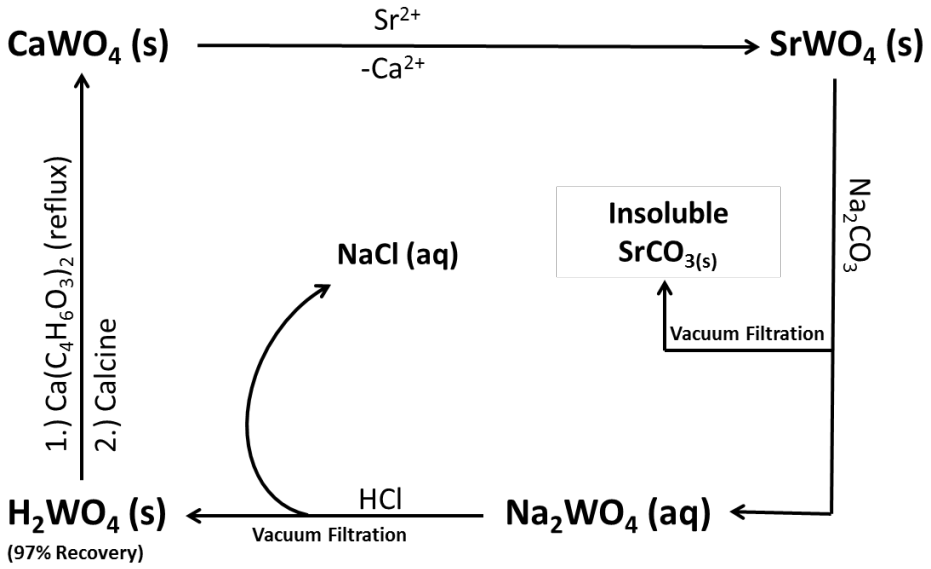

Figure 29: The Cyclic-Green Process for the Recovery of Strontium

The recovery processes can be applied to the supported materials; however, the insoluble analyte produced from the reaction with the base stays on the support. The analytes can then easily be stripped from the supports by treatment with a mineral acid.

Conclusion:

Calcium tungstate provides an excellent alternative to conventional methods for radionuclide separations. Further, the sorbent allows for the recovery of the analytes with high yields, allowing them to be recycled and reused. The high surface area of the supported materials led to much improved sorption capacities. This reaction gives the means to remove uranium from drinking water and a method to treat contaminated ground water using permeable reactive barriers. An advantage of supporting the materials on larger substrates is the elimination of the need for filtration to separate the materials from solutions. Modeling of the sorption of uranyl on calcium tungstate gave good results using the linear pseudo-second order, the nonlinear

pseudo first order model, and the nonlinear pseudo second-order models. However, the nonlinear first-order method describes the experimental data most accurately. Further research should implement these materials into natural water systems and industrial waste streams to test the efficiency of the material in real-world applications. Further study should also target other radionuclides for recovery from solutions.

References:

1. M. J. Manos, N. Ding, and M. G. Kanatzidis, Layered metal sulfides: Exceptionally selective agents for radioactive strontium removal. *Proceedings of the National Academy of Sciences* **2008,** *105* (10), 3696-3699.

2. Application of Ion Exchange Processes for the Treatment of Radioactive Waste and Management of Spent Ion Exchangers. In *Technical Reports No. 48*, Agency, I. A. E., Ed. Vienna, 2002.

3. J. H. Lehr, M. Hyman, T. Gass, and W. J. Seevers, Handbook of Complex Environmental Remediation Problems. Mcgraw-hill: 2001; pp 303–341.

4. K. M. A. El-Rahman, M. R. El-Sourougy, N. M. Abdel-Monem, and I. M. Ismail, Modeling the Sorption Kinetics of Cesium and Strontium Ions on Zeolite A. *Journal of Nuclear and Radiochemical Sciences* **2006,** *7* (2), 21-27.

5. S. Khan, Sorption of the long-lived radionuclides cesium-134, strontium-85 and cobalt-60 on bentonite. *Journal of Radioanalytical and Nuclear Chemistry* **2003,** *258* (1), 3-6.

6. W. F. Libby, Radioactive Strontium Fallout. *Proceedings of the National Academy of Sciences* **1956,** *42* (6), 365-390.

7. Rapid Simultaneous Determination of 89Sr and 90Sr in Milk: A Procedure Using Cerenkv and Scintillation Counting. Agency, I. A. E., Ed. Vienna, 2013; Vol. IAEA Analytical Quality in Nuclear Applications Series No. 27.

8. S. C. Skoryna and D. S. Kahn, The late effects of radioactive strontium on bone. Histogenesis of bone tumors produced in rats by high Sr89 dosage. *Cancer* **1959,** *12* (2), 306-322.

9. S. Pors Nielsen, The biological role of strontium. *Bone* **2004,** *35* (3), 583-588.

10. G. Steinhauser, V. Schauer, and K. Shozugawa, Concentration of Strontium-90 at Selected Hot Spots in Japan. *PLoS ONE* **2013,** *8* (3), e57760.

11. H. Tabuchi, High Level of Radioactive Strontium Found in Groundwater Near Fukushima Plant. *The New York Times* June 18, 2013.

12. G. Steinhauser, A. Brandl, and T. E. Johnson, Comparison of the Chernobyl and Fukushima nuclear accidents: A review of the environmental impacts. *Science of the Total Environment* **2014,** *470–471* (0), 800-817.

13. C. R. Porter, B. Kahn, M. W. Carter, G. L. Rehnberg, and E. W. Pepper, Determination of radiostrontium in food and other environmental samples. *Environmental Science & Technology* **1967,** *1* (9), 745-750.

14. C. Xu, J. Wang, and J. Chen, Solvent Extraction of Strontium and Cesium: A Review of Recent Progress. *Solvent Extraction and Ion Exchange* **2012,** *30* (6), 623-650.

15. B. P. Kiran, A. W. Apblett, and M. M. Chehbouni, Selective Absorption of Heavy Metals and Radionuclides from Water in a Direct-to-Ceramic Process. *Ceramic Transactions* **2003,** *143*, 385-394.

16. M. Chehbouni, H. Al-Busaidi, and A. W. Apblett, Green Process for Uranium Separations Utilizing Molybdenum Trioxide. In *Nuclear Energy and the Environment*, American Chemical Society: 2010; Vol. 1046, pp 155-167.

17. H. Al-busaidi and A. W. Apblett, Adsorption and Separation of Uranium Using Tungsten Oxides. In *Environmental Issues and Waste Management Technologies in the Materials and Nuclear Industries XII*, John Wiley & Sons, Inc.: 2009; pp 39-46.

18. S. Lagergren, Zur theorie der sogenannten adsorption gelöster stoffe. Kungliga Svenska Vetenskapsakademiens. *Handlingar* **1898,** *24* (4), 1-39.

19. S. Azizian, Kinetic models of sorption: a theoretical analysis. *Journal of Colloid and Interface Science* **2004,** *276*, 47–52.

20. K. V. Kumar, Linear and non-linear regression analysis for the sorption kinetics of methylene blue onto activated carbon. *Journal of Hazardous Materials B* **2006,** *137*, 1538-1544.

21. Y.-S. Ho and G. McKay, Pseudo-second order model for sorption processes. *Process Biochemistry* **1999,** *34* (5), 451-465.

22. J.-Z. Zhang, Avoiding spurious correlation in analysis of chemical kinetic data. *Chemical Communications* **2011,** *47* (24), 6861-6863.

CHAPTER XII

CONCLUSION AND FUTURE WORK

This dissertation presents an optimized method for the synthesis of sodium molybdenum bronze originally reported by Thomas and McCarron. The presented method shows a reduction of the amount of the expensive sodium molybdate buffer to roughly one-third of the original reported synthesis, while also eliminating the unneeded use of N_2 during the reaction. Further, by extending the reaction time, the reducing equivalents of the sodium bronze were improved from 0.28 to 0.31. Lastly, using the more economical Na_2HPO_4 buffer produced a purely sodium intercalated material with yields increased by roughly 7% compared to the Thomas and McCarron method. Further studies should focus on utilizing other buffer systems in the presented method for the production of sodium molybdenum bronzes.

Further, the work presented in this dissertation demonstrated the high affinity of molybdenum and tungsten oxides for the sorption of lead. More specifically, molybdenum trioxide shows a very high reactivity towards lead as a nanometric suspension. From the presented reaction, a very high yield (96.7%) of a highly uniform nanometric material can be produced. The nanometric suspension shows an affinity for other dissolved metals as well, including Ag^+ and Cs^+. However, due to the solubility of MoO_3, it should not find applications in drinking water purification applications due to the potential toxicity. Further studies should be carried out to determine the reactivity of the nanometric suspension of MoO_3 toward other

Metals in solution, in hopes of making functional nanometric metal molybdates.

The nontoxic and insoluble nature of the tungsten oxides proves they are a quality choice for implementation into real world applications. However, the surface area of the material proves to be a large factor in their effectiveness, thus higher surface area WO_3 has been shown to be a promising reagent for water remediation applications. Further, their affinity for ion-exchange applications has shown that they can be used in applications such as refining of metal containing ores or even the winning of metals from natural water, including oceans. Further, these reactions provide a green route to the recovery of metals used widely in industry with very high yields. By utilizing a mesoporous WO_3, the reactivity towards Pb^{2+} was largely increased. However, the sorption processes using the metal oxides produces two equivalents of protons, thus the further studies should implement a buffer to determine the reaction kinetics and the extent of the reaction. Research should also be conducted to determine if mesoporous WO_3 shows a similar high affinity toward other heavy metals and radionuclides.

This dissertation also demonstrates a method for synthesizing single source precursors of nanometric tungstates and molybdates. The method has shown the capability of producing a wide variety of molybdate and tungstate based materials in very high yields with relatively low decomposition temperatures. The water-soluble nature of the precursors allows them to be deposited on high surface area catalyst supports. Further, the crystal structures of the calcium and magnesium tungsten methyl lactate precursors were determined: confirming previous speculations on the structures of α-hydroxy carboxylate chelated group (VI) transition metals. Future work in this area should focus on making other metal tungstates and molybdates that find use in industrial applications.

The aluminum tungstate reported herein proved to be an attractive material for the sorption of Ga^{3+}. The material should be used to recover other trivalent metals from solutions, including actinides and lanthanides, especially ones present in nuclear waste. Future research should also be conducted to determine an effective method for recycling the spent materials.

Finally, this study highlighted the versatility of calcium tungstate for use in both heavy metal and radionuclide sorption processes. The material has shown high reactivity toward all of the divalent heavy metals presented herein, with the highest affinity towards lead. The material also showed a high affinity towards the radionuclide surrogates studied, with the affinity for uranyl being much higher than that of Sr^{2+}, understandably so, due to the similar size and chemistries of Sr^{2+} when compared to Ca^{2+}. The ability for insoluble tungstic acid to sorb uranyl was also determined, showing increased reactivity by synthesizing the material on high surface area catalyst supports compared to previously reported data. Future research should be directed towards determining the ability for $CaWO_4$ to sorb other divalent heavy metals and radionuclides. Further, the material should be tested for its effectiveness in industrial and nuclear waste effluents.

APPENDICES

CRYSTALOGRAPHIC DATA

APPENDIX A

Table 1: Crystal data and structure refinement for $(CaH_{12}O_6)^{2+}(C_8H_{12}O_8W)^{2-}$.

Empirical formula	$(Ca\ H12\ O6)^{2+}\ (C_8\ H_{12}\ O_8\ W)^{2-}$ $C_8\ H_{24}\ Ca\ O_{14}\ W$	
Formula weight	568.20	
Crystal system	monoclinic	
Space group	C2/c	
Unit cell dimensions	a = 15.8651(8) Å	α= 90°
	b = 11.0182(5) Å	β= 99.439(2)°
	c = 10.5105(5) Å	γ= 90°
Volume	1812.41(15) $Å^3$	
Z, Z'	4, 0.5	
Density (calculated)	2.082 Mg/m^3	
Wavelength	0.71073 Å	
Temperature	100(2) K	
F(000)	1112	
Absorption coefficient	6.721 mm^{-1}	
Absorption correction	semi-empirical from equivalents	
Max. and min. transmission	0.2548 and 0.1221	
Theta range for data collection	2.26 to 28.30°	
Reflections collected	24840	
Independent reflections	2255 [R(int) = 0.0329]	
Data / restraints / parameters	2255 / 0 / 130	
wR(F^2 all data)	wR2 = 0.0419	
R(F obsd data)	R1 = 0.0139	
Goodness-of-fit on F^2	0.998	
Observed data [I > 2♦(I)]	2244	
Extinction coefficient	0.00207(10)	
Largest and mean shift / s.u.	0.002and 0.000	
Largest diff. peak and hole	1.322 and -1.048 $e/Å^3$	

$wR2 = \{ \Sigma [w(F_o^2 - F_c^2)^2] / \Sigma [w(Fo\ 2)2] \}1/2$

$R1 = \Sigma ||F_o| - |F_c|| / \Sigma |F_o|$

Table 2: Atomic coordinates and equivalent isotropic displacement parameters for $(CaH_{12}O_6)^{2+}(C_8H_{12}O_8W)^{2-}$.U(eq) is defined as one third of the trace of the orthogonalized U_{ij} tensor.

	x	y	z	U(eq)
W(1)	0.0000	0.852886(9)	0.2500	0.00612(6)
O(1)	0.08668(10)	0.69672(14)	0.27686(15)	0.0102(3)
O(2)	0.14964(11)	0.56283(15)	0.42063(16)	0.0131(3)
O(3)	0.00963(10)	0.81135(14)	0.43173(15)	0.0088(3)
O(4)	-0.08738(10)	0.94922(15)	0.25117(15)	0.0111(3)
C(1)	0.10688(15)	0.65573(19)	0.3927(2)	0.0086(4)
C(2)	0.07688(14)	0.7346(2)	0.4963(2)	0.0096(4)
C(3)	0.15149(16)	0.8138(2)	0.5581(2)	0.0164(5)
C(4)	0.04157(19)	0.6584(2)	0.5963(3)	0.0173(5)
Ca(1)	0.2500	0.2500	0.5000	0.00865(12)
O(1A)	0.18357(12)	0.39378(16)	0.60846(18)	0.0139(3)
O(2A)	0.24869(12)	0.38739(17)	0.32442(17)	0.0135(3)
O(3A)	0.11994(13)	0.15126(15)	0.4203(2)	0.0139(4)

Table 3: Bond lengths [Å] and angles [°] for $(CaH_{12}O_6)^{2+}(C_8H_{12}O_8W)^{2-}$.

W(1)-O(4)	1.7477(16)	C(4)-H(4A)	0.9800
W(1)-O(3)	1.9456(15)	C(4)-H(4B)	0.9800
W(1)-O(1)	2.1919(16)	C(4)-H(4C)	0.9800
O(1)-C(1)	1.289(3)	Ca(1)-O(1A)	2.3052(18)
O(2)-C(1)	1.236(3)	Ca(1)-O(3A)	2.3615(19)
O(3)-C(2)	1.441(3)	Ca(1)-O(2A)	2.3844(18)
C(1)-C(2)	1.528(3)	O(1A)-H(1AA)	0.75(4)
C(2)-C(4)	1.522(3)	O(1A)-H(1BA)	0.79(4)
C(2)-C(3)	1.527(3)	O(2A)-H(2AA)	0.75(4)
C(3)-H(3A)	0.9800	O(2A)-H(2BA)	0.87(3)
C(3)-H(3B)	0.9800	O(3A)-H(3AA)	0.86(4)
C(3)-H(3C)	0.9800	O(3A)-H(3BA)	0.74(4)

O(4)-W(1)-O(3)	94.05(7)
O(4)#1-W(1)-O(3)	102.42(7)
O(3)#1-W(1)-O(3)	152.79(9)
O(4)-W(1)-O(1)	163.25(7)
O(4)#1-W(1)-O(1)	89.77(7)
O(3)#1-W(1)-O(1)	83.59(6)
O(3)-W(1)-O(1)	75.07(6)
O(1)#1-W(1)-O(1)	76.55(9)
C(1)-O(1)-W(1)	116.75(14)
C(2)-O(3)-W(1)	122.23(13)
O(2)-C(1)-O(1)	123.8(2)
O(2)-C(1)-C(2)	121.7(2)
O(1)-C(1)-C(2)	114.54(18)
O(3)-C(2)-C(4)	108.73(18)
O(3)-C(2)-C(3)	109.09(18)
C(4)-C(2)-C(3)	111.7(2)
O(3)-C(2)-C(1)	106.94(17)
C(4)-C(2)-C(1)	111.77(19)
C(3)-C(2)-C(1)	108.52(18)
C(2)-C(3)-H(3A)	109.5
C(2)-C(3)-H(3B)	109.5
H(3A)-C(3)-H(3B)	109.5
C(2)-C(3)-H(3C)	109.5
H(3A)-C(3)-H(3C)	109.5
H(3B)-C(3)-H(3C)	109.5
C(2)-C(4)-H(4A)	109.4
C(2)-C(4)-H(4B)	109.5
H(4A)-C(4)-H(4B)	109.5
C(2)-C(4)-H(4C)	109.5
H(4A)-C(4)-H(4C)	109.5
H(4B)-C(4)-H(4C)	109.5

O(1A)#2-Ca(1)-O(1A)	180.0
O(1A)#2-Ca(1)-O(3A)	87.23(7)

O(1A)-Ca(1)-O(3A)	92.77(7)
O(3A)#2-Ca(1)-O(3A)	180.0
O(1A)#2-Ca(1)-O(2A)	90.01(6)
O(1A)-Ca(1)-O(2A)	89.99(6)
O(3A)#2-Ca(1)-O(2A)	83.02(7)
O(3A)-Ca(1)-O(2A)	96.98(7)
O(2A)-Ca(1)-O(2A)#2	180.0
Ca(1)-O(1A)-H(1AA)	129(3)
Ca(1)-O(1A)-H(1BA)	116(2)
H(1AA)-O(1A)-H(1BA)	109(4)
Ca(1)-O(2A)-H(2AA)	118(3)
Ca(1)-O(2A)-H(2BA)	111(2)

H(2AA)-O(2A)-H(2BA)	107(3)
Ca(1)-O(3A)-H(3AA)	130(2)
Ca(1)-O(3A)-H(3BA)	118(3)
H(3AA)-O(3A)-H(3BA)	106(3)

Table 4: Anisotropic displacement parameters ($Å^2 x\ 10^3$) for $(CaH_{12}O_6)^{2+}(C_8H_{12}O_8W)^{2-}$. The anisotropic displacement factor exponent takes the form: $-2\ \pi^2[\ h^2\ a^{*2}\ U_{11} + ... + 2\ h\ k\ a^*\ b^*\ U_{12}\ ]$

	U_{11}	U_{22}	U_{33}	U_{23}	U_{13}	U_{12}
W(1)	6(1)	7(1)	6(1)	0	4(1)	0
O(1)	11(1)	12(1)	9(1)	1(1)	4(1)	4(1)
O(2)	16(1)	13(1)	13(1)	3(1)	8(1)	5(1)
O(3)	10(1)	11(1)	7(1)	1(1)	4(1)	2(1)
O(4)	10(1)	14(1)	11(1)	1(1)	5(1)	3(1)
C(1)	6(1)	11(1)	10(1)	0(1)	5(1)	-2(1)
C(2)	7(1)	13(1)	10(1)	1(1)	4(1)	5(1)
C(3)	15(1)	19(1)	14(1)	-6(1)	0(1)	3(1)
C(4)	22(1)	20(1)	12(1)	7(1)	10(1)	9(1)
Ca(1)	8(1)	9(1)	11(1)	0(1)	5(1)	0(1)
O(1A)	16(1)	13(1)	16(1)	4(1)	12(1)	4(1)
O(2A)	12(1)	14(1)	16(1)	1(1)	7(1)	-1(1)
O(3A)	11(1)	18(1)	15(1)	-6(1)	7(1)	-3(1)

Table 5: Hydrogen coordinates and isotropic displacement parameters for $(CaH_{12}O_6)^{2+}(C_8H_{12}O_8W)^{2-}$.

	x	y	z	U(eq)
H(3A)	0.1710	0.8640	0.4916	0.025
H(3B)	0.1985	0.7620	0.5988	0.025
H(3C)	0.1328	0.8663	0.6234	0.025
H(4A)	0.0230	0.7119	0.6608	0.026
H(4B)	0.0861	0.6035	0.6386	0.026
H(4C)	-0.0072	0.6107	0.5538	0.026
H(1AA)	0.156(2)	0.385(3)	0.659(4)	0.017
H(1BA)	0.169(2)	0.454(3)	0.570(3)	0.017
H(2AA)	0.291(2)	0.405(3)	0.306(3)	0.016
H(2BA)	0.221(2)	0.453(3)	0.336(3)	0.016
H(3AA)	0.110(2)	0.092(3)	0.366(3)	0.017
H(3BA)	0.087(3)	0.148(3)	0.462(4)	0.017

Table 6: Torsion angles [°] for $(CaH_{12}O_6)^{2+}(C_8H_{12}O_8W)^{2-}$.

O(4)-W(1)-O(1)-C(1)	-54.2(3)
O(4)#1-W(1)-O(1)-C(1)	99.46(16)
O(3)#1-W(1)-O(1)-C(1)	-166.44(16)
O(3)-W(1)-O(1)-C(1)	-3.47(15)
O(1)#1-W(1)-O(1)-C(1)	-90.31(16)
O(4)-W(1)-O(3)-C(2)	-176.60(16)
O(4)#1-W(1)-O(3)-C(2)	-70.06(16)
O(3)#1-W(1)-O(3)-C(2)	55.85(15)
O(1)#1-W(1)-O(3)-C(2)	94.08(16)
O(1)-W(1)-O(3)-C(2)	16.33(15)
W(1)-O(1)-C(1)-O(2)	174.19(18)
W(1)-O(1)-C(1)-C(2)	-8.3(2)
W(1)-O(3)-C(2)-C(4)	-145.21(16)
W(1)-O(3)-C(2)-C(3)	92.81(19)
W(1)-O(3)-C(2)-C(1)	-24.4(2)
O(2)-C(1)-C(2)-O(3)	-163.2(2)
O(1)-C(1)-C(2)-O(3)	19.2(3)
O(2)-C(1)-C(2)-C(4)	-44.4(3)
O(1)-C(1)-C(2)-C(4)	138.1(2)
O(2)-C(1)-C(2)-C(3)	79.2(3)
O(1)-C(1)-C(2)-C(3)	-98.3(2)

Symmetry transformations used to generate equivalent atoms:
#1 -x, y, -z+1/2

Table 7: Hydrogen bonds for $(CaH_{12}O_6)^{2+}(C_8H_{12}O_8W)^{2-}$[Å and °].

D-H...A	d(D-H)	d(H...A)	d(D...A)	<(DHA)
O(1A)-H(1AA)...O(1)#3	0.75(4)	2.00(4)	2.717(2)	160(4)
O(1A)-H(1BA)...O(2)	0.79(4)	1.96(4)	2.703(3)	157(3)
O(2A)-H(2AA)...O(4)#4	0.75(4)	2.16(4)	2.912(2)	177(4)
O(2A)-H(2BA)...O(2)	0.87(3)	1.97(3)	2.784(2)	157(3)
O(3A)-H(3AA)...O(4)#5	0.86(4)	2.00(4)	2.857(2)	177(3)
O(3A)-H(3BA)...O(3)#6	0.74(4)	2.08(4)	2.804(3)	164(3)

Symmetry transformations used to generate equivalent atoms:

#3 x, -y+1, z+1/2 #4 x+1/2, y-1/2, z #5 -x, y-1, -z+1/2 #6 -x, -y+1, -z+1

APPENDIX B

Table 1: Crystal data and structure refinement for $[Mg(H_2O)_6]^{2+}(C_8H_{12}O_8W)^{2-}$.

Empirical formula	$[Mg(H_2O)_6]^{2+}(C_8H_{12}O_8W)^{2-}$ $C_8\ H_{24}\ Mg\ O_{14}\ W$	
Formula weight	552.43	
Crystal system	monoclinic	
Space group	C2/c	
Unit cell dimensions	a = 15.6330(9) Å	α= 90°
	b = 10.6191(6) Å	β= 97.395(2)°
	c = 10.4320(6) Å	γ= 90°
Volume	1717.40(17) $Å^3$	
Z, Z'	4, 0.5	
Density (calculated)	2.137 Mg/m^3	
Wavelength	0.71073 Å	
Temperature	100(2) K	
F(000)	1080	
Absorption coefficient	6.831 mm^{-1}	
Absorption correction	semi-empirical from equivalents	
Max. and min. transmission	0.726 and 0.494	
Theta range for data collection	2.325 to 25.999°	
Reflections collected	13088	
Independent reflections	1695 [R(int) = 0.0271]	
Data / restraints / parameters	1695 / 18 / 129	
wR(F^2 all data)	wR2 = 0.0450	
R(F obsd data)	R1 = 0.0171	
Goodness-of-fit on F^2	0.987	
Observed data [I > 2♦(I)]	1637	
Largest and mean shift / s.u.	0.002and 0.000	
Largest diff. peak and hole	2.371 and -0.455 $e/Å^3$	

$wR2 = \{ \Sigma [w(F_o^2 - F_c^2)^2] / \Sigma [w(Fo\ 2)2] \}1/2$

$R1 = \Sigma ||F_o| - |F_c|| / \Sigma |F_o|$

Table 2: Atomic coordinates and equivalent isotropic displacement parameters for $[Mg(H_2O)_6]^{2+}(C_8H_{12}O_8W)^{2-}$. U(eq) is defined as one third of the trace of the orthogonalized U_{ij} tensor.

	x	y	z	U(eq)
W(1)	0.5000	0.85952(2)	0.7500	0.01036(7)
O(1)	0.41224(13)	0.69707(19)	0.72845(19)	0.0135(4)
O(2)	0.35164(14)	0.5565(2)	0.5877(2)	0.0161(4)
O(3)	0.49179(12)	0.81490(19)	0.56848(19)	0.0119(4)
O(4)	0.41123(13)	0.95822(19)	0.7523(2)	0.0146(4)
C(1)	0.39343(19)	0.6538(2)	0.6135(3)	0.0113(6)
C(2)	0.42369(18)	0.7356(3)	0.5072(3)	0.0130(6)
C(3)	0.4580(2)	0.6580(3)	0.4033(3)	0.0210(7)
C(4)	0.3485(2)	0.8191(3)	0.4511(3)	0.0207(7)
Mg(1)	0.2500	0.2500	0.5000	0.0119(3)
O(5)	0.25088(15)	0.36692(19)	0.6637(2)	0.0138(4)
O(6)	0.30948(15)	0.3833(2)	0.4034(2)	0.0149(4)
O(7)	0.13240(14)	0.3310(2)	0.4264(2)	0.0154(4)

Table 3: Bond lengths [Å] and angles [°] for $[Mg(H_2O)_6]^{2+}(C_8H_{12}O_8W)^{2-}$.

W(1)-O(4)	1.742(2)	C(4)-H(4A)	0.9800
W(1)-O(4)#1	1.742(2)	C(4)-H(4B)	0.9800
W(1)-O(3)	1.940(2)	C(4)-H(4C)	0.9800
W(1)-O(3)#1	1.940(2)	Mg(1)-O(6)	2.031(2)
W(1)-O(1)	2.198(2)	Mg(1)-O(6)#2	2.031(2)
W(1)-O(1)#1	2.198(2)	Mg(1)-O(7)#2	2.085(2)
O(1)-C(1)	1.283(4)	Mg(1)-O(7)	2.085(2)
O(2)-C(1)	1.233(4)	Mg(1)-O(5)#2	2.110(2)
O(3)-C(2)	1.441(3)	Mg(1)-O(5)	2.110(2)
C(1)-C(2)	1.531(4)	O(5)-H(5A)	0.73(3)
C(2)-C(3)	1.514(4)	O(5)-H(5B)	0.75(3)
C(2)-C(4)	1.527(4)	O(6)-H(6A)	0.74(3)
C(3)-H(3A)	0.9800	O(6)-H(6B)	0.73(3)
C(3)-H(3B)	0.9800	O(7)-H(7A)	0.72(3)
C(3)-H(3C)	0.9800	O(7)-H(7B)	0.74(3)

O(4)-W(1)-O(4)#1	106.01(13)
O(4)-W(1)-O(3)	101.99(9)
O(4)#1-W(1)-O(3)	94.94(9)
O(4)-W(1)-O(3)#1	94.94(9)
O(4)#1-W(1)-O(3)#1	101.99(9)
O(3)-W(1)-O(3)#1	151.73(12)
O(4)-W(1)-O(1)	89.19(8)
O(4)#1-W(1)-O(1)	163.54(9)
O(3)-W(1)-O(1)	75.31(8)
O(3)#1-W(1)-O(1)	82.54(8)
O(4)-W(1)-O(1)#1	163.54(9)
O(4)#1-W(1)-O(1)#1	89.19(8)
O(3)-W(1)-O(1)#1	82.54(8)
O(3)#1-W(1)-O(1)#1	75.31(8)
O(1)-W(1)-O(1)#1	76.56(11)
C(1)-O(1)-W(1)	116.23(18)
C(2)-O(3)-W(1)	121.88(16)
O(2)-C(1)-O(1)	123.7(3)
O(2)-C(1)-C(2)	121.4(3)
O(1)-C(1)-C(2)	114.8(2)
O(3)-C(2)-C(3)	109.1(2)
O(3)-C(2)-C(4)	108.6(2)
C(3)-C(2)-C(4)	111.6(3)
O(3)-C(2)-C(1)	106.8(2)
C(3)-C(2)-C(1)	112.4(2)
C(4)-C(2)-C(1)	108.2(2)
C(2)-C(3)-H(3A)	109.5
C(2)-C(3)-H(3B)	109.5
H(3A)-C(3)-H(3B)	109.5
C(2)-C(3)-H(3C)	109.5
H(3A)-C(3)-H(3C)	109.5
H(3B)-C(3)-H(3C)	109.5
C(2)-C(4)-H(4A)	109.5
C(2)-C(4)-H(4B)	109.5
H(4A)-C(4)-H(4B)	109.5
C(2)-C(4)-H(4C)	109.5
H(4A)-C(4)-H(4C)	109.5
H(4B)-C(4)-H(4C)	109.5
O(6)-Mg(1)-O(6)#2	180.0
O(6)-Mg(1)-O(7)#2	91.84(9)
O(6)#2-Mg(1)-O(7)#2	88.16(9)
O(6)-Mg(1)-O(7)	88.16(9)
O(6)#2-Mg(1)-O(7)	91.84(9)
O(7)#2-Mg(1)-O(7)	180.0
O(6)-Mg(1)-O(5)#2	87.94(9)
O(6)#2-Mg(1)-O(5)#2	92.06(9)
O(7)#2-Mg(1)-O(5)#2	88.22(9)
O(7)-Mg(1)-O(5)#2	91.78(10)
O(6)-Mg(1)-O(5)	92.06(9)

O(6)#2-Mg(1)-O(5)	87.94(9)
O(7)#2-Mg(1)-O(5)	91.78(10)
O(7)-Mg(1)-O(5)	88.22(9)
O(5)#2-Mg(1)-O(5)	180.0
Mg(1)-O(5)-H(5A)	113(3)
Mg(1)-O(5)-H(5B)	117(3)
H(5A)-O(5)-H(5B)	104(4)
Mg(1)-O(6)-H(6A)	116(3)
Mg(1)-O(6)-H(6B)	120(3)
H(6A)-O(6)-H(6B)	112(4)
Mg(1)-O(7)-H(7B)	121(3)
Mg(1)-O(7)-H(7B)	126(3)
H(7A)-O(7)-H(7B)	109(4)

Symmetry transformations used to generate equivalent atoms:
#1 -x+1, -y+1, -z+1 #2 -x+1, -y, -z

Table 4: Anisotropic displacement parameters ($Å^2 x\ 10^3$) for $[Mg(H_2O)_6]^{2+}(C_8H_{12}O_8W)^{2-}$. The anisotropic displacement factor exponent takes the form: The anisotropic displacement factor exponent takes the form: $-2\ \pi^2[\ h^2\ a^{*2}\ U_{11} + ... + 2\ h\ k\ a^*\ b^*\ U_{12}\ ]$

	U_{11}	U_{22}	U_{33}	U_{23}	U_{13}	U_{12}
W(1)	9(1)	11(1)	11(1)	0	2(1)	0
O(1)	13(1)	15(1)	12(1)	1(1)	3(1)	-3(1)
O(2)	19(1)	14(1)	16(1)	-2(1)	4(1)	-6(1)
O(3)	11(1)	14(1)	11(1)	1(1)	2(1)	-3(1)
O(4)	12(1)	16(1)	15(1)	-1(1)	2(1)	2(1)
C(1)	8(1)	11(1)	14(2)	-1(1)	3(1)	1(1)
C(2)	12(1)	16(1)	10(1)	-1(1)	1(1)	-5(1)
C(3)	21(2)	27(2)	17(2)	-7(1)	9(1)	-9(1)
C(4)	14(2)	25(2)	22(2)	9(1)	-4(1)	-3(1)
Mg(1)	11(1)	13(1)	12(1)	-1(1)	2(1)	-1(1)
O(5)	13(1)	13(1)	17(1)	-2(1)	6(1)	-2(1)
O(6)	15(1)	15(1)	16(1)	-3(1)	7(1)	-3(1)
O(7)	12(1)	18(1)	16(1)	4(1)	4(1)	1(1)

Table 5: Hydrogen coordinates and isotropic displacement parameters for $[Mg(H_2O)_6]^{2+}(C_8H_{12}O_8W)^{2-}$

	x	y	z	U(eq)
H(3A)	0.5060	0.6056	0.4424	0.031
H(3B)	0.4782	0.7142	0.3390	0.031
H(3C)	0.4119	0.6039	0.3611	0.031
H(4A)	0.3279	0.8679	0.5208	0.031
H(4B)	0.3016	0.7663	0.4094	0.031
H(4C)	0.3678	0.8766	0.3873	0.031
H(5A)	0.274(2)	0.425(3)	0.658(4)	0.017
H(5B)	0.2083(19)	0.388(3)	0.681(4)	0.017
H(6A)	0.325(2)	0.440(3)	0.440(3)	0.018
H(6B)	0.338(3)	0.365(3)	0.357(4)	0.018
H(7A)	0.096(2)	0.328(4)	0.461(4)	0.019
H(7B)	0.126(3)	0.384(3)	0.381(4)	0.019

Table 6: Torsion angles [°] for $[Mg(H_2O)_6]^{2+}(C_8H_{12}O_8W)^{2-}$.

W(1)-O(1)-C(1)-O(2)	173.1(2)
W(1)-O(1)-C(1)-C(2)	-9.4(3)
W(1)-O(3)-C(2)-C(3)	-147.2(2)
W(1)-O(3)-C(2)-C(4)	91.0(2)
W(1)-O(3)-C(2)-C(1)	-25.5(3)
O(2)-C(1)-C(2)-O(3)	-161.8(3)
O(1)-C(1)-C(2)-O(3)	20.7(3)
O(2)-C(1)-C(2)-C(3)	-42.2(4)
O(1)-C(1)-C(2)-C(3)	140.2(3)
O(2)-C(1)-C(2)-C(4)	81.5(3)
O(1)-C(1)-C(2)-C(4)	-96.1(3)

Table 7: Hydrogen bonds for $[Mg(H_2O)_6]^{2+}(C_8H_{12}O_8W)^{2-}$ [Å and °].

D-H...A	d(D-H)	d(H...A)	d(D...A)	<(DHA)
C(4)-H(4C)...O(4)#3	0.98	2.40	3.373(4)	171.6
O(5)-H(5A)...O(2)	0.73(3)	2.05(3)	2.736(3)	159(4)
O(5)-H(5B)...O(4)#4	0.75(3)	2.21(3)	2.950(3)	175(4)
O(6)-H(6A)...O(2)	0.74(3)	1.98(3)	2.681(3)	160(4)
O(6)-H(6B)...O(1)#5	0.73(3)	1.99(3)	2.719(3)	176(4)
O(7)-H(7A)...O(3)#6	0.72(3)	2.09(3)	2.810(3)	178(4)
O(7)-H(7B)...O(4)#7	0.74(3)	2.20(3)	2.936(3)	172(4)

Symmetry transformations used to generate equivalent atoms:

#3 x, -y+2, z-1/2 #4 -x+1/2, y-1/2, -z+3/2 #5 x, -y+1, z-1/2

#6 x-1/2, y-1/2, z #7 -x+1/2, -y+3/2, -z+1

APPENDIX C

Table 1: Crystal data and structure refinement for $[Al(H_2O)_6]^{3+}(AlH_6Mo_6O_{24})^{3-}\cdot 10(H_2O)$.

Empirical formula	$[Al(H_2O)_6]^{3+}(AlH_6Mo_6O_{24})^{3-}\cdot 10(H_2O)$	
	$Al_2\ H_{38}\ Mo_6\ O_{40}$	
Formula weight	1307.90	
Crystal system	triclinic	
Space group	$P\bar{1}$	
Unit cell dimensions	a = 6.7581(3) Å	α= 101.353(2)°
	b = 11.1251(6) Å	β= 97.030(2)°
	c = 11.6577(6) Å	γ= 102.298(2)°
Volume	827.16(7) $Å^3$	
Z, Z'	1, 0.5	
Density (calculated)	2.626 Mg/m^3	
Wavelength	0.71073 Å	
Temperature	100(2) K	
F(000)	636	
Absorption coefficient	2.392 mm^{-1}	
Absorption correction	semi-empirical from equivalents	
Max. and min. transmission	0.586 and 0.564	
Theta range for data collection	1.809 to 28.296°	
Reflections collected	13149	
Independent reflections	4084 [R(int) = 0.0186]	
Data / restraints / parameters	4084 / 73 / 277	
$wR(F^2$ all data)	$wR2$ = 0.0516	
R(F obsd data)	$R1$ = 0.0182	
Goodness-of-fit on F^2	1.003	
Observed data [I > 2♦(I)]	3995	
Largest and mean shift / s.u.	0.009and 0.001	
Largest diff. peak and hole	0.562 and -0.806 e/$Å^3$	

$wR2 = \{ \Sigma [w(F_o^2 - F_c^2)^2] / \Sigma [w(Fo\ 2)2] \}1/2$

$R1 = \Sigma ||F_o| - |F_c|| / \Sigma |F_o|$

Table 2: Atomic coordinates and equivalent isotropic displacement parameters for $[Al(H_2O)_6]^{3+}(AlH_6Mo_6O_{24})^{3-}\cdot 10(H_2O)$. U(eq) is defined as one third of the trace of the orthogonalized U_{ij} tensor.

	x	y	z	U(eq)
Mo(1)	0.13022(2)	0.32965(2)	0.60294(2)	0.00732(5)
Mo(2)	0.16218(2)	0.25573(2)	0.32139(2)	0.00813(5)
Mo(3)	0.52372(2)	0.43018(2)	0.21277(2)	0.00796(5)
Al(1)	0.5000	0.5000	0.5000	0.00657(14)
O(1)	0.2967(2)	0.53196(13)	0.59565(12)	0.0082(2)
O(2)	0.3871(2)	0.32755(12)	0.49664(11)	0.0083(2)
O(3)	0.3212(2)	0.46606(12)	0.35462(11)	0.0086(2)
O(4)	0.3584(2)	0.38888(12)	0.73196(11)	0.0099(2)
O(5)	0.0118(2)	0.32080(12)	0.44058(11)	0.0097(2)
O(6)	0.4117(2)	0.27035(12)	0.25194(11)	0.0103(3)
O(7)	-0.0600(2)	0.38454(13)	0.66795(12)	0.0113(3)
O(8)	0.0834(2)	0.17316(13)	0.60362(12)	0.0126(3)
O(9)	0.1313(2)	0.10169(13)	0.33201(12)	0.0139(3)
O(10)	-0.0065(2)	0.25328(14)	0.19896(12)	0.0139(3)
O(11)	0.3319(2)	0.43639(13)	0.10597(12)	0.0134(3)
O(12)	0.7115(2)	0.38952(14)	0.14036(12)	0.0142(3)
Al(2)	0.5000	0.0000	0.0000	0.00827(14)
O(13)	0.2307(2)	-0.09284(13)	-0.00905(12)	0.0119(3)
O(14)	0.3993(2)	0.13578(13)	-0.03549(12)	0.0112(3)
O(15)	0.5136(2)	0.06689(13)	0.16281(12)	0.0114(3)
O(1S)	0.5916(2)	0.16808(14)	0.56665(13)	0.0149(3)
O(2S)	-0.0139(2)	-0.12260(15)	0.14763(13)	0.0148(3)
O(3S)	0.3171(2)	-0.01826(15)	0.63207(14)	0.0154(3)
O(4S)	0.0193(2)	0.37226(14)	-0.08760(13)	0.0151(3)
O(5S)	0.6055(2)	0.26094(14)	0.83724(14)	0.0153(3)

Table 3: Bond lengths [Å] and angles [°] for $[Al(H_2O)_6]^{3+}(AlH_6Mo_6O_{24})^{3-}\cdot 10(H_2O)$.

Mo(1)-O(8)	1.7037(14)	O(2)-H(2)	0.87(3)
Mo(1)-O(7)	1.7294(14)	O(3)-H(3)	0.82(3)
Mo(1)-O(4)	1.9194(13)	O(4)-Mo(3)#1	1.9448(13)
Mo(1)-O(5)	1.9377(13)	Al(2)-O(13)#2	1.8710(14)
Mo(1)-O(2)	2.2546(13)	Al(2)-O(13)	1.8710(14)
Mo(1)-O(1)	2.3148(14)	Al(2)-O(14)	1.8793(14)
Mo(2)-O(10)	1.7060(14)	Al(2)-O(14)#2	1.8793(14)
Mo(2)-O(9)	1.7126(14)	Al(2)-O(15)	1.8806(13)
Mo(2)-O(5)	1.9365(13)	Al(2)-O(15)#2	1.8807(13)
Mo(2)-O(6)	1.9477(14)	O(13)-H(13A)	0.750(19)
Mo(2)-O(2)	2.2810(13)	O(13)-H(13B)	0.755(19)
Mo(2)-O(3)	2.2914(13)	O(14)-H(14A)	0.770(19)
Mo(3)-O(12)	1.6982(14)	O(14)-H(14B)	0.749(19)
Mo(3)-O(11)	1.7063(14)	O(15)-H(15A)	0.771(19)
Mo(3)-O(6)	1.9428(13)	O(15)-H(15B)	0.741(19)
Mo(3)-O(4)#1	1.9448(13)	O(1S)-H(1SA)	0.711(18)
Mo(3)-O(3)	2.3008(14)	O(1S)-H(1SB)	0.667(18)
Mo(3)-O(1)#1	2.3210(13)	O(2S)-H(2SA)	0.733(18)
Al(1)-O(3)#1	1.8781(13)	O(2S)-H(2SB)	0.721(18)
Al(1)-O(3)	1.8781(13)	O(3S)-H(3SA)	0.708(18)
Al(1)-O(2)#1	1.8984(13)	O(3S)-H(3SB)	0.681(18)
Al(1)-O(2)	1.8984(13)	O(4S)-H(4SA)	0.722(18)
Al(1)-O(1)#1	1.9197(13)	O(4S)-H(4SB)	0.709(19)
Al(1)-O(1)	1.9197(13)	O(5S)-H(5SA)	0.719(19)
O(1)-Mo(3)#1	2.3210(13)	O(5S)-H(5SB)	0.716(19)
O(1)-H(1)	0.80(3)		

O(8)-Mo(1)-O(7)	105.68(7)	O(9)-Mo(2)-O(6)	97.43(6)
O(8)-Mo(1)-O(4)	97.66(6)	O(5)-Mo(2)-O(6)	149.85(6)
O(7)-Mo(1)-O(4)	101.22(6)	O(10)-Mo(2)-O(2)	161.11(6)
O(8)-Mo(1)-O(5)	100.73(6)	O(9)-Mo(2)-O(2)	92.12(6)
O(7)-Mo(1)-O(5)	96.34(6)	O(5)-Mo(2)-O(2)	72.93(5)
O(4)-Mo(1)-O(5)	150.03(6)	O(6)-Mo(2)-O(2)	83.66(5)
O(8)-Mo(1)-O(2)	95.24(6)	O(10)-Mo(2)-O(3)	95.37(6)
O(7)-Mo(1)-O(2)	158.24(6)	O(9)-Mo(2)-O(3)	157.39(6)
O(4)-Mo(1)-O(2)	81.44(5)	O(5)-Mo(2)-O(3)	81.56(5)
O(5)-Mo(1)-O(2)	73.52(5)	O(6)-Mo(2)-O(3)	71.87(5)
O(8)-Mo(1)-O(1)	161.66(6)	O(2)-Mo(2)-O(3)	67.36(5)
O(7)-Mo(1)-O(1)	91.56(6)	O(12)-Mo(3)-O(11)	106.19(7)
O(4)-Mo(1)-O(1)	72.36(5)	O(12)-Mo(3)-O(6)	99.39(6)
O(5)-Mo(1)-O(1)	83.14(5)	O(11)-Mo(3)-O(6)	101.74(6)
O(2)-Mo(1)-O(1)	68.46(5)	O(12)-Mo(3)-O(4)#1	99.36(6)
O(10)-Mo(2)-O(9)	106.08(7)	O(11)-Mo(3)-O(4)#1	97.68(6)
O(10)-Mo(2)-O(5)	97.79(6)	O(6)-Mo(3)-O(4)#1	147.94(5)
O(9)-Mo(2)-O(5)	102.07(6)	O(12)-Mo(3)-O(3)	163.05(6)
O(10)-Mo(2)-O(6)	98.63(6)	O(11)-Mo(3)-O(3)	89.98(6)

O(6)-Mo(3)-O(3)	71.74(5)
O(4)#1-Mo(3)-O(3)	83.09(5)
O(12)-Mo(3)-O(1)#1	97.07(6)
O(11)-Mo(3)-O(1)#1	155.87(6)
O(6)-Mo(3)-O(1)#1	80.27(5)
O(4)#1-Mo(3)-O(1)#1	71.80(5)
O(3)-Mo(3)-O(1)#1	67.59(5)
O(3)#1-Al(1)-O(3)	180.0
O(3)#1-Al(1)-O(2)#1	84.36(6)
O(3)-Al(1)-O(2)#1	95.64(6)
O(3)#1-Al(1)-O(2)	95.64(6)
O(3)-Al(1)-O(2)	84.36(6)
O(2)#1-Al(1)-O(2)	180.0
O(3)#1-Al(1)-O(1)#1	94.79(6)
O(3)-Al(1)-O(1)#1	85.21(6)
O(2)#1-Al(1)-O(1)#1	84.65(6)
O(2)-Al(1)-O(1)#1	95.35(6)
O(3)#1-Al(1)-O(1)	85.21(6)
O(3)-Al(1)-O(1)	94.79(6)
O(2)#1-Al(1)-O(1)	95.35(6)
O(2)-Al(1)-O(1)	84.65(6)
O(1)#1-Al(1)-O(1)	180.00(5)
Al(1)-O(1)-Mo(1)	101.98(6)
Al(1)-O(1)-Mo(3)#1	102.50(6)
Mo(1)-O(1)-Mo(3)#1	91.74(5)
Al(1)-O(1)-H(1)	123.3(18)
Mo(1)-O(1)-H(1)	115.5(18)
Mo(3)#1-O(1)-H(1)	116.5(18)
Al(1)-O(2)-Mo(1)	104.90(6)
Al(1)-O(2)-Mo(2)	103.98(6)
Mo(1)-O(2)-Mo(2)	92.21(5)
Al(1)-O(2)-H(2)	123.9(16)
Mo(1)-O(2)-H(2)	111.1(16)
Mo(2)-O(2)-H(2)	115.8(16)
Al(1)-O(3)-Mo(2)	104.27(6)
Al(1)-O(3)-Mo(3)	104.62(6)
Mo(2)-O(3)-Mo(3)	92.72(5)
Al(1)-O(3)-H(3)	122.1(17)
Mo(2)-O(3)-H(3)	107.8(18)
Mo(3)-O(3)-H(3)	120.3(17)
Mo(1)-O(4)-Mo(3)#1	118.88(7)
Mo(2)-O(5)-Mo(1)	115.05(7)
Mo(3)-O(6)-Mo(2)	117.35(7)
O(13)#2-Al(2)-O(13)	180.0
O(13)#2-Al(2)-O(14)	90.08(6)
O(13)-Al(2)-O(14)	89.92(6)
O(13)#2-Al(2)-O(14)#2	89.92(6)
O(13)-Al(2)-O(14)#2	90.08(6)
O(14)-Al(2)-O(14)#2	180.0
O(13)#2-Al(2)-O(15)	89.97(6)
O(13)-Al(2)-O(15)	90.03(6)
O(14)-Al(2)-O(15)	89.77(6)
O(14)#2-Al(2)-O(15)	90.23(6)
O(13)#2-Al(2)-O(15)#2	90.03(6)
O(13)-Al(2)-O(15)#2	89.97(6)
O(14)-Al(2)-O(15)#2	90.22(6)
O(14)#2-Al(2)-O(15)#2	89.77(6)
O(15)-Al(2)-O(15)#2	180.0
Al(2)-O(13)-H(13A)	121(2)
Al(2)-O(13)-H(13B)	128(2)
H(13A)-O(13)-H(13B)	111(3)
Al(2)-O(14)-H(14A)	114.2(19)
Al(2)-O(14)-H(14B)	119(2)
H(14A)-O(14)-H(14B)	110(3)
Al(2)-O(15)-H(15A)	123.7(19)
Al(2)-O(15)-H(15B)	128(2)
H(15A)-O(15)-H(15B)	108(3)
H(1SA)-O(1S)-H(1SB)	119(3)
H(2SA)-O(2S)-H(2SB)	104(3)
H(3SA)-O(3S)-H(3SB)	106(3)
H(4SA)-O(4S)-H(4SB)	105(3)
H(5SA)-O(5S)-H(5SB)	101(3)

Symmetry transformations used to generate equivalent atoms:
#1 -x+1, -y+1, -z+1 #2 -x+1, -y, -z

Table 4: Anisotropic displacement parameters ($Å^2 x\ 10^3$) for $[Al(H_2O)_6]^{3+}(AlH_6Mo_6O_{24})^{3-} \cdot 10(H_2O)$. The anisotropic displacement factor exponent takes the form: $-2\ \pi^2[\ h^2\ a^{*2}\ U_{11} + ... + 2\ h\ k\ a^*\ b^*\ U_{12}\ ]$

	U_{11}	U_{22}	U_{33}	U_{23}	U_{13}	U_{12}
Mo(1)	7(1)	7(1)	8(1)	2(1)	1(1)	1(1)
Mo(2)	8(1)	7(1)	8(1)	0(1)	0(1)	0(1)
Mo(3)	8(1)	8(1)	7(1)	1(1)	1(1)	2(1)
Al(1)	6(1)	6(1)	6(1)	1(1)	1(1)	1(1)
O(1)	8(1)	8(1)	9(1)	2(1)	1(1)	4(1)
O(2)	8(1)	8(1)	9(1)	2(1)	1(1)	2(1)
O(3)	7(1)	9(1)	10(1)	2(1)	0(1)	2(1)
O(4)	10(1)	10(1)	9(1)	2(1)	1(1)	2(1)
O(5)	8(1)	11(1)	9(1)	1(1)	1(1)	2(1)
O(6)	11(1)	8(1)	10(1)	1(1)	2(1)	2(1)
O(7)	10(1)	13(1)	11(1)	2(1)	2(1)	4(1)
O(8)	12(1)	11(1)	14(1)	3(1)	2(1)	2(1)
O(9)	15(1)	10(1)	15(1)	1(1)	4(1)	1(1)
O(10)	11(1)	17(1)	11(1)	-1(1)	-1(1)	2(1)
O(11)	14(1)	14(1)	11(1)	3(1)	-1(1)	3(1)
O(12)	15(1)	14(1)	14(1)	3(1)	5(1)	4(1)
Al(2)	8(1)	8(1)	8(1)	1(1)	1(1)	2(1)
O(13)	10(1)	13(1)	9(1)	-1(1)	2(1)	-2(1)
O(14)	10(1)	10(1)	14(1)	4(1)	2(1)	2(1)
O(15)	16(1)	11(1)	8(1)	1(1)	2(1)	6(1)
O(1S)	16(1)	13(1)	14(1)	0(1)	2(1)	4(1)
O(2S)	16(1)	16(1)	12(1)	1(1)	2(1)	4(1)
O(3S)	13(1)	16(1)	18(1)	6(1)	2(1)	5(1)
O(4S)	14(1)	18(1)	12(1)	5(1)	-1(1)	1(1)
O(5S)	12(1)	12(1)	20(1)	6(1)	-3(1)	2(1)

Table 5: Hydrogen coordinates and isotropic displacement parameters for $[Al(H_2O)_6]^{3+}(AlH_6Mo_6O_{24})^{3-}\cdot 10(H_2O)$.

	x	y	z	U(eq)
H(1)	0.224(4)	0.578(2)	0.584(2)	0.010
H(2)	0.460(4)	0.276(2)	0.515(2)	0.010
H(3)	0.232(4)	0.505(2)	0.345(2)	0.010
H(13A)	0.175(4)	-0.140(2)	-0.0646(18)	0.014
H(13B)	0.170(4)	-0.097(2)	0.0408(19)	0.014
H(14A)	0.464(4)	0.175(2)	-0.072(2)	0.013
H(14B)	0.287(3)	0.125(2)	-0.059(2)	0.013
H(15A)	0.478(4)	0.127(2)	0.187(2)	0.014
H(15B)	0.561(4)	0.046(2)	0.214(2)	0.014
H(1SA)	0.662(4)	0.207(2)	0.6177(19)	0.018
H(1SB)	0.629(4)	0.137(3)	0.523(2)	0.018
H(2SA)	0.015(4)	-0.084(2)	0.2085(18)	0.018
H(2SB)	-0.020(4)	-0.1861(19)	0.155(2)	0.018
H(3SA)	0.216(3)	-0.010(3)	0.627(2)	0.018
H(3SB)	0.378(4)	0.036(2)	0.625(3)	0.018
H(4SA)	0.087(4)	0.392(3)	-0.0310(18)	0.018
H(4SB)	0.055(4)	0.418(2)	-0.120(2)	0.018
H(5SA)	0.547(4)	0.300(2)	0.814(2)	0.018
H(5SB)	0.697(3)	0.307(2)	0.868(2)	0.018

Table 6: Torsion angles [°] for $[Al(H_2O)_6]^{3+}(AlH_6Mo_6O_{24})^{3-}\cdot 10(H_2O)$.

O(3)#1-Al(1)-O(2)-Mo(1)	85.37(6)
O(3)-Al(1)-O(2)-Mo(1)	-94.63(6)
O(1)#1-Al(1)-O(2)-Mo(1)	-179.26(6)
O(1)-Al(1)-O(2)-Mo(1)	0.74(6)
O(3)#1-Al(1)-O(2)-Mo(2)	-178.47(6)
O(3)-Al(1)-O(2)-Mo(2)	1.53(6)
O(1)#1-Al(1)-O(2)-Mo(2)	-83.10(6)
O(1)-Al(1)-O(2)-Mo(2)	96.90(6)
O(2)#1-Al(1)-O(3)-Mo(2)	178.48(6)
O(2)-Al(1)-O(3)-Mo(2)	-1.52(6)
O(1)#1-Al(1)-O(3)-Mo(2)	94.35(6)
O(1)-Al(1)-O(3)-Mo(2)	-85.65(6)
O(2)#1-Al(1)-O(3)-Mo(3)	81.76(6)
O(2)-Al(1)-O(3)-Mo(3)	-98.24(6)
O(1)#1-Al(1)-O(3)-Mo(3)	-2.36(6)
O(1)-Al(1)-O(3)-Mo(3)	177.64(6)

Symmetry transformations used to generate equivalent atoms:
#1 -x+1, -y+1, -z+1 #2 -x+1, -y, -z

Table 7: Hydrogen bonds for $[Al(H_2O)_6]^{3+}(AlH_6Mo_6O_{24})^{3-}\cdot 10(H_2O)$ [Å and °].

D-H...A	d(D-H)	d(H...A)	d(D...A)	<(DHA)
O(1)-H(1)...O(5)#3	0.80(3)	2.16(3)	2.9530(19)	171(2)
O(2)-H(2)...O(1S)	0.87(3)	1.80(3)	2.658(2)	173(2)
O(3)-H(3)...O(7)#3	0.82(3)	1.88(3)	2.6938(19)	171(3)
O(13)-H(13A)...O(10)#4	0.750(19)	1.872(19)	2.6180(19)	173(3)
O(13)-H(13B)...O(2S)	0.755(19)	1.882(19)	2.631(2)	171(3)
O(14)-H(14A)...O(5S)#5	0.770(19)	1.795(19)	2.564(2)	177(3)
O(14)-H(14B)...O(2S)#4	0.749(19)	1.99(2)	2.728(2)	166(3)
O(15)-H(15A)...O(6)	0.771(19)	1.798(19)	2.5672(19)	176(3)
O(15)-H(15B)...O(3S)#6	0.741(19)	1.99(2)	2.725(2)	170(3)
O(1S)-H(1SA)...O(7)#7	0.711(18)	2.34(2)	2.919(2)	139(3)
O(1S)-H(1SA)...O(5S)	0.711(18)	2.61(2)	3.103(2)	129(3)
O(1S)-H(1SB)...O(3S)#6	0.667(18)	2.135(19)	2.791(2)	168(3)
O(2S)-H(2SA)...O(9)	0.733(18)	2.19(2)	2.853(2)	150(3)
O(2S)-H(2SB)...O(4S)#4	0.721(18)	2.07(2)	2.719(2)	151(3)
O(3S)-H(3SA)...O(8)	0.708(18)	2.44(2)	2.954(2)	131(3)
O(3S)-H(3SA)...O(9)#8	0.708(18)	2.50(2)	3.080(2)	141(3)
O(3S)-H(3SB)...O(1S)	0.681(18)	2.106(19)	2.766(2)	164(3)
O(4S)-H(4SA)...O(11)	0.722(18)	2.054(19)	2.761(2)	166(3)
O(4S)-H(4SB)...O(7)#5	0.709(19)	2.43(2)	2.870(2)	122(3)
O(4S)-H(4SB)...O(12)#9	0.709(19)	2.45(2)	3.094(2)	153(3)
O(5S)-H(5SA)...O(4)	0.719(19)	2.028(19)	2.742(2)	173(3)
O(5S)-H(5SB)...O(4S)#10	0.716(19)	2.11(2)	2.760(2)	152(3)

Symmetry transformations used to generate equivalent atoms:

#3 -x, -y+1, -z+1 #4 -x, -y, -z #5 x, y, z-1 #6 -x+1, -y, -z+1

#7 x+1, y, z #8 -x, -y, -z+1 #9 -x+1, -y+1, -z #10 x+1, y, z+1

VITA

CORY KYLE PERKINS

Candidate for the Degree of

Doctor of Philosophy

Thesis: SYNTHESIS AND APPLICATIONS OF EARLY TRANSITION METAL OXIDES

Major Field: CHEMISTRY

Biographical:

Education:

Completed the requirements for the Doctor of Philosophy in Chemistry at Oklahoma State University, Stillwater, Oklahoma in May, 2014.

Bachelor of Science in Chemistry at Western Oregon University, Monmouth, Oregon in June, 2009.

Experience:

NSF-REU Fellowship May-August 2008 - Oklahoma State University
Undergraduate Research Assistant September 2008 – June 2009 – Western Oregon University
Teaching Assistant August –December 2009 - Oklahoma State University
Research Assistant December 2009- May 2014 – Oklahoma State University

Publications:

C. K. Perkins, K. N. Barber, and A. W. Apblett, Direct conversion of a nanometric suspension of molybdenum trioxide into nanometric lead molybdate. *CrystEngComm* **2014,** *16* (14), 2869-2873. (Cover Article)

Professional Memberships:
American Chemical Society (2009-Present)